REFINEMENT OF SIMULATED POLYMER-FULLERENE PHOTOVOLTAIC DEVICES THROUGH SMALL ANGLE SCATTERING AND DYNAMIC MONTE CARLO

By

Daniel P. Olds

A DISSERTATION

Submitted to
Michigan State University
in partial fulfillment of the requirements
for the degree of

Physics - Doctor of Philosophy

2013

ABSTRACT

REFINEMENT OF SIMULATED POLYMER-FULLERENE PHOTOVOLTAIC DEVICES THROUGH SMALL ANGLE SCATTERING AND DYNAMIC MONTE CARLO

By

Daniel P. Olds

In order to better understand the effects of morphology on polymer-fullerene based organic photovoltaic devices (OPV), analysis is performed using a dynamic Monte Carlo simulation to study both the exciton and charge behavior. Theoretical morphologies are generated through the use of a modified Ising model which incorporates neutron reflectometry data, and these structures are then characterized and refined through the use of simulated small angle neutron scattering (SANS). A novel technique for quickly calculating the simulated SANS profile of a model, referred to as the distribution function method (DFM), is motivated and introduced.

We generate percolating fullerene/polymer bulk heterostructures that are consistent with experimental characterization of the nanostructure, in particular neutron reflectometry and small angle neutron scattering data from as cast and annealed poly(3-hexylthiophene) (P3HT) and [6,6]-phenyl C61-butyric acid methyl ester (PCBM) systems. Dynamic Monte Carlo transport calculations using these morphologies correlate changes in exciton dissociation efficiency and charge collection efficiency with morphological features including characteristic domain size, fullerene concentration profile, degree of fullerene dispersion, and the impact of polymer fiber crystallization.

To Marilyn, the strongest person I know.

ACKNOWLEDGMENTS

TABLE OF CONTENTS

LIST OF TABLES

LIST OF FIGURES

xvii

xviii

Chapter 1

Introduction

1.1 Motivation

Human beings have developed a rather addictive habit in the past century: the somewhat thoughtless consumption of great amounts of energy for our comfort and enjoyment. Unfortunately, our capability to safely and efficiently generate energy has not grown nearly as quick as our ability to consume it. As our population continues to grow (another habit we as a species are rather fond of) it becomes clear that if we wish to maintain our modern lifestyle, we must explore and develop sources of alternative energy. I have personally always thought the sun seemed rather full of energy, and why don't we try to harness some of that. Most current forms of easily accessible energy can be traced back to the sun's influence[10]. Coal and oil, perhaps two of our worst habits, began their stories as ancient plants and animals who millions of years ago found themselves sustained, directly or indirectly, by the energy of the sun. Today we go to great lengths to discover the high energy chemical bonds of these previous tenants, often found deep underground. After much industry and effort, we extract these complex carbon chains hidden below, and proceed to combust them for our comfort and entertainment or simply to pour them into our gas tanks. Wind and water both move turbines for us, but the currents and motions utilized therein are consequences of the complex thermal and weather cycles in which our sun plays the rather central role of "heater". It seems justified, given it's extensive past experience and outstanding track record, that

we directly consider the sun as principle energy provider for our species. I mean, it's just going to keep shining down on us for the foreseeable future anyway, so further development of photovoltaic, photothermal, and solar to fuel technologies seems fitting.

Arguably, the greatest hurdle one faces in order to fully realize the concept of a solar powered energy economy lies in the cost and efficiency levels of present day photovoltaic (PV) technologies[11, 12]. One promising avenue of research in the last decade has been thin film organic photovoltaic (OPV) devices. With devices typically composed of polymer and nanoparticles arranged creatively on the length scales of 100-300 nm thick, OPV devices have the potential to be both lighter and cheaper than conventional PV, not necessarily replacing them, but becoming a supplementary energy source in designs where conventional PV could not be used[13]. One of the remaining hurdles towards development of industrial quality OPV devices is that their current maximum efficiencies are much lower than conventional PV (about 10% compared to 40%)[14, 15]. It is a principle focus of this thesis to develop tools that help characterize and explain the emergence of the performance limiting behaviors in OPV devices.

Unlike their inorganic counterparts, absorption of a photon in OPV does not immediately generate a free charge, but instead a tightly bound exciton state. In order for this exciton to be dissociated into free charges an additional energetic asymmetry is required inside the active layer of the device, such as the difference in energy levels between the acceptor and donor material. A complication arises due to the relatively short lifetimes of excitons inside these materials ($\approx 10\,ps$), such that even though the exciton may be mobile throughout the device it is only capable of successfully separating into free charges if it is generated within close proximity of an acceptor/donor interface. The parameter known as the exciton decay length ($L_{\text{x-decay}}$), which corresponds to the approximate distance an exciton will diffuse

prior to it's radiative decay, is useful in describing system morphologies. This requirement has led to widespread use of the so called bulk-heterojunction (BHJ) design, in which acceptor and donor material are finely mixed on length scales of order $L_{\text{x-decay}}$ such that most photogenerated excitons easily discover an interface prior to decay. This ease of interface discovery increases the efficiency at which absorbed photons are converted into usable current, known as the quantum efficiency (QE) of the device, by minimizing exciton decay losses. An unfortunate downside to this design comes from the fact that once excitons dissociate into free charges (electrons in the acceptor material and holes in the donor material) the conductive transport path from the geminate location (site of exciton dissociation) to the charge contacts will inevitably be more tortuous and complex in a BHJ structure compared to a simple planar heterojunction. Thus, while the BHJ significantly enhances exciton dissociation efficiencies, it may lead to significant free charge loss. Great care must be taken to design BHJ morphologies which optimize overall quantum efficiency, not simply maximize exciton dissociation behavior while neglecting the effect on free charge.

This complex relationship between morphology and device performance[16, 17] is in no way unique to the field of organic photovoltaics. Many next-generation energy applications have material properties and device performance metrics which are strongly correlated to their internal nanoscale features or morphologies. Batteries, LEDs, fuel cells, sensors, and organic photovoltaics all rely on transport mechanisms intrinsically associated with the interpenetrating, percolative nanostructures employed by these devices[18, 19], and yet no models exist which attempt to directly extract morphology from experimental data, with transport calculations instead relying upon assumed or simplified models. We present a simple model which generates three dimensional interpenetrating percolative nanostructural morphologies that are simultaneously consistent with multiple types of experimental data. Though the

work emphasized in this thesis is on the P3HT/PCBM bulk heterojunction morphology, modeled using small angle neutron scattering (SANS) and neutron reflectometry data, the method is easily adapted to many other systems and forms of experimental data.

In order to characterize these morphological models, we employ transport calculations based on modified dynamic Monte Carlo (DMC) device simulations. The DMC model is excellent at exploring how subtle changes in the nanoscale features of a configurational morphology will influence exciton and charge behavior in the active layer of the OPV. In this thesis we focus on the effect of nanoscale morphology of a polymer/nanoparticle BHJ OPV device. The morphology models used are extracted directly from and then fit to SANS and neutron reflectometry data. We feel that by using morphological models which are more directly correlated with available experimental data, any subsequent theories derived from these models are inherently more accurate than those developed from assumed morphologies. We will compare how the use of assumed morphologies[2] versus the presented more realistic morphologies alters the outcome of transport calculations.

In this thesis, we focus on utilizing SANS and neutron reflectometry data as it pertains to the OPV devices under investigation, but many other viable experimental datasets exist which could readily be incorporated into future modeling efforts. A wide variety of techniques have been employed to better understand the complex systems involved in these BHJ morphologies, including AFM studies probing local photocurrents[20] and space-charge limiting behavior[21], STM[22], SEM[23], and electron tomography[6] based studies which have attempted to directly map the morphology, and attempts to directly observe carrier photo-generation with Kelvin probe force microscopy[24]. Each of these measurements is valuable in it's own right, however none so far have attempted to directly extract a morphological model required for device simulation.

While the reflectometry data used in this thesis has previously been fitted to an exact PCBM density profile[8], and is thus easily incorporated into our morphological model, SANS data is not as directly invertible. While previous standard methods utilizing polydisperse sphere fits have estimated aggregate PCBM cluster size[25], these fits have little physical correlation with the actual system. In order to fit our theoretical models directly to the SANS data, we have developed a novel algorithm we refer to as the distribution function method (DFM), which calculates the SANS profile of a theoretical morphology. Although not as conceptually straightforward as other methods of calculating a theoretical small angle scattering profile[26], the DFM method allows for a more flexible and scalable calculation of a simulated scattering profile, allowing us to easily tune the precision of the calculation while exploring the influence of various features of a morphology on the overall SANS profile.

Utilizing our modified Ising model, novel DFM scattering algorithm, and DMC based device simulation, we will present a step forward in characterization and understanding of the effect of nanoscale morphology on overall device performance of P3HT/PCBM based OPV devices.

1.2 Outline

The focus of this thesis is to describe the developed methods and results from an effort to better characterize and understand the effect of nanoscale internal morphology on various aspects of OPV performance. Though much work has gone into this question in the past[2, 27, 1, 28, 29], this thesis will present modifications to the dynamic Monte Carlo model frequently employed to study OPV, which act to directly refine the morphological model through the use of neutron reflectometry and small angle scattering data. Both the method

used to generate the model morphology itself and the calculations performed to evaluate the theoretical performance will be explained in detail, and the importance of incorporating previously underutilized experimental data will be demonstrated. The bulk of new work presented is to be found in chapters 4 through 6.

Chapter 2 explains the basic principles of photovoltaic devices as well as the differences between conventional PV and thin film OPV. This chapter will also introduce and motivate the strong relation between nanoscale morphology and OPV device performance. Finally, this chapter will present some of the attempts that have been made to enhance device performance through morphology manipulation. This chapter is principally review.

Chapter 3 describes the dynamic Monte Carlo (DMC) transport model used to characterize the performance of a particular morphology. The details of the model will be presented, along with example calculations on a set of simple morphologies. The modifications we introduce to the basic DMC model will then be motivated and explained in detail.

Chapter 4 presents a novel method to efficiently generate a simulated small angle scattering profile from any model morphology which we refer to as the distribution function method (DFM). The benefits and limitations of the DFM method will be discussed, particularly in comparison to the more straightforward direct method employed by other groups[26]. Several examples of well known structures will be presented, demonstrating the validity of the DFM method. This chapter reviews previous small angle scattering calculation methods, as well as introducing our new procedure, and the results of this chapter will be published in a techniques paper.

Chapter 5 describes the modified Ising model we use to generate theoretical P3HT/PCBM BHJ structures that are consistent with neutron reflectometry and SANS data. Though the reflectometry data is directly incorporated into the Ising model, SANS data is not as di-

rectly invertible, and thus we demonstrate how through the use of the DFM method we select and refine our structures until they are consistent with the experimental SANS data. Additionally, we will demonstrate how to expand the simple two-phase model for use in more elaborate system descriptions. One such presented case is a model where one differentiates between aggregate PCBM and dispersed PCBM, as is suggested to occur in real devices after annealing[30, 4]. Another presented model will incorporate P3HT crystallization. The modified Ising model we present, which allows for morphologies directly extracted from experimental data, is entirely new and has recently been published[31].

Chapter 6 presents the results of DMC device simulations performed on the modified Ising model morphologies introduced in chapter 5 and compares these results to those calculated from more primitive morphological models.

We will also discuss the ability to incorporate additional experimental data into this type of morphologically driven device simulation. As the contents of this chapter will summarize the bulk of the work, the results presented in this chapter have been recently published[31].

Chapter 7 presents conclusions of this work and directions for future work.

Chapter 2

The Basics of OPV

2.1 Solar Cell Devices

The essential mechanism for the generation of power in a photovoltaic (PV) device (solar cell) is unsurprisingly, the photovoltaic effect[32]. Similar to the photoelectric effect, wherein photon induced excitation ejects electrons from a material's surface, in the photovoltaic effect an absorbed photon's energy is transferred to an electron within the absorbing material. By absorbing this energy, the electron is freed from it's previously bound state such that it becomes mobile inside the material[33]. The sudden absence of an electron in the absorbing material generates a mobile vacancy site which acts as a positively charged particle in the system, called a hole[34]. In solar cell design, the goal is to collect these photoexcited free charges (both the electron and hole) at the contacts of the device where they may perform work on an external circuit. In this way a solar cell is not a voltage source like a battery, but rather a current source[35]. Not all photoexcited charges will successfully be collected at the contacts however, as there are a number of loss mechanisms inherent in photovoltaic devices.

As charges are being generated in oppositely charged pairs (one hole and one electron) a solar cell requires a mechanism to separate these opposite charges and drive them to the opposing contacts. Note that photocurrent is often defined as flowing in the reverse direction of a circuit (electrons moving to the cathode and holes to the anode) as the device is supplying
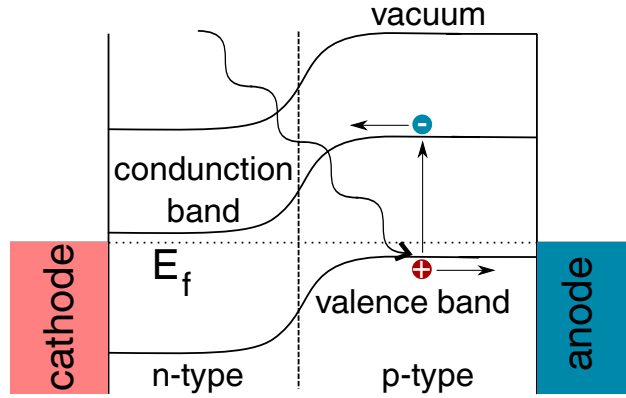
Figure 2.1   Schematic of a simple PN junction in a solar cell at short-circuit condition, as evidenced by the energy levels of the anode and cathode being equalized. Absorbed photon excites an electron from the valence band into the conduction band. The electron and hole can then follow the chemical potential gradient to the cathode and anode respectively. The Fermi energy, E_f, exists between the valence and conduction bands. For interpretation of the references to color in this and all other figures, the reader is referred to the electronic version of this dissertation.

power rather than consuming it, hence the convention that the photocurrent generated in a solar cell is negative. The principle physics inherent to conventional photovoltaic devices are well illustrated using a band structure diagram, such as the example presented in figure 2.1. In order to photoexcite charges, absorbed photons must have sufficient energy to excite an electron in the valence band across the band gap (E_{gap}) into the conduction band. Once excited, the now mobile electron and hole will follow the chemical energy gradient of the device. This gradient, represented by the slope of the bands in figure 2.1, may arise from a number of sources such as the depletion zone formed in a pn-junction, a charge population concentration gradient, the difference between the work functions of the contacts when connected to an external circuit, or an applied external potential. In band diagram representations electrons will flow down a potential gradient and holes (because of their opposite charge) will flow up. Both charges travel along the bands until they are either collected at the contacts or otherwise lost. The total power delivered has the familiar form

$$P = I \times V, \tag{2.1}$$

where P is the power, I is the current delivered, and V is the voltage at which this current is collected. This potential difference across the device from anode to cathode arises due to the quasi-Fermi level separation of the charges[36]. The maximum delivered photocurrent under no applied load is called the short-circuit current, I_{SC}. As photocurrent will be proportional to the total area of the solar cell upon which light is incident, it is often convenient to describe the current density rather than the absolute current. The short-circuit current density, J_{sc}, may be described by the function

$$J_{SC} = q \int dE_\gamma \, b_s(E_\gamma) \, QE(E_\gamma), \tag{2.2}$$

where the integral is taken over E_γ, which spans all photon energies incident upon the solar cell, q is the charge of an electron, $b_s(E_\gamma)$ is the incident photon flux as a function of photon energy, and QE is the quantum efficiency, which describes the probability that a photon with given energy (E_γ) incident upon the device will successfully deliver a charge to the external circuit.

At the contacts themselves, a slight energetic mismatch will likely exist between the active material of the solar cell (the p-type or n-type semiconductor) and the electrode. If the transition between the two materials results in an energetic barrier inhibiting charges from leaving the active layer to the contact, it is referred to as a Schottky barrier. Charge must tunnel through or be thermally excited over a Schottky barrier in order to be collected[37]. This delay in collection time can lead to the build-up of a space-charge layer near the contacts, which can further impede charge transport. By contrast, if the resultant barrier enhances

charge transport across the barrier by nature of being at a lower energy state for the charge relative to it's energy in the semiconductor, the contact is referred to as Ohmic[38, 39].

In any device with a quantum efficiency of less than unity, not all photogenerated charge is being successfully collected at the contacts. The three main loss mechanisms are radiative recombination, Auger recombination, and trap assisted recombination[35, 40]. Radiative recombination occurs when an electron relaxes across the band gap, emitting an associated photon of energy E_{gap}. Radiative recombination is a common loss mechanism in a conventional solar cell, with it's rate being governed by the width of the band gap. Auger recombination also involves relaxation of a charge carrier across the bandgap, but the energy released acts to push a different charge carrier to a higher energy level in the same band. In terms of PV devices, this sacrifices one charge with no particular energetic gain for the other, as the charge excited above the band edge will quickly thermalize back to it's previous energy level at the bandgap edge. Auger recombination is only a significant loss mechanism in systems with a high free charge density, which rarely occurs in conventional devices under normal operating conditions. Trap assisted recombination occurs when charges become trapped in energetic defects (traps)[41] which have an intermediate energy in the band gap, such that the trapped charge gives up this difference in energy in the form of phonon radiation (heat). Trap assisted recombination is often the dominant form of loss near the surface of a device, due to defects introduced by the bulk termination at the surface[38].

The potential difference applied by an external load will cause external charges present in the contacts to be injected into the active layer of the solar cell. The injected charges flow in the opposite direction to the flow of photogenerated charge current towards the contacts[35]. This injected opposing flow of charges is referred to as the dark current density, J_{dark}, as it will be present whether the solar cell is under illumination or not. Though "dark" charges

11
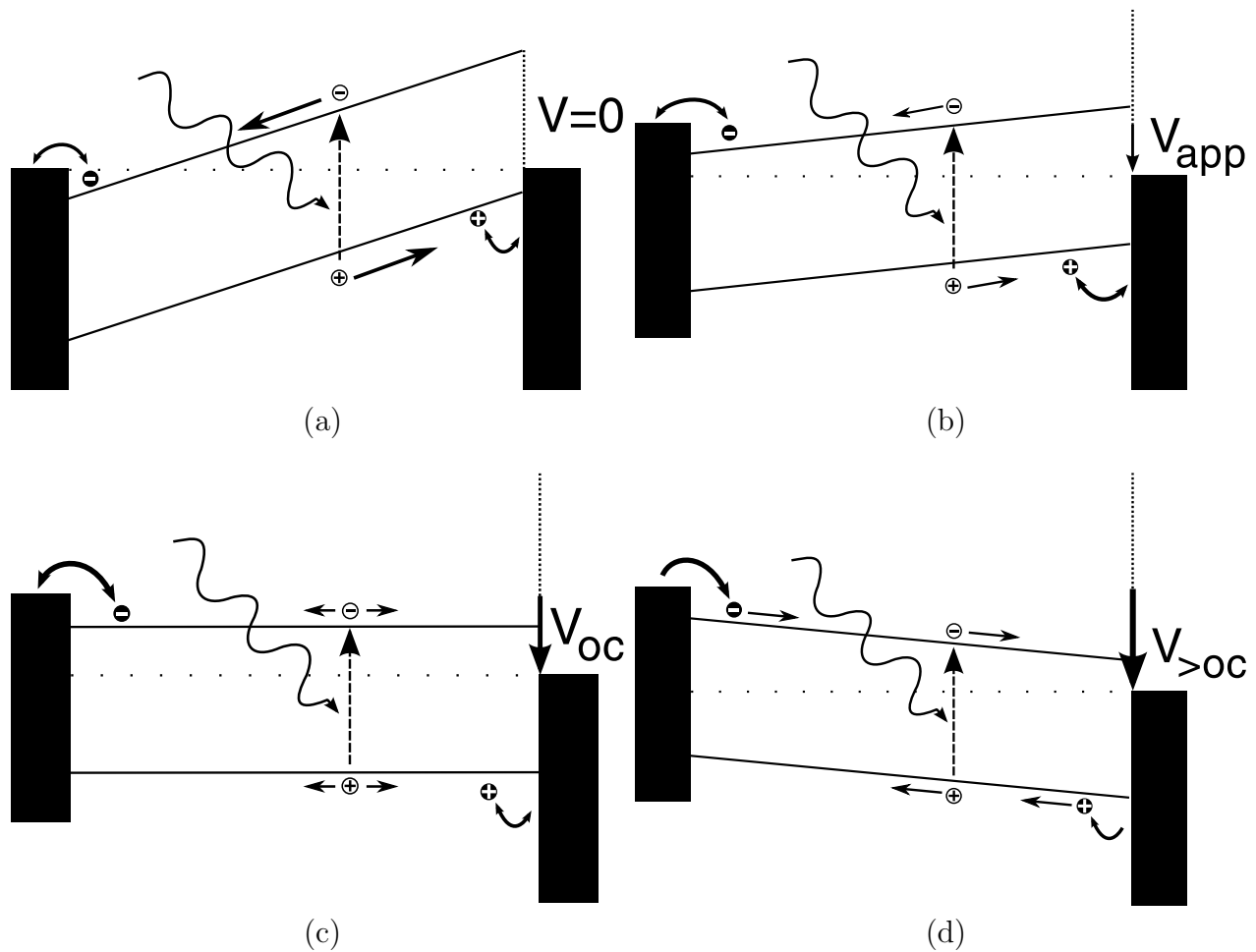
Figure 2.2 Demonstration of applied voltage to a simple solar cell band diagram. As the open circuit voltage, V_{oc} is passed, the runaway diode behavior emerges.

are continuously thermally injected from the contacts into the solar cell[37], because of the band structure design of conventional PV devices they will likely be unable to travel across the device until sufficient external bias is applied, as is demonstrated in figure 2.2. This diode-like behavior of the dark current is a common feature in solar cells, principally due to the rectifying features of their internal energetics favoring charge transport in one direction. One may describe the dark current density, J_{dark}, with an ideal diode equation

$$J_{\text{dark}} = J_o \left(e^{qV/k_B T} - 1 \right), \tag{2.3}$$

where J_o is a constant, V is the net voltage across the device, and $k_B T$ is the Boltzmann constant times the temperature.

The equivalent circuit for a solar cell, seen in figure 2.3, demonstrates a photon induced current source (J_{SC}), a dark current contribution modeled as a diode (J_{dark}), additional current losses modeled as a parallel and series resistance (R_p and R_s respectively), and the contact points across which a solar cell would be connected to an external circuit with a potential difference when a load is applied (V).

Though a solar cell will deliver the maximum photocurrent at short-circuit, it is often desirable to apply an additional external voltage which acts to oppose the flow of the photocharges. The reason for this applied voltage, V_{app}, is to increase the total power delivered by increasing the potential at which the photocharges are collected at the contacts. At a certain threshold voltage, however, the flow of the photocurrent will be stopped entirely rendering the solar cell useless. Because of the desire to maximize power delivered by the device, solar cells are often evaluated with a current versus voltage (IV-curve) or current density versus voltage (JV-curve), an example of which is seen in figure 2.4.
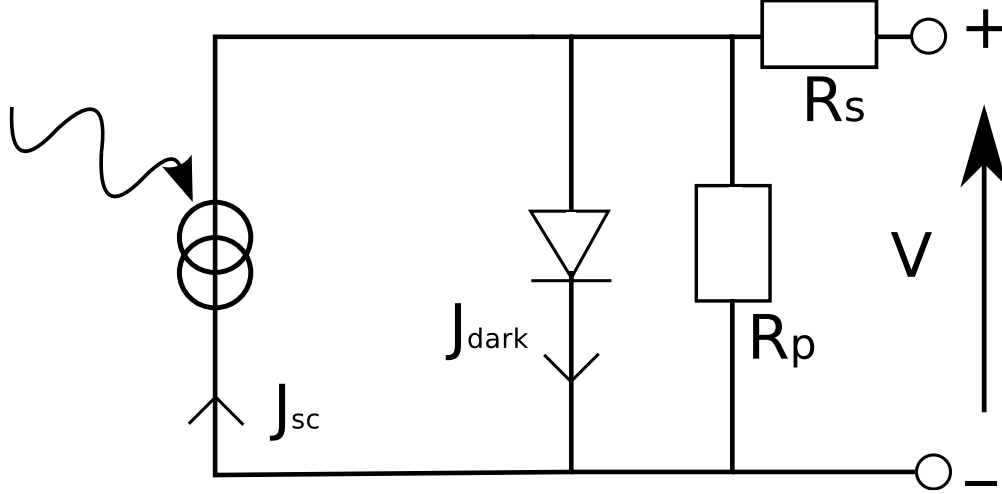
Figure 2.3   Equivalent circuit for a solar cell, showing photon absorption generating a short-circuit current density, J_{SC}, which has losses represented as a parallel and series resistances, R_P and R_S respectively.   Dark current, J_{dark}, is represented as a diode in the reverse direction of the photogenerated current.

Though figure 2.4 is a function of applied voltage, V_{app}, recall that the total voltage across the device will be the combination of the applied voltage and the built-in bias, V_{bi}, such that the total voltage across the system is denoted $V_{net} = V_{bi} - V_{app}$. Three important points of note on any JV-curve are the short-circuit current density (J_{sc}), the open-circuit voltage (V_{oc}), and the maximum power point[35]. The short-circuit current density describes how the system behaves when no external voltage is applied $(V_{app} = 0)$ and is the maximum possible collected current in the device. The open-circuit voltage is the point at which the applied voltage has caused the net potential across the cell to be zero[42], at which point the net current inside the device will be driven only by charge diffusion, which is typically much smaller then the contribution of the drift current. The maximum power point is the location on the JV-curve where total delivered power will be maximized, at voltage V_m and current density J_m, which is subsequently the point of optimal device operation. In any regime of the JV-curve outside this quadrant, either with applied voltages greater than V_{oc} or under a reverse bias with $V_{app} < 0$, the solar cell will consume rather than generate power. A solar

14
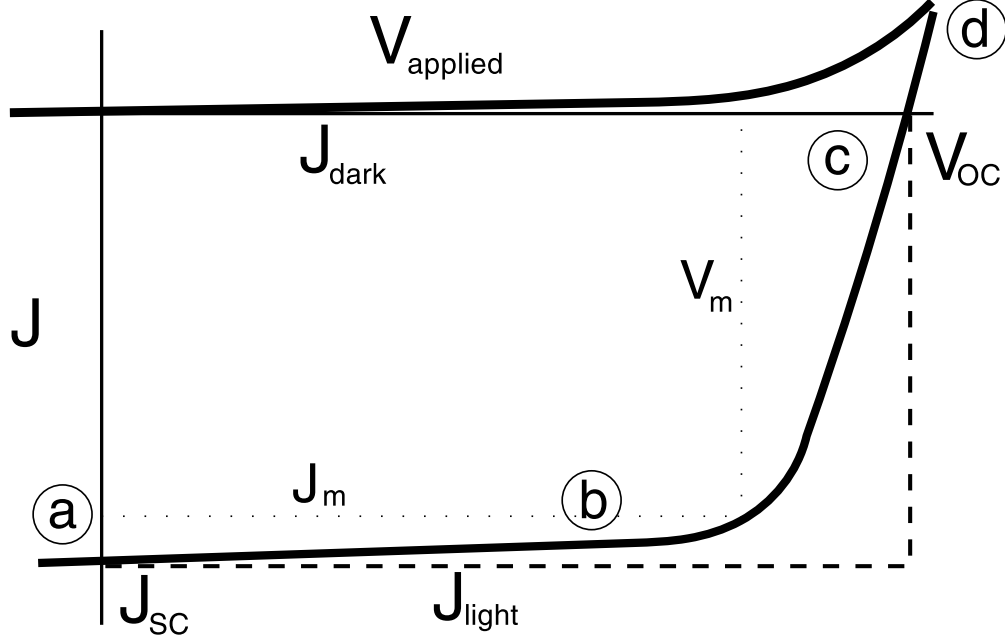
Figure 2.4 Example of a current density (J) versus applied voltage (V_{applied}) graph, demonstrating the diode like behavior of a solar cell. Curves are shown for both a device in the dark (J_{dark}) and under illumination (J_{light}). Also shown on the graph are the open circuit voltage, V_{OC}, short-circuit current, J_{SC}, thick dashed line to better understand the fill factor, FF. Notable behavior points occur at short circuit, ⓐ, near maximum power, ⓑ, near open circuit, ⓒ, and finally at runaway diode-like behavior, ⓓ.

cell's ability to "fill-out" the area of it's JV curve to the maximum possible power, $J_{sc} \times V_{oc}$, is described by the fill factor, FF, defined

$$FF = \frac{J_m V_m}{J_{sc} V_{oc}}. \tag{2.4}$$

The total efficiency, η, of a solar cell describes it's ability to convert incident light power into usable work, defined as

$$\eta = \frac{J_m V_m}{P_s} = \frac{J_{sc} V_{oc} \, FF}{P_s}, \tag{2.5}$$

where P_s is the incident power density, delivered by the photons, to the solar cell.

Photogenerated free charges will transport throughout the solar cell by a combination

15

of electrostatic field induced drift and concentration gradient driven diffusion. The current densities in a solar cell at equilibrium can thus be separated into a drift component and a diffusion component, described (in one dimension) as[35]

$$J_n = qD_n\nabla n + q\mu_n F_n \tag{2.6}$$

$$J_p = -qD_p\nabla p + q\mu_p F_p, \tag{2.7}$$

where $J_{n/p}$ is the net current density for electrons/holes driven by the diffusion due to the gradient of the charge population density, $\nabla n/p$, the charge mobilities, $\mu_{n/p}$, and the diffusion constants, $D_{n/p}$, through the use of the Einstein relationship

$$\mu = \frac{qD}{k_B T}. \tag{2.8}$$

Note that this approximation of current is only valid in the regime where charge populations are at thermal equilibrium with the Fermi level, the material has a relatively low density of defects or traps, the charge population is well described by Boltzmann statistics (non-degenerate semi-conductors), and the gradient of the effective field (band gradient) is relatively constant over the device[43]. This simple model does not explicitly incorporate any morphological information, utilizing only an average mobility and charge population to describe the photocurrent.

2.2 Organic Photovoltaics

Organic photovoltaic (OPV) devices have great promise for applications unsuitable for conventional solar cells, due to their light-weight and potentially less expensive fabrication costs[15, 13, 2]. The difference in underlying mechanics and design of OPV systems compared to their inorganic counterparts stems from the fact that the energetics in an OPV systems arise from disordered molecular systems, rather than continuous band structure seen in conventional semiconductors. These molecular materials cannot strictly be thought of as p-type and n-type semiconductors, as there are no inherent free charges to be exchanged and thus no depletion region will will form at pn-junctions. Instead, OPV systems are described as a combination of acceptor and donor materials[44], requiring their energetic design considered through molecular based HOMO (highest occupied molecular orbital) and LUMO (lowest unoccupied molecular level) levels, rather than valence bands and conduction bands. An example of a molecular based OPV HOMO/LUMO level diagram is shown in figure 2.5. In these materials, absorbed light will not immediately generate free charges as in conventional PV, but instead generate strongly bound Frenkel excitons. These photogenerated excitons must be dissociated prior to exciton decay if the charges are to be collected at the contacts.

The exciton is a bound state of an electron and hole pair, Coulombically bound to one another resulting in a bosonic particle (being the combination of two spin one-half particles). In these materials, excitons exist for a very brief period of time compared to free charges (on the order of picoseconds) before they decay[45], with the energy lost through radiative (photon emission) or non-radiative (phonon emission) processes. On a band diagram, excitons exist as states slightly inside the bandgap, such that they are at a lower energy state

than the two free charges unbound from one another. In most conventional photovoltaics, photogenerated excitonic states are readily separated via thermal excitation or internal field gradients, such that most models of conventional solar cells do not even take the exciton into account.

Unlike conventional PV, the internal energetics of an OPV device are often insufficient to naturally facilitate exciton dissociation, requiring an additional energetic asymmetry to do so. This asymmetry can be provided by the energetic contrast present at interfaces between acceptor and donor material, called a heterojunction[35]. This naturally suggests fabrication of devices in which exciton is likely to discover, via it's drift motion, a heterojunction interface prior to decay. The most widely studied morphology fitting this requirement is the bulk-heterojunction[46] (BHJ), in which the active layer of the device is composed of a finely mixed blend of acceptor and donor material such that the length scales of the absorbing material domains are of the same order as the exciton decay length.

Once an exciton reaches a BHJ interface, the difference in energies of the HOMO/LUMO levels between the acceptor and donor materials is sufficient to separate the tightly bound exciton into it free charge carriers. In these OPV systems, the dissociated electron is considered bound inside the acceptor material, as transport back to the donor would involve passing into a higher energy state and is therefore unfavorable. Similarly, the hole is bound inside the donor material. The limitation of the BHJ design is that while it greatly enhances exciton dissociation efficiencies, it decreases the overall charge collection efficiency[2, 47] due to the tortuous path a free charge is forced to follow (electrons through the acceptor material only, and holes through donor only) to reach the contacts. Optimization of the internal morphology such that it satisfies the transport requirements of both excitons and free charges is thereby a principle concern in the development of higher efficiency OPV devices.

18
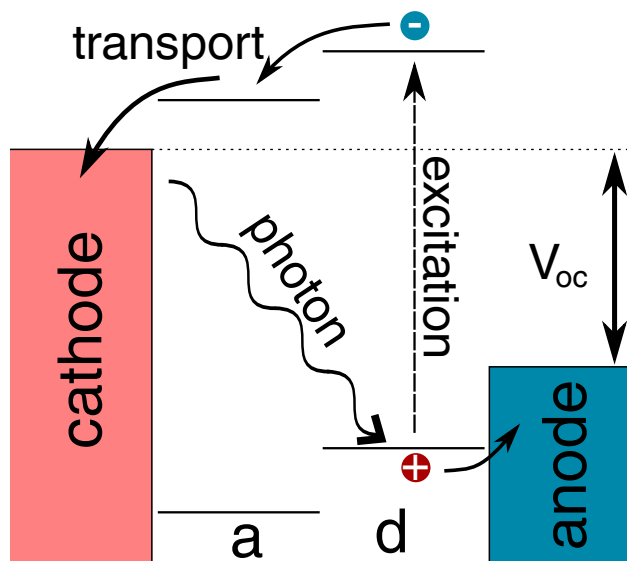
Figure 2.5 Example of a molecular PV device, showing photoexcitation occurring in the donor material, then charge separation and transport to the contacts. Note the lack of any band bending, but rather hopping between HOMO levels (hole transport) and LUMO levels (electron transport).

Free charges in molecular devices are typically more localized than their inorganic counterparts, due to the energetic disorder inherent in the complex disordered energies and morphologies associated with OPV. This leads to charge mobilities in OPV devices which are orders of magnitude smaller than those seen in their inorganic counterparts. Additionally, charge transport is often modeled as a hopping process as compared to a continuous current, with the hopping charges jumping between localized minima energy states on timescales associated with random energetic fluctuations inherent in the system, as is conceptually demonstrated in figure 2.6.

Free charge recombination is arguably a greater concern in organic systems, as evidenced by their lower quantum efficiencies compared to inorganic devices. This is in part due to the lower mobilities preventing free charge pairs from escaping the Coulombic attraction that exists between them. Additionally, the lack of free charge within molecular materials leads to a lack of any significant Debye screening effects. Consequently, the only energetic screening in
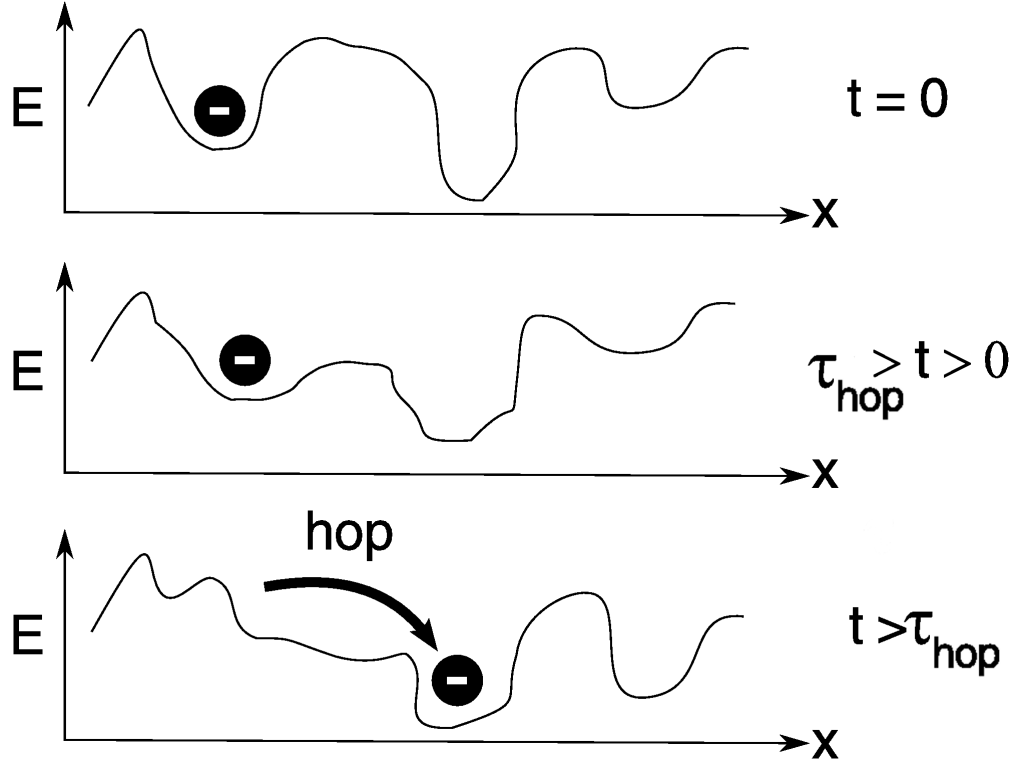
Figure 2.6   Qualitative illustration of how a charge hops on a length scale related to thermal vibration of a local energy landscape.

these devices originates from the fluctuating random thermal contributions to the energetic landscape, described by a Bjerrum length. Free charge recombination is often specified as being either geminate or bimolecular in nature. Geminate pair recombination refers to a pair of charges that were generated together (from the same photon absorption/exciton dissociation event) recombining and thus being lost. Bimolecular recombination refers to a charge which had successfully escaped it's initial partner but then recombines with an opposite charge some time later. Because of the low carrier densities present under normal illumination conditions, geminate recombination seems likely the dominant form of charge recombination, as opposed to bimolecular.

2.3 P3HT/PCBM OPV Device Design

The devices we model in this thesis are based on the work of Jonathan Kiel, of Michael Mackay's group at the University of Delaware. These solar cells were inspired by the popular polymer/nanoparticle bulk heterojunction design[48], which uses the conductive polymer, poly(3-hexylthiophene) (P3HT) as a donor material and the conductive nanoparticle, [6,6]-phenyl-C61-butyric acid methyl ester (PCBM) as an acceptor material. A simple schematic for the device is shown in figure 2.7.

The active layer of these devices is composed of a 1-to-1 by volume mixture of P3HT and PCBM, which is then spin coated onto a prepared front contact. The front contact must be transparent to incident photons, so that the photons may reach and be absorbed in the active layer. Indium tin oxide (ITO) is a common choice for the front contact material, but other common materials include fluorine doped tin oxide (FT) or doped zinc oxide. Prior to spin coating, the front contact is often coated with an electron blocking layer of poly(ethylene dioxythiophene):polystyrene sulfonate (PEDOT:PSS) so that only holes will be collected at the anode (ITO) contact. Post spin cast annealement of the active layer was found to cause an overall improvement in the final device performance[8, 25]. The back contact is typically a metal, often aluminum, which is carefully evaporated onto the active layer.

In these P3HT/PCBM devices, photons are absorbed only into the polymer (P3HT) generating excitons. These excitons diffuse, with hop rates influenced by local site energies[49], until they either discover a bulk heterojunction (BHJ) interface or decay. Though some evidence suggests that decaying excitons emit photons which may later be reabsorbed in the polymer and form a new exciton, for the purposes of our work we consider any decayed exciton as lost. This assumption is justified because the decay-generated photons would

likely have wavelengths just below the HOMO-LUMO gap energy, and thus the likelihood of re-absorption in these materials would be small.

Dissociated excitons form a pair of charges which are localized within separate materials (electrons in the acceptor and holes in the donor) but are still strongly attracted to one another via their Coulomb potential[50]. As the density of photogenerated free charges is relatively low in these devices under normal operating conditions, no screening due to local charge induced fields need be considered. We consider the attraction between these charges to be a function of only their separation distance and the difference in dielectric constants of the acceptor and donor materials. We may write the potential, ϕ, experienced by a charge due to it's geminate partner as

$$\phi(r, z) = \frac{2q}{(\epsilon_2 + \epsilon_1)} \left(\frac{1}{r} \right) - \frac{(\epsilon_1 - \epsilon_2) q}{(\epsilon_2 + \epsilon_1) \epsilon_1} \left(\frac{1}{2z} \right), \tag{2.9}$$

where q is the charge sitting in a material of relative dielectric constant ϵ_1 at a distance of z from the interfacial boundary, while it's geminate partner (having opposite charge) resides in the opposing material of relative dielectric ϵ_2, at a total distance of r from the charge. The full derivation of equation 2.9 is provided in appendix A.1. As the force on a charge q_1 by charge q_2 is given $F = -q_1 \frac{\partial \phi}{\partial r}$, this will generate an overall attractive force due to the opposing charge, given in the first term of equation 2.9. The second term of equation 2.9 will either be positive or negative, dependent on whether the image charge is generated in a material of lower relative dielectric constant (resulting in a repulsive force) or higher relative dielectric (resulting in an attractive force).

If the relative dielectric constants are equal, such that $\epsilon_1 = \epsilon_2 = \epsilon$, then equation 2.9 will simplify to the familiar form

$$\phi(r,z) = \frac{2q}{(\epsilon + \epsilon)}\left(\frac{1}{r}\right) - \frac{(\epsilon - \epsilon)\,q}{(\epsilon + \epsilon)\,\epsilon}\left(\frac{1}{2z}\right)$$
$$= \frac{2q}{(2\epsilon)}\left(\frac{1}{r}\right)$$
$$= \frac{q}{\epsilon r}. \tag{2.10}$$

Conformational variations and deep energy traps lead to a Gaussian like density of states, σ_r, throughout the transporting medium with some width [43] which for these devices has assumed values around $\sigma_r \approx 1 \times 10^{-20} J \approx 1/16\,eV$ [51]. If the geminate pair separates to a distance such that the Coulomb potential between the charges is less than the energetic width of density of states, we may consider a pair now fully separated free charges. This is not to say charges reaching this range are certain to be collected at the contacts, only that any further recombination is to be considered bimolecular rather than geminate. The average size of a geminate pair will thus be determined by the dielectric constants of the materials and the hop rate of the charges.

Free charges are considered localized to $1\,nm$ in these systems, with a single charge confined in a thermally oscillating energetic landscape. Charge transport is driven by a hopping mechanism well described by Marcus theory[51, 43, 52], which will be further discussed in section 3.3 of this thesis. Free charges within the confines of their respective material (electrons in acceptor and holes in donor) will hop throughout the morphology until they are either collected at the contacts or lost due to recombination.
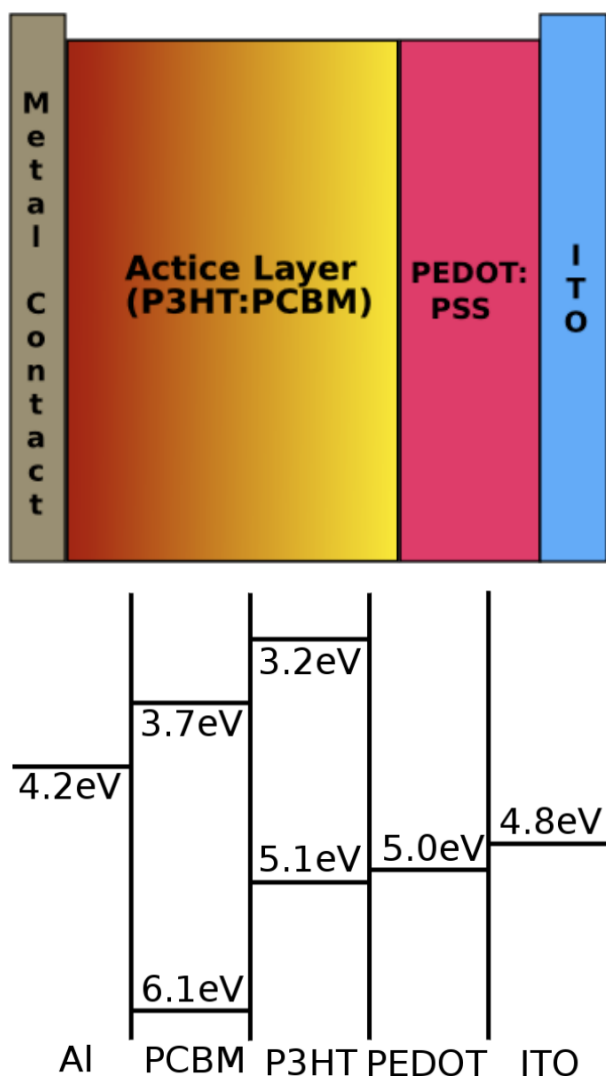
Figure 2.7 Schematic of a P3HT/PCBM based OPV device, with the physical layers shown in the top figure and the corresponding energy levels on the bottom. In this diagram, light passes in from the right hand side and is absorbed in the active layer. Electrons travel to the back metal contact (typically aluminum) and holes, passing through the PEDOT:PSS, are collected at the top contact (ITO).

Chapter 3

Monte Carlo Device Model for OPV

In this chapter, we begin by summarizing the different scales of modeling used in OPV simulations and giving a background of the calculations that have been performed. We motivate our use of the dynamic Monte Carlo (DMC) model for use in exploring the effects of morphology on OPV device performance, summarizing how the DMC method has been used previously. We will explain the DMC model in detail as well as the origin of the event rates used for both excitons and charges. We will demonstrate an application of the DMC model on simple bilayer systems with a number of different calculations, testing both the effect of system energetics and morphology. Though we ultimately modified the presented DMC method to better fit our focus on the direct effects of morphology on transport (see chapter 6), we present the standard method in full detail here.

3.1 The Scales of Modeling and Literature Review

Modeling of organic photovoltaic devices is useful to both better understand how internal mechanisms effect device performance and to help design higher efficiency devices[53]. The principle factors involved in an OPV device's performance, and thus the factors under investigation by simulation, may include photon absorption and conversion, exciton generation and transport, charge generation and transport, carrier loss mechanisms, trapping, internal field effects, HOMO/LUMO levels, charge extraction at contacts, and dark charge injec-

tion. With so many different mechanisms influencing OPV device performance, no single model exists which simultaneously incorporates all these mechanisms on a device scale[54]. The models used in OPV device simulations can be separated into three scales, macroscopic models, mesoscopic models, and atomistic models.

Atomistic models are those which occur on the smallest length scale (1 Å - 5 nm) and are the most precise calculations of the processes occurring inside the device, often treating these processes with the most physically precise theories. Examples of atomistic scale calculations include quantum mechanical calculations of exciton transport dynamics across polymers[55], photon absorption and localized exciton mechanics [56], calculations of charge transfer or separation across a heterojunction[57, 58, 59, 60, 61], self-consisted field theory studies of polymer phases[62], and Monte Carlo calculations of charge dynamics across HOMO/LUMO gaps[43, 63]. Simulations on the atomistic scale, while more accurate than larger scale models, are computationally infeasible to implement on length scales required for full device simulations.

Macroscopic models are those which simulate the largest ($100nm - 1\mu m$) and subsequently coarsest length scales. These models are capable of simulating an entire device, but to do so must approximate the internal features in some way. Additionally, these models rarely simulate individual charges, instead modeling charge densities and net currents and often producing full IV characteristics for a device. One of the most common types of macroscopic models are the so called drift-diffusion calculations[64, 65, 28, 66, 67], which examine the influence of effects such as trap states[68, 69], mobility dependence[70], material mixture ratios[71], and doping effects[72]. Other examples of macroscopic models include simple reaction rate calculations[73] or detailed balance studies[74].

While atomistic scale models are the most physically accurate, their small scale pre-

vents their use in exploring device-spanning phenomena. On the other end of the spectrum, macroscopic models are quite capable of full device characterization, but only when utilizing simplified morphological models which may wash out detailed nanoscale features. We feel a third scale of simulation, the mesoscopic models ($2nm - 400nm$), are ideal for investigating the influence of nanoscale morphology on a wide breadth of physical mechanisms of interest in these OPV systems.

Mesoscopic models often simulate individual charge and exciton transport over a sample or cross-section of the total device. The transport mechanisms in mesoscale models are often abbreviated or simplified from those used in atomistic models. Many mesoscopic models utilize the Dynamic Monte Carlo (DMC) method and include studies of the influence of nanoscale structure on device performance[2, 51, 1, 75, 76, 77]. These models are readily expanded to include many different effects, such as energetic disorder[27, 78, 79, 80], charge separation and recombination[81, 82], surface wetting effects[83], localized trapping[84], electrode heterogeneity[85], material roughness[86], and light intensity[87]. Because of their simplified transport mechanisms, mesoscopic scale models inherently lack the precise detail provided by atomistic scale calculations. However, because of the much broader view accessible by models of this scale, the influence of internal nanoscale features may be explored over lengths associated with charge lifetimes. We believe that mesoscale models, specifically the dynamic Monte Carlo model, offer an ideal tool with which to bridge the information gap between the accuracy of atomistic scale calculations and the macroscopic scale calculations required for efficient full device characterization.

3.2 Basics of the Dynamic Monte Carlo OPV Model

In it's simplest form, the dynamic Monte Carlo (DMC) device model simulates a solar cell's active layer, a nanoscale morphology composed of two materials: an electron acceptor (such as PCBM) and donor (such as P3HT)[88]. The precise structure is defined on a cubic lattice, with each site being defined as one material or the other. System dynamics are simulated via modeling the transport of individual excitons, electrons, and holes; all of which are modeled as single lattice-site occupying particles. The DMC model is viable in both two[89] and three dimensions[2], though we will focus on to the three dimensional case for this thesis. The assumption is made that free electrons are bound inside the acceptor material, and free holes are bound inside the donor material. This assumption is justified because of the difference in energy levels between the HOMO/LUMO levels of the acceptor and donor material, as seen in figure 2.7.

Excitons are generated randomly throughout the bulk of the morphology's donor sites, and diffuse until they either discover a heterojunction interface (a donor site adjacent to an acceptor site) where they may dissociate into free charges or decay. Free charges are generated in electron-hole pairs, and proceed to drift/diffuse throughout the morphology until they either discover an electrode and are collected, or are lost due to recombination. Real devices typically have an electron blocking layer, such as PEDOT:PSS, between the active layer and the hole collecting electrode in order to prevent photogenerated electron injection into the wrong contact (as this would generate current flowing in the wrong direction, and thus consuming power). In this simple model, we approximate this by only allowing charges to be collected at their respective contacts (electrons at the cathode, holes at the anode).

The model morphology is mapped onto a cubic lattice with all sites being assigned as

either pure acceptor or pure donor, with a typical lattice spacing of $a_l = 1$ to $3\,nm$. Periodic boundary conditions are considered to occur in the x and y (horizontal) directions, with reflective boundaries assumed in the z (vertical) direction. Additionally, electrodes are assumed at the edges of the z direction, with the electron collecting electrode (a metal, such as aluminum) at the air interface ($z = 0$) and the hole collecting electrode (transparent conductive contact, such as ITO) on the substrate ($z = L_{\mathrm{z}}$). Due to the assumed confinement of electrons in acceptor material and holes in the donor material, there must exist a nearest neighbor percolative path from any site to the corresponding contact if charges generated upon such a site are to be collected.

3.2.1 First Reaction Method

The first reaction method (FRM) is a common algorithm used in Monte Carlo transport simulations of OPV systems[2, 47], and is useful in efficiently handling a number of dynamic particle trajectories simultaneously. The basic premise is that one keeps a chronologically ordered queue of future events and their associated times. Every possible event in the system (such as charge movement, recombination, collection at electrode, etc) is assigned an associated rate. During each simulation step, the top event is removed from the queue and, so long as that event is still possible, executed. After event execution, all candidate next events for the involved particles are considered, with associated times generated from a characteristic rate as

$$\tau_{\mathrm{event}} = \frac{-1}{\omega_{\mathrm{event}}} \ln X, \qquad (3.1)$$

where τ_{event} is the candidate event time, ω_{event} is the associated characteristic event

rate, and X is a uniform random number between 0 and 1. Equation 3.1 is taken directly from the Gillespie algorithm[90], and will produce stoichiometrically correct results for the rate given while still being dynamically unpredictable. For example, an event with a characteristic rate of $\omega_a = 20$ would be selected 4 times more often than an event with rate $\omega_b = 5$. All candidate events have associated times generated in this manner, but only the candidate event which produced the fastest time is selected and inserted into the queue at it's chronologically associated position.

3.2.2 Exciton Events

For excitons in our model, possible events and their associated rates include exciton generation on a donor (P3HT) site due to light absorption ($\nu_{\text{X-gen}}$), hopping movement to any neighboring site ($\nu_{\text{X-hop}}$), exciton decay ($\nu_{\text{X-decay}}$), and dissociation into free charges when adjacent to a heterojunction (HJ) site ($\nu_{\text{X-diss}}$). Commonly used values are shown in table 3.1.

3.2.2.1 DMC exciton generation

As excitons in this model are generated due to photon absorption, one could apply the Beer-Lambert law in order calculate the exciton generation rate. The Beer-Lambert law describes photon absorption in a material with an exponential decay as a function of thickness and density of the material, cumulatively describing a path-length. A simple derivation for the Beer-Lambert law begins by dividing the absorbing sample into a series of thin slices, perpendicular to the incident light.

The assumption is made that the beam intensity decreases as it passes through each slice of the material due to molecular absorption and that all particles absorbing light in the slab

have a perpendicular cross-section to the beam, σ, such that any light not absorbed in a thin slab passes through. The thickness of a layer, $\mathrm{d}z$, is considered to be thin enough that one absorbing particle does not obscure the interaction of the photons with another particle. As each slab has a definable area, A, and we assume each absorbing particle has a specific cross-section, we define each slab to have a particle density, n. The fraction of photons absorbed by a specific slab will be proportional to it's opaque surface area $(\sigma A N \mathrm{d}z)$ divided by the area of the slab such that one may write the intensity absorbed by a given slab as

$$\mathrm{d}I_z = -\sigma n I_z \mathrm{d}z, \tag{3.2}$$

where we specified the intensity lost, I_z, due to a specific layer, $\mathrm{d}z$. After rearranging and integrating, we come to the equation

$$\ln[I_z] = -\sigma n z + C, \tag{3.3}$$

where C is a constant due to integration. If we assume the difference in intensity for a sample of thickness, l, is described such that it has intensity I_0 at the surface $(z = 0)$ and final intensity I_l at the bottom of the sample $z = l$, then the difference in intensity across the sample may be written

$$\ln[I_l] - \ln[I_0] = (-\sigma l n + C) - (0 + c) = -\sigma l n. \tag{3.4}$$

Defining the transmission through a sample, T, as the fraction of light intensity at the bottom of the sample (I_l) over the intensity at the surface (I_0), we see the expected exponential decay of intensity, as a function of thickness and other absorption parameters

$$T = \frac{I_l}{I_0} = e^{-\sigma ln} = e^{-\alpha l}, \tag{3.5}$$

where we have combined the absorption parameters of number of particles and particle cross-section into one parameter, α.

For many thin film OPV devices, however, the photon absorbing active layer is so thin (on the order of 100 nm) that the Beer-Lambert law is not required to accurately simulate device performance, as photon absorption may be treated as a constant throughout the thickness of the active layer[2].

In the simple DMC OPV simulation, the exciton generation rate, $\nu_{\text{x-gen}}$, is defined

$$\nu_{\text{x-gen}} = I_{\text{incident}}\alpha_x\, L_x\, L_y, \tag{3.6}$$

in which I_{incident} is the flux of photons incident upon the cell based upon the AM1.5 spectrum, α_x is a material constant representing what percentage of photons incident upon the device are absorbed (assumed 1 in the DMC simulations), and $L_{x/y}$ are the simulated morphologies dimensions in x and y, producing incident surface area. As noted previously, our model assumes thin morphologies where absorption of photons does not have a depth dependence.

3.2.2.2   DMC exciton hop rates

Once an exciton is generated, it proceeds to diffuse throughout the device with a rate $\nu_{\text{x-hop}}$ until it decays or dissociates. The decay rate is based on experimentally observed lifetimes of $\nu_{\text{x-decay}} = 1/\tau_{\text{x-lifetime}} = 500\,ps^{-1}$. Note that due to the scales of morphological area being simulated in the DMC model (1000 nm^2 to .16 μm^2), and given that $\nu_{\text{x-gen}} \ll \nu_{\text{x-decay}}$,

only rarely will there exist more than a single exciton in the model at any given time. Experimental measurements suggest exciton diffusion lengths on the order of $\approx 10nm$. For these P3HT/PCBM systems, we set the exciton hop rate to reproduce the desired mobility through the use of the diffusion equation and the Einstein relationship. A detailed explanation on the selection of hop rates to achieve a desired mobility is found in appendix A.3 of this thesis, but briefly the Einstein relation is defined

$$D = \frac{q}{k_B T}\mu, \tag{3.7}$$

which relates the diffusion constant, D, to the mobility, μ, via the charge, q, temperature, T, and Boltzmann's constant, k_b. The relationship between the diffusion constant and the average hop rate and average rate of a particle on a cubic lattice is defined

$$D = l^2 \omega_i / 6, \tag{3.8}$$

which gives the average hop distance, l, and average hop rate, ω_i, required to generate a specific diffusion constant. Note that the derivation of equation 3.8 is also found in appendix A.3. Taking the average hop length used in our DMC model to be the lattice constant ($l = a$) we may combine equations 3.7 and 3.8 to to final form

$$\omega_i = \frac{6k_B T \mu}{qa^2}. \tag{3.9}$$

3.2.2.3   DMC exciton dissociation rate

Exciton dissociation may only occur when the exciton is directly adjacent to a heterojunction, such that a geminate pair may form across the two materials. We take the dissociation rate

33

to be much faster than all other processes when the exciton is adjacent to a HJ (on the order of $1000 \times \nu_{\text{x-hop}}$), but 0 otherwise. If an exciton is simultaneously adjacent to several HJ interfaces (for instance, in a corner), the target interface to dissociate across is selected at random.

3.2.3 Charge Events

Although charge diffusion can be correctly modeled in bulk material by selecting a single time through the use of 3.1 and then assigning a random hop direction, we simulate the drift behavior due to internal fields by dynamically modifying hop rates as particles move through the morphology. These fields originate from a wide variety of sources including built-in bias due to differences in work function, $\Delta\phi$, applied field, V_{applied}, coulombic interaction with nearby free charges, E_{coulomb}, image charge effects near contacts, $E_{\text{image-c}}$, and inherent energetic disorder[91] throughout the morphology, E_{disorder}. In the DMC model, these various field effects are maintained on a set of field maps, $E_{e/h/x}(i,j,k)$, which specify the current potential value of site (i,j,k). For convenience, we separate field effects into three different maps for electrons, hole, and excitons (as E_e, E_h, and E_x respectively).

The random site energies, E_{disorder} simulate the effect of thermally induced energetic disorder in the systems[92, 93], and are assigned at the start of any simulation with a Gaussian distribution centered at 0 with a width of σ_{rand}. The net field across the device, being the difference of the built in bias and applied bias ($V_{net} = V_{bi} - Vapp$) is applied as a static linear field gradient, $E_{e/h}$, across the system.

A free charge occupying site (i', j', k') will coulombically contribute to nearby site (i,j,k) with potential

$$V(i,j,k) = \frac{q^2}{\epsilon_r} \frac{1}{R_{(i',j',k')}}, \tag{3.10}$$

where $V(i,j,k)$ is the contribution to the field, 1 is the elementary charge, ϵ_r is the relative permittivity of the material, and $R(i',j',k')$ is the distance from site (i,j,k) to the charge generating the field. $V(i,j,k)$ is added to the field map of the same-type charge (being a repulsive potential) and subtracted from the field map of the opposite type charge (being an attractive potential).

Image charge effects may occur near the contacts, and are treated by generating an equivalent field as one due to a charge placed at the site $(i,j,-k)$, that has the opposite polarity as the original charge at site (i,j,k). In these systems, the image charge will act to enhance charge collection at the contacts by attracting free charges, though this is a function of material permittivity and is further discussed in appendix A.1 of this thesis. In DMC models of these BHJ systems, the permittivity of the two materials involved are often taken to be the same such that no image charge effects at the heterojunction itself need be considered. This is an acceptable approximation, as the charge recombination rate is already being fit to experimental results, which likely encompasses any enhanced recombination due to image charges effects across the heterojunction.

While exciton dissociation generates a pair of free charges across a heterojunction, these charges are still somewhat bound to one another due to the strong coulombic attraction, and are thus referred to as a geminate pair. Though the precise mechanism of geminate pair separation is somewhat debatable, from the standpoint of the DMC model a charge must escape the energetic influence of it's geminate partner in order to become a truly free charge. The Debye length is commonly used in simulations of conventional PV devices for

the effective charge field cutoff length as it is brought about by the Coulombic fields of nearby free charge, and previous OPV simulations have used the Debye length in a similar way[2]. However, as OPV systems have a relatively low density of thermally excited free charge, it is not entirely correct to characterize geminate pair separation in this way. In discussions of OPV devices it is more fitting to use the Bjerrum length as a field cutoff radius, being the separation distance at which the electrostatic interaction between a pair of charges is of equal magnitude to the local thermal excitations[94]. The Bjerrum length, λ_B, is defined as

$$\lambda_B = \frac{q^2}{\epsilon_r k_B T},$$ (3.11)

where q is the elementary charge, ϵ_r is the relative dielectric constant, T is the temperature. In our simulations, if a pair of charges is at distance λ_B or greater, we may consider their electrostatic interaction effectively masked by natural thermal diffusive processes, and as such, we need not calculate the effects of any single charge generated Coulombic fields beyond the length λ_B. This allows for significant speed increases in the calculation.

Both the built in bias ($\Delta\phi$) and the applied field (E_{applied}) are treated as static throughout the simulation. In most cases, this net static field is treated independently of BHJ morphology, because of the assumption that the relative permittivity, and thus relative dielectric constant, are identical in the acceptor and donor. The means the internal static field is typically treated as a simple linear potential gradient across the morphology. In reality, the field may be more complex, particularly near the contacts, but for most simple models a linear field approximation is used. The common notation is that a positive $\Delta\phi$ generates a field which enhances charge transport to the charge's respective contact (electrons to the anode, holes to the cathode), while a positive E_{applied} field acts to oppose charge transport. As

such, we write an effective vertically linear static field, E_{static}

$$
\begin{aligned}
E_{\text{e-static}}(k) &= E_{\text{applied}} - \Delta\phi\left(\frac{k}{L_z}\right) &&\text{:for electrons} \\
E_{\text{h-static}}(k) &= E_{\text{applied}} - \Delta\phi\left(\frac{L_z-k}{L_z}\right) &&\text{:for holes,}
\end{aligned}
\tag{3.12}
$$

where L_z is the largest lattice site value in the z-coordinate representing the substrate interface, which is modeled as the hole collecting contact. At high applied field, diode like behavior emerges. As has been previously discussed in section 2.2, this behavior is expected as a high applied field will sweep the dark-charges being injected from the contacts across the device to the opposing contact, thus providing a source for the runaway current in the non-desirable direction.

3.2.3.1 DMC charge hop rates

Charge hop rates, $\nu_{\text{c-hop}}$, are calculated dynamically between all nearest neighbor sites, m and n using a simplified form of the Marcus rate equation

$$
\nu_{\text{c-hop}_{mn}} = \nu_c \exp \frac{-(E_m - E_n + E_R)^2}{4k_B T E_R},
\tag{3.13}
$$

where ν_c is a constant, E_m and E_n are the energies of the sites based on the sum of static and dynamic site energies, E_R is the reconfiguration energy, and $k_B T$ is the simulation temperature. Note that the Marcus rate equation will be discussed in further detail in section 3.3. Careful consideration must be taken in the selection of the prefactor hopping constant, ν_c, such that the desired diffusive rate is produced. Additionally, the desired effects of confinement on charge behavior must be considered, which are discussed in detail in appendix A.3. For purposes of the simple model it is sufficient to calculate the hop rate to all surrounding sites regardless of site assignment (acceptor or donor) and only later,

37

as the selected hop execution, reject movement to forbidden sites (hops out of confining material). This mechanism will model the situation where charges that have become caught up in tortuous morphologies have difficulty finding an acceptable hop site, and thus their effective mobility will drop.

3.2.3.2   DMC charge collection and dark charge injection

The charge collection rate at electrodes, $\nu_{\text{c-collect}}$ is considered fast compared to all other processes due to image charge effects, on the order of $100 \times \nu_{\text{c-hop}}$.

Dark charge injection is modeled using rates derived from theoretical thermionic emission from the contacts. The total electron current over a Schottky barrier can be described[39]

$$J_{dark} = A^* T^2 \exp\left[-\frac{q\phi_B}{k_B T}\right],$$ (3.14)

where ϕ_B is the barrier height and the Richardson constant, A^*, can be approximated (neglecting tunneling and reflection)

$$A^* = \frac{4\pi q m^* k_B^2}{h3},$$ (3.15)

where m^* is the effective mass. In the DMC simulations, dark charge injection is simulated by generating either an electron or a hole (chosen at random) at a random site of the confining material (i.e. electrons in acceptor sites) which is adjacent to the injecting contact. The simulation injection rate is based on the current density from equation 3.14 and the area of the contact being simulated. Under typical OPV operating conditions, dark charges will almost always be recollected at their respective contacts. If the applied voltage becomes great enough, however, the dark charges will be swept across the device and col-

lected at their non-corresponding contact. This mechanism is the principle reason why dark charge injection must be modeled in order to calculate full JV-characteristics in a model morphology, as they provide the runaway current seen at high applied voltage as in figure 2.4.

3.2.3.3   DMC charge recombination rate

The charge recombination rate, $\nu_{\text{c-recomb}}$, is typically a fit parameter in these DMC simulations with a value selected such that the simulation reproduces actual device performance. Charge recombination is only a candidate event when an electron and hole are directly adjacent to each other at a HJ site. Typical values used for $\nu_{\text{c-recomb}}$ are on the order of $100\,s^{-1}$, which is significantly slower than any other rate used in the simulation. The very slow rate of $\nu_{\text{c-recomb}}$ can be understood because, despite referring to them as "free charges", recently generated geminate pairs are anything but free. The coulomb attraction, defined in equation 3.10, is typically much stronger than any other effect geminate charge pairs will encounter. This tends to lead to the behavior of two "free" charges actually spending a majority of their simulated existence bound to each other across an interface of the HJ. This pair of charges is unlikely to drift apart, even when the interface runs parallel with the built in field. Because of this, charge recombination rates must be low otherwise most geminate pairs would simply recombine before ever having a chance to escape one another. This mechanism can be considered one of the weaknesses of this simple model. Note that if the selected next event for a charge is a recombination action, the opposite charge must still exist and be present at the time of recombination, and a new action will be selected via the standard FRM procedure.

3.3 Marcus Hop Rates

As charge hopping transport in this model is derived directly from Marcus theory, we will briefly explain it's origin in this section. Marcus theory was developed to explain the rates associated with electron transfer reactions. In the case of the DMC model employed here, the transfer reaction represents a charge hopping between localized energy sites. One may conceptualize the energetic landscape inside this system as a series of local energy minimas with the barriers between sites oscillating due to thermal excitations, as was illustrated in figure 2.6. The motion of the localized charge carrier itself is a function of the charge's capability to hop between localized minima (lattice sites in the DMC model), and is limited by the details of the current energy landscape. The oscillations are essentially phonon-mitigated interactions with nearby sites, such that when a potential crossing path does come about (at some specific energy level) the charge may readily hop to an adjacent site as charge transport is presumed to be much faster than the reorganization speed of the energetic landscape. It is this subtle phonon interaction between the system's energetic landscape that creates the possibility for charge transfer, and not the reverse.

In order to calculate a hop rate, the Gibb's free energy of activation, ΔG^o, is used as it represents the minimum energy required to excite a charge out of one localized energy site and into another. The Marcus transition is conceptually visualized in figure 3.1 as a function of free energy versus the reaction coordinate[52]. The reaction coordinate is an abstract variable which describes the energy path involved in a reaction, with each point along the axis corresponding to a different configuration of molecular distances and angles related to the reactants and bonds. The standard thermally activated rate equation, known as the Annherius equation[95], is given
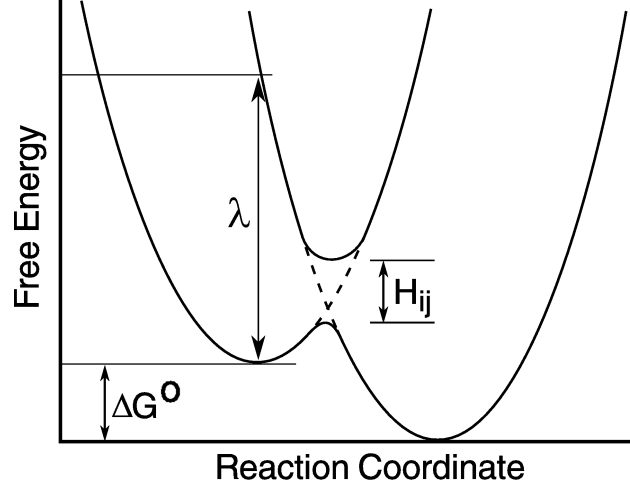
Figure 3.1   Parabola geometry used to derive Marcus rate activation energy. The net energy change from the reaction is the Gibb's free energy of reaction, ΔG^o. λ is energy of reorganization. Gibb's free energy of activation is found by solving for the crossover point of the parabolas. H_{ij} is the interaction energy at the intersection of the two states. In the two states shown, the state on the right has a lower overall configurational energy by ΔG^o, but the activation barrier must be overcome for charges to transport to this lower configuration.

$$k_{ab} = A_{ab} \, \exp\left(-\frac{\Delta G_{ab}}{k_B T}\right), \tag{3.16}$$

where k_{ab} is the rate of a transition from state a to state b, A_{ab} encompasses the probability of crossing from configuration a to b, and ΔG_{ab} is the Gibb's free energy difference between the states. This exponential term can be thought of as expressing the probability of forming a transitionary state between states a and b, which the charge may readily transition through.

Solving for the activation energy given by the crossover point of the two parabolas in figure 3.1, one finds that the free energy of activation is

$$\Delta G = \frac{(\lambda + \Delta G^o)^2}{4\lambda}, \tag{3.17}$$

where λ is the reorganizational energy of the system and ΔG^o is the total energy change

41

due to the reaction or hop. Typically, it is the reorganization energy which dominates the activation energy, producing somewhat predictable results that hop rates to lower energy sites will be faster than hop rates to a higher energy sites.

Note that an interesting consequence of Marcus theory is the prediction that hop rates to configurations of much lower energy might be slower than the rate to a slightly higher energy state (due to the squaring of the numerator in the exponential). This result is a phenomena referred to as a Marcus inverted region, and has been experimentally observed[96].

For the DMC method, a simplified form of the Marcus theory is used to derive charge hop rates. The prefactor term of equation 3.16 is set as a hopping rate constant, ν_o, the exact choice of which is further discussed in appendix A.3. Incorporating the specific site energies into the Gibb's free energy term, the final form of the hopping rate is found

$$\nu_{ij} = \nu_o \cdot \exp\left[-\frac{-\left(E_j - E_i + E_R\right)^2}{4E_R k_B T}\right], \tag{3.18}$$

where ν_{ij} the hop rate from site i to j, ν_o is a prefactor, $E_{i/j}$ are the site energies involved in the transition, the difference of which generates the Gibb's free energy of reaction, and E_R is the reconfigurational energy. This simplification of the prefactor is used to set the hop rate to be consistent with the desired mobility for an isoenergetic system, set by the Einstein relation.

3.4   Simple Bilayer Morphology Example

To demonstrate the effectiveness of the DMC model, we here present the case of a simple bilayer[97]. Even though modern devices typically use a BHJ morphology[98], the bilayer system allows us to explore the DMC model independent of complex morphological consid-

erations. We model the bilayer as two equally sized slabs of acceptor and donor material, each $10\,nm$ thick, that have periodic boundary conditions in the x and y dimensions with contacts assumed on either side of the device in the z dimension, such that final system size is $35\,nm \times 35\,nm \times 20\,nm$. Excitons are generated uniformly throughout the morphology, with a rate constant derived from the AM 1.5 light spectrum[82], scaled to the total volume being simulated. Note that this example morphology is made intentionally thin, such that more excitons will discover the interface and dissociate prior to decay and is not representative of typical devices. The values of the various rates used in the simulation are given in table 3.1, and are consistent with the values frequently used in DMC calculations of PCBM/P3HT devices[47, 27, 2].

3.4.1 The effects of energetic disorder on a bilayer system

In order to demonstrate how the DMC model may be used to explore key features in OPV devices, we first demonstrate the effect of increasing energetic disorder on the system. We test this by widening the Gaussian distribution, σ_r, used to assign initial random site energies, E_R. Excitons are generated uniformly through the P3HT (donor) sites, and no dark charge injection is modeled for this example. A difference in work functions of 1.2 eV is assumed to exist across the morphology (V_{bi}) which acts to drive charges toward their respective contacts. We compare 4 values of increasing site disorder, $\sigma_r = 0, 1/16, 1/8,$ and, $3/16\,eV$ at 21 different applied voltage values between 0 and 2 eV. For each combination of σ_r and V_{applied}, 20 simulations were averaged for each point simulated over $10\,ms$ of illumination, which was found to be sufficient to generate reliable statistics in the equilibrium region of the device response. The results of these calculations are shown in figure 3.2, along with error bars representing the standard deviation of each point.
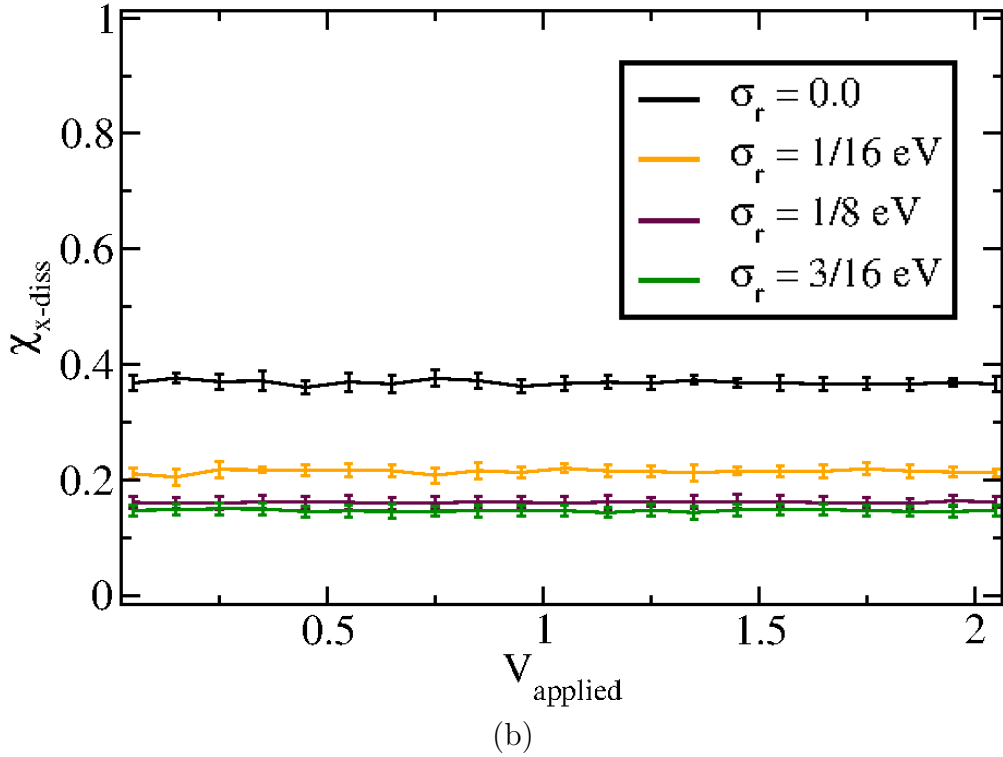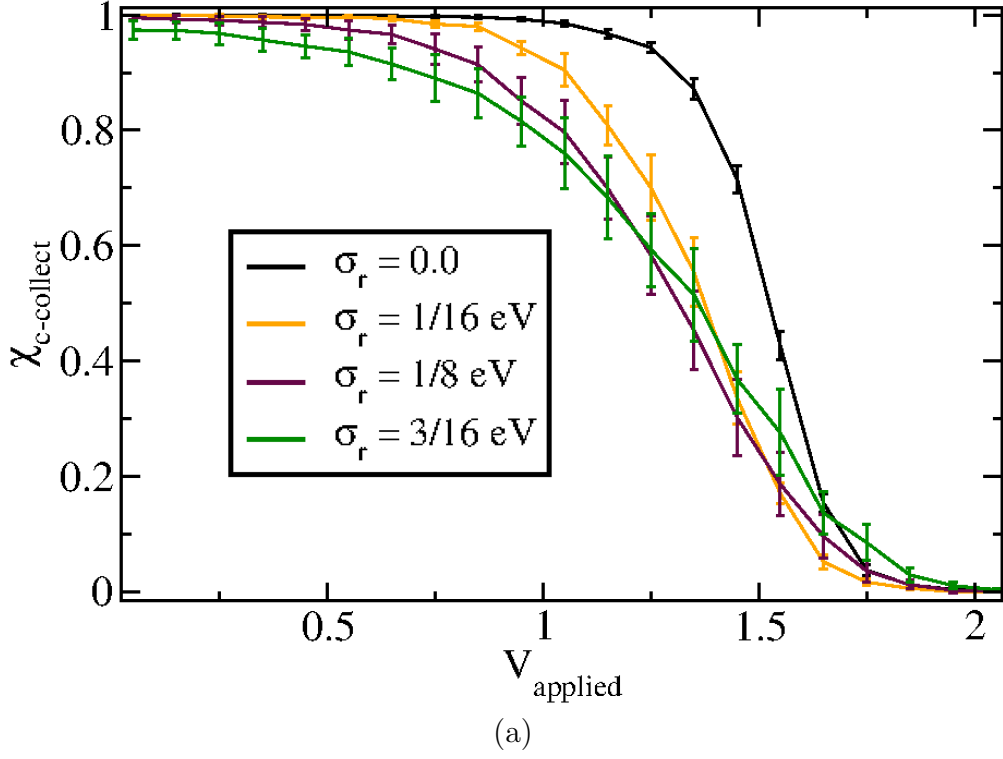
Figure 3.2 Example of how energetic roughness would effect a bilayer. Data presented as collection efficiency versus applied voltage ($V_{applied}$), demonstrating the well known diode-like behavior. Note that no dark current is being simulated, so no runaway current in the opposite direction is possible. Figure 3.2a is the charge collection efficiency, $\chi_{c\text{-collect}}$, while figure 3.2b is the exciton dissociation efficiency, $\chi_{x\text{-diss}}$.

Table 3.1   Parameters used in the bilayer example, except when otherwise specified.

Parameter	Value
exciton generation rate	$5 \times 10^{27}\,m^{-3}s^{-1}$
exciton hop rate	$0.02\,ps^{-1}$
exciton decay rate	$0.002\,ps^{-1}$
exciton diss rate	$100\,ps^{-1}$
charge hop rate	$.676\,ps^{-1}$
charge recombination rate	$5 \times 10^{-7}\,ps^{-1}$
charge collection at electrode rate	$.00646\,ps^{-1}$
ϕ_0	1.2 eV
E_B (contact injection barrier)	.4 eV
a (lattice constant)	$1\,nm$
T (temperature)	$298K$
E_R (reconfigurational energy)	.25 eV
σ_r (width of random site energies)	.062415 eV
$L_{x/y/z}$ (lattice dimensions)	35 / 35 / 20 nm

Note the emergence of a dramatic turn-off voltage occurring between 1 and $1.5\,V$ (depending on σ_r), at which point charges are no longer capable of efficiently escaping the interface and are lost due to recombination. As the energetic roughness is increased, the voltage required to effectively pin the charges to the interface drops, such that they are more likely to recombine. This result is not surprising, as the charge hop rates, given by equation 3.18, have a clear dependence on the difference of site-to-site energies. As the disorder in random site energies was increased, so was the average difference between adjacent site energy values and thus the hop times between them. Longer average hop times meant charge recombination became a more common event candidate and thus, occurred more often. Additionally, energetic traps formed by random low energy wells become more prevalent, which act to inhibit efficient charge transport.

Exciton behavior for this bilayer system is shown in figure 3.2, demonstrating that while

applied voltage has no effect on the exciton behavior (as they are unaffected by the electric field in this model), the dissociation efficiency dropped as the site disorder was increased. Similar to the charge behavior, this is a consequence of decreased average hop rates, such that exciton decay become more frequent.

3.4.2   The effects of sample depth on a bilayer system

To demonstrate that the DMC model can capture effects introduced by the morphology itself, we look at a bilayer system in which the total length of the morphology, in the z dimension, is gradually increased. We will look at bilayer systems with total vertical dimension length $L_z = 20, 40, 60, 80$, and 200, with the heterojunction occurring in the xy-plane at depth $L_z/2$ in each case. All other parameters of the simulation are shown in table 3.1. Once again, calculations are performed at 21 different values of V_{applied} between 0 and $2\,V$, simulating $10\,ms$ of illumination, with the data presented being the average of 20 full simulations. Excitons are generated through the bulk of the donor sites and no dark charges are simulated in this example. The results of these simulations are shown in figure 3.3.

As one can see, lengthening the z-dimension of the morphology (normal to the contacts) has a dramatic effect on exciton collection. This illustrates the need in OPV for excitons to be generated in close proximity to a HJ interface if they are to be successfully dissociated into free charges. As the size of the morphology was increased, so was the average path length from an acceptor site to the HJ, and thus excitons were capable of diffusing to the interface prior to decay.

The charge collection efficiency, by contrast, had a much more subtle change across different device lengths, as the data shows only a slight decrease in charge collection efficiency, most notable near the cutoff voltage of approximately $1.5\,V$. This illustrates that so called

"geminate" charge recombination is the dominant loss mechanism in the DMC model, as most charge pairs that escape the interface (and subsequently each other) are successfully transported to their corresponding electrode, no matter what the path distance might be. The minimum charge escape distance is dictated here by the Bjerrum length, as was discussed in section 3.2.3. The effects of the Bjerrum length are will illustrated in this bilayer example, as there are essentially no confinement effects influencing charge transport to the contacts (other than the reflective wall of the interface).

3.5 Conclusions

In this chapter, we have introduced a characterization of the different scales of modeling used in OPV simulations; these scales being atomistic (1 Å- 5 nm), mesoscopic (2 - 400 nm), and macroscopic (100 nm - 1 μm) models. We discussed previous calculations which were performed with each of the model scales, and motivated our selection of a mesoscopic model in order to study the effects of nanoscale morphology on OPV device performance.

We then introduced the dynamic Monte Carlo OPV device model, and explained it's ability to simulate exciton and charge transport behavior in detail. Derivations of a number of the key mechanism rates were presented. Example calculations were presented on a simple bilayer morphology, demonstrating the effects of energetic disorder and layer thickness. Clearly, the DMC model presents a tool to explore how both energetics of a system and morphology would influence the internal transport properties of a device.

Deficiencies of the DMC model, as it was presented in this chapter, are computational efficiency and the reliance on fitting parameters. Additionally, the demonstrated effects of both model parameters (such as energetic roughness) and specific morphology (such as
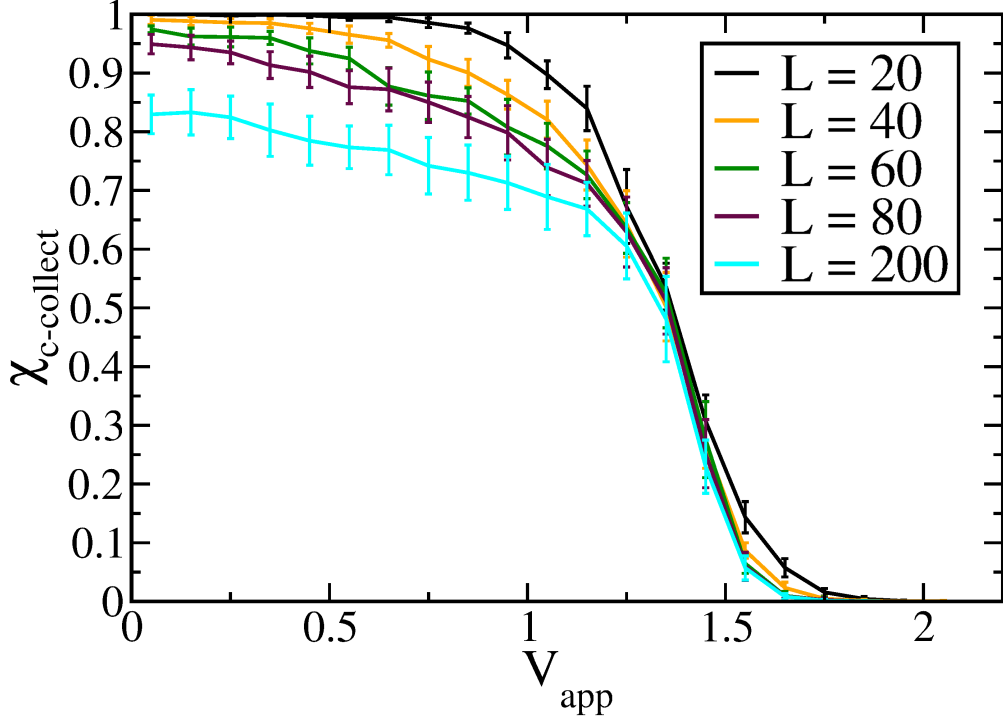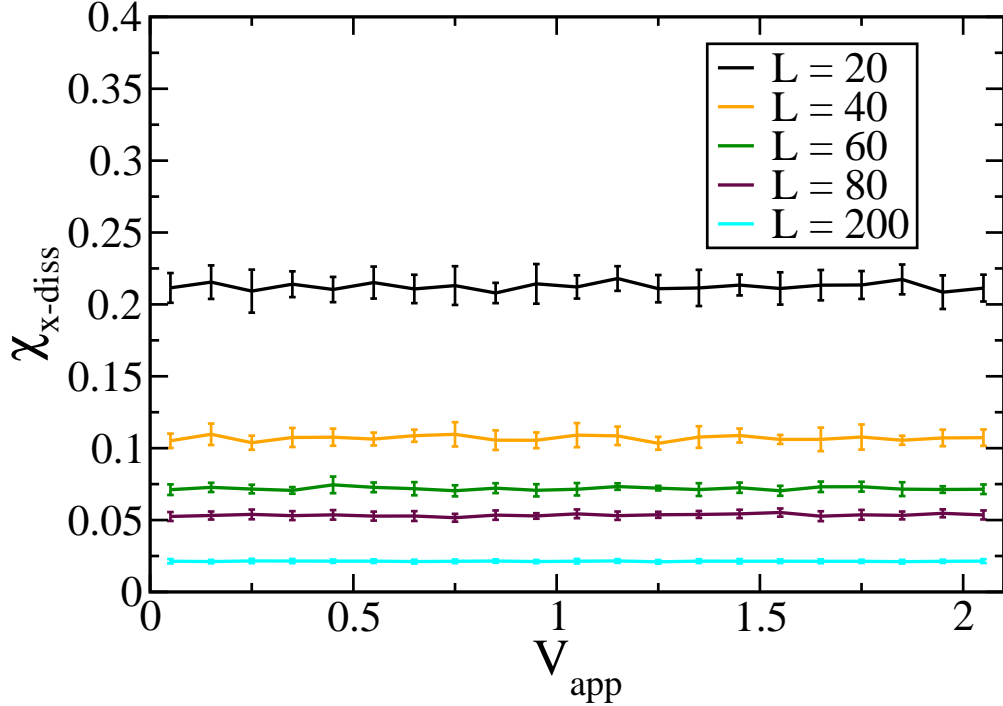
Figure 3.3   DMC calculations showing the effect of varying total bilayer thickness on charge collection efficiency, $\chi_{\text{c-collect}}$ (top), and exciton dissociation efficiency, $\chi_{\text{x-diss}}$ (bottom). Presented are the results for systems of thickness $L = 20, 40, 60, 80,$ and 200, with total morphology size $35 \times 35 \times L$, and with periodic boundary conditions in the x and y dimensions. No dark charge is simulated here. All other parameters used in the simulation are shown in table 3.1.

the dimensions of model used) suggest that it's crucial to use the most realistic model morphologies possible in order to improve the reliability and use of the DMC simulation results.

Chapter 4

A Novel Method to Simulate Small Angle Scattering

Many materials under study for modern energy and industrial applications are composed of percolative, interpenetrating, complex nanostructures, such as Nafion networks in fuel cells[99, 100, 101], structural materials[102, 103], organic photovoltaics[16, 18], batteries[104, 105], OLED's[106, 107], and sensor materials[108]. Though the exact mechanisms influencing device performance in many of these systems are not yet well understood, the transport properties are known to be strongly correlated with the details of the complex nanoscale material networks, and as such much recent work has involved structural characterization of these morphologies. One such measurement is small angle scattering, which can inform on nanometer scale internal structure. Of particular interest to the study of organic systems is small angle neutron scattering (SANS), which often can provide contrast between material components that are indistinguishable with small angle x-ray scattering (SAXS). The challenge of SANS and SAXS measurements lies in interpreting the data, as standard analysis requires fitting experimental data to well defined analytical form factors and structure factors. Although informative, these standard fitting procedures do not directly extract a 3-D model, which is necessary for device simulation. Reverse Monte Carlo methods are capable of handling small scale structures (on the order of 5-10 nm) but larger structures required for

full scale device modeling are computationally difficult to refine using conventional methods.

To extract large scale nanostructural models from SAS data we developed a novel algorithm to efficiently calculate the theoretical scattering structure function for morphological models of arbitrary scale and resolution that we refer to as the distribution function method (DFM). We will present the DFM algorithm here, discuss the limits of it's applicability, and demonstrate it's usefulness through a range of simple to complex morphological model examples.

4.1   Principles of the Fourier Transform

Before delving into the principles of scattering, it is worthwhile to discuss the principles of the Fourier Transform as they relate to scattering. The Fourier transform (*F.T.* for short) is a decomposition of a function into the sum of it's complex periodic frequencies. One commonly defined form of a FT is

$$F(k) = \frac{1}{\sqrt{2\pi}} \int_{-\infty}^{\infty} f(x)\, e^{-\mathrm{i}kx}\, \mathrm{d}x. \tag{4.1}$$

To give an example, consider a simple cosine with frequency ν, defined in real-space as $f(x) = \cos(\nu x)$. Recalling that cosines may be written as $\cos(x) = (e^{ix} + e^{-ix})/2$, the Fourier transform into wave number space, k, is

$$\begin{aligned}
F(k) &= \frac{1}{\sqrt{2\pi}} \int_{-\infty}^{\infty} \cos(\nu x)\, e^{-\mathrm{i}kx}\, \mathrm{d}x \\
&= \frac{1}{2\sqrt{2\pi}} \int_{-\infty}^{\infty} e^{-\mathrm{i}x(k-\nu)} + e^{-\mathrm{i}x(k+\nu)} \mathrm{d}x \\
&= \sqrt{\frac{\pi}{2}} \left(\delta_{(k+\nu)} + \delta_{(k-\nu)} \right)
\end{aligned} \tag{4.2}$$

where we have used the definition of the Dirac Delta function

$$2\pi\delta_{(k-k_o)} = \int_{-\infty}^{\infty} e^{-ix(k-k_o)}\, \mathrm{d}x = \begin{cases} 1 & \text{if } k = k_o \\ 0 & \text{otherwise.} \end{cases} \tag{4.3}$$

The result expresses the function, $f(x) = \cos(\nu x)$, in wave number space, $F(k) = \sqrt{\frac{\pi}{2}}\left(\delta_{(k+\nu)} + \delta_{(k-\nu)}\right)$, which demonstrates that this function is composed only of periodic frequencies with wavenumbers $k = \nu$ and $k = -\nu$. It's important to note that $f(x)$ and $F(k)$ carry identical information, only in different forms, and that performing a Fourier transform from one form to the other will not cause any inherent loss of information. Also, note the choice of Fourier function used in this example is not unique, as many different forms are acceptable so long as they conform to principles of a Fourier Transform. Here, we used a form that generated functions in terms of wave number, k, from a real space coordinate, x, but could have just as easily used a form which converted functions in time, t, to functions in frequency space, f. Wave number is a natural corollary to frequency, as it expresses the number of waves which may fit in a distance of 2 pi (units of cycles per unit length), being defined as $k = 2\pi/\lambda$, where λ is wavelength.

A more complex FT example is given in figure 4.1, which demonstrates how a complex function (in this case, a series of broad delta-functions) would generate a series of peaks which are symmetric about zero. As is explained in detail in appendix A.2, if the real space function represented an aperture (series of slits), the Fourier transform would be the transmitted intensity of an incident wave through the aperture.

Some important principles of Fourier transforms are that first, they work through decomposition of periodic functions into their symmetric (cosine) and asymmetric (sine) components. Though this might at first seem a narrow band of functions (periodic only), realize

<p align="center">(a)   (b)   (c)</p>
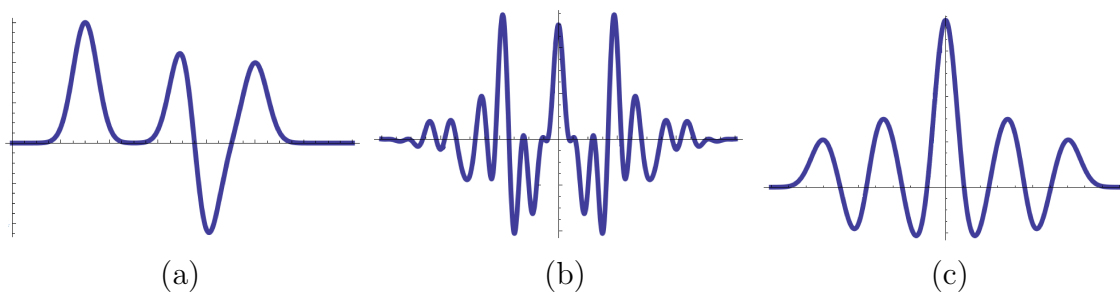
Figure 4.1   A demonstration of the Fourier relationship. Figure 4.1a shows an arbitrary function composed of superimposed Gaussian distributions of varying heights. Figure 4.1b demonstrates the real component of the Fourier transform of the function in figure 4.1a. Figure 4.1c demonstrates the auto-correlation of the function in figure 4.1a.

as the length of the periodic cell grows to infinity, no repetitions become necessary and thus any function may in principle be Fourier transformed. Second, Fourier transforms of real and symmetric functions produce a function which is real and even, while Fourier transforms of functions which are real and antisymmetric produce a function which is imaginary and odd. Finally, the value of the Fourier transform at the origin, $F(k = 0)$ is proportional to the total area under the curve of the original function, $f(x)$.

A useful mathematical concept in Fourier transforms and their applications is the convolution theorem, which states that two functions, $g(x)$ and $h(x)$, may be convoluted by one another (defined with the symbol $\otimes$) as

$$g(x) \otimes h(x) = \int_{-\infty}^{\infty} g(t)h(x - t) \, \mathrm{d}t. \tag{4.4}$$

The effect of a convolution is to "blur out" the function $g(x)$ and $h(x)$ by each other, as the two functions are essentially dragged across one another, causing the resultant convolution to be significantly different than a simple product of the two functions. An example is given in figure 4.2, showing a series of delta function peaks, of various amplitudes, convoluted with a Gaussian distribution.

<p align="center">53</p>

(a)   (b)   (c)
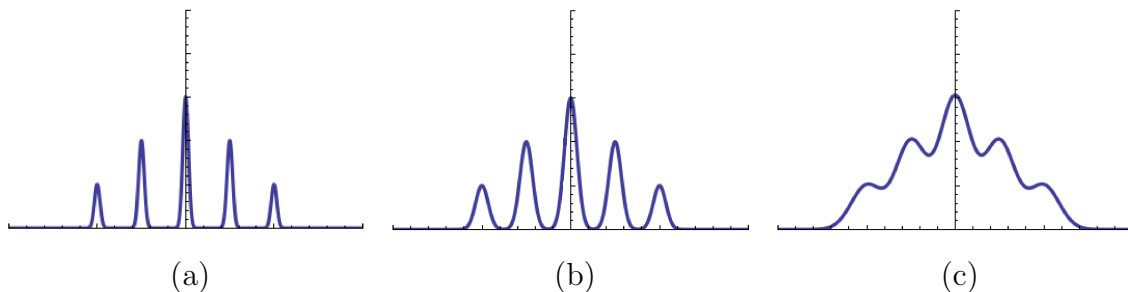
Figure 4.2   Convolutions of Gaussian functions of varying widths with a series of delta function peaks. The function describing the delta functions is $f(x) = \delta(x+10) + 2\delta(x+5) + 3\delta(x) + 2\delta(x-5) + \delta(x-10)$. The Gaussian is described as $g(x) = \exp\left(-x^2/2\sigma^2\right)$. Widths of Gaussian distributions used in these three examples are $\sigma^2 = .1$ in figure 4.2a, $\sigma^2 = .5$ in figure 4.2b, and $\sigma^2 = 3$ in figure 4.2c.

One convenient aspect of convolutions relates to their effect on the Fourier transforms of resultant functions, giving the relation

$$f(x) = g(x) \otimes h(x) \Leftrightarrow F(k) = \sqrt{2\pi}\, G(k) \times H(k). \tag{4.5}$$

Notice that functions $g(x)$ and $h(x)$ have been convoluted ($\otimes$) to produce $f(x)$, but the Fourier transform of this new function, $F(k)$ is the result of the product of the Fourier transforms of the two initial functions, $G(k)$ and $H(k)$. This result is useful, as many times taking the convolution of two systems can be complex, where as the Fourier transform and subsequent product is simple.

4.2 Basics of scattering

Scattering measurements are characterizations of how an incident particle, say an x-ray or a neutron, is effected by a sample. We describe the incident particle through it's energy and momentum, with the basic equations

$$\lambda = \frac{h}{p} \tag{4.6}$$

$$E = h\nu = \frac{hc}{\lambda} = eV = \hbar\omega = \hbar c |\vec{k}|, \tag{4.7}$$

where λ is particle wavelength, h is Planck's constant, $\hbar$ is the reduced Planck's constant ($\hbar = h/2\pi$), p is a particle's momentum, E is it's energy, ν is it's frequency, and c is it's velocity (the speed of light). It is common to express the energy of a wave in units of electron volts (eV), a measurement of the energy required to take a single electron of charge $e \approx -1.6 \times 10^{-19}C$ across a potential of 1 volt.

The incident particle's momentum can be expressed in terms of wavenumber, k, as

$$k = \frac{2\pi}{\lambda} = \frac{2\pi}{h}p. \tag{4.8}$$

Wave number describes the number of times a wave oscillates in a given length, which is directly proportional to momentum through a constant.

In the case of neutrons, their kinematic energy may also be described via the wavenumber as

$$E = \frac{p^2}{2m} = \frac{h^2}{2m\lambda^2} = \frac{\hbar^2 k^2}{2m}, \tag{4.9}$$

where m is the mass of the neutron. Scattering particles are described through their waveform, ψ. The equation of a propagating plane wave is written

$$\psi = Ae^{i\left(\vec{k}\cdot\vec{r}-\omega t\right)} \tag{4.10}$$

$$A = |A|e^{i\phi_o}, \tag{4.11}$$

where A is the complex amplitude of the wave which has absolute amplitude, $|A|$, and phase offset, ϕ_o, with frequency ω at time t.

When a particle scatters from a sample, the interaction may be characterized by the change in momentum and energy. The momentum change, $\vec{P}$ is

$$\vec{P} = \hbar\vec{k_i} - \hbar\vec{k_f} = \hbar\vec{q}, \tag{4.12}$$

where $\hbar = h/2\pi$ is the reduced Planck's constant, $\vec{k}_{i/f}$ is the initial and final momentum of the particle, and $\vec{q}$ is the transferred momentum. The energy transfer from the incident particle to the sample, ΔE, is

$$\Delta E = \hbar\left(\omega_i - \omega_f\right). \tag{4.13}$$

When no energy is transferred ($\Delta E = 0$), the scattering is referred to as elastic. All scattering events discussed in this thesis will be in the elastic regime. The implications of elastic scattering and equation 4.7 is that the wavelength, λ, cannot change before and after a scattering event, and by extension neither can the magnitude of the wavevector, $|\vec{k}|$. This condition leads to the result

$$|k_f| = |k_i| = \frac{2\pi}{\lambda}. \tag{4.14}$$

Thus we have introduced momentum transfer, q, which is a common variable in many scattering measurements.

4.2.1 Single Scattering Event

An example of a simple elastic scattering event is shown in figure 4.3, where an incident wave with momentum $\vec{k_i}$ is scattering off a sample at an angle 2θ, such that it has final momentum $\vec{k_f}$. Described using momentum transfer, $\vec{q} = \vec{k_f} - \vec{k_i}$, we see that the amplitude of q is

$$q = \frac{4\pi \sin \theta}{\lambda}. \tag{4.15}$$
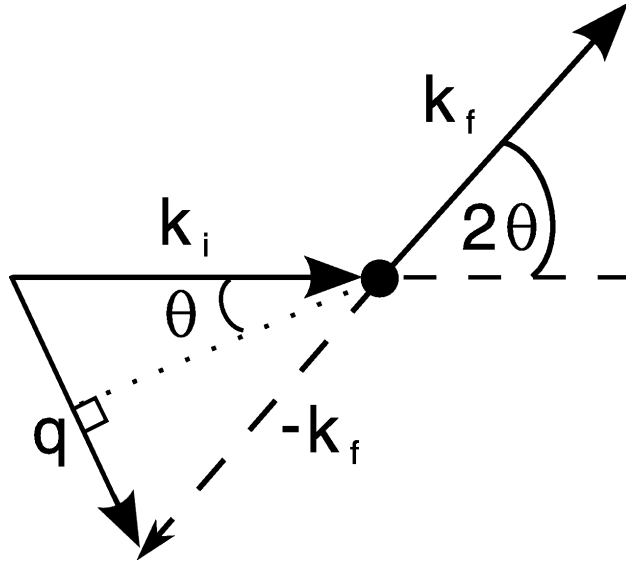
Figure 4.3   Single scatter event example

We may describe the spherical scattered wave, ψ_f, as

$$\psi_f = \psi_o \, f(\lambda, \theta) \frac{e^{i\vec{k}\cdot\vec{r}}}{r}, \tag{4.16}$$

where ψ_o describes the incident plane wave, $f(\lambda, \theta)$ is a function describing the fraction of an incident wave of wavelength λ that is deflected in the direction, θ. Note that there is no azimuthal (ϕ) dependence on the function $f(\lambda, \theta)$ due to the spherical symmetry. The

scattering strength of a particle, $f(\lambda, \theta)$, explicitly describes how strongly the incident wave interacts with the scatter. Note that the term "scatterer" is used here, as although the scattering is principally caused by interactions with atoms, it is sometimes more convenient to consider average scattering from a molecule or small volume of material. The scattering interaction itself is caused by a number of different specific mechanisms, dependent on incident wave and sample. For instance, electrons may scatter due to their Coulomb interaction with an atom's electric field, hence larger atoms (with greater Z number) scatter x-rays stronger than smaller atoms. Neglecting magnetic interactions, neutrons interact only with the nucleus of the atom and thus their scattering strength has no simple correlation with atomic size. As these scattering interactions can be dependent on incident particle wavelength and angle, we have up until now included their explicit dependence in $f(\lambda, \theta)$. As we shall discuss later, in the q-range used in many small angle scattering measurements the strengths of these interactions can often be approximated as a constant.

4.2.2 Multiple Atom Scattering

Scattering from an ensemble of atoms can be calculated by applying the principles of superposition to the methods introduced for scattering due to a single atom. Assuming the total scattered wave, ψ_f, will be composed of the sum of the scattering due to each individual atom, $\left[\delta\psi_f\right]_j$, where the index, j, identifies the scattering atom, one may rewrite equation 4.16 as

$$\left[\delta\psi_f\right]_j = \psi_o\, \mathrm{e}^{\mathrm{i}\vec{k_i}\cdot\vec{r}_j}\, f_j(\lambda, \theta)\frac{\mathrm{e}^{\mathrm{i}\vec{k}_f\cdot(\vec{r}-\vec{r}_j)}}{|\vec{r}-\vec{r}_j|}, \tag{4.17}$$

where the j-th atom is at coordinate, $\vec{r}_j$. Taking the sum over all N atoms in this

ensemble, with each atom located at $\vec{r_j}$ we find

$$
\begin{aligned}
\psi_f &= \sum_{j=1}^{N} \left[\delta\psi_f\right]_j \\
&= \sum_{j=1}^{N} \psi_o\, e^{i\vec{k_i}\cdot\vec{r_j}}\, f_j(\lambda,\theta) \frac{e^{i\vec{k_f}\cdot(\vec{r}-\vec{r_j})}}{|\vec{r}-\vec{r_j}|} \\
&= \psi_o\, e^{i\vec{k_f}\cdot\vec{r}} \sum_{j=1}^{N} f_j(\lambda,\theta) \frac{e^{i\left(\vec{k_f}-\vec{k_i}\right)\cdot\vec{r_j}}}{|\vec{r}-\vec{r_j}|},
\end{aligned}
$$

where as we have rearranged the terms, it's straightforward to rewrite the exponential in the sum in terms of momentum transfer, $\vec{q}$. Additionally, we may assume that the inter-atomic distances, $|\vec{r_j}-\vec{r_k}|$, in the system is much smaller than the distance to the detectors, $|\vec{r}|$, and thus the far-field approximation can be made, $|\vec{r}-\vec{r_j}| \approx |\vec{r}| = r$. Taking this limit into account, we may write

$$
\psi_f = \psi_o\, e^{i\vec{k_f}\cdot\vec{r}} \sum_{j=1}^{N} f_j(\lambda,\theta) \frac{e^{i\vec{q}\cdot\vec{r_j}}}{|\vec{r}|}. \tag{4.18}
$$

Finally, as we are interested in the net intensity ($I \propto |\psi_f|^2$) measured at the detectors, we take the modulus squared of ψ_f to find

$$
|\psi_f|^2 = \frac{\psi_o^2}{r^2} \left|\sum_{j=1}^{N} f_j(\lambda,\theta)\, e^{i\vec{q}\cdot\vec{r_j}}\right|^2. \tag{4.19}
$$

As we shall see later, this result is of particular use when we derive the Debye formalism in section 4.3.2.

4.2.3 Scattering strength

The principle mechanism by which matter scatters an incident wave is dependent on the incident scattering particle. In the case of x-rays and electrons, scattering is primarily dominated by electrostatic interactions with the electrons surrounding an atom, hence the stronger interaction with atoms of greater Z number. Electrons primarily scatter due to the Coulomb interaction with the electron cloud, whereas x-rays primarily scatter due to interaction with the electron cloud itself[109]. For this reason, x-rays may penetrate deeper towards the nucleus than an electron. For neutrons, scattering may occur either due to the nuclear interaction at the nucleus of the atom or via a dipole-dipole interaction referred to as magnetic scattering[110].

In the classical image of scattering, we may imagine the incident wave as a single particle and the scattering atom as a single spherical body of finite size. In this picture, the relative scattering strength of an atom may be represented by a larger overall scattering area. Although this is a simple classical interpretation of scattering, it inspires the common unit of relative scattering strength called the scattering cross-section, σ. Because of the strength of the scattering interactions, electrons will encounter much larger overall scattering cross-sections than x-rays, and neutrons will encounter the smallest cross-sections overall. For this reason, neutrons are capable of probing much deeper into many materials than electrons or x-rays, particularly those with high Z number such as metals.

The value of σ may be measured by looking at the rate of incident particle scattering over all angles, $R(s^{-1})$, over the total amount of incident flux on the scattering sample, $\Phi(s^{-1}m^{-2})$. The scattering cross-section is related as $\sigma = R/\Phi$, with units of m^2.

In principle, the scattering cross-section will be dependent on both the incident angle (θ)

and wavelength (λ) of the incident wave, as the driving scattering interaction mechanisms are so dependent. However, in the regime that small angle scattering measurements are taken the relative q-values of incident scatterers will be such that little variation occurs in the $\sigma(\theta, \lambda)$[111], and as such we may refer to a constant scattering cross-section, σ. The scattering length, b, is another quantity which may describe material scattering strength. Scattering length is related to the scattering cross-section, similar to the relationship between the radius of a sphere and it's surface area

$$\sigma = 4\pi|b|^2. \tag{4.20}$$

As the measurement taken in any small angle scattering experiment is the number of incident scatterers deflected to a specific solid angle defined by the measurement detector, a useful quantity to discuss is the differential cross-section

$$\left(\frac{\mathrm{d}\sigma}{\mathrm{d}\Omega}\right) = \frac{R(2\theta, \phi)}{N\Phi\Delta\Omega}, \tag{4.21}$$

where the number of scatterers deflected per solid angle, $R/\Delta\Omega$, is normalized by the total number of scattering particles incident on a sample, Φ, and the number of scattering units (such as atoms) in a sample, N. All scattering due to internal structural features inside a sample will be present in the differential cross-section[111, 110]. Although scattering from a sample will always be composed of an elastic ($\Delta E = 0$) and inelastic ($\Delta E \neq 0$) component, the inelastic scattering will generally be small compared to the elastic component, and constant across the q-ranges of interest here. As such, we treat total differential cross-section and elastic differential cross-section as one-in-the-same for the purposes of this thesis.

The elastic scattering to a specific solid-angle due to a sample may be written

$$R(2\theta, \phi) = |\psi_f|^2 \, \delta A, \tag{4.22}$$

where δA is the area subtended by the solid angle defined by $(2\theta, \phi)$.

Along with the definition of scattered wave due to an ensemble of scatterers provided by equation 4.19, we may describe the differential cross-section as

$$\left(\frac{\mathrm{d}\sigma}{\mathrm{d}\Omega}\right) = \frac{1}{N} \left| \sum_{i=1}^{N} b_i \, \mathrm{e}^{\mathrm{i}\vec{q}\cdot\vec{r_i}} \right|^2 , \tag{4.23}$$

where the sum is taken over all N scatterers of the system, each of which has scattering length density, b, and exists at vector r_i in the system. Note that here, the differential cross-section has been normalized by total number of scatterers, N, but the exact normalization may vary between disciplines to include such values as mass, volume, average scatterer strength, and so forth[110]. The overall shape of the differential cross-section in all cases is always a function of the particular arrangement of scatterers in a given sample, as well as the scattering strength of each of these components. This is why all structural information of a sample is found in the differential cross-section.

4.2.4 The Full SAS Picture

Up to now, we have discussed scattering due to individual scatterers, each described by a scattering length, b. However, we may instead treat scattering from a large number of atoms in a finite region with a scattering length density, $\beta(\vec{r})$. The scattering length density (SLD) may be defined by assuming that scattering from a point source of constant scattering strength, b, is described as

$$b = \beta(\vec{r})\mathrm{d}V, \tag{4.24}$$

where the vector, $\vec{r}$, defines the coordinate of the total scattering volume $\mathrm{d}V$. Using $\beta(\vec{r})$ and equation 4.23, we may generalize the differential cross section as

$$\left(\frac{\mathrm{d}\sigma}{\mathrm{d}\Omega}\right)_{el} \propto \left| \iiint_V \beta(\vec{r})\mathrm{e}^{\mathrm{i}\vec{q}\cdot\vec{r}}\mathrm{d}^3\vec{r} \right|^2. \tag{4.25}$$

Notice that by defining the differential cross-section in this way, we see that the structure of a sample (explicitly defined by the function $\beta(\vec{r})$) is related to the differential cross-section by a Fourier transform.

The absolute measured intensity due to elastic scattering in a SAS measurement may be written

$$I(\mathbf{q}) = I_o(\lambda)\eta(\lambda)T(\lambda)\Delta\Omega\left(\frac{\mathrm{d}\sigma}{\mathrm{d}\Omega}\right)\otimes R_{\mathrm{inst}}(\vec{q}) + B(\vec{q}), \tag{4.26}$$

where the incident flux, I_o, efficiency of the detector, η, and transmission through the sample, T, are all dependent on incident wavelength. $\Delta\Omega$ represents the angle subtended by the detector at momentum transfer $\vec{q}$. All these factors are convoluted with the instrument resolution, R_{inst}, except for the background signal, B.

4.2.5 Form Factor vs. Structure Factor

Often times, small angle scattering data is discussed in terms of a form factor, $P(q)$, and a structure factor, $S(q)$. In principle, a form factor (or atomic form factor) is the scattering profile due to the scattering from an individual scatterer, such as an atom or a spherical

nanoparticle. If a sample is composed of an ensemble of scatterers, the arrangement itself contributes to the scattering profile as a structure factor. The overall scattering profile will be the product of the form factor and structure factor

$$I(q) = P(q) \times S(q). \tag{4.27}$$

Because of the Fourier relationship between real space structural information and q-space scattering data, scattering from small physical features (small r information) will be represented inversely by large q-scale features and vice verse. Thus, if a system is composed of well dispersed scatterers in medium transparent to the incident wave (the dilute limit), then any contributions due to long range ordering of individual scatterers will occur in the low-q region of the data, well separated from the form factor contributions of the individual scatterers.

4.3   Scattering Simulation

In this section, we introduce two general methods of calculating the scattering profiles of model morphologies, which we refer to as the direct method and the Debye method. Both methods rely on the inherent Fourier relationship between real space data and scattering data. We will describe both these methods in detail, and discuss the strengths and weaknesses of each. While other forms of structural scattering simulations exist[112, 113, 114, 115, 116, 117], we limit our comparison here to the direct and Debye formalisms because of their underlying mathematical symmetry.

Both the direct method and the Debye formalism require discretization of a scattering

Define a 3D cubic lattice of SLD values: $\rho(x, y, z)$

Direct Method

Debye Method

Generate 3D FT: $I(q_x, q_y, q_z)$

Capture structural correlations: $\rho(r)$, $g(r)$, *etc.*

Project down to 1D function: $I(q)$

Take 1D Fourier Transform (Sine): $I(q)$

Smear I(q) for comparison to experiment
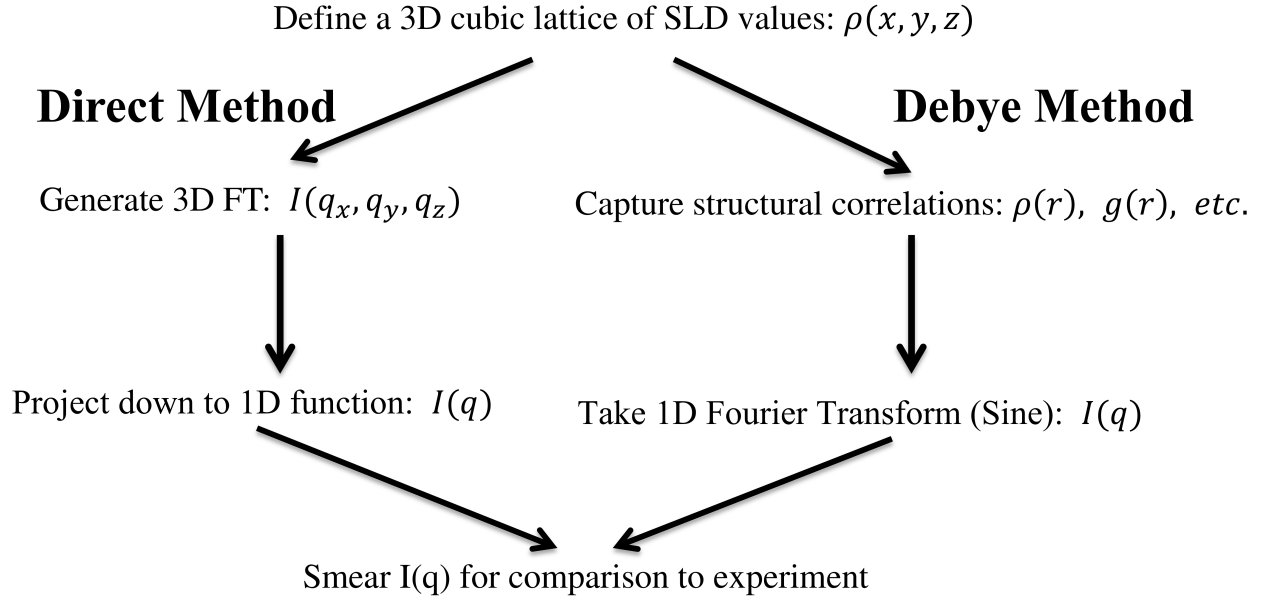
Figure 4.4   Comparison of methods used to simulate small angle scattering, highlighting the overall mathematical similarities of the two methods.

structure into essentially point scatters and rely on the Fourier relationship between a morphologies' real space function and it's scattering profile. The differences between the two methods are qualitatively illustrated in figure 4.4. Note that both of these methods assume the scattering data involved is angle averaged[111].

4.3.1   Direct Method

The direct method of simulating small angle scattering begins by defining a morphological model on a discrete lattice and then taking a full 3-d Fourier transform of the structure, before finally projecting the resultant 3-d complex lattice down into one dimension[26].

In detail, the values of the typically cubic lattice sites on the real space model correspond to the scattering length densities of the associated material. This results in a discretized lattice of SLD values, $\rho(x, y, z)$. The full 3-D Fourier transform is then calculated on $\rho(x, y, z)$, which results in a a 3-D lattice of scattering intensities, $I(q_x, q_y, q_z)$. In order to compare

directly to experiment, it is necessary to project this scattering information down into one dimension, resulting in $I(q)$. This projection involves first summing cylindrical shells of $I(q_x, q_y, q_z)$, centered about the z-axis (considered parallel to the direction of the detector from the sample), which results in a 2-D rings of scattering intensity. These rings are integrated, much as they are in experiment, to generate the final angle averaged 1-D scattering intensity plot, $I(q)$. Finally, in order to account for the natural resolution limits of experimental measurements, a smearing function is often applied to $I(q)$. This smearing may also be used to mask the effects of the lattice spacing.

In order to alleviate the effects of discretizing a morphology into point scatterers, one can convolute a sinc function in 3 dimensions with the 3-D scattering data prior to projection. The reasoning for this is that the Fourier transform of a sinc function is a square wave, and considering the relationship described in equation 4.5, this is equivalent to calculating the scattering from a structure generated by point scatters multiplied by cubic scatterers, thus filling the void space between the point scatterers so long as the width of the sinc function is selected accordingly[26]. The downside to this approach is that, while one does effectively eliminate void space, one is left with a structure of sharply transitioning non-physical densities which thus must be later smoothed out with a smearing function regardless. The only information added to the structure is unphysical, and thus we feel this step is superfluous.

The advantage of the direct method is that it is a straightforward calculation which scales as $N \ln N$, which is relatively efficient for small systems. However, the need to perform a 3D Fourier transform and convert these results into a 1D form can become computationally intensive for large systems.

4.3.2 Debye Method

The Debye method involves construction of a function containing structural correlation information in real space, followed by Fourier transforming this function to generate scattering information in reciprocal space. The derivation of the Debye formalism begins by defining the scattered amplitude due to an ensemble of atoms

$$A(\vec{q}) = \sum_k A_k = C \sum_k b_k \, \mathrm{e}^{-\mathrm{i}\,\vec{q}\cdot\vec{r}_k}, \tag{4.28}$$

where C is the scattering amplitude of a single atom. The measured scattering intensity from the ensemble of atoms, $I(q) = A^*A$, may thus be written

$$
\begin{aligned}
I(q) &= A^*A \\
&= C^2 \sum_j \sum_k b_j b_k \, \mathrm{e}^{-\mathrm{i}\,\vec{q}\cdot\vec{r}_j} \, \mathrm{e}^{\mathrm{i}\,\vec{q}\cdot\vec{r}_k} \\
&= C^2 \sum_j \sum_k b_j b_k \, \mathrm{e}^{-\mathrm{i}\,\vec{q}\cdot\left(\vec{r}_k - \vec{r}_j\right)}.
\end{aligned}
$$

$$\tag{4.29}$$

Every segment in this arrangement of atoms, $(\vec{r}_i - \vec{r}_j)$, will have a corresponding reverse segment of equal magnitude but opposite direction, $(\vec{r}_j - \vec{r}_i)$, we may combine both these contributions as follows

$$
\begin{aligned}
e^{-i\vec{x}\cdot(\vec{a}-\vec{b})} &= \frac{1}{2}\left(e^{-i\vec{x}\cdot\left(\vec{a}-\vec{b}\right)} + e^{-i\vec{x}\cdot\left(\vec{b}-\vec{a}\right)}\right) \\
&= \frac{1}{2}\left(e^{-i\vec{x}\cdot\left(\vec{a}-\vec{b}\right)} + e^{i\vec{x}\cdot\left(\vec{a}-\vec{b}\right)}\right) \\
&= \cos\left(\vec{x}\cdot\vec{r}_{ab}\right) = \cos\left(xr_{ab}\cos\phi\right),
\end{aligned}
\tag{4.30}
$$

where $\vec{r}_{ab} = \vec{a} - \vec{b}$, and ϕ is the angle between $\vec{a}$ and $\vec{b}$, $\phi = \angle_{a,b}$. Using the results of equation 4.30 in equation 4.29, we may write the intensity as

$$
\begin{aligned}
I(q) &= C^2 \sum_j \sum_k b_j b_k \cos\left(\vec{q}\cdot\vec{r}_{jk}\right) \\
&= C^2 \sum_j \sum_k b_j b_k \cos\left(qr_{jk}\cos\phi_{jk}\right),
\end{aligned}
\tag{4.31}
$$

where ϕ_{jk} here defines the angle between the incident scattering wave, $\vec{q}$, and the pair-position vectors, $\vec{r}_{jk}$, where $\phi \in [0, \pi]$. Under the assumption that scattering from all angles are equally likely, in the words of Guinier, "the mathematical problem" is in finding the average value: $\left\langle \cos\left(\vec{q}\cdot\vec{r}_{jk}\right)\right\rangle$.

To calculate this average, we begin by stating that if all angles, ϕ_{jk}, are equally likely, then the probability that an angle exists between ϕ and $\phi + d\phi$ is given by: $\frac{1}{2}\sin\left(\phi\right)d\phi$. The average of the phase function, $\cos\left(\vec{q}\cdot\vec{r}_{jk}\right)$, can thus be written

$$\langle \cos(\vec{q} \cdot \vec{r}_{jk}) \rangle = \int_0^\pi \cos(q\, r_{jk} \cos\phi)\, \frac{\sin\phi}{2}\, \mathrm{d}\phi$$

$$= \int_0^{\pi/2} \cos(q\, r_{jk} \cos\phi) \sin\phi\, \mathrm{d}\phi$$

$$= -\frac{1}{q\, r_{jk}} \int_0^{\pi/2} \cos(q\, r_{jk} \cos\phi)\, \mathrm{d}\,(q\, r_{jk} \cos\phi)$$

$$= -\frac{q}{q\, r_{jk}} \int_{hr}^0 \cos(u)\, \mathrm{d}u$$

$$= \frac{1}{q\, r_{jk}} \left[\sin(q\, r_{jk}) \right], \tag{4.32}$$

where $u = (h\, r_{jk} \cos\phi)$. Simplifying variables such that $\vec{r}_{jk} = \vec{r}$, this produces the result

$$\langle \cos(\vec{q} \cdot \vec{r}) \rangle = \frac{\sin(qr)}{qr}, \tag{4.33}$$

such that when utilized in the angle averaged form of equation 4.29, we generate the well known Debye formula for scattering intensity

$$I(q) = \sum_j \sum_k b_j b_k \frac{\sin(qr_{jk})}{qr_{jk}}. \tag{4.34}$$

While a straightforward calculation of equation 4.34 is acceptable for small scale systems, it becomes computationally difficult as the number of scatterers increases. This can be somewhat circumvented by first calculating a weighted pair density, $\zeta(r)$, defined as

$$\zeta(r) = \sum_j \sum_k b_j b_k \delta(r - r_{jk}), \tag{4.35}$$

such that a sine-transform (often referred to in the scattering community simply as the Fourier transform) of $\zeta(r)$ needs only to be calculated once (for each value of r seen),

generating the scattering intensity

$$I(q) = \int_0^\infty \mathrm{d}r\, \zeta(r) \frac{\sin(qr)}{qr}. \tag{4.36}$$

Note that the Fourier relationship between scattering data and the real space structural data, as defined by $\zeta(r)$ here, may be written in a variety of forms. Any function which contains real-space structural pair data, such as the atomic pair distribution function, radial distribution function, etc., can be Fourier transformed into scattering data, with the differences being only in normalization and scaling. We compare a number of different relationships commonly used in the literature in appendix A.4 of this thesis.

As compared to the direct method, the Debye method requires the additional step of calculating pair-structural information $(\zeta(r))$, however this step circumvents the need to later project the scattering data down into one-dimension, as $\zeta(r)$ is one-dimensional. It is the calculation of $\zeta(r)$, requiring a sum over $N(N-1)/2$ pair distances, which is the dominant computational step. Thus, the Debye method scale as N^2, making them less efficient than the direct method that scaled as $N \ln N$. However, we found neither method to be acceptably efficient for use in reverse Monte Carlo-like structural refinement of large scale morphologies.

4.4 DFM Algorithm

We have found that for many systems, the full calculation of the structural correlations is not necessary to estimate the Debye form factor to high precision, as one may instead randomly sample the structure to generate a weighted distribution function, $w(r)$, which acts as the real space structural data (defined by $\zeta(r)$ previously) for the morphology. We

thus refer to our algorithm as the distribution function method (DFM). The number of pairs sampled per calculation may be scaled according to the demands of the application and morphology itself, with higher sampling rates corresponding to greater accuracy and lower rates with faster calculation time. Once generated, a sine-transform of $w(r)$ generates an approximated scattering profile, $I^a(q)$. This allows the calculation to scale as $f \times N^2$, where f is the ratio of random pairs sampled, N_p, over the total number of pairs possible in the system such that $0 < f < 1$. Thus, the DFM approach can be adjusted such that it is more efficient than the direct method when $f < \ln N/N$ by sacrificing some level of accuracy.

For our systems, we find that a $w(r)$ which has been calculated with as little as 0.001% of the total pairs to be found in the system will generate an accurate scattering profile. Though further sampling refines high-q details and may increase confidence in the simulated scattering structure, for purposes of empirical reverse Monte Carlo-like refinement, the abbreviated sampling works remarkably well.

We will begin by detailing the algorithm and sampling method used in the DFM algorithm, demonstrating it's validity through a series of simple examples. We then examine the limitations of the model as well as methods to improve results as demonstrated with examples of more complex morphologies, such as systems of monodisperse and polydisperse spheres and an interpenetrating two-phase structure typical of the nanoscale morphologies found in many energy applications.

4.4.1 Methodology

The DFM algorithm assumes a morphology defined by a discrete set of points, with each site assigned a scattering strength based upon the scattering length density (SLD) of the represented material. A sites which is considered a mix of different materials should be

assigned an appropriately weighted SLD value. The approximated scattered intensity, $I^a(q)$, is thus

$$I^a(q) = C \sum_{r=R_{min}}^{R_{max}} w(r) \frac{\sin(qr_{ij})}{qr_{ij}}, \tag{4.37}$$

where the constant, C, is typically adjusted to compare the experimental system of interest. For direct comparison to the full Debye calculation (over all pairs), one can set $C = (N^2 - N)/N_s$, where N is the total number of scatterers and N_s is the number of pairs sampled. The sum is taken over all binned distances in the system, R_{min} to R_{max}, and we have incorporated the weighted distribution function, $w(r)$. Here we define $w(r)$ as

$$w(r) = \sum_{pairs}^{N_s} b_i\, b_j\, \delta(r - r_{ij}), \tag{4.38}$$

where the sum is taken over N_s sampled pairs of sites, i and j, which are distance r_{ij} apart with corresponding scattering weights b_i and b_j. Typical material SLD values (for neutrons) are $-1 \times 10^{-6}\mathrm{\mathring{A}}^{-2}$ to $5 \times 10^{-6}\mathrm{\mathring{A}}^{-2}$. To simplify the sum of $w(r)$, if the SLD values used in the model have integer ratios to each other it is convenient to reduce the weights to integer values for computational efficiency. The difference between using the real values and representative integer values can be later adjusted in the normalization. The weighted distribution function, $w(r)$, is defined similarly to the atomic distribution function, $\rho(r)$, with differences in the normalization (see appendix A.4).

We find that $C \times I^a(q)$ calculated from $w(r)$ quickly converges to $I(q)$ (the results of the full calculation) for many systems, particularly those with strong contrast between different scattering species such as the 1-to-0 scattering values assigned in the examples here. As in our simulation $w(r)$ is not a continuous distribution but rather a histogram, care must

be taken to select an appropriate number of bins, $N_{bins} = D/dr$ where D is the longest

length measured and dr is the width of a single bin. Note that in a cubic system of width

L, the longest possible distance is $\sqrt{3}L$ in a non-periodic system, and $\sqrt{3}L/2$ in a periodic

system. Sufficient binning of the sampled data is necessary to avoid violating the Nyquist

limit of $dr \leq \pi/q_{\max}$ and related aliasing effects. By contrast, a much finer grid than that

dictated by the Nyquist limit is unnecessary, as information on distances smaller than dr is

not representative of any actual morphological features. Though acceptable if smoother data

is desired, over binning will slow down the Fourier transform and thus the overall algorithm

efficiency. Additionally, when over-binning care must be taken not to misinterpret features

smaller than the Nyquist limit as these are unphysical. We typically use 10,000 bins in

producing $w(r)$ in equation 4.38, and 30,000 when transforming to $I^a(q)$ in equation 4.37,

as we find this number is sufficient for the size $L = 400$ systems we typically model.

While it's possible to use different sampling methods in order to weight different re-

gions of the morphology preferentially, here we sample all pairs with equal probability. A

demonstration of the accuracy of the method is shown in figures 4.5 and 4.6, which compare

the analytical form factor and DFM calculated structure for a sphere and set of cylinders

respectively, where the structures have been modeled with coordinates on a cubic lattice.

The analytical form factors shown in these two examples were generated using Irena Igor

macros[118]. As can be seen, the form factor of these systems is recovered to a high preci-

sion by sampling a total of 10^7 total pairs, as compared to the total number of pairs in the

models, being approximately 1.7×10^{10} for the sphere in figure 4.5, 1.9×10^{10} for the smaller

cylinder and 3.1×10^{11} for the larger cylinder in figure 4.6.

In each of these examples the constant C is selected such that the simulated scattering

intensity, $I(q)$, is normalized to unity as $q \to 0$. Note also that only in the case of the large
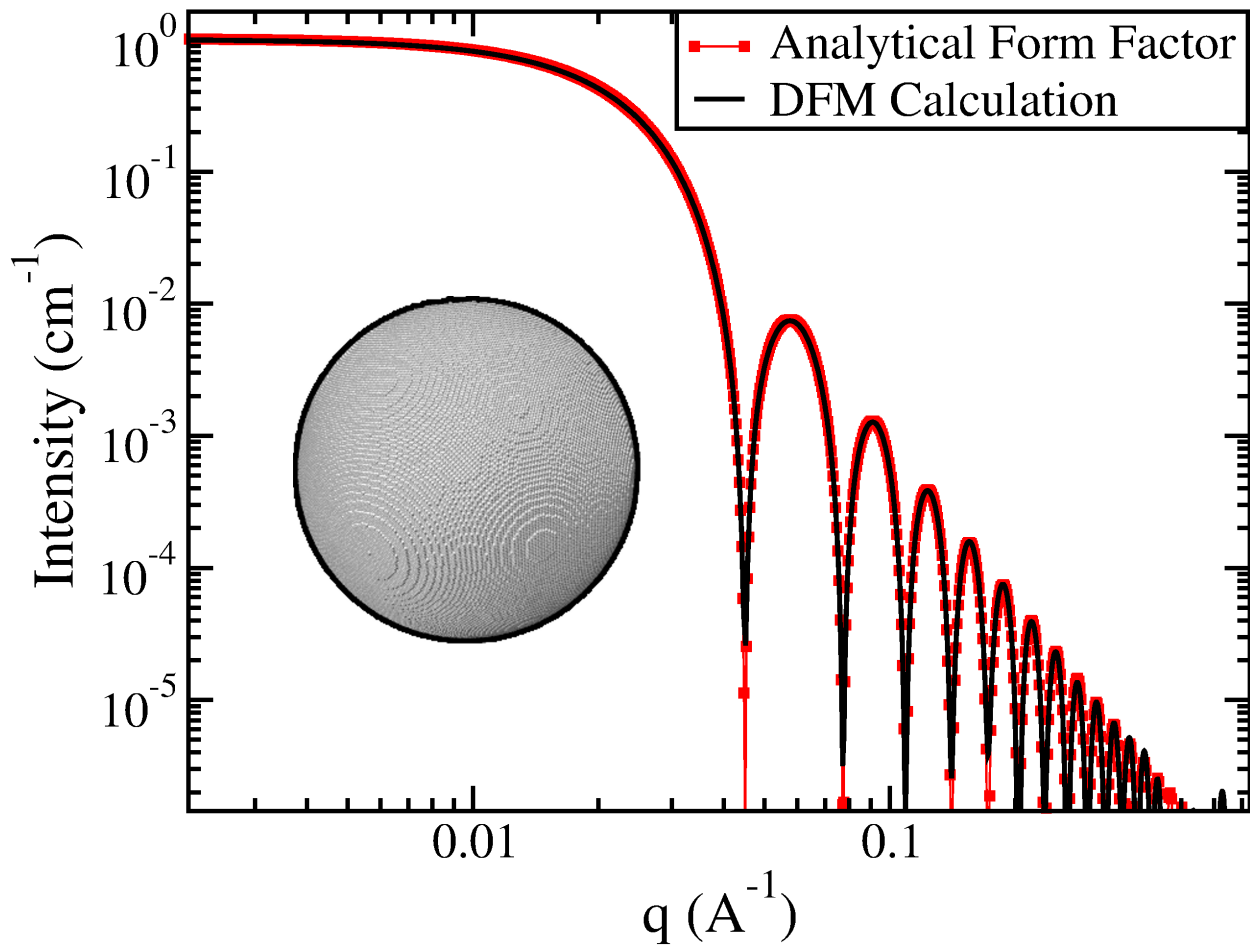
Figure 4.5   Comparison of scattering from a single $R = 100\,\text{Å}$ sphere calculated using the analytical form factor and the DFM algorithm. Analytical form factor provided by the IRENA SAS Macros in Igor, where sphere to solvent contrast is taken 1-to-0. DFM calculation performed over a randomly sampled set of 10^7 pairs, or .05% of the total model pairs. The lattice spacing here is taken as $a_l = 1$ Å.
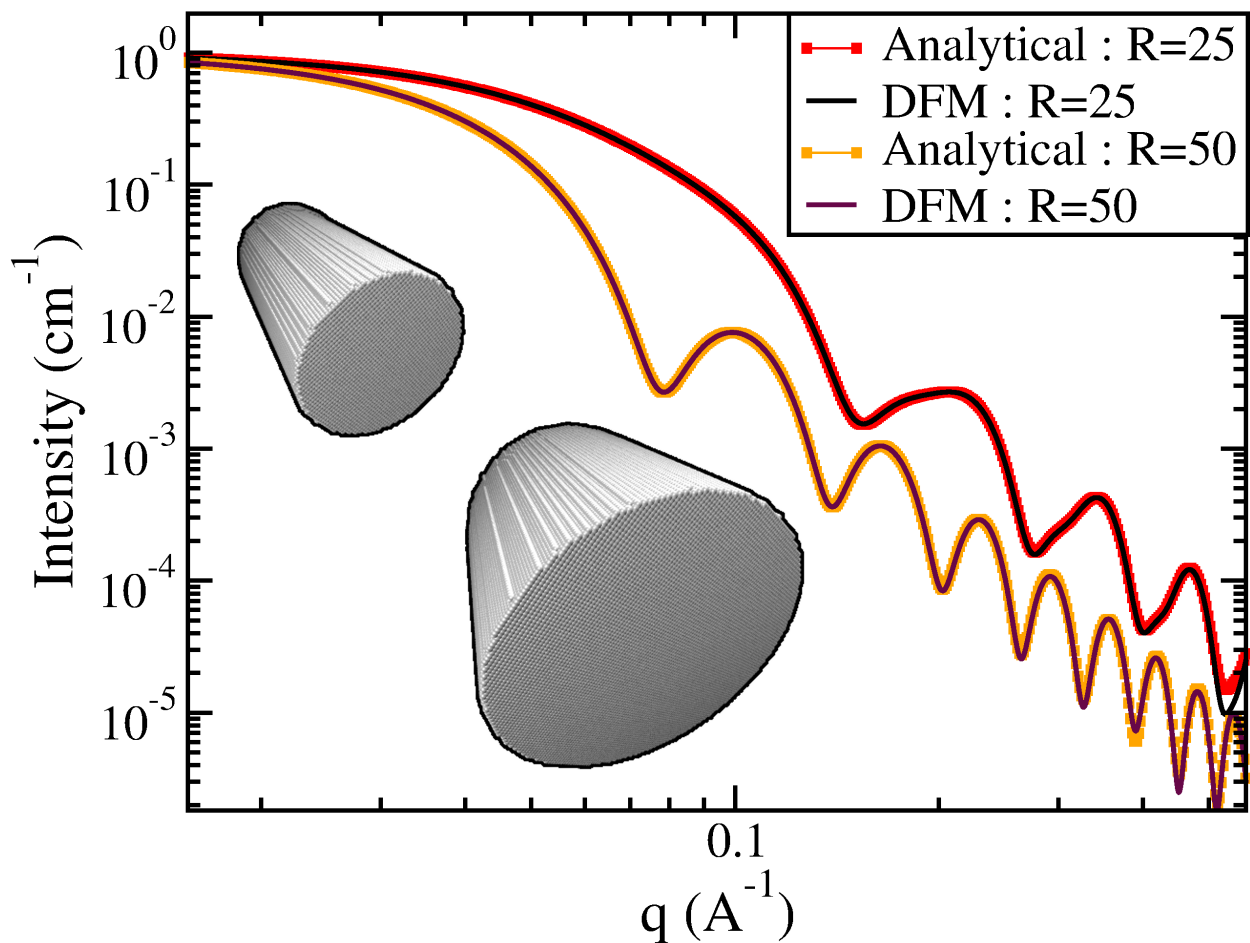
Figure 4.6 Simulated scattering from cylinders of length, $L = 100\,\text{Å}$, and radius, $R = 25, 50\,\text{Å}$, calculated using the analytical form factor for a cylinder and compared to the scattering calculated with the DFM algorithm. Analytical form factors provided by IRENA SAS macros in Igor, where cylinder to solvent contrast is taken as 1-to-0. DFM calculation performed over a randomly sampled set of 10^7 pairs, or .005% of the total system pairs.

cylinder, $R = 50$, $L = 100$, constructed from $N_{\rm p} = 785524$ discrete points, do we see any deviation from the analytical from factor. The deviation we do see corresponds to small scale features which are not as well represented due to the number of pairs sampled. We find that when the number of pairs sampled is set equivalent to the total number of pairs in the system, there is no discernible difference in the resultant simulated scattering implying that the sampling method itself does not introduce any additional structure-like features in the scattering profile.

As small angle scattering data is useful for a number of polymeric system studies such as observing phase transitions[119, 120], we next look at an example of scattering from an ideal polymer chain. For this calculation, we simulate a polymer with one million monomers, generated through an unbiased (non-self avoiding) random walk in real-space, with bond length of 1Å. For each calculation, 1000 polymers are generated and then each sampled to generate $w(r)$, and the results are shown in figure 4.7. The measured radius of gyration for the simulated polymers was found to be $\bar{r}_g = 398$ Å, and we compare the calculated scattering to the Debye form factor[121] for this value of r_g. To explore the effects of sampling rate, scattering profiles were generated using both 10^6 pairs and 100 pairs per configuration.

We see that the results from the DFM algorithm match the Debye form factor to a high degree in both sampling rates, though the errors introduced by the lower sampling rate are evident at high-q. Note that this result is of particular interest, for while the higher sampling rate (.0002% total pairs sampled) captures the analytical solution exactly, the low sampling rate manages to captures all critical information up to the high-q limits of the model where it begins to deviate. This result demonstrates the usefulness of the DFM algorithm as even though the low sampling rate is looking at 10 orders of magnitude less total pairs than the full Debye formalism, a nearly identical scattering profile is generated.
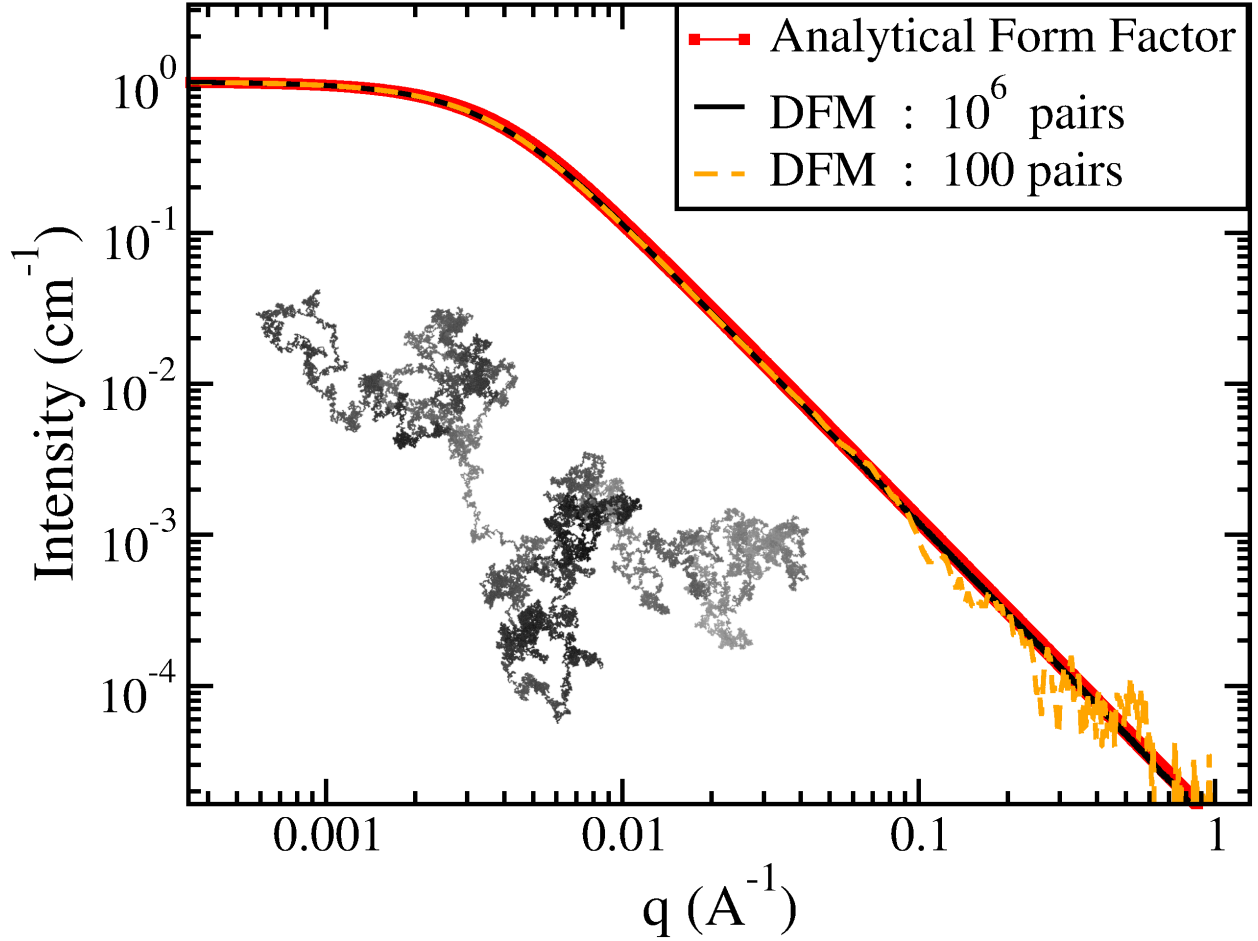
Figure 4.7   Simulated scattering from an ideal chain polymer model with 10^6 monomers with resultant radius of gyration, $r_g \approx 398\,\text{Å}$. The DFM calculation is performed by sampling the given number of random pairs on 1000 random polymer configurations. Note that for the size of polymer simulated here, the total calculation would require a sum of nearly 5×10^{11} total pairs per polymer configuration. Even with only 100 pairs sampled per polymer, the analytical solution is exactly recovered up to high-q values.

4.4.2   Limits of method

Though the examples shown in figures 4.5 - 4.7 are presented as evidence of the validity of the DFM algorithm, it's primary use is in the efficient calculation of scattering profiles for complex structures which are not well described via analytical formalism. However, it is important to understand the natural limits of this method if the profiles generated are to be considered reliable. The two primary limitations on any DFM algorithm are finite size effects and sampling rate errors.

4.4.2.1   Finite size effects

Finite size effects are seen as comparatively high-frequency oscillations in $q-$space, where the frequencies correspond to the length scales of the sample box. In cases where the relevant structural information is contained at higher q-values, which are well separated from the low-q finite size effects, interpretation of the data may seem straightforward. However, the oscillations induced by the finite size effects may still interfere with correct data analysis due to the hard-wall like nature inherent in the abrupt termination of the structural information at the box edge. To alleviate this effect, we suggest a Gaussian "fuzzying" routine be performed on the morphological models prior to scattering profile calculation, which acts to roughen the box edges. Every site in a morphology is assigned a random number, $X \in [0, 1]$, which is then compared to the value of a Gaussian distribution, $G(\sigma)$, with origin at the center of the morphology with a width of σ. If for a given site, if $X > G(\sigma)$, the site is pruned from the list of sites to be used in generating $w(r)$. Thus, the surfaces of a morphological model are roughened such that the contributions to the scattering profile will be damped as compared to a hard-wall sample box.

An example of the Gaussian "fuzzying" routine is given in figure 4.8, which demonstrates
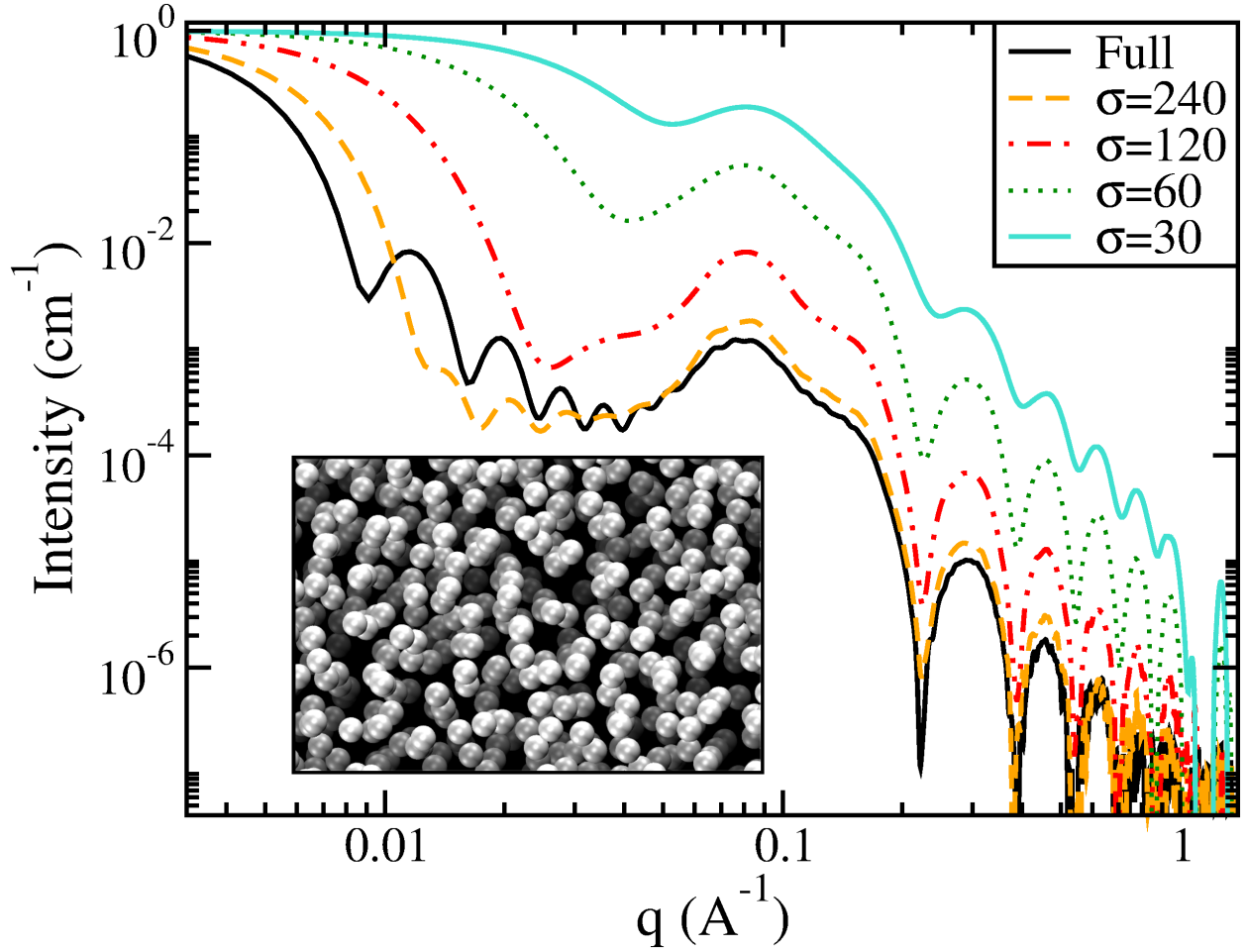
Figure 4.8 DFM calculation of scattering from a system of 697 spheres of radius $r = 20\,\text{Å}$ placed randomly inside a box of size 800^3Å^3 which were selected to have a minimum distance between sphere centers of $L = 100$ Å. Demonstrated are the effect of calculating the scattering on this morphology while points were randomly removed from the structure using a "fuzzying" routine via a Gaussian probability with width σ. This procedure reduces the inherent hard-edged box effects seen as high frequency oscillations at the expense of total signal contrast and sample size.

the routine for a system of monodisperse spheres of radius $r = 20\,\text{Å}$ which have been randomly placed at a minimum center-to-center distance of $D = 100\,\text{Å}$ from one another in a cubic sample box of size $L = 800\,\text{Å}$. Presented in figure 4.8 are the full data (no "fuzzying" routine performed) for comparison with data from $\sigma = 30, 60, 120,$ and $240\,\text{Å}$. The Guinier regime of the plot, seen as a plateau at $q \to 0$, will have an intensity dependent on the total number of scatterers. We thus expect higher intensities for systems which have larger values of σ, as less points will have been removed from the structural model. For purposes of comparison, we normalize all the presented data such that $I(0) = 1$, leading to the apparent rise in intensity of the scattering peaks as σ is decreased. Note also that as the width of the Gaussian is decreased, the shrinking overall model size is evident in the shift of the left most bend in the scattering profile, which is increasing in q-value as the system size is shrinking in real space. In large box simulations, it is important that the box size contributions to the scattering are kept well separated from the sample features of interest.

By applying an appropriate σ to the fuzzying routine, one is able to dampen the finite size effects at the expense of contrast between structures found at long range in the sample and overall model size. For example, in figure 4.8, one might select $120 < \sigma < 240\,\text{Å}$ (between 15% to 30% the total box width) in order to better resolve both the average center-to-center structure factor peak seen at $q \approx (2\pi/100)\,\text{Å}^{-1}$ as well as the spherical form factor seen at $q > .2\,\text{Å}^{-1}$. Smaller σ values than this, correlating with more sites pruned, do little to further clarify the data and may actually begin to obscure the information of interest. This trade-off between total information sampled and clarity of the signal must be evaluated for each morphology.

If using a lattice model, the lattice constant employed (a) will contribute a strong signal at $q = 2\pi/a$, which typically occurs at much higher q-values than the features one is

investigating. Undesirable contributions of the lattice constant will rarely be a problem as long as the lattice resolution employed by a model is sufficient to capture morphological characteristics of interest. Peaks due to the bin size used in generation of $w(r)$ or $I(q)$ will also occur, but as long as the bin width is less than the lattice constant, these will not occur until much higher-q.

4.4.3   Sampling rate errors

When using the DFM algorithm, choice of sampling rate is critical in the generation of a $w(r)$ that will lead to an accurate $I(q)$. The ideal rate to use, however, is highly dependent on individual morphology. If the structure is isolated and a simple fit is all that's required, such as was the case with the polymer in figure 4.7, surprisingly few pairs are required to accurately generate a scattering profile up to high values of q. When insufficient sampling occurs, the effects will be most evident in the high-q regions, as this corresponds to the smallest length-scale features in a morphology and are thus less precisely sampled than those features which exist on longer length scales. It is recommended that when employing the DFM algorithm on an unfamiliar system, a careful examination of how sampling rate effects resultant scattering profiles be performed.

One of the most useful aspects of the DFM algorithm is that once a system's minimum sampling rate is established, dramatic speed increases are possible for many classes of morphologies. If one is interested in larger scale morphological features only (i.e. $q < 1\,a^{-1}$), we have found that applying a smearing function to $I^a(q)$ can alleviate high frequency oscillations introduced by sampling rates too low to accurately capture the high-q information. As a demonstration, we generate large (400^3) lattice box models of 3-d interpenetrating two-phase morphologies where the goal is to characterize the growth of average cluster size

in these models under Ising model simulated annealing[46, 2].

We initially generate structures by randomly assigning sites as one of two materials assignments, $s = 1$ or -1. A simple nearest-neighbor site energy Hamiltonian is employed, $H_i = -\sum_j s_i\, s_j$, where a site i with material assignment s_i will have an energy based on the sum of it's nearest neighbor site assignments, s_j. Sites are selected at random and evaluated with Metropolis Monte Carlo, driving the morphology towards increasing phase segregation. We quantify the degree of phase segregation with the characteristic feature size, $a = 3V/S$, where V is total morphology volume and S is total surface area between the two phases. Further details of the Ising model employed are given in section 5.1 of this thesis. We fix the planar density along one direction of the morphology so that the system cannot completely phase segregate, thus keeping a somewhat homogeneous mix throughout the model. DFM calculations were performed as the system was annealed from $a = 4$ to $a = 16$, sampling with a rate of 10^6 pairs (approximately 10 orders of magnitude less pairs than required by the full Debye calculation), using the Gaussian "fuzzying" routine with $\sigma = 120$. Once calculated, the smearing function suggested by Kline for use in neutron scattering data[118] was employed. The results are shown in figure 4.9. The smearing function used is defined by

$$I_s(q_0) = \int_0^\infty R(q, q_0) I(q) dq \tag{4.39}$$

$$R(q, q_0) = \frac{1}{\left(2\pi\sigma_q^2\right)^{1/2}} \exp\left[\frac{-(q - q_0)^2}{2\sigma_q^2}\right]. \tag{4.40}$$

Here, I_s, is the smeared intensity, σ_q is the standard deviation of the resolution in q. In practice, this smearing function encompass all effects that cause resolution losses in a system. Values of σ_q between five and ten percent were often found to best match experiment.
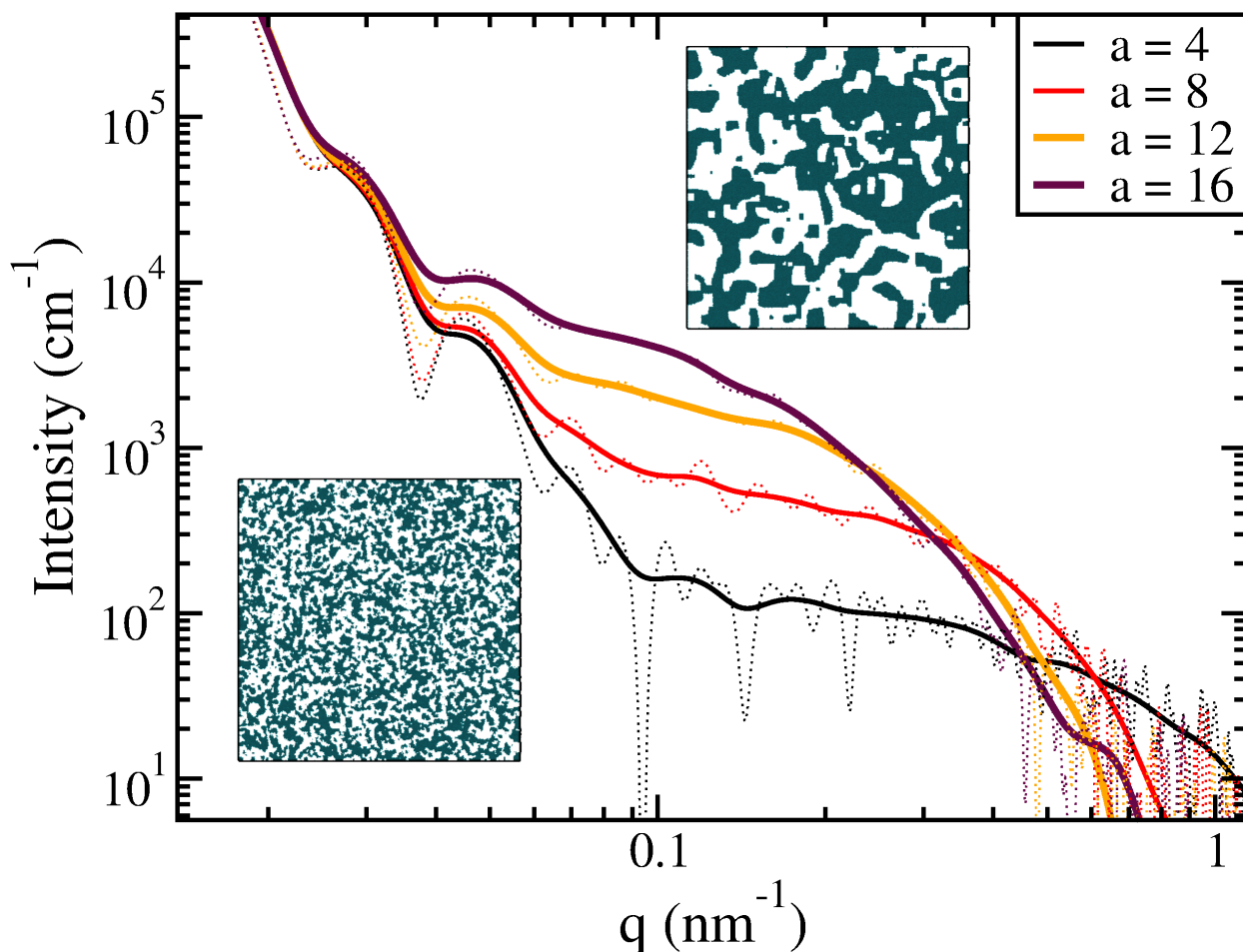
Figure 4.9 A demonstration of how simulated scattering can be used to study the effects of annealing a complex, interpenetrating structure such as the Ising model shown here. Also demonstrated is the use of applying a smearing function to somewhat under-sampled data. The raw data is presented as dashed lines and the $\sigma_q = 10\%$ smeared data is presented as solid lines. Inset figures show cross-sections of these two-phase morphologies as they are annealed from $a = 4$ to $a = 16$.

As demonstrated in figure 4.9, the scattering profile before smearing (dashed lines) and after a smearing function (solid lines) show the same large trends in plateau position and overall profile, but the unsmeared data contains significantly more noise and would thus be difficult to fit to experimental data. If DFM were being employed to observe the drift of the characteristic plateau, as it shifts to higher intensity and lower-q as feature size is increased, it is clear that the sampling rate used here would be sufficient and the presented high-q inaccuracies would be acceptable. The smearing effect itself is less necessary as a increases, as there are few small scale features left in the morphology.

4.4.4   The effects of Interaction

A novel aspect of the DFM approach is that structure factors and form factors need not be treated independently. In theory, one considers the form factor, $P(q)$, to be the contribution to the scattering due to the shape of the individual scatterer and the structure factor, $S(q)$, to be the contribution due to the arrangement these individual scatterers. The overall scattering is a product of these two terms

$$I(q) = S(q) \times P(q). \tag{4.41}$$

In it's simplest interpretation, the DFM algorithm treats all scatterers as points, and thus it is the structure factor that is being calculated. However, if the model resolution is sufficiently high we may construct "scatterers" from a series of points, and then build a larger superstructure out of these scatterers to generate a unique structure factor. Here, we demonstrate this by looking more closely at the case of monodisperse spheres randomly placed inside a large box with different minimum center-to-center distances.

Similar to the morphology modeled in figure 4.8, we randomly place spheres of radius $r = 10$ Å inside a cubic sample box of side length $L = 400$ Å, varying the minimum allowed sphere center-to-center distance as $D = 20, 40$, and 100 Å. Given the resolution we employed (1 Å) and that we constructed the morphology on a cubic lattice, each sphere was composed of 4169 individual scatterers. The number of spheres used in each case was varied such that each configuration was filled to high density. DFM calculations were performed on these systems, sampling 10^9 pairs and the resultant scattering profiles were smeared by 5%. For direct comparison, the scattering profiles were normalized such that $I(0) = 1$. The results of these calculations are shown in figure 4.10. For comparison, the form factor for a $r = 10$ Å sphere is also shown.

In all cases, the average center-to-center distance, D, is clearly observable in figure 4.10 as a small peak at $q = (2\pi/D)$, with subsequent damped oscillations. Note that while both the spherical form factor (clearly visible at $q = 2\pi/r$) and structure factor due to the average center-to-center distance, $\approx D$, are clearly distinguishable for the $D = 100$ and $D = 40$ Å cases, the form and structure factor contributions become somewhat indistinguishable when the average center-to-center distance becomes comparable to the diameter of the spheres, $D \propto 2r = 20$ Å. While no overlap of spheres is occurring, the effects of the structure factor peak in the $D = 20$ Å case are clearly interfering with the normally well defined $r = 10$ Å spherical form factor, highlighting the inherent difficulties present in interpreting high density non-crystallized systems, even when they are composed of very regular nanostructures. This simultaneous modeling of both a form factor and structure factor is possible because of the fine-grained mesh we are employing here, and such a high-resolution model is computationally simple to probe with the DFM algorithm.

As a final example we model a fixed number of polydisperse spheres inside a large box.
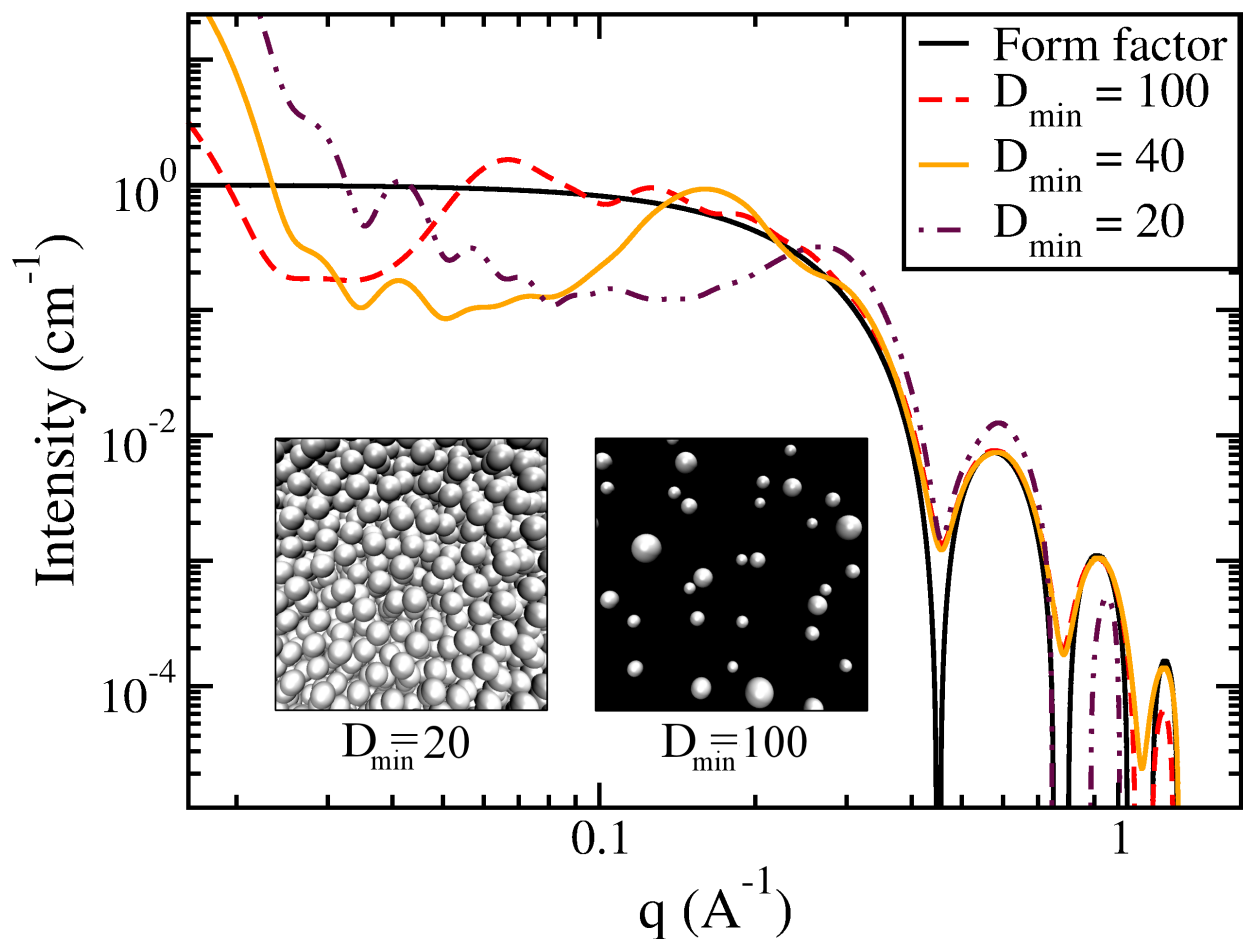
Figure 4.10   Spheres of constant radii, $r = 10\,\text{Å}$, randomly placed inside an $L = 400\,\text{Å}$ box with a minimum center-to-center distance of $D = 20, 40$, and $100\,\text{Å}$. For comparison, the form factor for a single sphere of radius $r = 10\,\text{Å}$ is also shown. The DFM calculation is performed by sampling 10^9 pairs, and smearing resultants by 5%.

We enforce a minimum center-to-center distance between spheres of $D = 100\,\text{Å}$ using a cubic sample box of side length $L = 800\,\text{Å}$, and fix the number of randomly placed spheres in each case to be $N = 370$. For each sphere, a radius is selected based on a polydisperse Schulz distribution with an average of $\bar{r} = 20\,\text{Å}$ and width $\sigma = 5, 10$, and 15. The Schulz distribution being defined[122]

$$P(r) = \left[\frac{z+1}{\bar{r}}\right]^{z+1} r^z \exp\left[-\left(\frac{z+1}{\bar{r}}r\right)\right] \frac{1}{\Gamma(z+1)}, \qquad (4.42)$$

where $\bar{r}$ is the average radius, $z = \bar{r}/\sigma$, and $\Gamma(z+1)$ is the gamma function defined at $z+1$. The polydispersity index (PDI) of each resultant morphology was measured.

The results of the DFM calculated scattering profiles, along with an equivalent system with monodisperse spheres ($PDI = 1.0$) are shown in figure 4.11. Of note is the emergence of clear polydispersity effects as soon as the sphere radii is permitted to vary, seen as a natural blurring of the sphere peaks visible at $q > .2$ in the $r = 20\,\text{Å}$ form factor case. As the polydispersity is increased, the bend over point continues to decrease, as is consistent with polydisperse sphere form factors. Similar to the results of monodisperse spheres in figure 4.10, the structure factor contribution of the average center-to-center distance, $D = 100\,\text{Å}$, is plainly visible at $q = (2\pi/D) \approx .06\text{Å}^{-1}$ for all cases except the most polydisperse, $PDI = 8.15$, at which point the polydispersity induced bending occurs at small enough q that it obscures the structure factor peak.
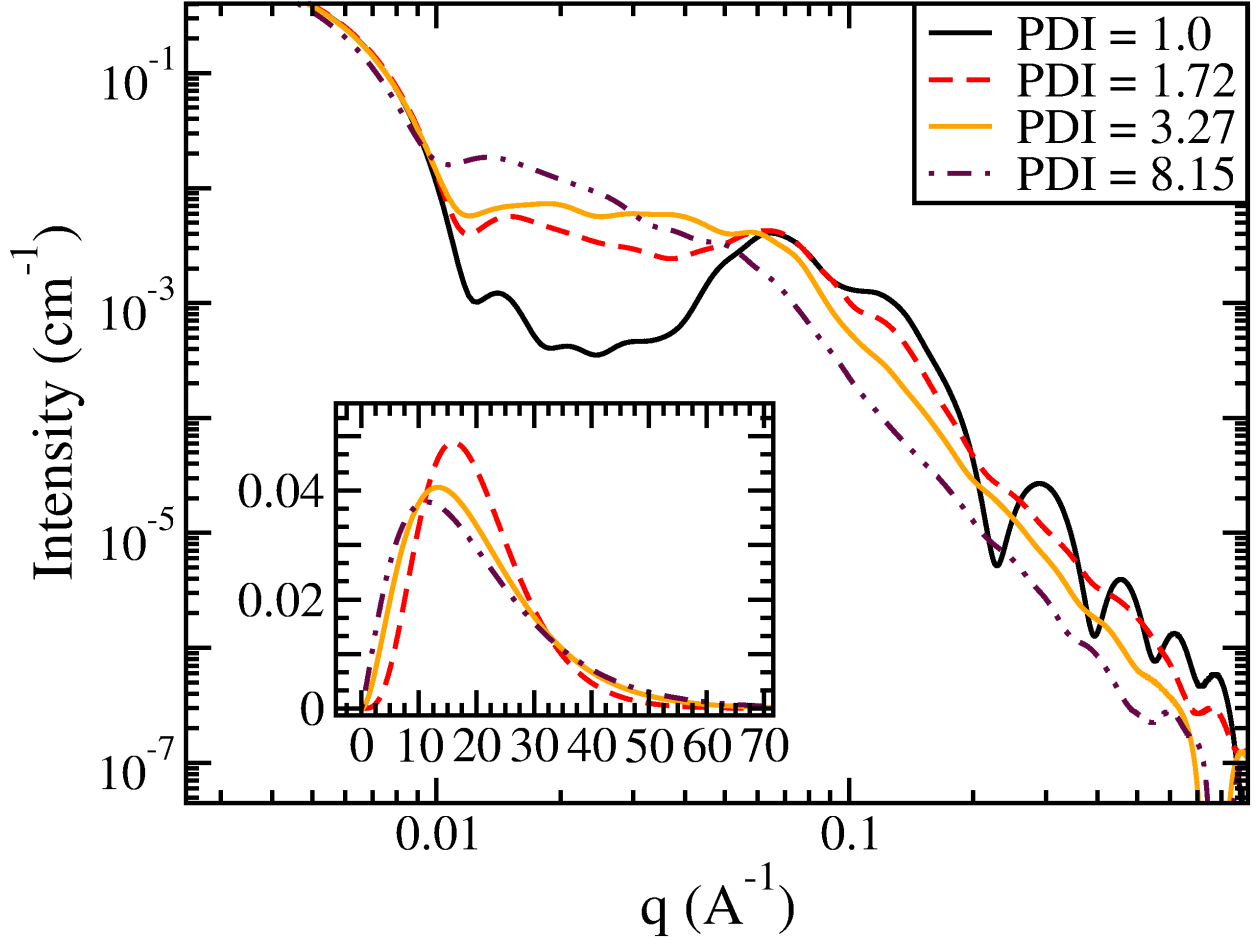
Figure 4.11 Scattering from a series of 370 spheres randomly placed in a $L = 800\,\text{Å}$ box at a minimum center-to-center distance of $D = 100\,\text{Å}$. The sphere radii are selected from a Schulz distribution shown in the inset to the figure. For each distribution, the average radius is $r = 20$ Å, but the deviation used in each case is $\sigma = 5, 10,$ and 15, which generated resultant polydispersity of $PDI = 1.36, 3.27,$ and 8.15 respectively. For comparison, also shown is the scattering from spheres placed under similar conditions with constant radius, $r = 20\,\text{Å}$, corresponding to $PDI = 1.0$. DFM calculation performed by sampling 10^9 pairs, and smearing results 5%. The inset shows the Schulz polydisperse sphere distributions used to select radii.

Chapter 5

Nanoscale Morphologies Incorporating Reflectometry Data and Assessing Effects on Percolative Processes

Both characterization of the BHJ structure and a greater understanding of how morphological effects influence overall OPV device performance are active areas of research[123, 116, 124, 125, 126, 127, 128]. Arguably, the most successful models that relate morphological features to device performance have relied on Ising models[86, 84, 2, 129], published examples of which are shown in figure 5.1. While the Ising model is in no way the only acceptable method for addressing the effects of morphology on device performance, it's simplicity and versatility make it ideal for studying the effects of morphology on transport mechanisms present in an OPV device. In this chapter, we will begin with a detailed description of the simple lattice Ising model as it has been used for generating BHJ morphologies.

In order to generate more realistic model morphologies, we introduce modifications to the simple Ising model which incorporate experimental data by refining the structure using Monte Carlo methods. Specifically, we will demonstrate models which incorporate neutron

reflectometry data taken on P3HT/PCBM BHJ films. We will present derivations of the basic principles of reflectometry and demonstrate how a density profile may be derived from the reflectometry data[130]. The derivations presented are taken from texts[110, 121] unless otherwise noted.

We will present 3-d interpenetrating, percolative morphologies consistent with the experimental reflectivity data, and compare DMC performance calculations performed on these realistic morphologies to results from previous simple "Ising only" models, which contain no reflectivity data. We will then demonstrate modifications to the model to examine the effects of P3HT crystallization and degree of PCBM sequestration.

Finally, we will show that reflectivity data on it's own is insufficient to select a morphology for use in DMC calculations, as a large number of qualitatively varying morphologies may be generated to fit the reflectivity data to high precision.

5.1 Simple Three Dimensional Ising Model

Originally formulated to model the statistical dynamics of ferromagnetism, the Ising model presents a straightforward and efficient method to generate two-phase systems which are formulated with a simply defined configuration based Hamiltonian. The principles of a spin-flip Ising model are that each site of a lattice is assigned a designation (say, 1 or -1) which define the site as being one of two possible states/spins/etc. We use the word "spin" interchangeably with "material" in this discussion, as they are only meant to designate site assignment. Model morphologies are generated through the use of Metropolis Monte Carlo (MC) procedures, wherein potential site flips are evaluated based on their overall effect on a defined Hamiltonian, $H(a)$, where the evaluated energy will be based upon the specifics

(a)

(b)
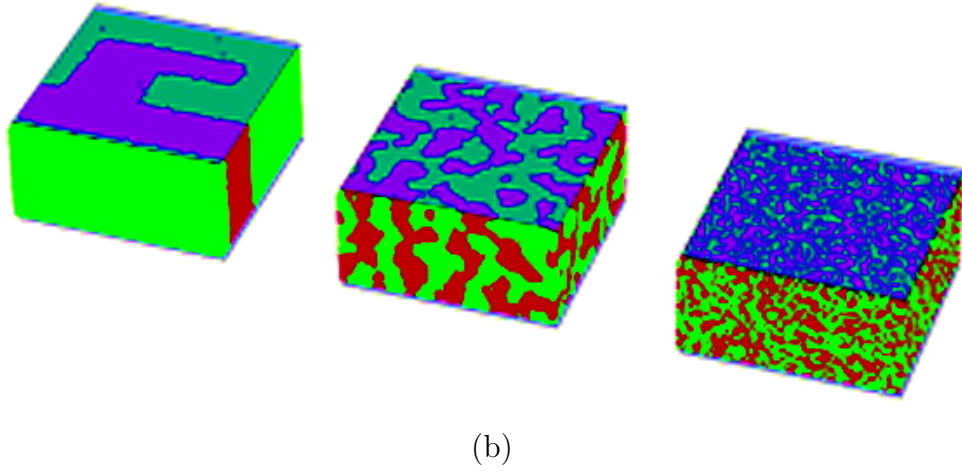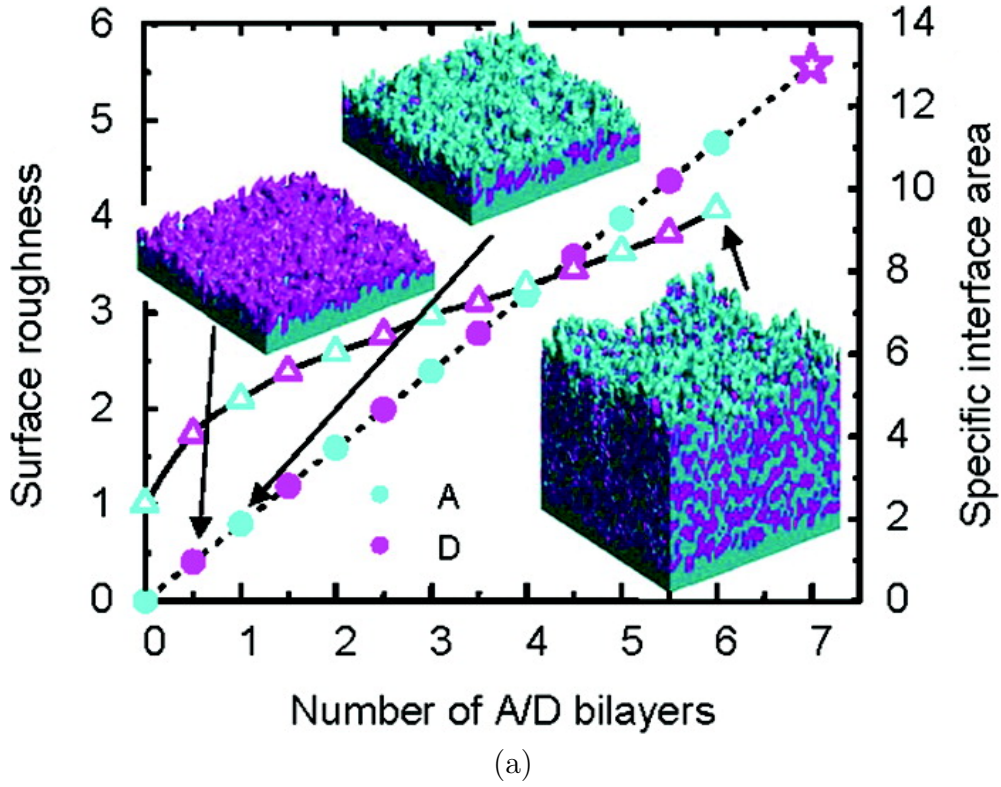
Figure 5.1 Figure 5.1a demonstrates the work of Steve Forrest's group using a simple Ising model to roughen the interface between a set of bilayers[1]. Figure 5.1b demonstrates the work of Alison Walker's group using an Ising model to study the effect of BHJ feature size on device performance[2].

of the configuration. The system is modified via careful acceptance or rejection of spin flips based on randomly chosen sites. Candidate spin flips generate altered configurations, b, whose ideality is evaluated in comparison to the initial configuration, a, via the defined Hamiltonian as a change in system energy $\Delta E_{ab} = H(b) - H(a)$. Candidate flips which generate a more energetically favorable configuration such that $\Delta E_{ab} < 0$ are always accepted. Candidate spin-flips which generate less favorable configurations ($\Delta E_{ab} > 0$) are only accepted with a certain probability based on the magnitude of ΔE_{ab} and the simulation temperature. Through the use of the well known Metropolis algorithm[131]. The overall acceptance probability can be summarized as

$$
P_{accept}(\Delta E) = \begin{cases} 1 & \text{if } \Delta E < 0 \\ \exp\left[-\frac{\Delta E}{k_b T}\right] & \text{otherwise,} \end{cases} \tag{5.1}
$$

where $P_{accept}(\Delta E)$ is the probability of accepting a candidate spin-flip, ΔE is the energy change of a system due to this candidate spin-flip, and $k_b T$ is the simulation temperature. In the high-temperature limit, almost all flips will be accepted where as in the low-temperature limit, no energetically unfavorable flips from the ground state will occur.

The nearest neighbor spin 1/2 Ising Hamiltonian function, H_{o}, is defined as

$$
H_{\mathrm{o}}(S_i) = -\sum_{\substack{i \neq j}}^{\text{n.n. sites}} J S_i S_j, \tag{5.2}
$$

such that the energy contribution of a site, i, which has spin assignment S_i, is related to the interaction strength, J, with nearest neighbor sites j, that have spin assignment, S_j. Sites may have spin designation of $S = +1$ or $S = -1$. With such a Hamiltonian, values of $J > 0$ will coarsen the morphology, minimizing surface area between the two spin-phases. If

$J < 0$, the system will tend towards a mixed configuration, maximizing surface area between the two spin-phases. A common metric used to describe the current state of a two-phase morphology is the characteristic feature size, a, defined as

$$a = 3V/S, \tag{5.3}$$

where V is the total volume and S is the total surface area between the two spin-phases. Smaller values of a correspond to a greater level of mixing between the two materials, whereas larger values of a designate a coarser grained-structure.

A time-step in an Ising model MC process is defined to be attempting to make a number of random site spin flips equal to the number of sites in the lattice, $N = L_x \times L_y \times L_z$ for a 3-d cubic lattice. Candidate sites are selected at random for each potential flip, rather than a constant sweep through the morphology as this would bias the structure. This random-selection method means that in a single MC step, some sites may not be given an opportunity to flip while others could potentially flip many times. One can correct for this by initially generating a list of all sites in a lattice, randomly ordering this list every time step, and going through this list to select candidate sites; but the results of the two methods are essentially the same.

The total number of time-steps required to anneal an Ising morphology to a desired characteristic feature size, a_{target}, will be dependent on the specific Hamiltonian used and the simulation temperature. For values of $J > 0$ the morphology feature size evolution will grow as $T^{1/2}$ where T is the number of Ising steps, as is demonstrated in figure 5.9. Higher values of T will permit the morphology to more quickly explore configurational phase-space, but one must be careful as too high a temperature will prevent the morphology from

converging on the ideal energetic minima configuration.

Two versions of the Ising model MC algorithm are the Kawasaki (spin-swap) dynamics method and the Glauber (non-conserved) Monte Carlo (GMC) method. In the GMC method[132], a single site's contribution to the Hamiltonian is considered for each spin flip, and if that flip is found acceptable (passes the Metropolis test) then the site's spin-assignment is flipped. In the Kawasaki method[133], two sites of different spin values are considered simultaneously, having their individual candidate spin-swap energy contributions summed to generate ΔE. If the candidate swap is accepted, then the two site spins are exchanged, effectively exchanging their spin assignments. In the Kawasaki method total spin is thus conserved, which is not guaranteed in the GMC method. By nature of single site evaluation compared to pairs of sites, the GMC method will anneal a structure to coarser grained structures (greater a) more rapidly, but the lowest energy configuration will be one in which all sites are assigned a single spin value. However, by adding a term to the Hamiltonian defined by equation 5.2, which is a function of total population density, we may overcome this and find structures with a target population. An example of such a modified Hamiltonian is

$$H_{\text{config}}(S_i) = -\sum_{i \neq j}^{\text{n.n. sites}} J S_i S_j + J_{pop} \left| \nu_{config} - \nu_{target} \right|^p , \qquad (5.4)$$

where the prefactor J_{pop} and the parameter p constrains the current population of a spin species, ν_{config}, to the target population, ν_{target}.

As Ising models have been used extensively to describe nanomorphology present in OPV devices, our goal is to improve the techniques in order to incorporate experimentally provided information about the morphology. Reflectometry is one experimental method which lends itself easily for incorporation into an Ising model, and we introduce the principles of

reflectometry measurements here.

5.2   Principles of Reflectometry
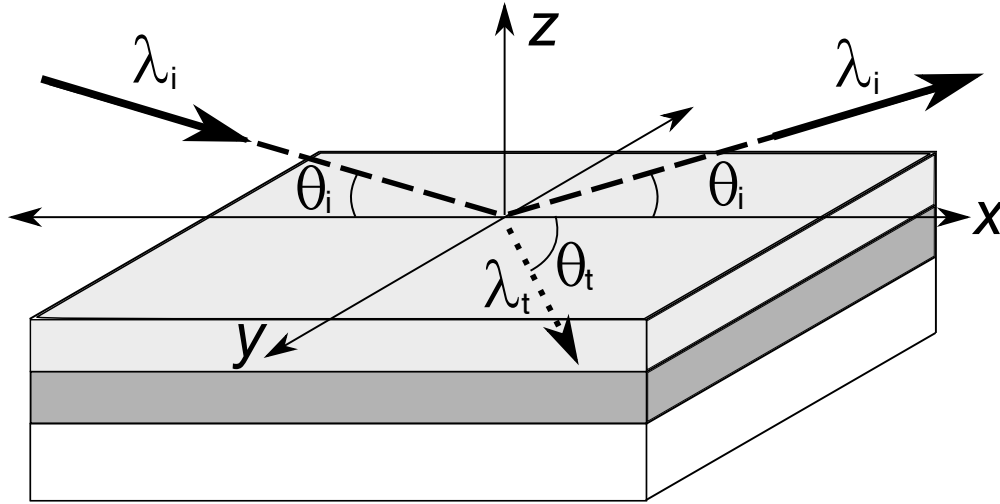
Figure 5.2   Schematic of reflectometry measurement, with incident wavelength, λ_i reflecting at an angle of θ_i off of the surface, with a transmitted wave having associated wavelength λ_t at angle θ_t. Note that this figure demonstrates the reflection and transmission angles associated with only the first layer of a multilayer system. Further reflections/transmissions are implied but not shown.

Reflectometry is a measurement which probes the scattering properties of a very flat sample, typically described by a 1-d vertical function normal to the surface of the sample. In a reflectometry experiment, a beam of particles (neutrons or x-rays) is incident nearly parallel to the surface of a sample (see figure 5.2). Based on the properties of the sample, a fraction of the incident beam intensity will be specularly scattered off the sample, being reflected symmetrically forward at the incident angle, θ_i, which is then measured with a detector placed far from the sample. That fraction of the beam which is not reflected is transmitted into the sample, at angle θ_t, and based on the material will have an associated transmitted wavelength, λ_t. The measurement thus characterizes reflectance from a sample with values ranging $0 \leq R \leq 1$, where 0 represents total absorption in the sample and 1

being total reflection. The incident beam is characterized by it's momentum transfer, q, which is defined

$$q = \frac{4\pi \sin \theta_i}{\lambda_i}. \tag{5.5}$$

The measurement will thus inform on a sample's reflectivity as a function of momentum transfer, $R(q)$. As the beam is incident over a large surface area of the sample, all structural information due to lateral (x-y dimension) features will be averaged together and only those details in the vertical (z-dimension) are discernible.

The reflectivity measured off a sample will be related to the scattering strength of the materials in the sample, described most directly by their scattering length density (SLD). Standard reflectivity data analysis involves fitting an experimentally measured reflectivity profile to a modeled SLD profile, $\beta(\mathbf{r})$, which due to the lateral averaging of the sample may simply be considered as $\beta(z)$.

5.2.1   Kinematic Derivation

To begin with, let us examine the Fourier transform relationship between the elastic differential cross-section and the SLD function. Recall the relationship derived in equation 4.25, we may write this more straightforwardly as

$$\frac{\mathrm{d}\sigma}{\mathrm{d}\Omega} \propto \left| \iiint_V \mathrm{d}\mathbf{r}\, \beta(\mathbf{r})\, e^{\mathrm{i}\mathbf{Q}\cdot\mathbf{r}} \right|^2, \tag{5.6}$$

noting again that the proportionality is used instead of an equals sign as the RHS has not been normalized by a constant such as the number of scatterers, mass, or volume, as this normalization varies across disciplines but this core concept relation remains the same.

If we define a sample to have dimensions $(2L_x, 2L_y, 2L_z)$ (with lengths selected to simplify the calculation), and assume $\beta(\mathbf{r})$ is equal to $\beta(z)$ inside the sample, and 0 outside, we may rewrite equation 5.6 as

$$\frac{d\sigma}{d\Omega} \propto 16 \frac{\sin^2\left(L_x q_x\right)}{q_x^2} \frac{\sin^2\left(L_y q_y\right)}{q_y^2} \left| \int_{-\infty}^{\infty} dz\, \beta(z) e^{izq_z} \right|^2 , \qquad (5.7)$$

where the two sinc-squared prefactors come from the scattering of a rectangular slab of width $2L_x \times 2L_y$. Thus, the scattering will have a maximum at $q_x = 0$ and $q_y = 0$ of the value $16 L_x^2 L_y^2$ and be focused in the small region $\left|q_{x/y}\right| < \frac{\pi}{L_{x/y}}$.

The relationship between elastic differential cross-section and the specular reflectivity measured in a reflectivity measurement is best understood by comparing the definitions

$$\frac{d\sigma}{d\Omega} = \frac{\text{Number of particles deflected an angle } (2\theta, \phi) \textit{ per unit solid angle}}{\text{Number of incident particles } \textit{per unit area of beam}}$$

and

$$R = \frac{\text{Rate of specular reflective scattering}}{\text{Rate of incidence}}.$$

Clearly, both values are based on the ratio of scattered particles to the illuminated portion of the sample, which in the case of the reflectometry is $4L_x L_y \sin\theta$, whereas the differential cross section is integrated over a solid angle, $\Delta\Omega$. Thus, in the range of specular condition, we may write the reflectivity in terms of the differential cross-section

$$R(Q) = \frac{1}{4L_x L_y \sin\theta} \iint_{\Delta\Omega} d\Omega \frac{d\sigma}{d\Omega}. \qquad (5.8)$$

Using the substitution

$$\iint_{\Delta\Omega} \mathrm{d}\Omega \, \frac{\mathrm{d}\sigma}{\mathrm{d}\Omega} \approx \frac{\Delta\Omega}{4} \times \left. \frac{\mathrm{d}\sigma}{\mathrm{d}\Omega} \right|_{qx=0,qy=0,qz=-q} \tag{5.9}$$

and approximating $\Delta\Omega$ as

$$\Delta\Omega \approx \frac{16\pi^2 \sin\theta}{L_x L_y q^2}. \tag{5.10}$$

Assuming that the area under illumination is large compared to the wavelength of the incident particle, this yields the relation

$$R(q) = \frac{16\pi^2}{q^2} \left| \int_{-\infty}^{\infty} \mathrm{d}z \, \beta(z) e^{-\mathrm{i}qz} \right|^2. \tag{5.11}$$

Notice also that unlike the differential cross section definitions, which were left as proportionalities, the reflectivity is a direct equality as the former was a consequence of a variety of conventions used in normalization, but this is not required for the SLD as one may define

$$\beta = n \langle b \rangle, \tag{5.12}$$

where the SLD, β, is defined as the product of the atomic density (atoms per unit volume), n, and the coherent scattering length, $\langle b \rangle$. Thus, utilizing integration by parts we can redefine the reflectivity data as a function of the derivative of the SLD

$$R(q) \approx \frac{16\pi^2}{q^4} \left| \int_{-\infty}^{\infty} \mathrm{d}z \, \frac{\mathrm{d}\beta}{\mathrm{d}z} e^{-iqz} \right|^2. \tag{5.13}$$

Here we have written the result as only an approximation, not direct equivalence. As we will show, this is because any result derived using the kinematical assumption is not valid

98

for reflectometry, particularly at low values of q.

5.2.2   Dynamical Derivation

While an excellent first order approximation, the Fourier relationship derived in equation 5.13 was formulated under the Born or kinematical approximation, which assumes that the scattering process is weak and that the scattered wave has a negligible effect on the incident beam. In such a kinematical picture, multiple scattering is ignored, hence the simple superposition of the scattering due to individual scatterers. In neutron reflectometry, however, measurements are taken in a regime where all incident neutrons are specularly reflected from the surface of a sample, which is not weak scattering and thus, not in the Born regime.

The perturbation of the incident wave by the scattering process is considered negligible in the Born approximation. However, a "thick" sample is used in neutron reflectometry due to the path the neutrons take being $L = T/\sin\theta$ where T is the thickness and θ is the incident angle. This leads to the failure of the approximation of equation 5.13, particularly as θ becomes close to 0 or the thickness, T gets large. Deviations at higher λ values come from the reciprocal relationship between momentum of an incident particle and wavelength, meaning that the more energetic a particle is, the less it will be perturbed.

In order to generate accurate models of reflectivity, one must use a dynamical theory of scattering, rather than a kinematical (Born based) one used previously. We present that derivation here.

Using the standard definition of a refractive index
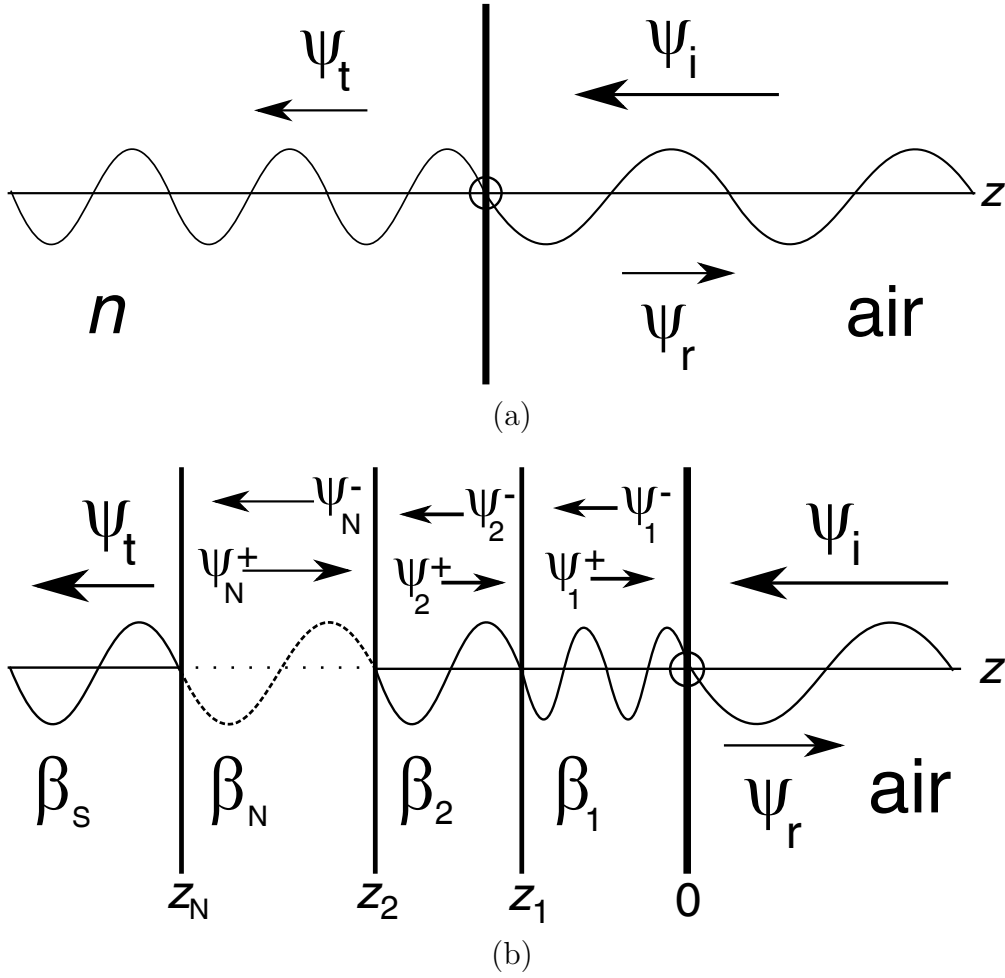
Figure 5.3 Two qualitative 1-d examples of an incident wave, ψ_i, which originates in air ($\beta_{\mathrm{air}} = 0$) interacting with a sample. Figure 5.3a demonstrates a incident wave ψ_i incident on a sample with index of refraction n, with subsequent transmitted wave ψ_t and reflected wave ψ_r. Figure 5.3b demonstrates the incident wave on a multilayered sample, with N different layers atop a substrate layer S. Each layer has a propagating component, ψ^- to the left and a reflected component ψ^+ to the right.

$$n(\lambda_i) = \frac{\cos(\theta_i)}{\cos(\theta_t)} = \frac{\lambda_i}{\lambda_t}, \tag{5.14}$$

where the index of refraction is considered a function of incident wavelength, λ_i, it is

defined as the ratio of the cosine of the incident angle, θ_i, over the cosine of the transmitted

wave angle, θ_t. This is equivalent to the ratio of the incident wavelength over the transmitted

wavelength, noting that the frequency of the wave will be unchanged through the boundary.

To derive the dynamical scattering expression we begin with a simple one dimensional

single boundary example, as defined in figure 5.3a, with the interface at z=0. The incident

wave is defined

$$\psi_i(z) = \psi_o e^{-izk_i \sin\theta_i}, \tag{5.15}$$

where ψ_i is the incident wave as a function of coordinate z, ψ_o is the incident amplitude,

k_i is the incident wavenumber defined as $k_i = \frac{2\pi}{\lambda_i}$. At the boundary, a fraction of the wave

will be transmitted and the rest reflected. We may define these transmitted and reflected

waves similarly as

$$\psi_t = t e^{-izk_t \sin\theta_i} \tag{5.16}$$

$$\psi_r = r e^{izk_i \sin\theta_i}, \tag{5.17}$$

where the coefficients, t and r, define the amplitude of transmitted and reflected wave

respectively. The sign convention denotes propagation direction, as is seen in figure 5.3a.

Using equation 5.14, the transmitted wave vector can be written $k_t = \frac{2\pi n}{\lambda_i}$. Similarly, the

relation of the incident angle to reflected angle can be written as $1 - \sin^2 \theta_t = \frac{1 - \sin^2 \theta_i}{n^2}$. The boundary conditions which must be satisfied are thus

$$\psi_i + \psi_r = \psi_t \tag{5.18}$$

$$\frac{\mathrm{d}}{\mathrm{dz}}(\psi_i + \psi_r) = \frac{\mathrm{d}}{\mathrm{dz}}\psi_t, \tag{5.19}$$

the solution of which can be found to be

$$t = \frac{2\psi_o}{1 + \alpha} \quad \text{and} \quad r = \left(\frac{1 - \alpha}{1 + \alpha}\right)\psi_o \tag{5.20}$$

where

$$\alpha = \frac{k_t \sin \theta_t}{k_i \sin \theta_i} = \frac{n}{\sin \theta}\left[1 - \frac{(1 - \sin^2 \theta_i)}{n^2}\right]^{1/2}. \tag{5.21}$$

Clearly, we can see that total reflection ($r = 1$) will occur when α is equal to 0. Additionally, if the term in brackets of equation 5.21 is less than 0, then α will be imaginary, which cannot occur if any wave is to be transmitted. We may thus define the fraction of reflected wave as the ratio of the amplitude reflected to the incident amplitude, squared, as

$$R = \left|\frac{r}{\psi_o}\right|^2 = \frac{1 - 2\Re(\alpha) + |\alpha|^2}{1 + 2\Re(\alpha) + |\alpha|^2}. \tag{5.22}$$

Total external reflection will occur when $R = 1$. Thus, in order to have total external reflection the necessary condition exists

$$\sin^2 \theta_i \leq 1 - n^2. \tag{5.23}$$

102

Complete reflection thus occurs for materials with $n < 1$ (for an interface with the incident wave passing through air) below a critical angle of

$$\theta_c = \sin^{-1}\left(\sqrt{1 - n^2}\right).\tag{5.24}$$

Recalling the definition of momentum transfer, $q = \frac{4\pi}{\lambda}\sin\theta_i$, and the condition given by equation 5.23, we may rewrite equation 5.21 as

$$
\begin{aligned}
\alpha &= \frac{n}{\sin\theta_i}\left[1 - \frac{(1 - \sin^2\theta_i)}{n^2}\right]^{1/2} \\
&= \frac{n}{n\sin\theta_i}\left[n^2 - (1 - \sin^2\theta_i)\right]^{1/2} \\
&= \frac{1}{\sin\theta_i}\left[-(1 - n^2) + \sin^2\theta_i\right]^{1/2} \\
&= \frac{\sin\theta_i}{\sin\theta_i}\left[1 - \frac{n^2 - 1}{\sin^2\theta_i}\right]^{1/2} \\
&= 1 - \frac{1}{2}\frac{n^2 - 1}{\sin^2\theta} \\
&\approx 1 - \frac{8\pi^2(1 - n^2)}{\lambda_i^2 q^2}.
\end{aligned}\tag{5.25}
$$

Note that the last step of this derivation takes advantage of the binomial expansion, $\sqrt{1 - A} = 1 - A/2 - \ldots$, and this approximation will be more accurate as q increases. Noting that $\alpha \approx 1$, we may rewrite equation 5.22 in the form

$$R = \left|\frac{1 - \alpha}{1 + \alpha}\right|^2 \approx \frac{16\pi^2}{q^4}\left[\frac{\pi(1 - n^2)}{\lambda^2}\right]^2,\tag{5.26}$$

which when compared to equation 5.13, implies that the term in brackets must be equated with the SLD, such that

103

$$n^2 \approx 1 - \frac{\beta \lambda_i^2}{\pi}. \tag{5.27}$$

Note that this is the same result Fermi derived for the transmission of a signal through a planer slab of uniform material in 1950. Referring back to the critical angle as defined in equation 5.24, we see that we may define a critical value for q where total external reflection will abruptly cease

$$q_c = 4\sqrt{\beta \pi}. \tag{5.28}$$

Having derived the dynamics of reflection and transmission for a single boundary, we may generalize to treat multiple boundaries. Having a series of boundaries, defined by their SLD profiles

$$\beta(z) = \begin{cases} \beta_s & \text{for } z < z_N \\ \beta_j & \text{for } z_j < z < z_{j-1} \\ 0 & \text{for } z > 0, \end{cases} \tag{5.29}$$

where $j = 1, 2, 3, \ldots, N$ are the indices defining the N layers of the structure, with an air interface at $z = 0$, as seen in figure 5.3b. The wave function in a single slab, j, may be written

$$\psi_j(z) = A_j \, e^{izk_j} + B_j \, e^{-izk_j}, \tag{5.30}$$

where A_j and B_j are the amplitudes for waves in the reflected (positive in z) and transmitted (negative in z) direction, respectively. The wavenumber for each component may be written

$$k_j = \left(\frac{2\pi}{\lambda_j}\right)\sin\theta_j = \left(\frac{2\pi n)j}{\lambda_i}\right)\sqrt{1 - \frac{1 - \sin^2\theta_i}{n_j^2}}. \tag{5.31}$$

In a similar method to the single layer, we may rewrite the wavevector for the j-th layer

$$k_j = \frac{1}{2}\sqrt{q^2 - 16\pi\beta_j}. \tag{5.32}$$

The boundary conditions for this set of wavefunctions is

$$\psi_{j+1}(z_j) = \psi_j(z_j) \quad \text{and} \quad \frac{\mathrm{d}}{\mathrm{d}z}\psi_{j+1}(z_j) = \frac{\mathrm{d}}{\mathrm{d}z}\psi_j(z_j). \tag{5.33}$$

The solution, similar to equation 5.20, has the form

$$A_j = \frac{\mathrm{i}k_j\psi_j(z) + \psi_j'(z)}{2\mathrm{i}k_j\mathrm{e}^{\mathrm{i}zk_j}} \quad \text{and} \quad B_j = \frac{\mathrm{i}k_j\psi_j(z) - \psi_j'(z)}{2\mathrm{i}k_j\mathrm{e}^{-\mathrm{i}zk_j}}. \tag{5.34}$$

The reflectivity is measured as the ratio of reflected amplitude to transmitted amplitude at the surface interface $(j = 0)$, will be given by $|A_0/B_0|^2$

$$R(q) = \left|\frac{\mathrm{i}k_0\psi(0) + \psi'(0)}{\mathrm{i}k_0\psi(0) - \psi'(0)}\right|^2. \tag{5.35}$$

As transmission occurs when $A_{N+1} = 0$ (implying no reverse wave inside the substrate), we may write that at the substrate the wave is defined

$$\psi'(z_N) = -\mathrm{i}k_s\psi(z_N), \tag{5.36}$$

which has the solution

$$\psi(z_N) = 1 \quad \text{and} \quad \psi'(z_N) = -ik_s. \tag{5.37}$$

Starting with this solution, one may recursively solve the wave function inside each previous layer, $\psi(z_j - 1)$, as a function of the following layer with the relationship

$$\psi(z_j - 1) = \cos(k_j T_j)\psi(z_j) + \frac{\sin(k_j T_j)}{k_j}\psi'(z_j) \tag{5.38}$$

and

$$\psi'(z_j - 1) = -k_j \sin(k_j T_j)\psi(z_j) + \cos(k_j T_j)\psi'(z_j), \tag{5.39}$$

up to $j = N$ where the surface of the multiple layers is reached at $z = 0$. This iterative process for calculating reflectivity was proposed by Abelés and Parratt, and this is the method used by many modern reflectivity calculations, such as those demonstrated in figures 5.4 to 5.7.

Examples of the relationship between SLD density profiles and associated reflectometry data are shown in figures 5.4 to 5.7, which have all been generated with the commonly used motofit macros[134] for IGOR. In all examples of figures 5.4 to 5.7 and discussions here, SLD values have units of 10^{-6} Å^{-2}. In the first example, figure 5.4, a single step of thickness 25 Å ($\beta_{step} = 5$) between an air interface ($\beta_{air} = 0$) and a substrate ($\beta_{sub} = 5$) is shown with different step "roughness" of 0, 5, and 10 Å, where roughness is a somewhat counterintuitive term used in the motofit macros to denote a blending transition between two adjacent layers of an SLD density profile. The first important features of note in figure 5.4 is the sudden drop from total external reflection ($R = 1$) at the critical angle, $q_c = 4\sqrt{\pi\beta}$, at which point the reflectometry takes on the $R(q) \propto q^{-1/4}$ dependence as seen in equation 5.13. At angles

106
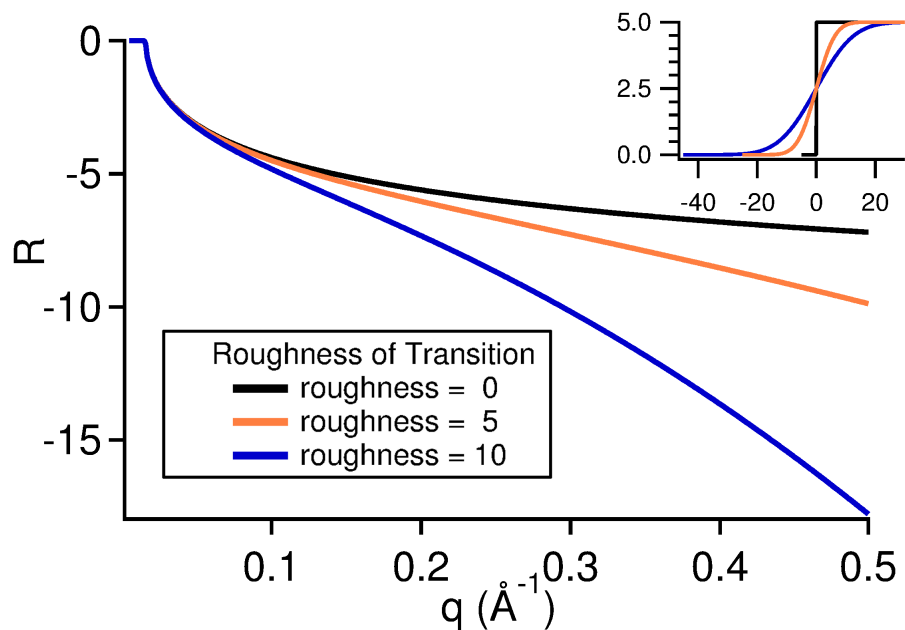
Figure 5.4   A demonstration of the simulated reflectometry data from a simple step function, with various amounts of "roughing" of the edges to smooth the transition between layers.
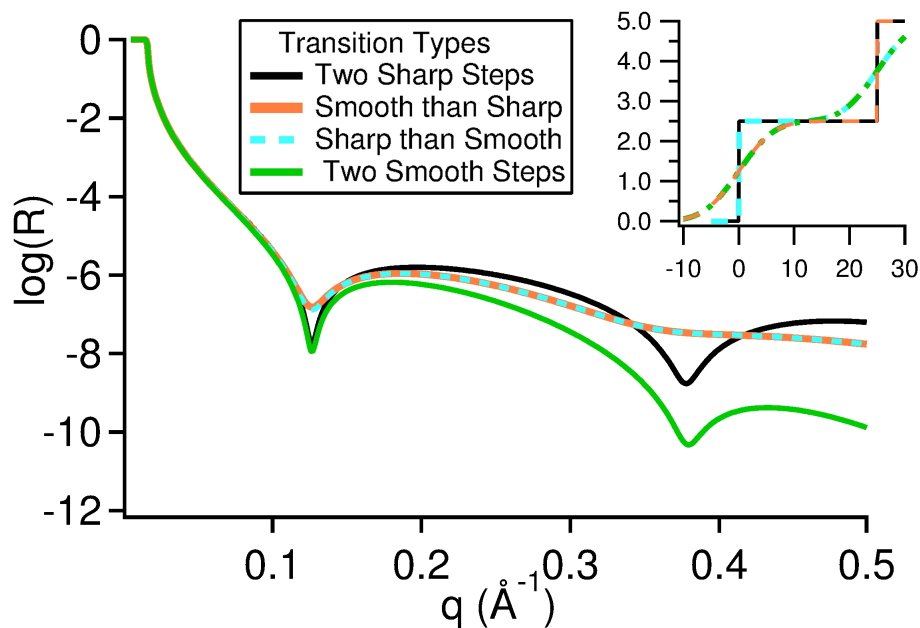
Figure 5.5   An example of various step functions with combinations of sharp and smooth transitions between steps, demonstrating how identical reflectometry data can be generated from structures with different SLD density profiles.
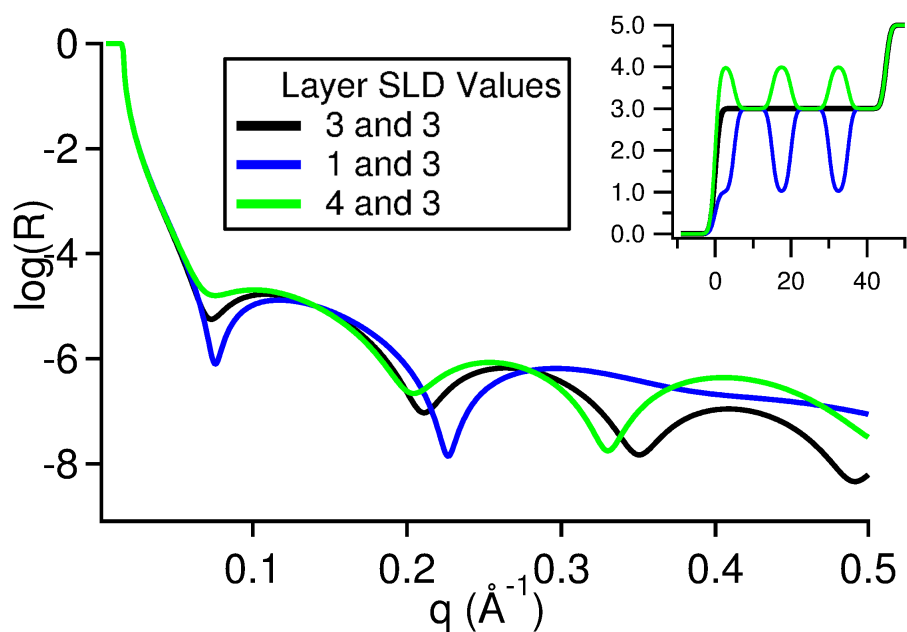
Figure 5.6 An example of simulated reflectometry data from layers of alternating SLD values, in order to demonstrate how SLD contrast effects reflectometry data.
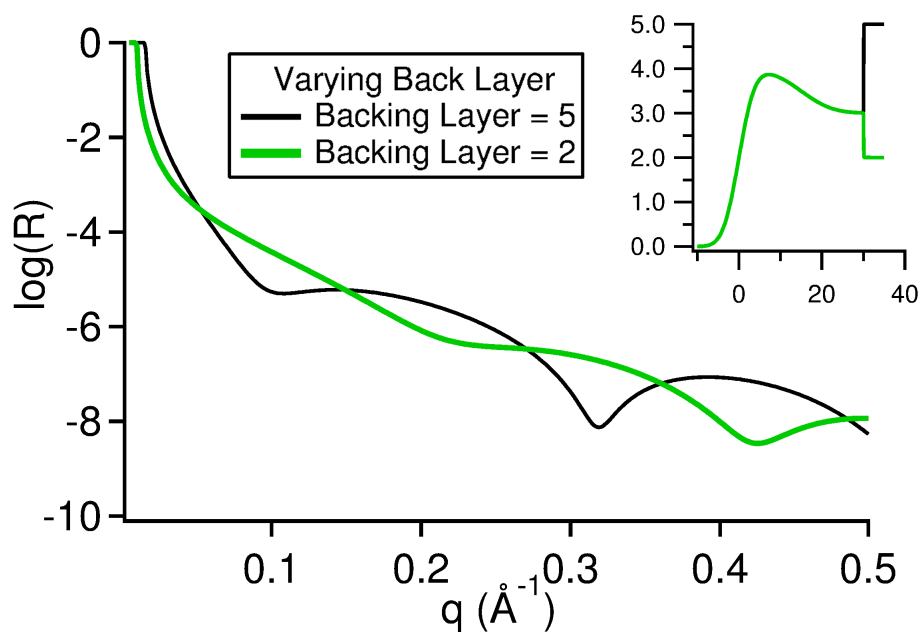
Figure 5.7 A demonstration of the effect of varying the background layer of an otherwise fixed SLD density profile.

lower than the q_c, neutrons will be entirely reflected from the interface, thus no information on the internal structure is probed. This initial drop at q_c often provides a clear picture on the SLD value of the first layer the neutrons pass though, so long as the SLD value of this material is positive. The second feature to note from figure 5.4 is that increasing roughness causes a further Gaussian like decay from the $R(q) \propto q^{-1/4}$ relationship, which can be described as

$$R(q) \approx R_o(q) \times \exp(-\sigma^2 q^2), \tag{5.40}$$

where $R_o(q)$ is the reflectometry due to a sharp interface (no roughing) and σ is the thickness of the associated Gaussian which has been convoluted with the sharp interface structure to generate a smoothed transition between two adjacent layers.

The second example, seen in figure 5.5, exhibits different transitions between an air interface, 25 Å thick layer of $\beta_{step} = 2.5$, and substrate ($\beta_{sub} = 5$). There are essentially two transitions which must be made, from air to the step layer ($\Delta\beta = 2.5$) and from the step layer to the substrate ($\Delta\beta = 2.5$), with the effects of different combinations of these transitions (sharp interfaces or smooth) being shown. Note that while the two sharp interfaces (black line) decay the least at higher q, while the two smooth interfaces (green line) decay the most, the mixed transition states of sharp-smooth or smooth-sharp (blue and orange, respectively) are indistinguishable from one another. This highlights an important shortcoming of the reflectometry method, that different SLD-density profiles may generate identical reflectometry graphs, as the relationship between them is based on the integral of all SLD derivatives ($\mathrm{d}\beta/\mathrm{d}z$) throughout the sample, as seen in equation 5.13, and thus $R(q)$ contains no inherent information about the ordering of the layers, nor the SLD values inside

the system, only the transitions between layers.

The third example in figure 5.6 shows the reflectometry for a system of 6 total layers between air ($\beta_{air} = 0$) and a substrate ($\beta_{sub} = 5$) which have three different sets of alternating SLD values for the layers, of 3 and 3 (black line), 1 and 3 (blue line), and 4 and 3 (green line). This example demonstrates the importance of contrast difference between components in a complex system, as the greater the difference in SLD values of the layers is, the more significant the deviation of the $R(q)$ profile from the uniform case. Note that the sign of the difference doesn't matter, only the magnitude, a result of the loss of phase information in the scattering measurement. Contrast is often a principle concern in scattering experiments, leading to the frequent use of deuterated samples in neutron based studies as deuterium has a significantly different SLD value than hydrogen ($\approx .67$ to $\approx -.37$ respectively).

The final example in figure 5.7 is a specific demonstration of altered contrast in a system, wherein an arbitrary complex layer between the air and substrate is held constant, but the substrate SLD is altered from $\beta_1 = 5$ to $\beta_2 = 2$. This subtle change to the system can be seen to cause a dramatic shift in $R(q)$ at all values of q. This highlights a technique of backing-layer contrast change, in which an unknown morphology is probed using a variable backing layer, such that two measurements for the same system are taken with a well known difference between them. The resultant two reflectometry profiles, $R_1(q)$ and $R_2(q)$, may then be solved with the constraint that the density profile must be consistent with both measurements, as only the backing SLD value will have altered. This method produces density profiles of significant confidence, as the morphologies are fit not just to a single measurement, which we know to be underconstrained (as shown in fig. **??**) but two measurements simultaneously. This is the method utilized by Jon Kiel to generate reflectometry fits from the annealed and as cast P3HT/PCBM solar cells[8], the results of which are shown in figure 5.10.

5.3 Generation of BHJ Morphologies Consistent with Reflectometry Data

First and foremost, the models we generate should be consistent with the general picture of these OPV BHJ morphologies. We first motivate our structures by presenting recently published images and models of various polymer/fullerene BHJ morphologies, shown in figure 5.8. Though subtle differences between sample preparation or model picture will vary from group to group, a clear consensus is that the nanomorphology present in these BHJ structures is one of 3-d interpenetrating, percolative structure.

The bulk heterojunction morphology has been modeled extensively in previous work through the use of a simple spin-flip Kawasaki lattice Ising model[2, 47], with sites being assigned as either pure PCBM (acceptor) or pure P3HT (donor). For our initial models, we employ a methodology similar to that used previously, with the addition of a constrained Ising model to incorporate an experimentally provided target density profile, ρ_{target}. At this point we impose no other constraints on the morphologies, such as P3HT crystallization or PCBM sequestration. The Hamiltonian we use is

$$H_{\text{config}}(S_i) = -\sum_{i \neq j}^{\text{n.n. sites}} JS_iS_j + J_{pop} \left|\nu_{config} - \nu_{target}\right|^{p1}$$
$$+J_{dens} \int_0^L dz \left|\rho_{config}(z) - \rho_{target}(z)\right|^{p2}, \tag{5.41}$$

where the Hamiltonian evaluating a specific site i with material assignment, S_i, is defined by three terms. The first term defines the phase-segregation energy, J, looking at nearest neighbor material assignments, S_j. The third term, defined by the energy J_{dens}, evaluates

(a) (b) (c)

(d) (e) (f)
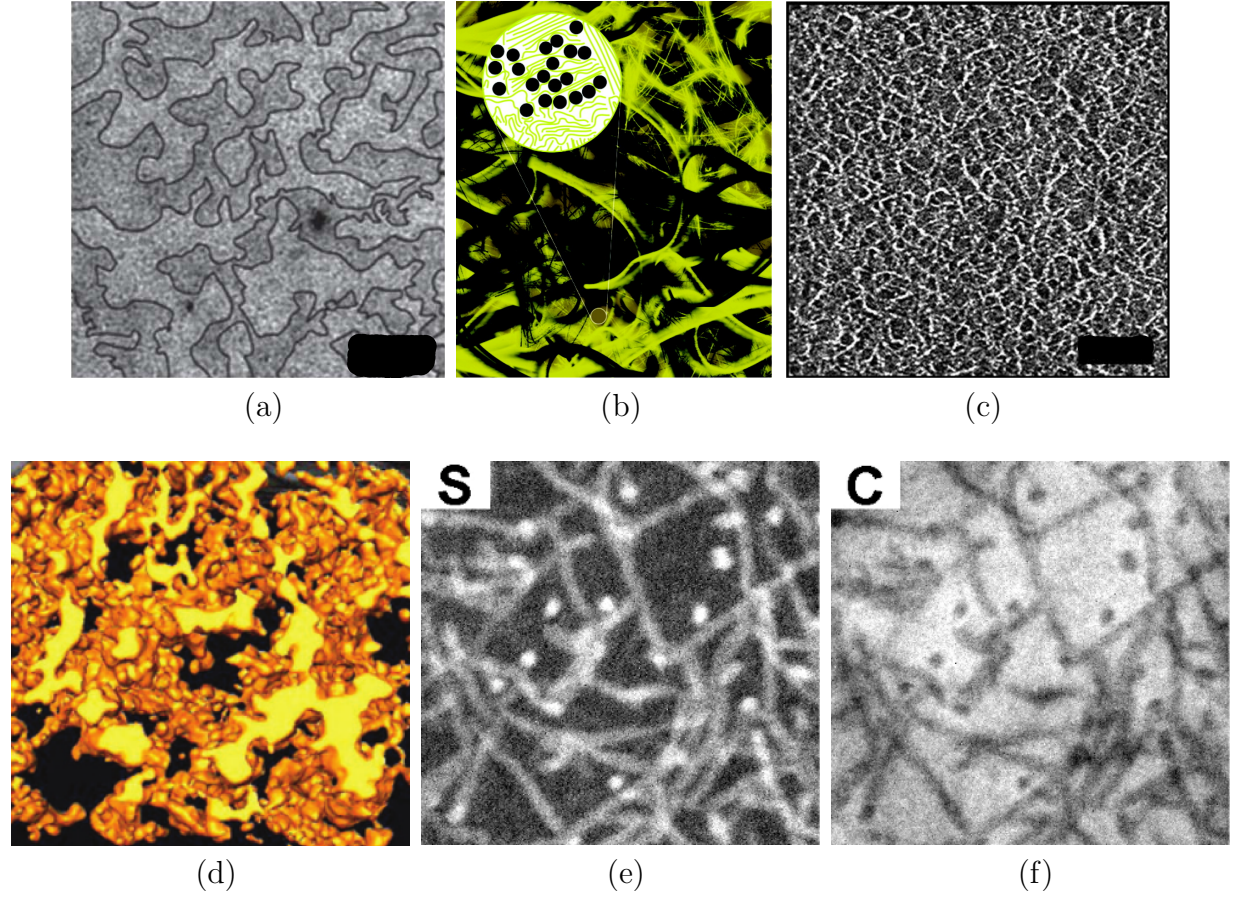
Figure 5.8 Various images and models of polymer/fullerene BHJ morphologies. Figure 5.8a shows bright field TEM images of an polymer/fullerene BHJ OPV film composed of PTB7:PC61BM/DCB + DIO, with artificial black lines added to highlight differences between the polymer-rich and nanoparticle-rich domains[3]. Figure 5.8b is a cartoon illustrating the nanomorphology proposed in BHJ OPV devices under the "Rivers and Streams" model[4]. Figure 5.8c is an image of the x-y plane in a polymer(PF10TBT)/nanoparticle(PCBM) film generated from electron tomography data, with the polymer regions highlighted in light and PCBM regions in dark[5]. Figure 5.8d shows a sample cross-section of reconstructed data taken on a P3HT/ZnO OPV device obtained through electron tomography with ZnO being yellow and P3HT being transparent[6]. Figures 5.8e and 5.8f show sulfur maps and carbon maps, respectively, taken through energy filtered electron tomography (EFTEM) for 1:1 weighted P3HT/PCBM films which were annealed for 30 minutes at zero defocus and with dimensions approximately 400 nm across. Light regions in the sulfur map correspond to higher concentrations of P3HT-domains[7].
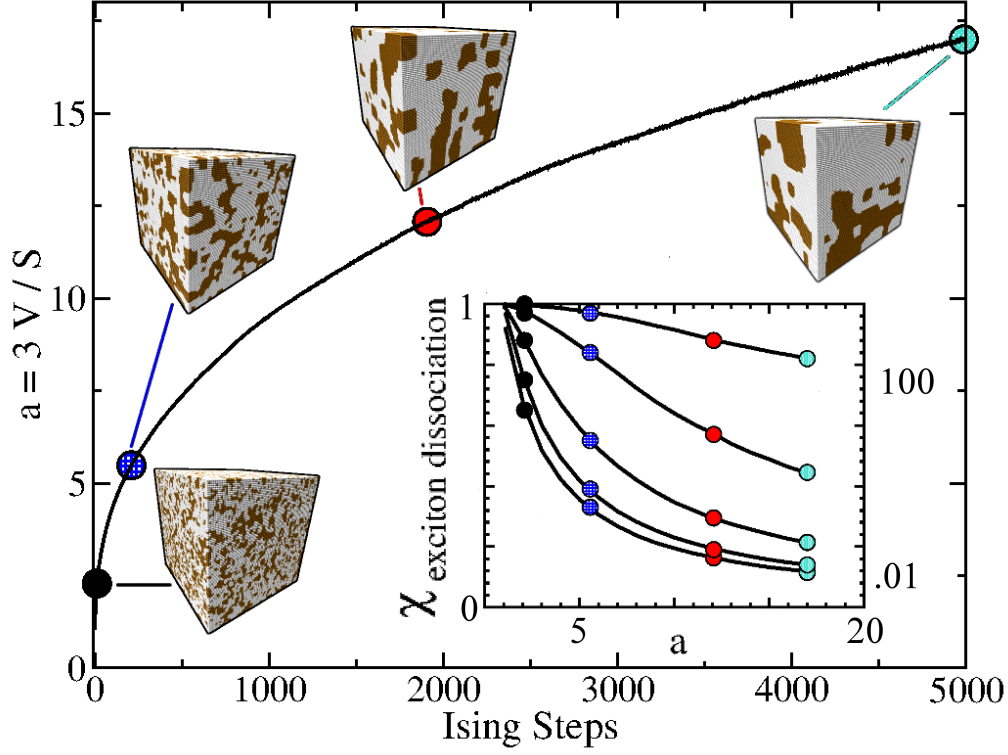
Figure 5.9   Demonstration of Ising annealement over time on an example morphology annealed with parameters $J = 2.0$, $k_B T = 2.0$, $J_{dens} = 15.0$, and $J_{pop} = 4.1$, fitting the annealed reflectivity profile shown in figure 5.10. As the morphology was being annealed, exciton transport calculations were performed for each integer value of feature size reached $(a = 1, 2, 3, \ldots)$ using a simplified form of the DMC model as is described in chapter 6. The results of these calculations are presented in the inset as exciton dissociation efficiency versus characteristic feature size (a). The calculation was performed using decay of lengths, $L_x = [.01, .1, 1, 10, 100]$, which are shown. Four specific morphologies are highlighted, with their corresponding results also highlighted in the inset.

how closely a candidate configuration's in-plane density, $\rho_{config}(z)$ adheres to the target density profile, $\rho_{target}(z)$. The final term, defined by the energy J_{pop}, evaluates how closely the candidate configuration's target population density, ν_{config}, adheres to the target as provided by integration of the target density profile, ν_{target}. The terms p_1 and p_2 are fitting parameters which for the models presented here we set to unity, but which can be varied to tune the strength of the constraints.

With the addition of the second term (defined by J_{pop}) we may change from the previously utilized pair-swapping Kawasaki Ising method to the non-conserved single-site flipping

113

Glauber Metropolis Monte Carlo method. The introduction of this third term adds a constraint such that the population of the entire morphology will not deviate far from the target population value, ρ_{target}.

So long as J_{dens} is sufficiently large, all generated morphologies will fit the reflectivity profile to high precision. For our models, we utilize PCBM density profiles derived from neutron reflectometry measurements taken by Jon Kiel on spin-cast P3HT/PCBM BHJ OPV mimics before and after annealing, the fits for which are shown in figure 5.10. At this stage, the model contains no information which informs on the target characteristic feature size (a), so we generate many morphologies with a wide range in a. 2-D cross-sections of some morphologies generated using this method are shown for the as-cast morphology in figure 5.11 and the annealed morphology in figure 5.12. Clearly, this method generates morphologies which are qualitatively similar to previous models, but also consistent with neutron reflectometry data.
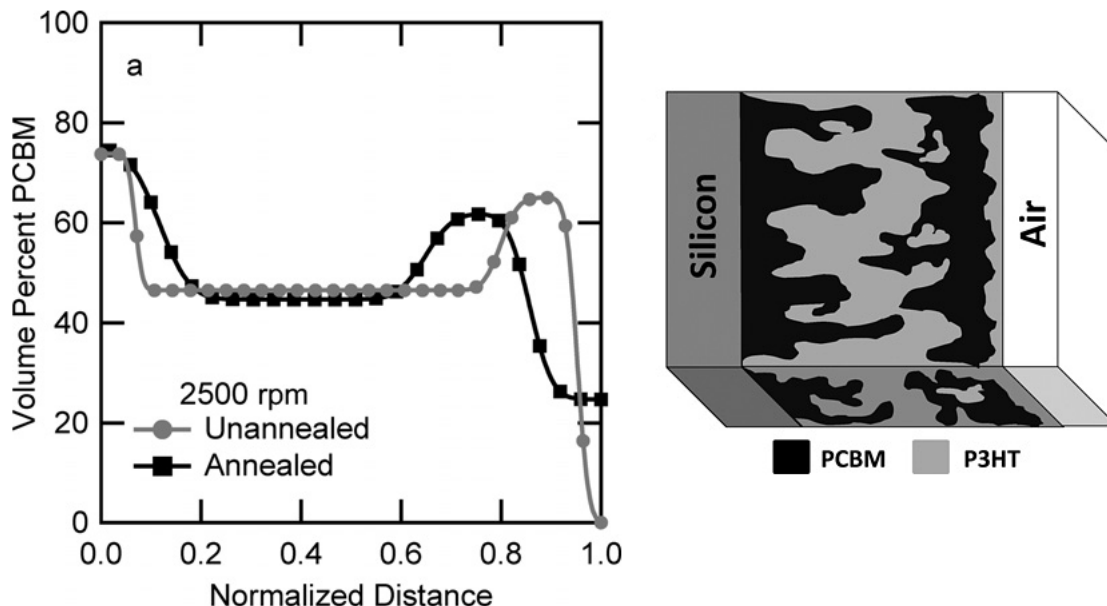
Figure 5.10   PCBM density profile fits derived from neutron reflectivity data and an associated cartoon theorizing the morphology[8].

The cross-sections illustrate that as characteristic feature size, a, is increased, the model morphologies become increasingly phase segregated. The effects of the imposed density profile are immediately visible, in that while phase-segregation is clearly perceivable with increasing values of a, the material is tethered to span the entirety of the morphology because of the target density profile. The details of these reflectivity informed density fluctuations are seen most dramatically in the sudden drop in PCBM (acceptor) sites on the top electron collecting (metal) side of the as-cast morphologies, which is clearly seen comparing the top-down views of the as-cast and annealed morphologies in figures 5.14a and 5.14b respectively. More subtle effects of the imposed density profiles are perceptible, as higher density PCBM sites (brown) correlate with higher PCBM densities in the target profile.

For a straightforward comparison between the models generated here, and the experimental picture of BHJ morphology, we take a $400 \, nm \times 400 \, nm$ section of a published image of electron tomography of a BHJ morphology[5] which is similar to those used in the Kiel reflectometry study, artificially color it similarly to how we have presented our models, and present the results in figure 5.13. Note that the polymer used in the tomography study was poly[2-methoxy-5-(30 ,70 -dimethyloctyloxy)-1,4-phenylene vinylene] (MDMO-PPV), and not the P3HT used in the neutron reflectometry studies here, so this example is shown only for qualitative comparison of a polymer/fullerene BHJ nanostructure.

While these models are similar to previous Ising model morphologies, generating 3-D interpenetrating percolative morphologies, the method presented provides a simple and easily expandable framework on which to incorporate additional details into the model. To demonstrate this, we first explore the theoretical effect of PCBM sequestration, as proposed in the "Rivers and Streams" model[4].

5.3.1 The Three-Phase BHJ Picture

Though much work has been done on the P3HT/PCBM bulk heterojunction solar cell with a so-called two-phase model, describing the morphology as either a site of acceptor (PCBM) or donor (P3HT) material, recent work has suggested that the BHJ internal morphology is better described by a three phase model. Yin and Dadmun[4] suggest a picture of the morphology they refer to as as the "Rivers and Streams" model, with three distinct components; a phase of pure aggregate PCBM particles, a phase of pure crystallized P3HT, and a mixed phase of non-crystallized P3HT with dispersed PCBM. A principle assumption in this model is that charge transport is dominated by transport through the pure material phases (non-mixed), with hole mobility greatly enhanced in the crystallized polymer and electron mobility higher in the aggregate PCBM regions. The colloquial name, "Rivers and Streams" comes from Yin and Dadmun's theory that charges flow through small "streams" of pure material percolating through the bulk of the mixed phase, connecting with large "rivers" of pure material which connect more directly with the contacts. Yin and Dadmun propose that the fraction of dispersed PCBM is around 20% the total PCBM in a morphology.

Here, we explore the effects of the three-phase model picture using our constrained Ising morphologies. To begin with, we reduce the complexity of the three-phase model by treating the crystallized P3HT and mixed phases as one and the same. Yin and Dadmun themselves suggest that crystallized P3HT phases likely do not occur within films as thin as those used in OPV devices[4], requiring films an order of magnitude thicker in order to be observed with small angle x-ray scattering. Additionally, the difference between crystallized and amorphous P3HT are imperceptible in neutron scattering studies, as the SLD for the two are very similar. For these reasons, we model two-phases for the "Rivers and Streams" morphologies; a phase

of pure aggregate PCBM and a phase of dispersed PCBM in P3HT.

The density profiles, provided by the Kiel neutron reflectometry data, are assumed to represent the features of aggregate PCBM throughout the film and we assume that PCBM present in the mixed phase is evenly dispersed. We define a variable, x, which defines the fraction of total PCBM in a film that has become dispersed in the amorphous P3HT, and reduce the annealed PCBM density profile evenly at all sites by this dispersed PCBM fraction, x, as shown in figure 5.15. Using these modified aggregate PCBM density profiles, we generate morphologies using the modified Ising model as described in section 5.3 and select those morphologies which have a characteristic feature size of $a \approx 16$ (selected for reasons explained in section 6.1.1) in order to compare to the previous annealed morphology. We generate morphologies with dispersed PCBM fractions of $x = 0, x = .1, x = .15$ and $x = .2$. Cross-sections of the generated morphologies are shown in figure **??**, which upon initial inspection reveal only subtle differences. However, closer examination reveals that as the faction of dispersed PCBM (x) is increased, a discontinuity develops between the network of agglomerate PCBM sites and the electron collecting electrode. To visualize this effect, we superimpose cross-sections 15 layers thick, labeling those sites which have a connected aggregate PCBM path to the electrode of interest in green, those sites which contain no such path and are thus disconnected from the contact are shown in white, and removing all sites which are the mixed PCBM/P3HT phase, the results of which are shown in figure 5.17.

Qualitatively, the cross-sections in figure 5.17 reveal several initial features of note, foremost being that the majority of the aggregate PCBM in the $x = .2$ morphology is disconnected from the electron accepting contact. Comparing the $x = .15$ and $x = .2$ cases, we see that a sudden and dramatic transition occurs, implying that a percolative threshold for this sort of morphology was crossed. Note also that the $x = 0$ case does have aggregate

PCBM sites which are disconnected from the contact (marked as white in figure 5.17) but that the size of these non-viable PCBM aggregates are much smaller, typically on the order of a single site, as compared to all other cases where $x > 0$ in which the non-viable PCBM has formed larger aggregates.

The qualitative differences between the cases are a direct consequence of having less PCBM available as the value x is increased, because the models compared here were all generated to have a feature size of $a \approx 16$. In each case, the volume is fixed by the dimensions of the morphology ($V = 400^3$) yet there are a decreasing number of aggregate PCBM sites overall, meaning on average, each site must be more likely to be an interfacial site and subsequently less of the sites can be interior bulk of aggregate PCBM (directly adjacent to only other aggregate PCBM sites). This can be seen somewhat in the "beading" of aggregate PCBM as x increases. For a similar reason the distance between aggregate PCBM clusters must increase.

5.3.2   Crystallized P3HT Fiber Networks

Recent studies have shown that transport through crystalline polymer regions are an important factor in overall OPV BHJ device performance[135]. Extensive study of crystalline P3HT (c-P3HT) has been performed[136, 30, 4, 137, 138, 139], which found crystalline structures forming with cross-sectional areas of $20\,nm \times 4\,nm$ and lengths of up to $400\,nm$. The molecular structure and packing of individual fibers is well understood. The packing of fibers is highly dependent on processing conditions, with annealing typically leading to higher crystallinity. Here, we explore the morphological effects of generating models which directly incorporate crystallized fiber networks through a templating procedure.

We begin by seeding the morphology with semi-aligned non-overlapping c-P3HT fiber

118

regions. The fibers are added layer by layer with each layer being 4 lattice units thick (in the z-dimension). The orientation of each layer alternates between spanning the x and y dimension. For each layer, an initial propagation angle is randomly selected, $\theta \in -\frac{\pi}{4}$ to $\frac{\pi}{4}$ radians, though each individual fiber may deviate by a random angle of $\Delta\theta \leq .3$ radians. If a fiber would overlap with a previously placed fiber, it is rejected. All fibers are placed down segment by segment, with each segment having the dimensions of 20×4 lattice units^2. As segments are being placed, there is a random chance of breaking the crystal fiber, taken here to be .25%. A break causes a gap to form in a specific fiber, with this gap having a random width based on a Gaussian distribution with average size 60 and width 20. The c-P3HT fiber segments resume placement once the break gap is completed. This break behavior leads to fibers with an average length of $250 \, nm$. Figure 5.18b demonstrates the c-P3HT fiber lattice structure, from a top-down perspective. c-P3HT fibers are placed down in this way up to a predetermined maximum density for a given layer set by the P3HT profile derived from the reflectivity data in figure 5.10 up to a maximum of 30%, generating a density of c-P3HT such as that seen in figure 5.18a.

Once the initial c-P3HT template is constructed, the remaining P3HT sites required to match the density profile of the model with the target density are randomly placed on each layer. A model morphology seeded in this way is shown in figure 5.19. At this point, Ising annealement is performed on the morphology in order to generate structures with greater characteristic feature sizes. This annealement is similar to the procedure described in section 5.3, however those sites which are marked as c-P3HT (shown in blue in figures 5.19) are frozen. The interaction energy, J, between c-P3HT and other sites is taken to be the same as the interaction between amorphous P3HT sites with some adjustment to the parameters used in the Hamiltonian (given in equation 5.41), principally using higher

temperatures in the simulation, we are able to again generate model morphologies with the characteristic feature size of $a = 16$ (this value was selected for reasons discussed in section 6.1.1 of this thesis). For calculations of surface area required to define a, we calculate the surface area between all PCBM and P3HT sites. This annealed c-P3HT morphology is shown in figure 5.20, again with PCBM sites shown in brown, amorphous P3HT shown in white, and crystallized P3HT shown in blue. The c-P3HT templating procedure has introduced a clearly visible anisotropy into the system, whereby the static framework of the crystallized polymer network forces additional constraints into how the system may anneal.

5.4   Conclusions

In this chapter, we have introduced a simple method to generate 3-d interpenetrating, percolate nanostructures which are consistent with neutron reflectivity data. Though we choose to use a constrained Ising model, this method could easily be expanded to other morphological models such as Cahn-Hilliard, phase-field models, interpenetrating sphere models, and so on. We have also demonstrated how these sorts of morphological models may be used to qualitatively explore the effect of various system features, which we demonstrated by comparing morphologies generated with a simple two-phase model, a more complex three-phase sequestered PCBM model (like Yin and Dadmun's "Rivers and Streams" model) and a crystallized P3HT fiber network model.

As noted earlier, many model morphologies are consistent with reflectometry data as this system is underconstrained. These model morphologies are being developed for use in transport dynamic simulations, but we can assume that any model in which morphology plays a significant role could produce very different results for two different morphologies that

120

are fit to the same target density profile, but significantly differ in other internal features. A clear example of this is shown in the inset to figure 5.9 which shows a sample DMC calculation, looking at exciton dissociation ability, as a function of not only parameters used in the model, but also morphology used. In order to further constrain the model, in chapter 6 we take advantage of small angle neutron scattering (SANS) measurements, which were also performed on the annealed and as cast BHJ OPV devices by Jon Kiel[25].
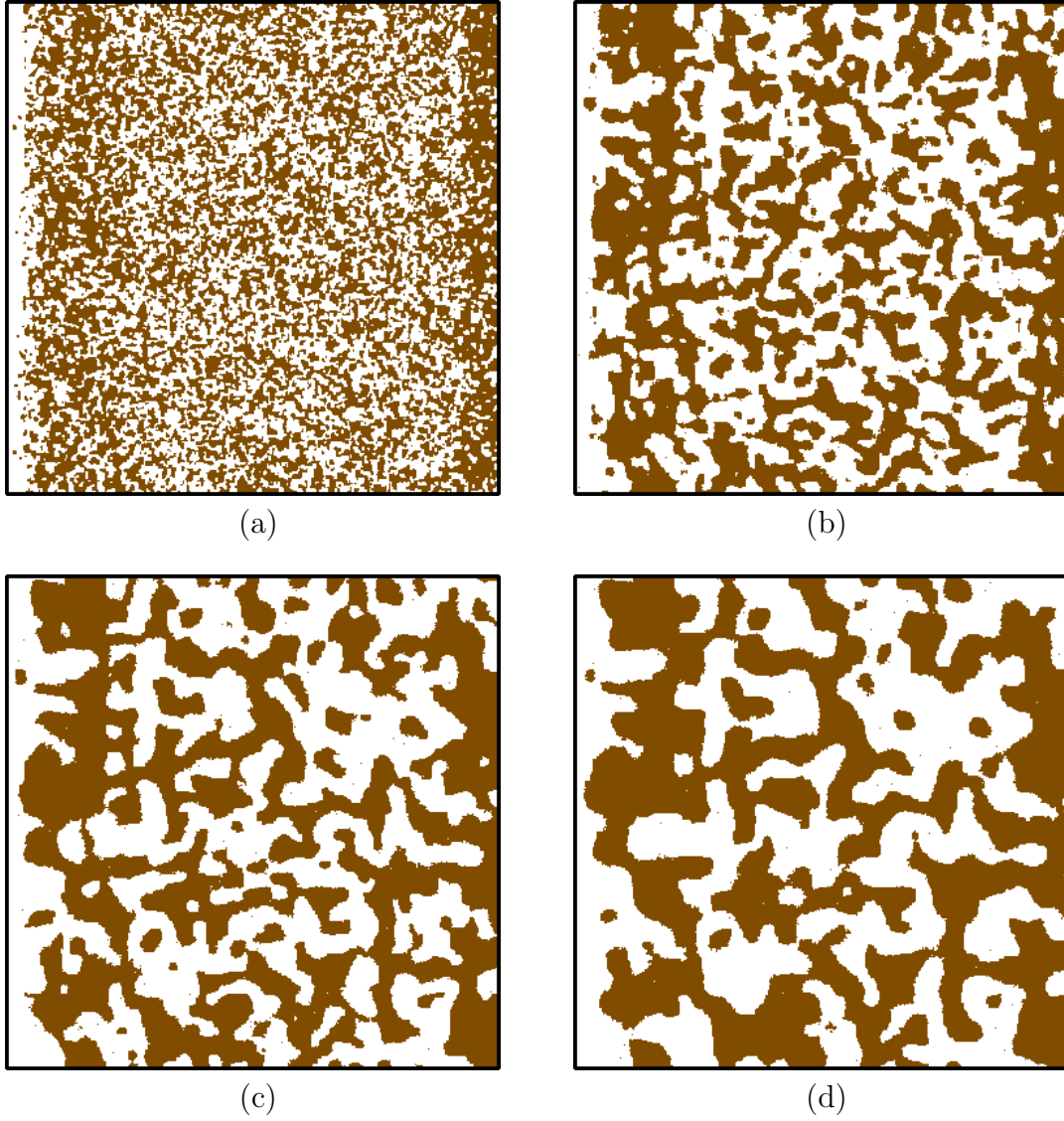
Figure 5.11 Model morphologies ($L = 400 \times 400 \times 400$) fit to the unannealed (as-cast) density profile in figure 5.10. Cross sections of the x-y plane are shown for 4 different feature sizes, $a = 4$ (5.11a), $a = 8$ (5.11b), $a = 12$ (5.11c), and $a = 16$ (5.11d). Brown represents PCBM sites and white represents P3HT sites.

(a)

(b)

(c)

(d)
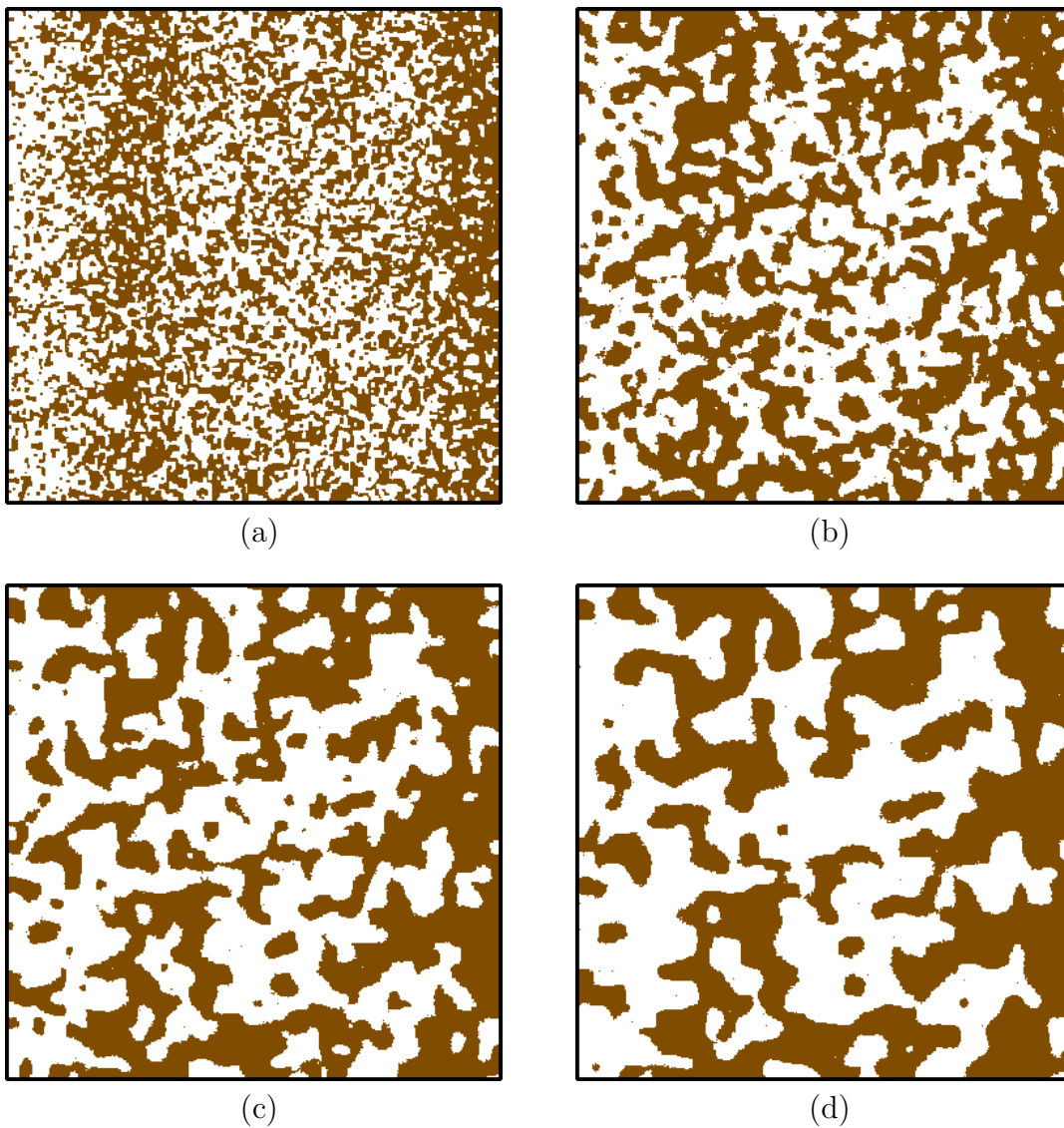
Figure 5.12   Model morphologies fit to the annealed density profile seen in figure 5.10. Cross sections of the x-y plane are shown for 4 different feature sizes(figure), $a = 4$ (5.12a), $a = 8$ (5.12b), $a = 12$ (5.12c), and $a = 16$ (5.12d). Brown represents PCBM sites and white represents P3HT sites.

(a)   (b)   (c)
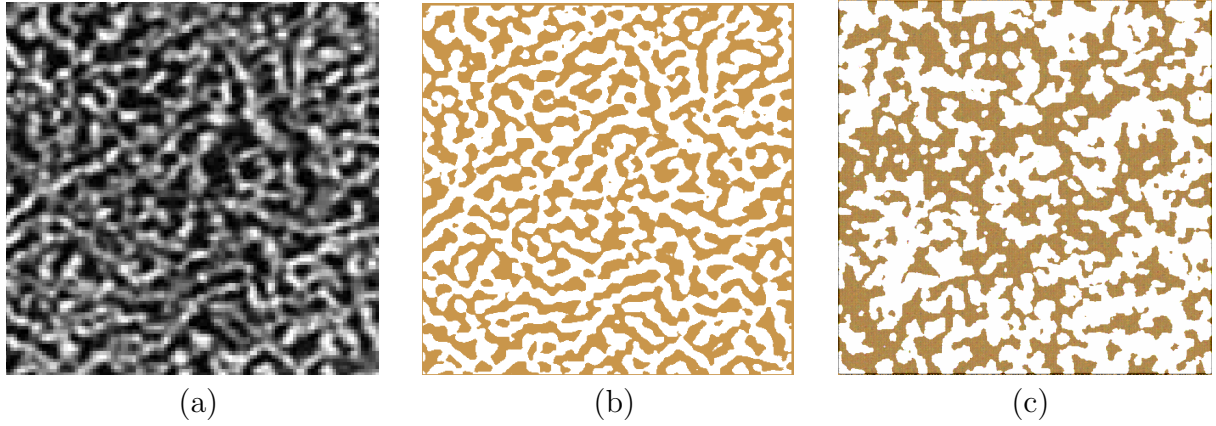
Figure 5.13   A comparison of electron tomography[5] performed on PPV:PCBM BHJ solar cells to simple morphologies generated using the constrained Ising model method. First, figure 5.13a demonstrates a zoomed in $400\,nm \times 400\,nm$ section of electron tomography taken of a BHJ morphology[5]. Next, in figure 5.13b, is an artificially colored two-phase view of this image. Finally, figure 5.13c is a sample side-cut of an example morphology generated with our model with comparable scale, containing feature size $a = 8.1$. The interpenetrating morphology of figures 5.8b and 5.8c are evident.

(a)   (b)

(c)   (d)
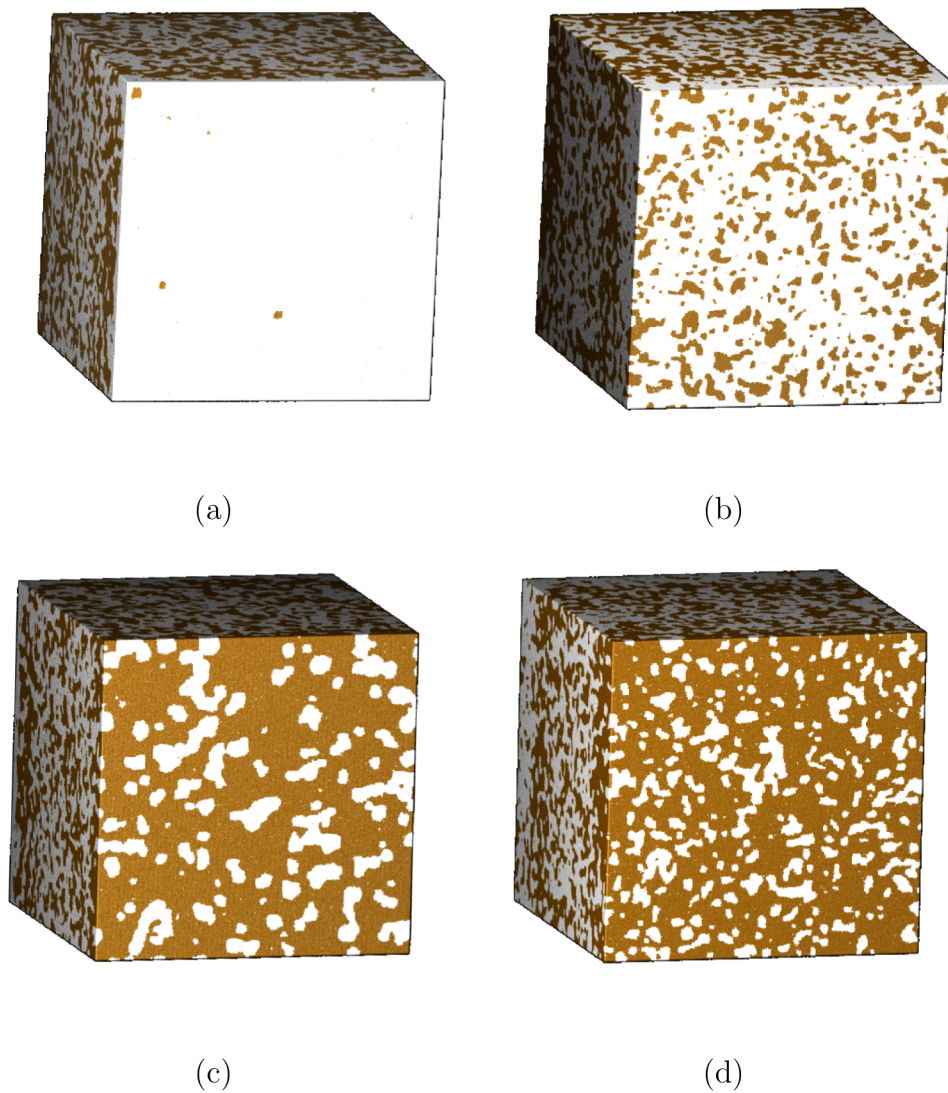
Figure 5.14   3-d views of the as-cast and annealed model morphologies, at feature size $a = 8$, presented such that the abrupt change in PCBM density seen near the contacts which dramatically alters the pathways to the contacts is visible. Brown represents PCBM sites and white represent P3HT sites. Note that as each of these cases has the same feature size, the morphological differences are consequences of the utilized density profiles.
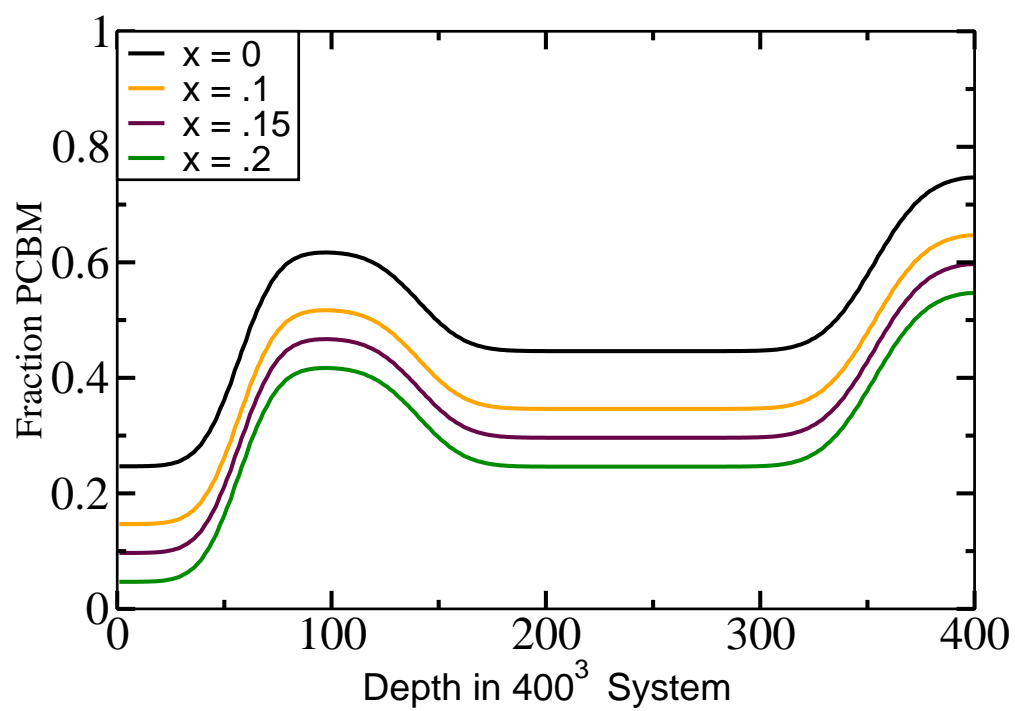
Figure 5.15   Assumed aggregate PCBM density profile from the three-phase model.
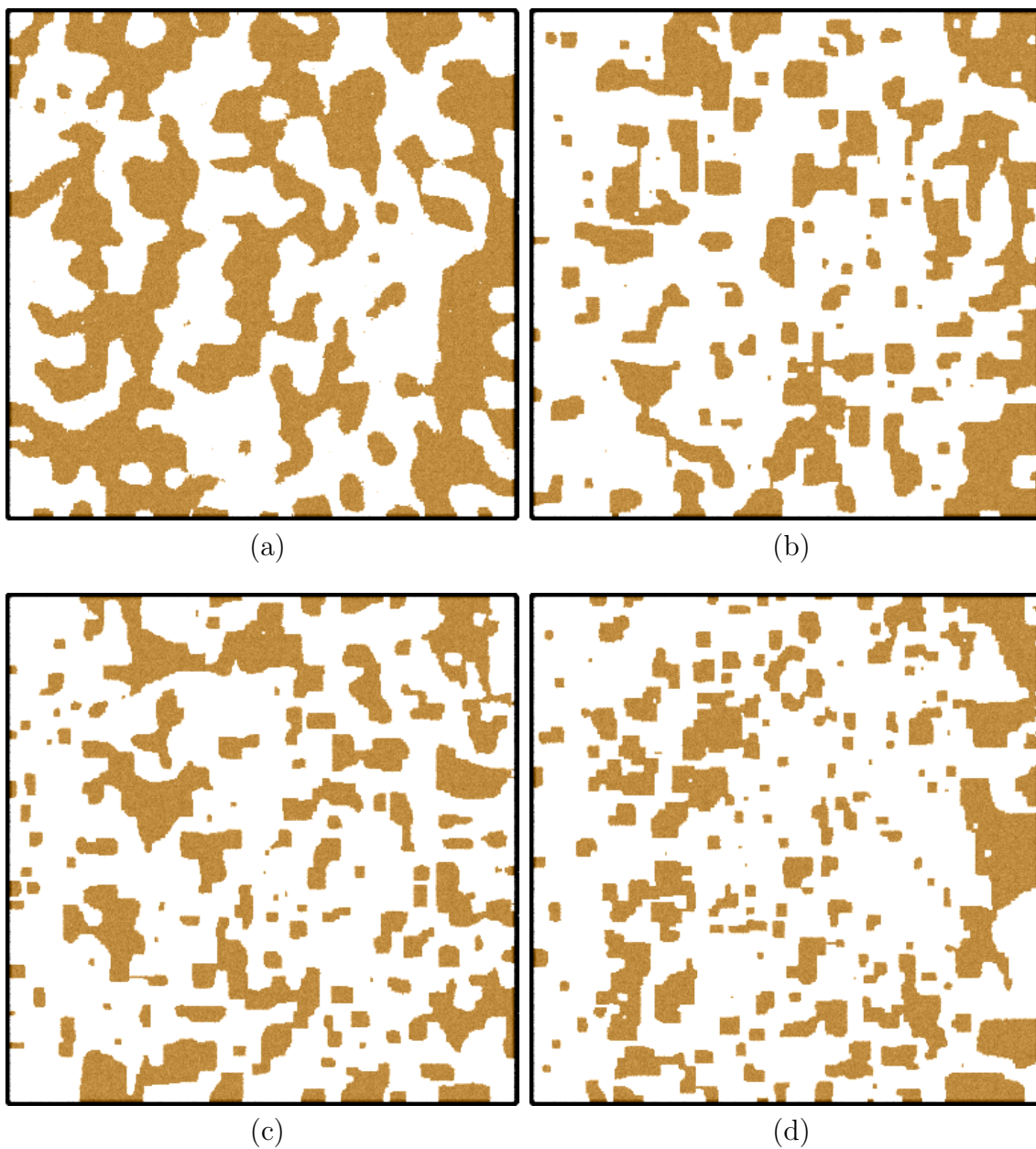
Figure 5.16 2-d cross-sections demonstrating the sequestered PCBM morphologies, with figures 5.16a, 5.16b, 5.16c, and 5.16d representing $x = 0, x = .1$, $x = .15$, and $x = .2$ reduced volume fractions respectively. Brown sites represent aggregate PCBM, white represents the mixed PCBM/P3HT phase.
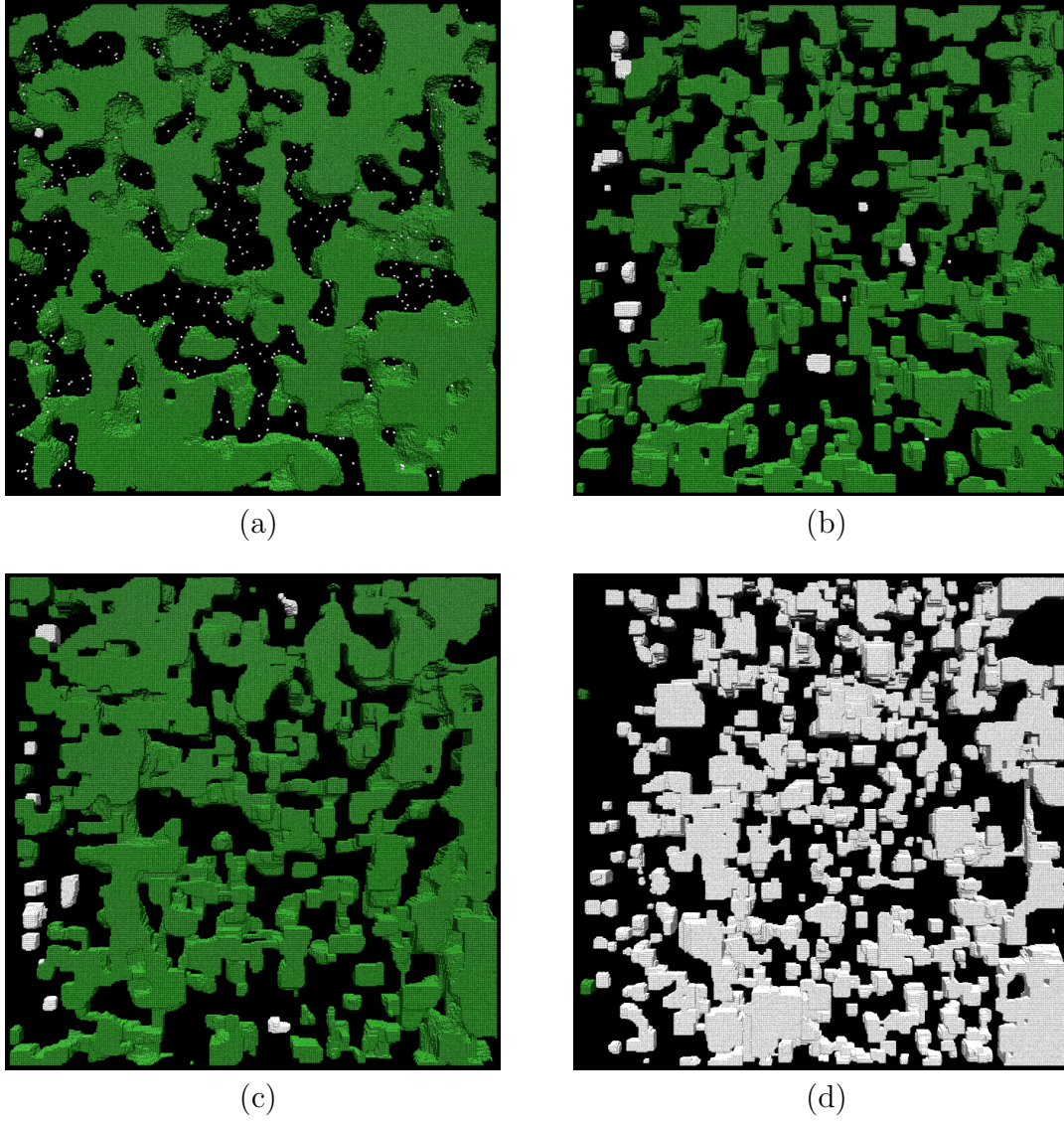
Figure 5.17 Superpositions of 15 cross-sections of the reduced aggregate PCBM morphologies, where only aggregate PCBM is displayed as green for sites connecting to the electron collecting electrode and white for sites which are disconnected. The four cross sections shown are for the $x = 0, x = .1, x = .15$, and $x = 2$. dispersed PCBM cases.

(a)   (b)
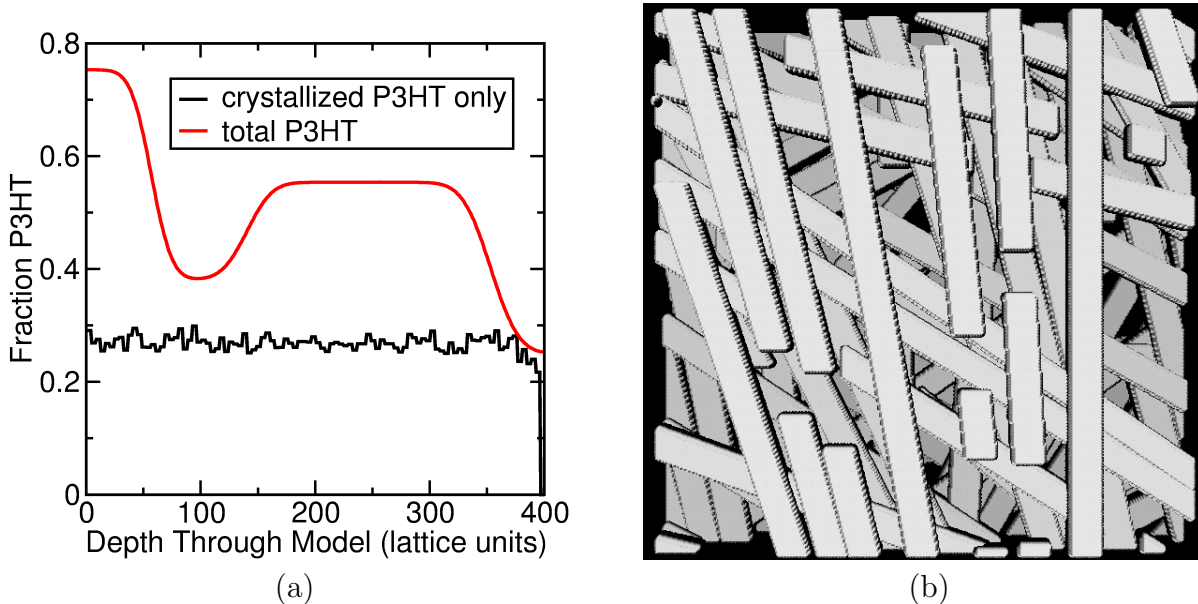
Figure 5.18   Figure 5.18a shows the P3HT density profiles used in model generation here, demonstrating both the crystallized fraction (c-P3HT) and the total fraction. Figure 5.18b shows a top down view of c-P3HT fiber network. Superposition of 20 total layers shown, with each fiber being 4 layers deep.

(a)   (b)
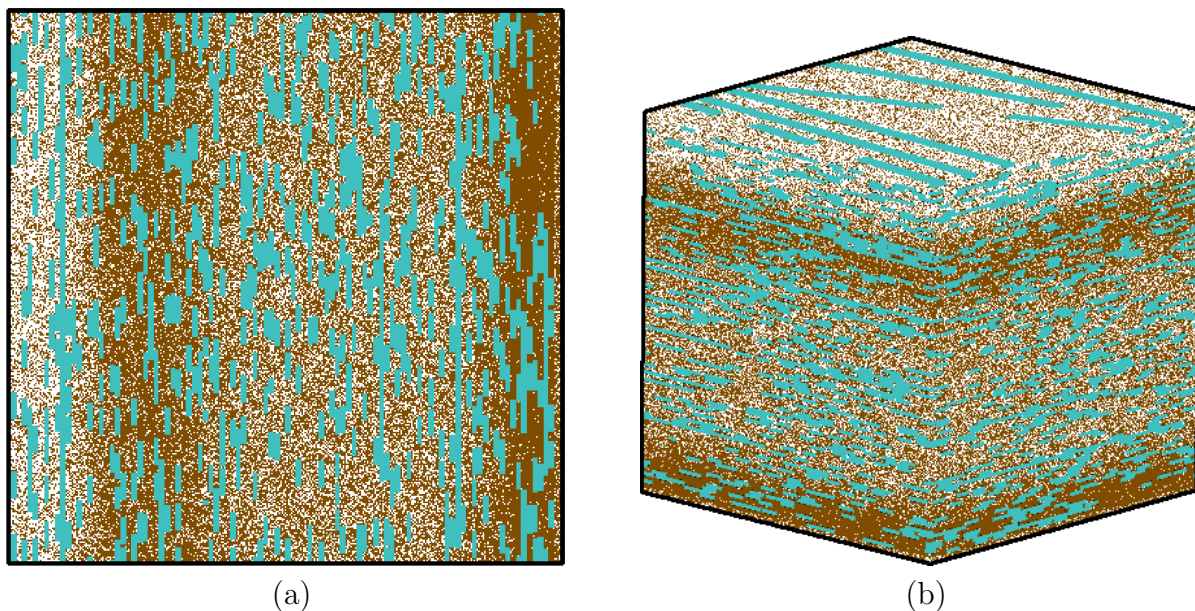
Figure 5.19   Views of the unannealed c-P3HT fiber-network based morphologies. Figure 5.19a shows a 2-d cross section of the initial configuration of a model morphology, which has had a c-P3HT fiber network inlaid but has not yet undergone annealing, such that the PCBM (brown) and amorphous P3HT (white) are still well mixed. Figure 5.19b is a 3-d view of the same morphology.

(a)

(b)
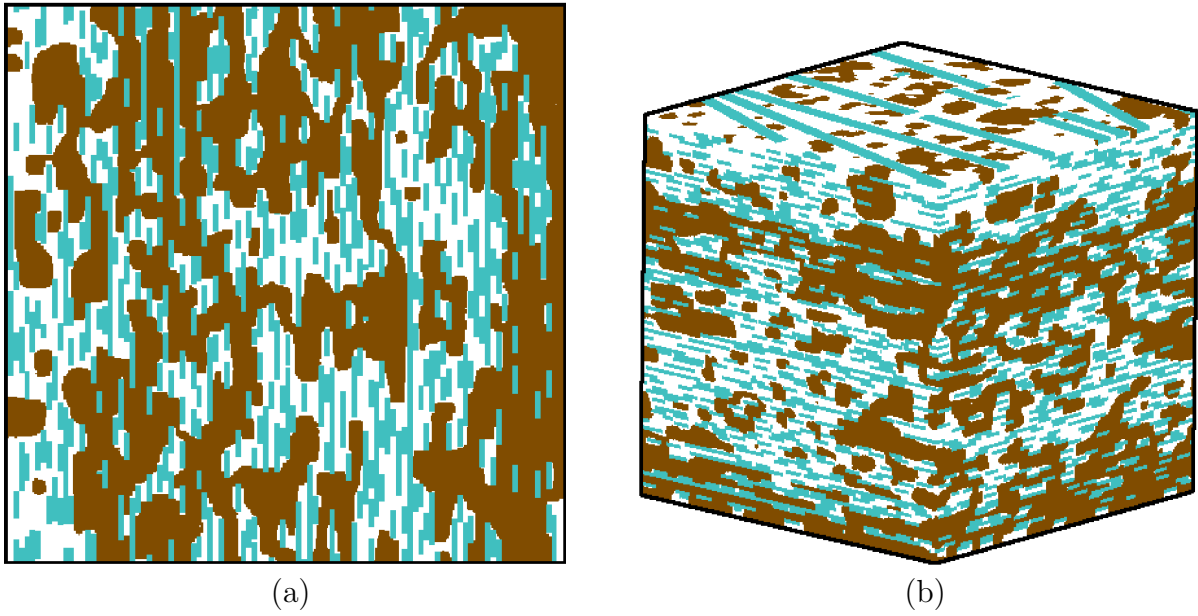
Figure 5.20   Views of the annealed (a=16) c-P3HT fiber-network based morphologies. Figure 5.20a shows a 2-d cross section of the final configuration of a model morphology, which has undergone annealing of the amorphous P3HT and PCBM (but left the c-P3HT network frozen) to characteristic feature size, a=16, such that the phases are now well segregated. Figure 5.20b is a 3-d view of the same morphology.

Chapter 6

Transport in nanostructures consistent with SANS data

As was highlighted in the end of chapter 5, reflectometry data on it's own provides no information about the nature of the internal structure in-plane, only informing on an averaged density profile in the xy-plane, at a given height through the morphology (z-dimension). Unfortunately, this information may yield models with dramatically different performance characteristics, as was demonstrated through the wide variety of models fitting the neutron reflectometry data in chapter 5. This wide variation in modeled morphologies comes from the simple fact that the system is underconstrained. Clearly, if we are to generate more realistic morphological models for use in transport calculations we must incorporate experimental data which is complementary to the neutron reflectivity provided density profiles. Fortunately, Jon Kiel also took small angle neutron scattering (SANS) measurements of these P3HT/PCBM BHJ systems[8], which informs on internal structural information we may use to further constrain our models.

SANS provides angle averaged information about the internal structure of a film in all dimensions, rather than composition as a function of depth as was the case with reflectivity measurements. Previous analysis of SANS measurements on P3HT/PCBM BHJ morphologies employed standard fitting procedures, which modeled the BHJ morphology as a system

of polydisperse spheres. Though these polydisperse sphere fits do provide information on the nature of the nanoparticle agglomeration and highlight average changes in agglomerate size due to system annealing, this type of analysis does not provide exact morphological models required for use in morphologically driven device simulations. Indeed, while the use of a polydisperse sphere model does fit the SANS data, it's use is in no way meant to imply that the morphology itself is composed of spherical agglomerates, as we know these BHJ contain 3-d percolative interpenetrating nanostructures.

We find that by incorporating small angle scattering data into our models, we are able to select an appropriate characteristic feature size, a, to use for the as cast and annealed cases. By simultaneously fitting to both the reflectivity data and the SANS data, new morphological insights are possible in these complex systems. In this chapter, we look at what effects the use of models consistent with both SANS and neutron reflectometry data has on DMC device performance calculations which rely on model morphology.

Unlike the reflectometry data, we do not directly incorporate the experimental SANS data into the Hamiltonian used to generate morphologies. Instead, we refine the model morphologies to fit the SANS data though the use of the simulated small angle scattering algorithm introduced in chapter 4. In this chapter, we will describe the reasons for this procedure, as well as describing the methods used to fit to the SANS data in detail. We will first demonstrate this procedure on the commonly used two-phase model, but then expand to the sequestered (dispersed) PCBM model and the crystallized P3HT fiber model, all introduced in chapter 5. In each case, after refining the models to the experimental SANS data, relevant DMC transport calculations will be performed to understand what effects different morphological models would have on overall device performance. The DMC model we employ in this chapter is slightly modified from the traditional form which was presented

Table 6.1   Parameters extracted from SANS based on polydisperse sphere model

Morphology	As Cast	Annealed
PCBM agg. radius (nm)	1.0 ± 0.75	5.9 ± 2.4
Total PCBM volume in film	52%	51%
Dist. between PCBM agg. (nm)	9.2	16.3

in chapter 3. We will explain the reasons for the modifications, and go through our modified DMC model in detail.

6.1   Nanostructures consistent with SANS and neutron reflectometry data

Jon Kiel performed small angle neutron scattering (SANS) measurements on P3HT/PCBM BHJ OPV systems on the NG-1 reactor at NIST[8], fitting the data to a set of polydisperse spheres with a Schulz distribution to study the effects of annealing on the BHJ morphology. The results of these fits are summarized in table 6.1, which suggest that annealing the film caused the PCBM agglomerates to increase in radius by a factor of 6, while at the same time the agglomerates were separating from one another.

Unlike neutron reflectometry data, SANS data is not directly invertible as there are potentially countless morphologies that would generate seemingly identical SANS profiles. Indeed, the original polydisperse sphere fits should not be interpreted as implying that the nanostructure itself is composed of agglomerate spheres, only to highlight how the dominant scattering structure (agglomerates of PCBM) increased in relative size. We generated a wide variety of candidate morphologies by varying the Hamiltonian, simulating SANS profiles for each. We tuned the parameters used in the Ising model until a morphology is generated whose simulated scattering profile fits both the neutron reflectometry data and experimental

SANS data to high precision.

For the SANS simulation, the site weights used (the values used for b in equation 4.38) are based on the corresponding scattering length densities (SLD) as the pure real materials, $SLD_{P3HT} = .74 \times 10^{-6} \text{Å}^{-2}$ and $SLD_{PCBM} = 3.7 \times 10^{-6} \text{Å}^{-2}$. A low-q upturn will be ever present in the calculated SANS profile due to the sample box size itself, which may not directly fit the experimental data. However, as we are looking to model the internal morphological characteristics of the BHJ thin films, and not model the entire film to scale, this is acceptable so long as the features of interest are distinguishable from the effects of sample box size. Previously described methods in section 4.4 of convoluting the scattered data or reducing the box size contributions are employed, with typical smearing values of 10%.
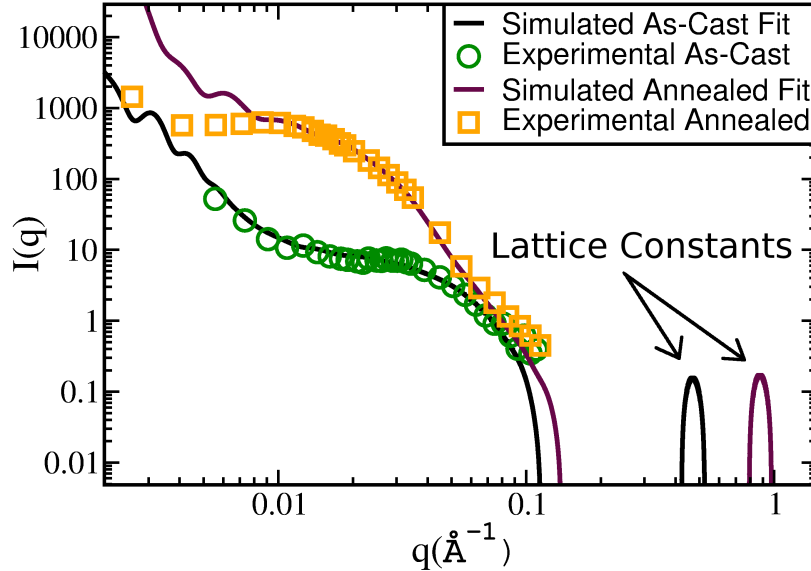
Figure 6.1 Demonstration of how a lattice constant, $b_{lattice}$, can be extracted from the Bragg-like nearest neighbor peak generated by the DFM method. Once final scaling is performed such that the calculated scattering profile is best it to experimental data, these lattice peaks (as highlighted here) will correspond to $2\pi/b_{lattice}$. Shown are the fits for the annealed and as cast two-phase morphology seen in figure 6.5.

Once model morphologies with SANS profiles comparable to those seen in experiment

are generated, a final fit to the experimental data is performed in which the scales of the simulated SANS plots are adjusted until the features of interest best match the data. As we are using a cubic lattice model, there will be a very strong Bragg-like peak due to the lattice spacing itself seen at the $q = 2\pi/b_{lattice}$ in the calculated scattering, where $b_{lattice}$ is the lattice constant, as is demonstrated in figure 6.1. This final scaling fit allows us to precisely extract the lattice constant for a specific model morphology, which is useful in transport calculations utilizing this morphology.

6.1.1 Two phase model

We first discuss the simple two-phase model, in which the nanoscale morphology is described as a lattice of sites, each assigned either pure P3HT (donor site) or pure PCBM (acceptor site).

The two key features of interest in the original SANS data are the amplitude and position of the plateau-terminating bend, shown in figure 6.2. For the as cast BHJ film, this plateau has an amplitude of approximately $8\,cm^{-1}$, with the bend cresting at $q \approx .05 \text{Å}^{-1}$. For the annealed BHJ film, the plateau has an amplitude of approximately $600\,cm^{-1}$ and the bend cresting at $q \approx .015 \text{Å}^{-1}$. This plateau shift to a higher intensity and bend at a lower q-value is indicative of an increase in characteristic feature size. As the generation of $w(r)$ from equation 4.38 involves the product of the SLD values of pairs, the contrast in the intensity contribution between those features with the strongest SLD values (b_S) and the weakest (b_w) will go as the difference of squares ($b_S^2 - b_w^2$). In the case of the P3HT/PCBM system under investigation in this thesis the contrast in intensity between PCBM features to P3HT features will be $3.7^2 - .74^2 \approx 13$, a significant signal difference. For this reason, characteristics seen in SANS profile will be predominantly caused by PCBM features of the

morphology.

Simple Guinier analysis of the intensity change of the plateau informs on the aggregation number[110], defined as the number of basic scattering units per scattering particle. In this case, the scattering unit is taken as an individual PCBM molecule and the scattering particle is the agglomeration of many PCBM molecules. If we assume the density of these particles remains constant before and after annealing, then the number of scattering particles is proportional to the volume of the scatterer ($N \propto r^3$ in the case of spheres). Noting that the relative intensity of the as cast and annealed SANS plateaus are 8 and $600\,cm^{-1}$ respectively, this allows for a quick estimation of average agglomerate growth due to annealing

$$\frac{r_{\text{annealed}}}{r_{\text{as cast}}} = \left(\frac{N_{\text{annealed}}}{N_{\text{as cast}}}\right)^{1/3} \approx \left(\frac{600}{8}\right)^{1/3} \approx 4.2. \tag{6.1}$$

This back-of-the-envelope calculation is consistent with the results of the polydisperse sphere fits, which showed an aggregate radius increase of 5.9 ± 5.0 (taking fractional error propagation into effect). Though these error bars seem large, recall that a Schulz distribution has a particularly long tail which and can be described as

$$P(r) = \frac{\exp\left[-\frac{r \cdot R}{\sigma^2}\right] \left(\frac{r}{R}\right)^{\frac{R^2}{\sigma^2}} \left(\frac{R^2}{\sigma^2}\right)^{\frac{R^2}{\sigma^2}}}{r \cdot \Gamma(\frac{R^2}{\sigma^2})}, \tag{6.2}$$

where $P(r)$ is the probability of a sphere with radius r, the average sphere size is defined by R, the width of the distribution is defined σ, and Γ is the gamma function. An example of a polydisperse Schulz distribution is given in figure 6.3, which demonstrates the distributions found by Jon Kiel in his fitting of the annealed and as cast morphologies. A polydisperse Schulz sphere function is often used to fit SANS data of polymer systems[121] not because

the system is thought to be composed of spheres, but because this wide distribution of length scales is thought to be similar to the length scales present in the actual systems.

For our modeling here, we use the two phase morphologies as described in section 5.3 of this thesis. Figures 5.11 and 5.12 show examples of the as cast and annealed morphologies we tune using our simulated SANS algorithm. Sites are assigned scattering weights based on the pure material SLD values (found by Jon Kiel in his previous fitting methods[8]) of $b_{donor} = .74$ and $b_{acceptor} = 3.7$. We roughen the edges of the sample box by randomly removing sites via the algorithm described in section 4.4.2.1 of this thesis, with a Gaussian width of 120 lattice sites from the center of the box (thus covering 60% the box edge width), as this length was found to remove a majority of high frequency sample-size oscillations without effecting the larger scale internal features of interest.

We find best fit models to the experimental SANS data to have features sizes of $\approx 4b$ for the as cast cast and $\approx 16b$ for the annealed case, where b is the model lattice constant. Final scaling to the experimental data extracts lattice constants of $b = .667$ nm for the as cast model and $b = 1.25$ nm for the annealed model. Taking the lattice constants into effect, these results imply the annealed morphology has increased in average aggregate radius by a factor of approximately 7.5 over the as cast morphology, which is consistent with the standard polydisperse Schulz spheres fit, which had an average feature size growth of 5.9±5.0. Comparison of the experimental and modeled SANS data is presented in figure 6.5.

Having selected the characteristic feature sizes to be used in these percolative, inter-penetrating BHJ structure models ($a_{\text{as cast}} = 4$ and $a_{\text{annealed}} = 16$), we now generate a complimentary set of morphologies with identical feature sizes but incorporating a flat target density profile rather than one provided by the neutron reflectivity data. In this way, we may explore the effects of the density profile on model predictions independent of feature

size. These so called "Ising Only" morphologies are shown in figure 6.7c and 6.7d.

6.1.2 Modified DMC Method

As we are interested in characterizing how nanoscale morphology effects device performance, independent of the particular parameter set used in the simulation, we alter our dynamic Monte Carlo calculations from the previously employed method presented in section 3.4 of this thesis. Rather than specifying a specific set of model parameters for use in each calculation, such as applied voltage, electron mobility, hole mobility, work function, etc, we instead attempt a more general characterization by sweeping over a broad range of recombination lengths for all carriers, which we define as:

$$L = b \left(\frac{\nu_{hop}}{\nu_{loss}} \right)^{1/2} \tag{6.3}$$

where L is the relevant recombination length, b is the lattice constant, ν_{hop} is the associated particles hop rate, and ν_{loss} is the associated particles recombination or decay rate.

6.1.2.1 Exciton behavior in the 2-phase model

We will first look at how morphology effects exciton dissociation efficiency when comparing the as cast and annealed morphologies. The results of the DMC calculation are summarized in figure 6.8. Exciton dissociation, χ_{diss}, is defined as the ratio of excitons successfully dissociating at a heterojunction over the total number of excitons generated. The exciton decay length is defined $L_x = b \left(\frac{\nu_{\text{x-hop}}}{\nu_{\text{x-decay}}} \right)^{1/2}$. Excitons are generated with equal probability at all P3HT sites, and then diffuse with hop/decay rate combinations which provide the specific decay lengths given on the axis of figure 6.8. The data presented is taken at

100 different decay length values, with each point being averaged over one million exciton lifetimes. Exciton dissociation at a heterojunction is treated as exceptionally fast compared to all potential DMC actions, such that excitons will almost always dissociate upon reaching a site which is a heterojunction (adjacent to an acceptor site).

As the results in figure 6.8 show, the as cast morphology with it's much finer characteristic feature size ($a \approx 4$), is much more efficient at dissociating excitons at any given exciton decay length compared to the annealed morphology ($a \approx 16$). This is a predictable outcome, as the excitons are generated in the donor material (P3HT) and must diffuse to a heterojunction interface in order to dissociate. Any morphology which offers shorter average paths to a heterojunction will naturally outperform systems with longer paths, and thus smaller feature sizes are always preferable from the standpoint of exciton dissociation efficiency. In the case of the as cast morphology, it is observable that once the decay length is of order equal to the feature size, essentially all excitons generated will successfully dissociate. While this effect is not as clear in the annealed model data, this is only due to the bounds of L_x used in the simulation and the trend is still seen.

Now, we look at the differences between the so called "realistic" morphologies, being those generated with the reflectivity informed density profile, and the "Ising only" morphologies. This comparison data is also shown in figure 6.8. We note that in both cases, the Ising only morphologies exhibit better exciton dissociation than their realistic counterparts, other than a small deviation from this trend for the $a \approx 4$ morphologies for $L_{\text{x-diss}} < 1$. To understand this low $L_{\text{x-diss}}$ discrepancy, one can look at the average characteristic feature size of each individual layer in the morphologies, shown in figure 6.9. While the Ising only models are generally consistent at maintaining constant feature size at every depth in the morphology, the realistic morphologies contain significant feature size fluctuations,

particularly in regions where the target density profile was far from 50% such as near the edges. These regions of anisotropic feature size must exist in order to fit any non-uniform density profile, as some regions will have greater average P3HT agglomerates (and thus, sites to form a heterojunction) to the rest of the model, and others less. As excitons are generated in P3HT, those regions containing lower PCBM volume fractions present, on average, a longer path excitons must travel in order to discover a heterojunction interface. Additionally, as excitons are generated uniformly through the bulk of the donor material (P3HT), those regions with more total donor material will have a greater number of exciton generation events, and thus the behavior of excitons in these regions will be slightly more significant in the DMC averaged results. This subtle difference, entirely due to PCBM density profile fluctuations, is what leads to a slight diminishing of exciton dissociation efficiency for the "realistic" morphologies. For a fixed characteristic feature size, density fluctuations are detrimental to exciton dissociation efficiency in these morphological device calculations.

At very low recombination lengths ($L_{\text{x-diss}} \ll 1$) essentially no excitons will be able to hop from the site they originate at prior to decay. Those excitons that do dissociate must be generated on sites of P3HT which are already adjacent to PCBM (at the heterojunction), where due to the selected high exciton dissociation rate, successful dissociation may occur. The crossover behavior we see in the $a \approx 4$ cases at $L_x \approx .3$ nm has been traced to the small difference in BHJ surface area between the two models, as careful inspection of each morphologies reveals that the as cast has an exact feature size of $a_{\text{as-cast}} = 4.007997$, where as the Ising only has an exact feature size of $a_{\text{Ising}} = 4.023306$. As feature size is inversely proportional to surface area, this shows that the as cast morphology has more total P3HT sites sitting directly next to PCBM sites, which coupled with the understanding of how density fluctuations are detrimental to overall exciton dissociation efficiency, explains

the crossover behavior seen in the data. For comparison, the morphology used in the annealed morphology, compared to the Ising only a=16 morphology, had exact feature sizes of $a_{\text{annealed}} = 16.014643$ and $a_{\text{Ising}} = 16.000523$ respectively, which fits with our understanding as there is no such crossover for the $a \approx 16$ morphologies.

6.1.2.2 Charge behavior in the 2-phase model

We now compare the morphologies from figure 6.7 in terms of their ability to collect free charges as they diffuse throughout the morphology. The results of the simulations are presented in figure 6.10, where charge collection efficiency, χ_q, is defined as the ratio of free charges collected at their respective contacts over total charges generated due to exciton dissociation. The charge recombination length, $L_q = b \left(\dfrac{\nu_{\text{c-hop}}}{\nu_{\text{c-recomb}}} \right)^{1/2}$, is defined as the lattice constant (b) times the ratio of the free charge hop rate to the free charge recombination rate.

The results in figure 6.10 show that for all morphologies under consideration, free charge is collected with roughly the same efficiency, with a notable exception of electron collection efficiency in the as cast morphology, which was significantly reduced compared to all other morphologies. This poor charge collection efficiency is due to the abrupt drop in PCBM density which occurs at the electron collecting electrode visible on the left-hand side of the as-cast density profile in figure 6.6. This leads to a situation where a bulk of the PCBM sites in the morphology have no percolative paths which would allow free electrons to reach the electron collecting electrode, regardless of the recombination length used. This is clearly seen by comparing the PCBM sites (brown) which reach the contact layer in the top-down views of the as cast (figure 5.14a) and annealed (figure 5.14b) morphologies.

We see a subtle ($\approx 15\%$) drop in the maximum possible charge collection efficiency of

electrons in the annealed morphology compared to the Ising only morphologies, and again find this effect is due to electrons which are generated on regions of acceptor (PCBM) material which had no percolating paths to the electron accepting electrode.

If one compares electron collection to the hole collection efficiency (in figure 6.10) for the as cast and annealed cases, hole collection efficiency is nearly the same in both cases, and very similar to the electron collection efficiency for the annealed case. While this implies that differences in morphology between the as cast and annealed morphologies did effect hole collection efficiency, the majority of the P3HT sites here are connected to the hole collecting contact and thus no significant disconnect in the hole current occurs. For the Ising only data we found the electron and hole collection efficiencies to be essentially identical, such that we present it here as a single solid line. This is understandable, as the Ising only morphologies are isotropic at all layers, due to their flat target density profile, and thus there is no morphological differences between the behavior of electrons and holes. Looking at the Ising only data from $L_q = 10$ to 400, we see that charge transport is more efficient in the larger features size, $a = 16$, compared to the finer grained $a = 4$ morphology. This observation is consistent with the conventional understanding that larger aggregates of material allow for easier diffusion of the charges, or to put it another way, morphologies with smaller feature size offer more tortuous paths which diffusing charges must transverse. At recombination lengths $L_q > 400$ the charge collection efficiency of the two different feature size models merge together, as this is outside the regime in which the tortuous path for the diffusing particles is the limiting factor. The only upper limits on charge collection efficiency when L_q gets sufficiently large are therefore the limits based on charges being generated on sites which do not connect to the associated charge's electrode, or so called "islands".

Overall, we see that charge collection efficiency is enhanced by greater characteristic

feature sizes, but that subtle effects introduced by using an experimentally measured density profile are significant enough to alter the results of a calculation, regardless of the set of device model parameters used.

6.1.3   Sequestered PCBM model

We now look at the effects of the so called three-phase or sequestered PCBM model on DMC device calculations. Recall that, similar to the "Rivers and Streams" model[4], the sequestered PCBM picture models the system as sites assigned to be either a pure phase of aggregate PCBM or a mixed phase of P3HT and dispersed PCBM. In order to directly compare to the previously employed annealed two-phase model, we generate models with feature size $a \approx 16$. Using the model morphologies generated in section 5.3.1, simulated SANS profiles were generated using the distribution function method (DFM) with associated scattering strength weights proportional to the SLD value of pure PCBM for the aggregate PCBM phase ($b_{PCBM} = 3.7$) and a weighted mixture of pure PCBM and pure P3HT ($b_{P3HT} = .74$) for the mixed phase, the results of which are shown in table 6.2.

Table 6.2   SLD values for the four different fractions of dispersed PCBM morphologies seen in figure 5.17, used in simulated scattering in figure 5.17.

x	$b_{\text{d-PCBM/P3HT}}$	$b_{\text{agg-PCBM}}$
0	0.74	3.7
.1	1.04	3.7
.15	1.18	3.7
.2	1.33	3.7

Simulated SANS calculations were performed on the morphologies shown in figures 5.16 and 5.17, with identical Gaussian fuzzying and smearing routines as those used in the previous two-phase model. The results of the SANS simulation is shown in figure 6.11.

As each of the three-phase models shown here have been generated to feature size $a = 16$,

it is not surprising that the simulated SANS profiles are quite similar. The primary difference in the simulated scattering profiles is that as the fraction of dispersed PCBM (x) increases, the scattering intensity decreases slightly. This can be attributed both to the decrease in PCBM present and the decreasing contrast between the two materials (PCMB and mixed phase) as x increases. However, all volume fractions presented generate SANS profiles which are quite comparable to one another based on fits to the experimental SANS data, and thus no strong conclusion can yet be drawn on which model is more accurate.

We now compare these four sequestered PCBM model morphologies through the use of our modified DMC transport calculation, as we did previously with the two-phase model.

6.1.3.1 Exciton behavior in the sequestered PCBM model

The results of the DMC exciton transport calculations are shown in figure 6.12, with results presented as a function of a exciton decay length, $L_x = b \left(\frac{\nu_{x-hop}}{\nu_{x-decay}} \right)^{1/2}$. These graphs were generated using 66 different values of L_x, with each point being the average of one million exciton lifetimes.

We note that the most efficient exciton dissociation occurs in the original $x = 0$ case (no PCBM sequestered), and that progressively less excitons successfully dissociate as the fraction of dispersed PCBM is increased. As excitons are being generated uniformly though the bulk of the mixed phase (as photons are absorbed only in P3HT) an exciton will have, on average, a further distance it must travel to discover a heterojunction as x is increased because the average distance to an aggregate of PCBM increases. Note that while we already demonstrated that increasing feature size decreases exciton dissociation efficiency, this is not the same effect here as feature size between all four morphologies studied here is held at $a \approx 16$. Instead, this is an effect of the decreasing average surface area each donor site

(mixed phase) will have, as the total number of donor sites is increasing with x, but feature size (and thus surface area) is held constant.

6.1.3.2 Electron collection in the sequestered PCBM model

Next we look at the results of DMC based electron collection efficiency calculations in figure 6.13. The most striking feature of the data is the $x = .2$ result, which shows electron collection efficiency of essentially zero. This result comes from the apparent transition of the system to a non-percolative network (in regards to reaching the electron collecting contact) which occurs in the $x = .2$ morphology. It is clear that in these morphological models, some critical threshold exists between $x = .15$ and $x = .2$, wherein the PCBM network becomes too disconnected in order to function successfully as an OPV device. This result is consistent with our qualitative analysis of the morphology, which showed an overwhelming volume of disconnected PCBM sites as is demonstrated in figure 5.17 (in white). While all other morphologies with $x < .2$ show relatively similar electron collection efficiency, it is worth noting that the $x = .1$ case exhibits slightly improved electron collection. We have investigated this, and found it to be an effect of well defined "rivers" of aggregate PCBM which extend from the electron collecting contact into the bulk of the morphology. Though one would intuitively consider more aggregate PCBM to produce a more favorable electron transport profile, we found that due to the morphologies specific exciton dissociation dynamics, excitons were more likely to dissociate onto sites which had a further average path length to the electron collecting contact in the $x = 0$ case as compared to those excitons which dissociated successfully in the $x = .1$ case. This result is directly related to the anisotropic density profile introduced by the neutron reflectometry data, and would not have come about without it's inclusion. Note that hole collection efficiency is not discussed here, as the

principle effects of sequestering PCBM in this model will be on electron transport.

6.1.4   Crystallized P3HT fiber model

Finally, we look at morphologies generated with a crystallized P3HT (c-P3HT) template, as were shown in figure 5.20. To directly compare to previous models, the morphologies studied here have been Ising annealed to characteristic feature size, $a = 16$. Simulated SANS profiles were calculated for the c-P3HT model using site scattering weights of $b_{P3HT} = .74$ and $b_{PCBM} = 3.7$, just as with the two-phase model. Sites assigned as c-P3HT or amorphous P3HT are weighted the same in the simulated SANS, as the neutron SLD of the two materials is identical. Once again, we utilize a fuzzying procedure with the same parameters as the two-phase model, and apply a smearing function of 10% to the resultant profiles, shown in figure 6.14.

Comparing the simulated SANS profile of the c-P3HT model to the simple two-phase model, we see the two are very similar. The fiber template method introduced a structural anisotropy to the system, yet as the model morphology was annealed to characteristic feature size $a = 16$, it's angle averaged scattering profile (which is sampled by our method) is nearly indistinguishable from those structures generated without the fiber template.

DMC device performance calculations were performed on the c-P3HT model, looking at both exciton, electron, and hole dynamics, similar to the method used to characterize the simple two-phase morphologies. Transport through crystallized polymers is known to exhibit significantly higher in-plane mobility, while their through-plane mobility is thought to be significantly lower[140]. In order to examine the effect of enhanced hole mobility due to c-P3HT regions, we also perform so-called "fast" hole transport calculations, where mobility inside c-P3HT is enhanced in the planer (xy) direction.

6.1.4.1 Exciton behavior in the c-P3HT fiber model

DMC device calculations were performed on the c-P3HT model morphology and compared to those results found for the two-phase model, the results of which are presented in figure 6.15, 66 values of L_x were modeled, with each data point being the averaged behavior of one million exciton lifetimes. Recall that the feature size for the as cast model was $a = 4$, compared to the features size of $a = 16$ for the annealed model, which is also the feature size we use in the c-P3HT model. As was explained in discussions on exciton transport dynamics in the two-phase system, this feature size difference explains why the as cast case exhibits significantly better exciton dissociation than either of the $a = 16$ morphologies. Comparing both $a = 16$ morphologies, however, we see the c-P3HT model had consistently better exciton dissociation efficiencies than the two-phase annealed morphology. This can be attributed to the introduction of a fiber network in the c-P3HT morphology, which lead to a significant anisotropy not present in the two-phase model. In the c-P3HT morphology, a greater fraction of the total surface area (acceptor/donor bordering sites) is stretched across the xy-plane, rather than evenly distributed in all three dimensions.

Excitons in the c-P3HT model can thus, on average, diffusively discover heterojunctions more quickly because of the smaller average feature size in the z-dimension. This interesting result demonstrates that characteristic feature size alone is not sufficient to predict transport dynamics, as any inherent anisotropic factors must also be considered in any morphologically dependent calculation.

6.1.4.2 Charge behavior in the c-P3HT fiber model

We now perform charge transport calculations on the c-P3HT model. In addition to the standard calculations of charge collection efficiency (χ_q) versus charge recombination length

(L_q), we also perform a so called "fast" transport calculation, where we examine the effect of enhanced hole transport through crystallized P3HT regions. For these fast-transport calculations, we treat the hole hopping rate on sites assigned c-P3HT as $100\times$ faster than the given L_q. As this enhanced mobility is considered only in-plane[140], hop rates through the plane (in the z-direction) are not enhanced. The results from these calculations as well as the two-phase model for comparison are shown in figure 6.16.

The c-P3HT model displays very similar results for electron and hole transport, with both charges' collection efficiency being comparable to the annealed two-phase morphology. When examined closely, we see the measured difference between the electron and hole collection efficiencies is in fact even smaller than the two-phase model, which is likely due to the c-P3HT templating, which induced the generation of a more connected network for not only the P3HT (donor) sites, but also the PCBM (acceptor).

The hole collection efficiency in the "fast" c-P3HT model was significantly enhanced, which is somewhat surprising considering that hole transport dynamics through the plane (z-direction) were in no way explicitly enhanced, yet it is the transport through the plane which must occur efficiently in order for holes to quickly reach and be collected at the contact. This result can be understood because holes in the "fast" system may now very quickly explore the xy-plane such that "dead-end" regions of the morphology, which previously would have presented a significant hazard to transport, are now easily explored. This allows the holes to more efficiently explore the morphology and quickly discover those percolative paths to the contacts which, based on our studies of the sequestered PCBM morphologies, we know can enhance charge collection efficiencies.

These final results are of particular interest, as they demonstrates that both exciton and charge transport would be enhanced by a crystal fiber network from a purely morphological

standpoint, and even more so when considering the increased mobility granted by crystallized materials.

6.2 Conclusions

In this chapter, we have demonstrated how the inclusion of experimentally measured data can alter the results of device performance calculations in morphologically dependent systems, such as the BHJ OPV systems. In our work, we utilized small angle neutron scattering data (SANS) from PCBM/P3HT systems to refine and more precisely select a realistic model morphology which would otherwise be underconstrained. Although we utilized two forms of complementary neutron scattering data, the techniques presented could readily be adapted to a variety of other experimental data such as AFM, SEM, STM, x-ray scattering, etc. We have shown how the inclusion of experimentally measured data can have a significant effect on device calculations when compared to predictions made with simple assumed morphologies.

The DMC method we applied here makes no assumptions about specific device parameters, instead sweeping over a wide range of potential material properties to give an overall picture of the morphological effects on the system. Indeed, our results show that logical modifications to the simple Ising model, such as the inclusion of sequestered PCBM or a network of crystallized P3HT fibers, can have significant effects on device performance calculations entirely independent of the parameter set used.

While we are unable to make claims on the accuracy of one particular model over another, as every morphology used herein has been simultaneously consistent with both neutron reflectometry and SANS data, we suggest that the methods used here (inclusion of experimental data into a modified Ising model) are an ideal framework to explore the effects of

many other forms of data and theoretical model systems.
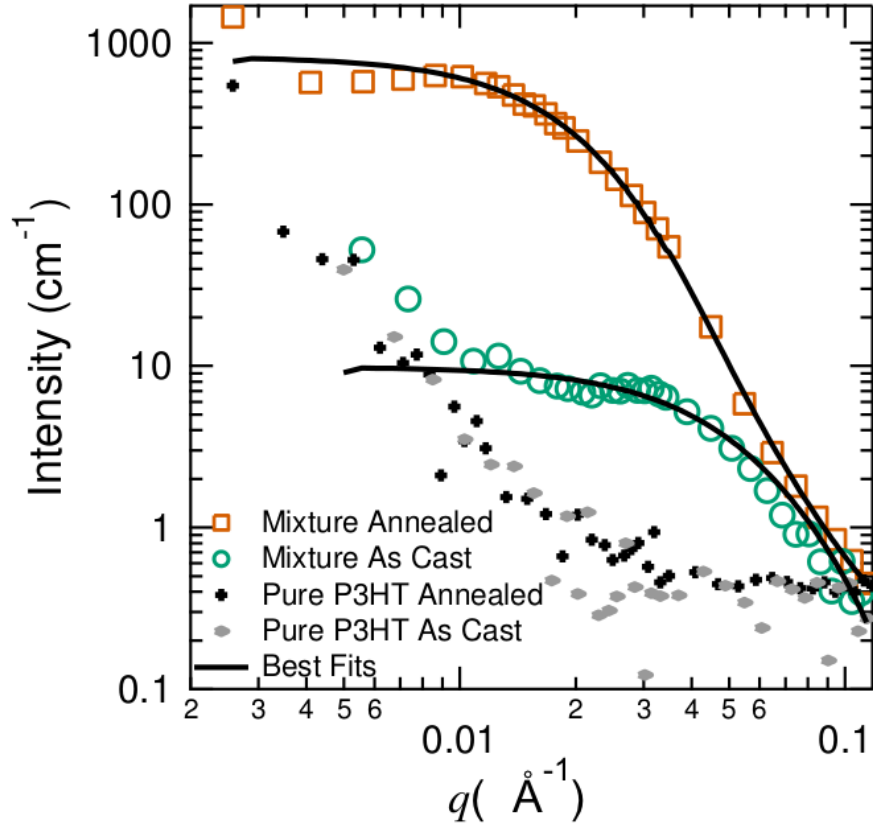
(a)
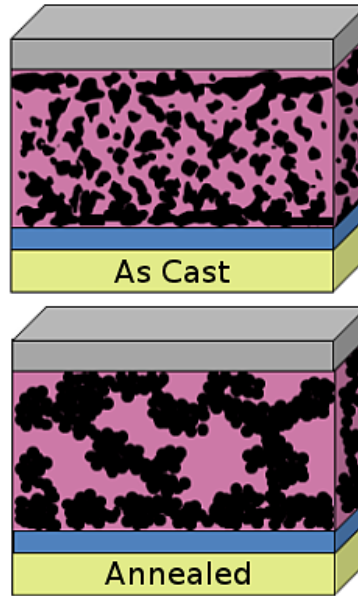
(b)

Figure 6.2   Small angle neutron scattering (SANS) data of the P3HT/PCBM BHJ thin film mimics, from the thesis of Jon Kiel[9]. Figure 6.2a shows the original SANS data for the as cast and annealed systems, as well as the polydisperse sphere fits. Figure 6.2b is a cartoon by Jon Kiel, suggesting how the agglomerate PCBM size increases might be interpreted.

151
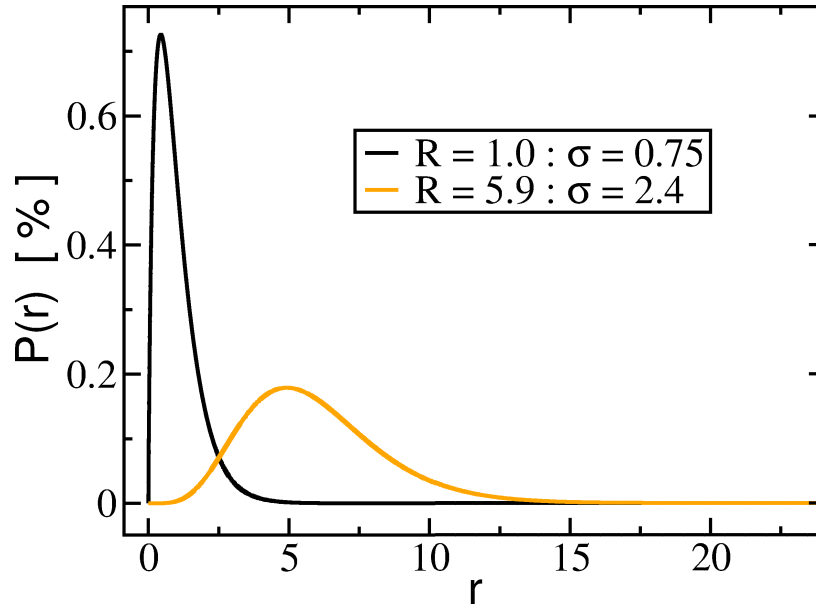
Figure 6.3 Demonstration of Schulz Distributions of the polydisperse fits for the as cast experimental SANS data($R = 1.0, \sigma = .75$) and the annealed experimental SANS data ($R = 5.9, \sigma = 2.4$).
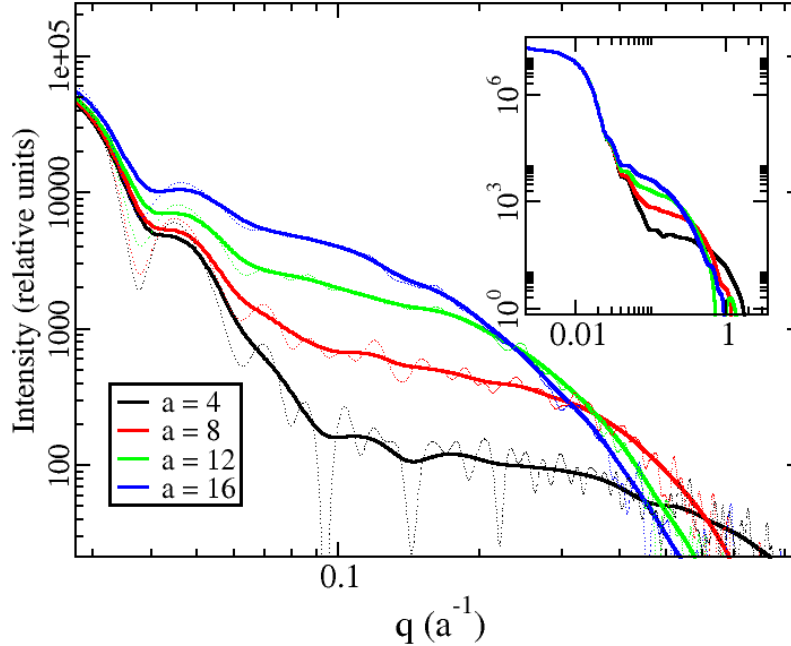
Figure 6.4 Demonstration of how the plateau shifts to greater intensity and the bend shifts to lower q as the constrained Ising model anneals a BHJ morphology to greater values of a. Dashed lines are the unsmeared data and solid lines have been smeared 10%. The inset presents the same data (smeared only), zoomed out so as to better observe the plateau.
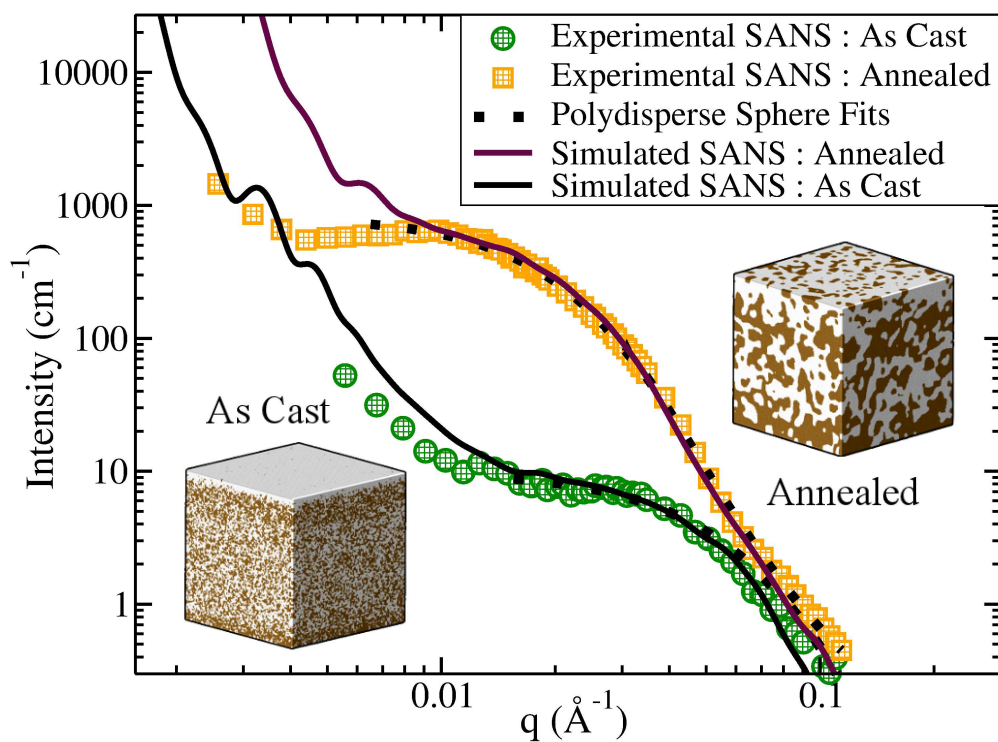
Figure 6.5 Simulated SANS profiles for the as cast and annealed morphologies, showing fits to the experimental SANS data, as well as previous fits performed with a polydisperse sphere model. Inset in the figure are 3-d views of the as cast and annealed morphologies.
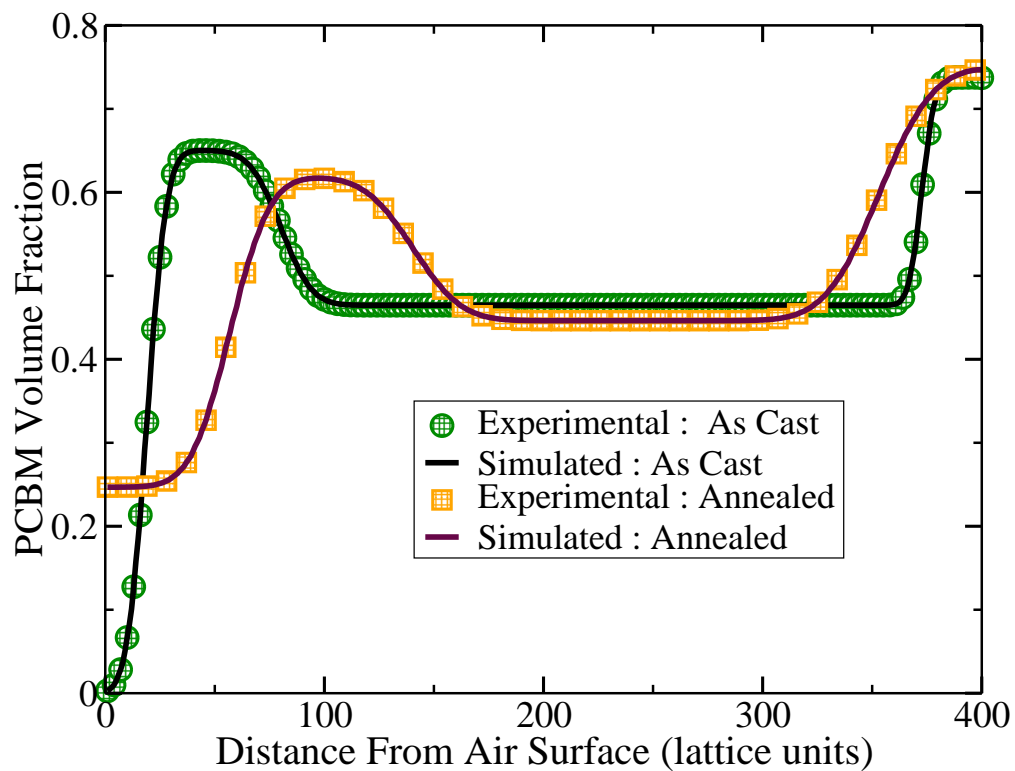
Figure 6.6   Density profiles of the as cast and annealed morphologies, with the simulated morphologies compared to the experimental reflectometry fits.
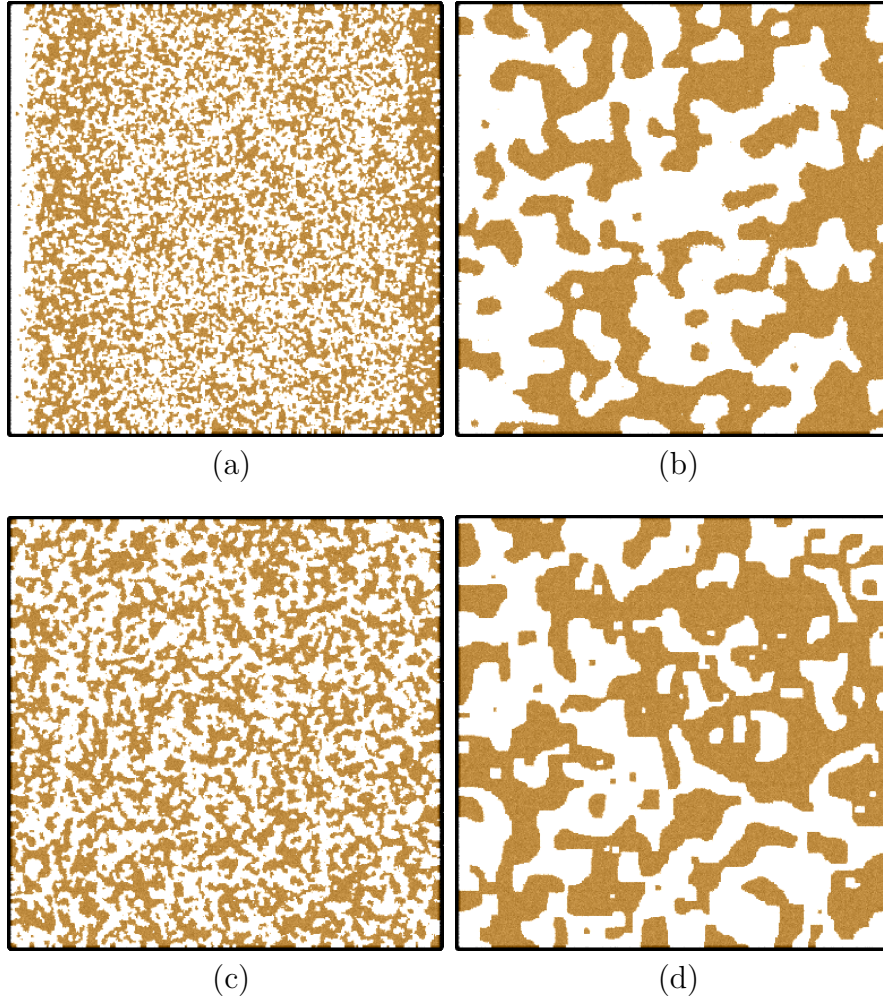
Figure 6.7 Cross sections of the model morphologies, generated with experimentally measured density profiles, and those generated to an identical characteristic feature size, a, but with a flat target density, which we refer to as Ising-only. The left hand column has feature size $a = 4$, while the right hand column has feature size $a = 16$. The top row are morphologies generated with the corresponding reflectivity informed density profile, while the bottom row is the Ising-only models, with a flat target density profile.
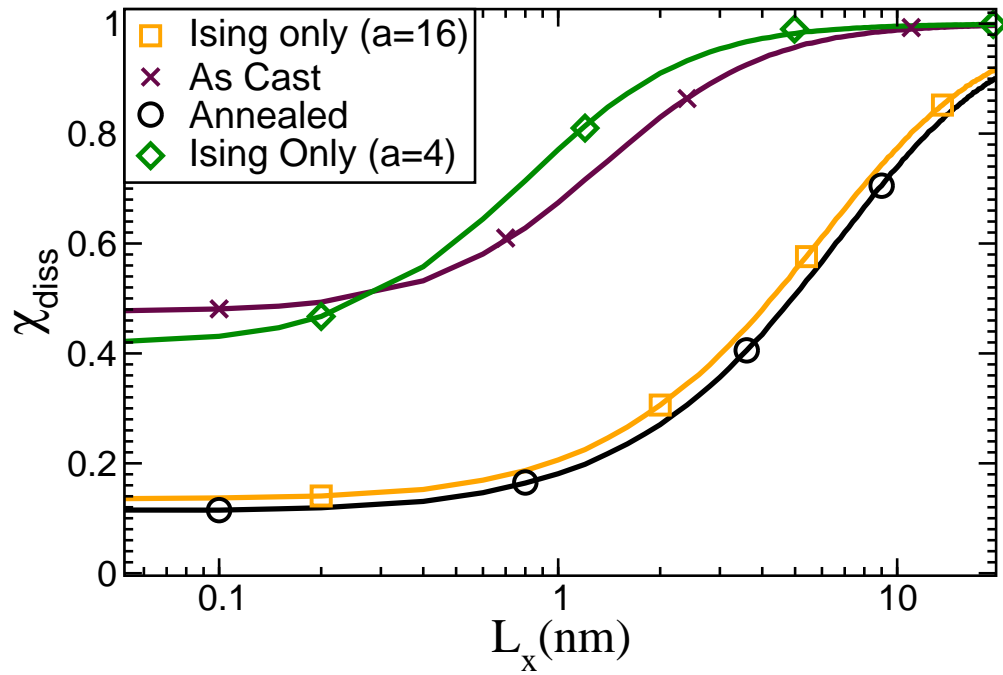
Figure 6.8   Results of exciton behavior comparing realistic morphologies to Ising only morphologies. Plot is of exciton dissociation efficiency (χ_{diss}) vs. exciton decay length (L_x). Maroon crosses represent the as cast morphology, black circles the annealed morphology, green diamonds the Ising only of feature size as cast (a=4) and yellow boxes the Ising only of feature size annealed (a=16).
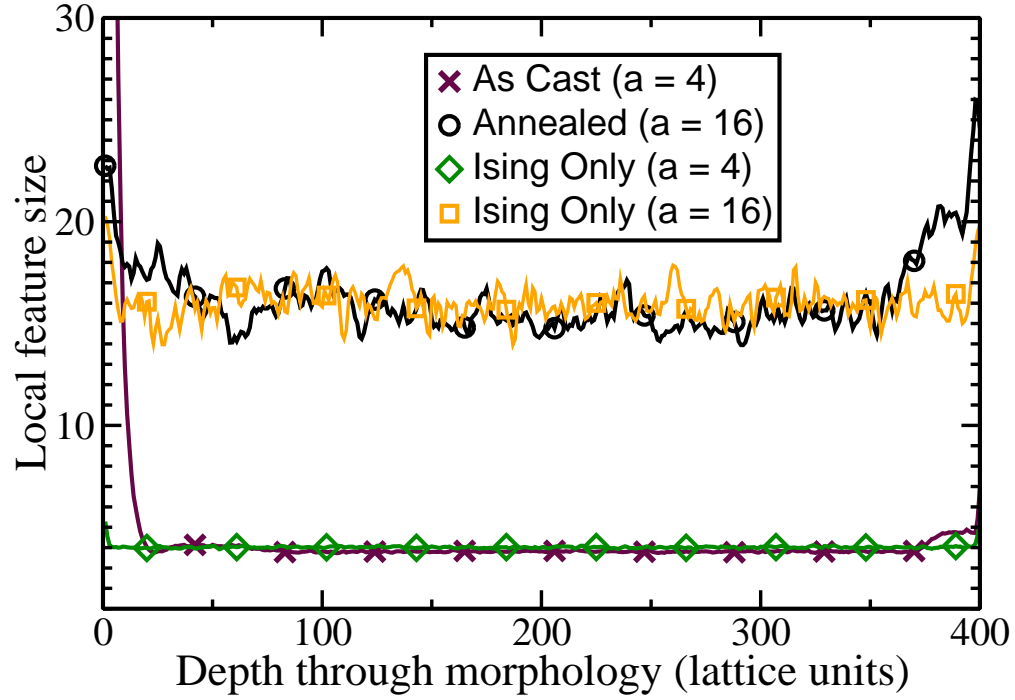
Figure 6.9 Local feature sizes for the as cast, annealed, and Ising only (a=4,16) morphologies. Local feature size is calculated with the familiar form $a = 3V/S$, but V is taken as the number of sites in a single slab $V = L \times L$ and S is taken as the total number of BHJ interfaces seen by the sites on a specific layer.
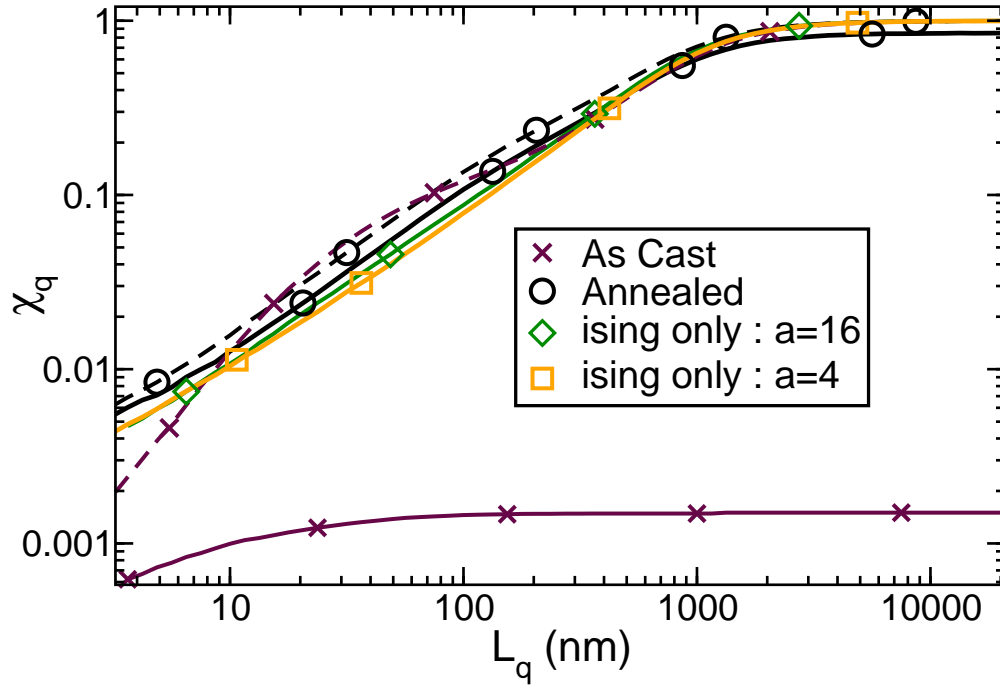
Figure 6.10   Charge collection efficiency comparison between the as cast, annealed, and Ising only (a=4,16) morphologies. Presented as the ratio of total charges collected at their respective contacts versus charge recombination length. For the realistic morphologies, solid lines represent electron collection and dashed lines represent holes. For the Ising only morphologies, there was no difference between electron and hole collection efficiencies, so they are presented as a single solid line.
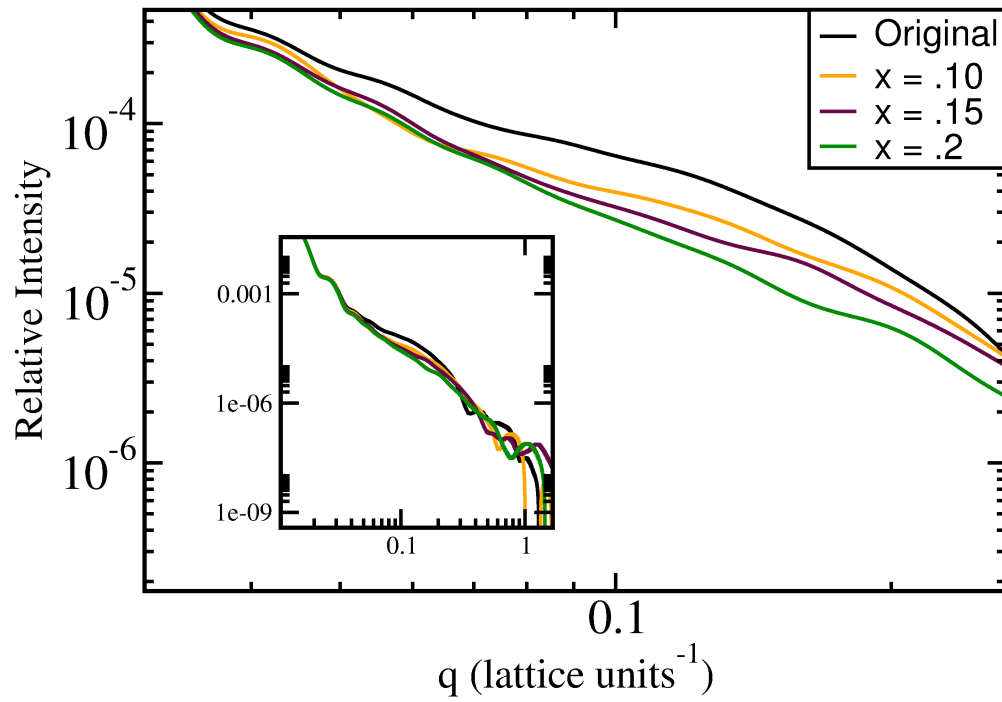
Figure 6.11   Simulated SANS scattering for the four cases of $x = 0, x = .1, x = .15$, and $x = 2$. fractional dispersed PCBM. The inset demonstrates the zoomed out view of the same simulated scattering.
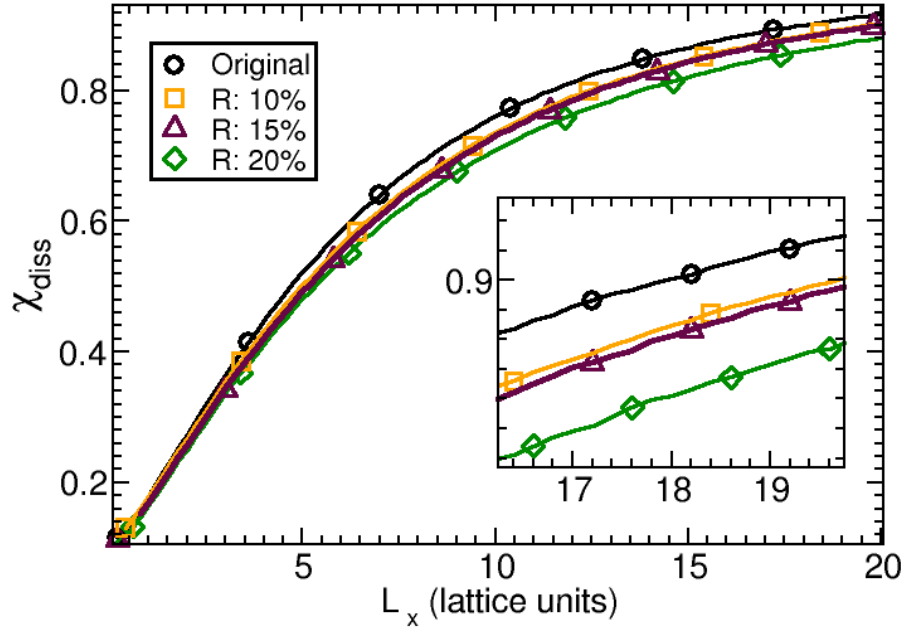
Figure 6.12   Exciton dissociation efficiency, χ_{diss}, versus exciton decay length, L_x, for the four cases of figure 5.17. Inset is a magnified portion of the data.
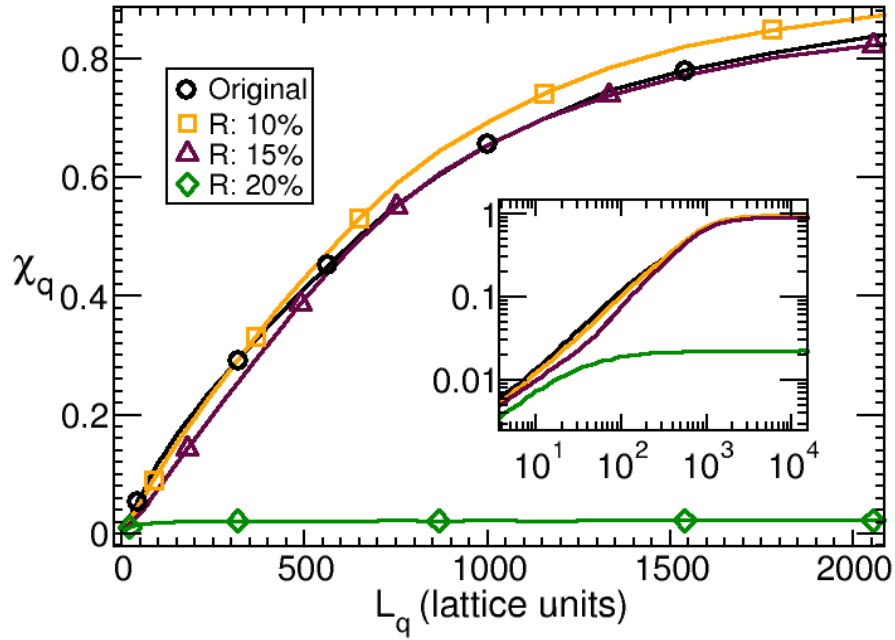
Figure 6.13 Electron collection efficiency, χ_q, versus free charge recombination length, L_q, for the four cases of figure 5.17. Inset is a zoomed out version of the data, on a log-log graph.
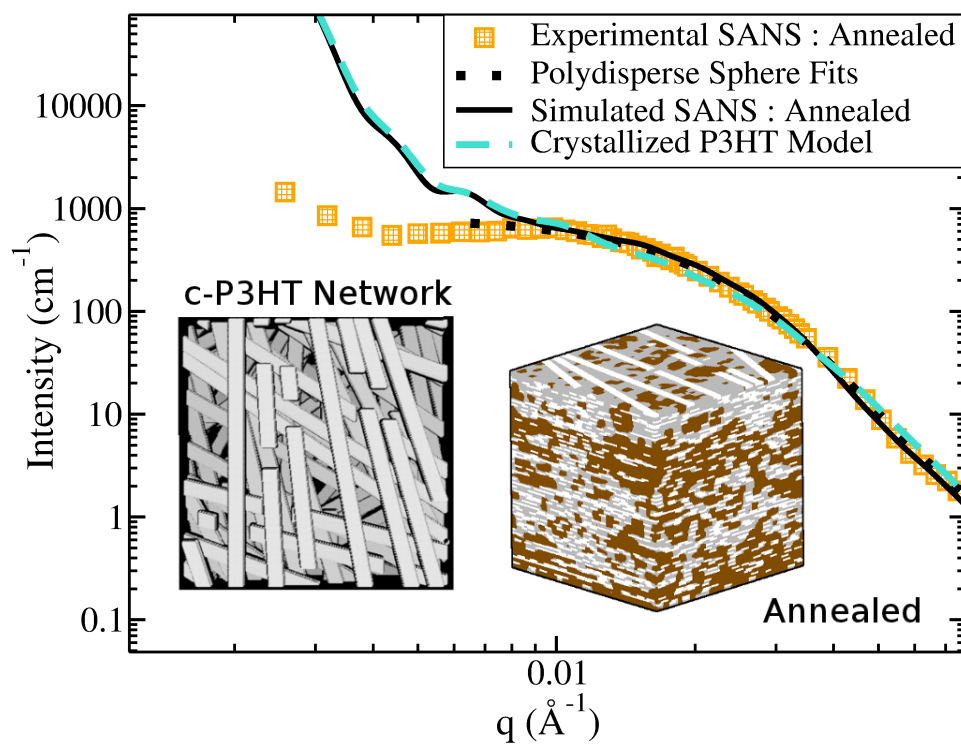
Figure 6.14   Simulated SANS comparisons of the simple two-phase model (black) and the crystallized P3HT model (dashed blue), as well as the experimental data (yellow boxes) and polydisperse sphere fits (black dots). Shown inset are views of the c-P3HT crystal network on the left, and a 3-d view of this morphology where PCBM has been colored brown, c-P3HT is white, and amorphous P3HT is gray.
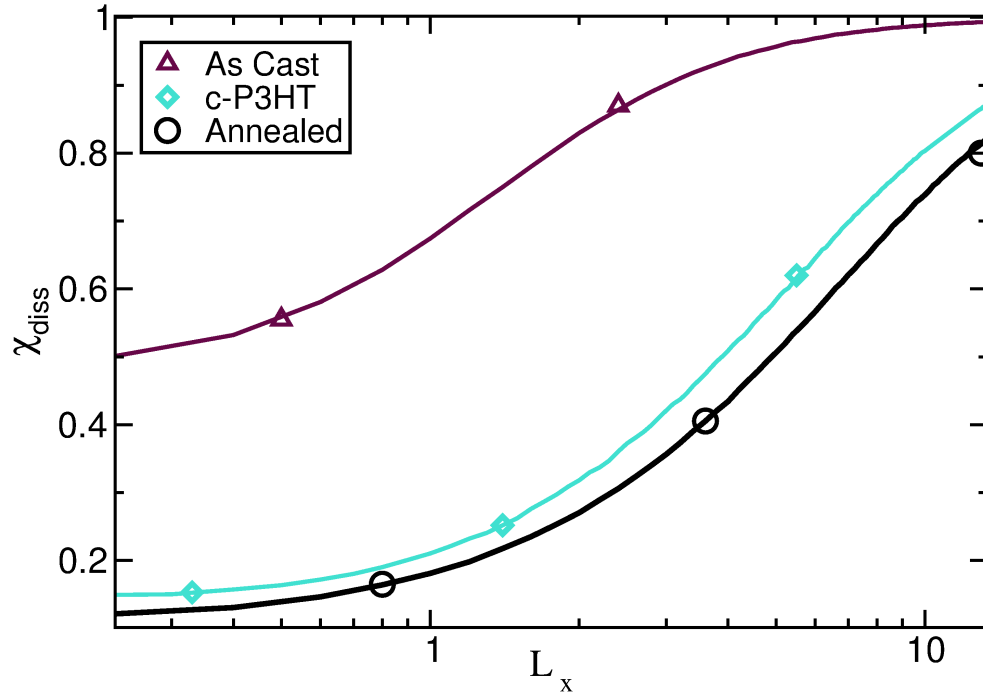
Figure 6.15   Exciton dissociation efficiency for the as cast (maroon triangles), annealed (black circles), and c-P3HT (light blue diamonds) morphologies. Exciton dissociation efficiency, $\chi_{\text{x-diss}}$, is defined as the ratio of excitons successfully diffusing to and dissociating at a heterojunction interface over total excitons generated. Exciton decay length, L_x, is defined as the lattice constant times the ratio of the exciton hop rate to the exciton decay rate.
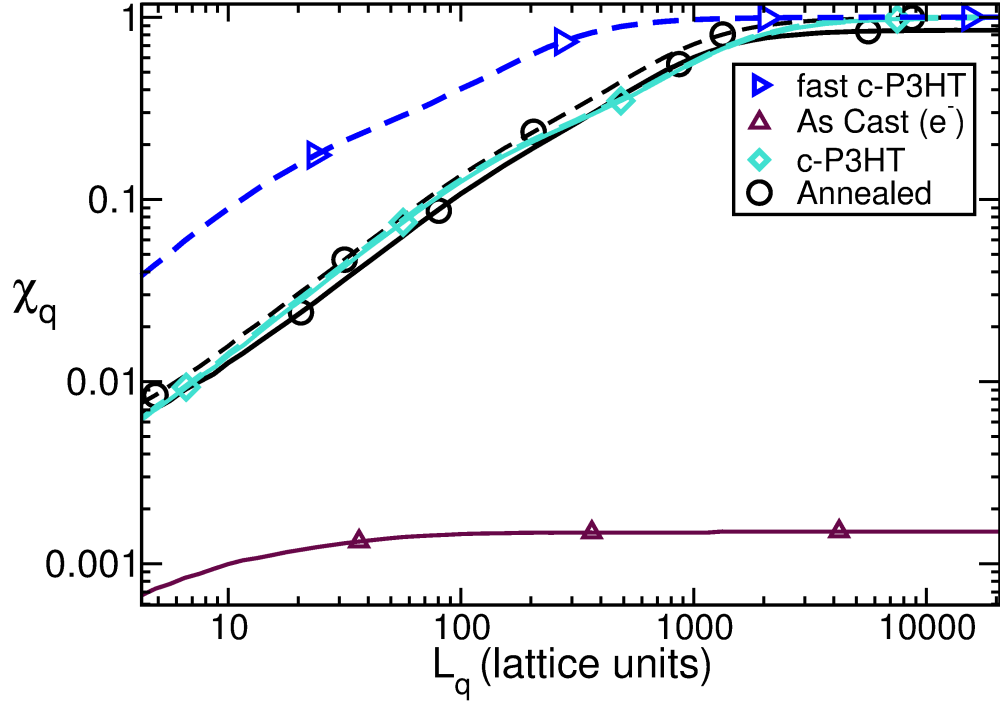
Figure 6.16   Charge collection efficiency for the as cast (maroon up-pointing triangles), annealed (black circles), c-P3HT (light blue diamond) models. Solid lines represent electron collection efficiency, while dashed lines represent hole collection. The enhanced mobility hole transport is also shown (dark blue right-pointing triangles). Charge collection efficiency, χ_q, is defined as the ratio of charges successfully collected at their respective contacts over total charges generated. Data presented as a function of charge recombination length, L_q.

Chapter 7

Conclusions

We have developed a method to efficiently generate three dimensional, interpenetrating, percolative nanostructures which are consistent with experimental data. In this thesis, we utilized neutron reflectometry and small angle neutron scattering data to model the bulk heterojunction nanostructure morphology as is found in many thin-film polymer based organic photovoltaic devices, specifically the P3HT/PCBM devices generated by Jon Kiel[8, 25] of Micheal Mackay's group at the University of Delaware. The development of higher efficiency thin film OPV devices is currently limited by our understanding of the influence nanoscale morphology has on overall device performance. Though several models have been proposed in order to explain this relationship[2, 27, 141, 136, 65, 4], none so far have extracted morphological characteristics directly from experimental data, but rather used a simple assumed morphology. As we have shown, small changes in model morphology produce measurable effects on calculated transport dynamics. Because of the strong influence morphology has in these systems it is important to use the most realistic model morphology possible, as this will lead to more accurate models and a better understanding of the system as a whole.

Previous fitting methods, using standard polydisperse sphere models[25] provide information on aggregate PCBM cluster size changes due to post-spin casting annealement of the device, but grant no insight into the percolative interpenetrating structure which defines this bulk heterojunction morphology and dictates many transport properties. Complex nanoscale morphologies exhibiting such a structure are not only important in OPV, but many other

modern energy applications such as LEDs, batteries, fuel cells, and sensors. Each of these fields can benefit in their modeling efforts through the use of morphologies extracted directly from experimental data, and we feel the method presented here offers a framework to accomplish this task.

The methodology of incorporating experimentally observed features through the use of an Ising model is quite similar to the reverse Monte Carlo technique, but distinct as we modify the Hamiltonian of the Ising model in order to facilitate refinement, rather than comparing directly to the scattering data. This general procedure can easily be extended to morphological models beyond the lattice Ising model, such as a Cahn-Hillard model, phase-field models, interpenetrating sphere models, and so on. The choice of experimental data to refine to is also much broader than the SANS and neutron reflectometry used here, as one could easily incorporate many other forms of data such as x-ray scattering data, AFM, STM, SEM, etc.

In this thesis, using morphologies generated with the modified Ising model, we looked at the effects of incorporating SANS and reflectometry data into a number of different nanoarchitecture systems, including the simple two-phase system, the sequestered PCBM system, and a model incorporating crystallized P3HT fibers. With our modeling efforts, we confirmed a number of well known previous postulates as well as discovering several previously undiscussed effects of nanoscale morphology on transport in these BHJ OPV devices. First, we confirmed the findings of previous studies[2, 18] which showed larger characteristic feature size in nanoscale morphology lead to greater charge collection efficiency, but also lower exciton dissociation. Second, we showed with our two-phase model that incorporation of experimental data, here in the form of neutron reflectometry and SANS data, has a significant effect on the results of DMC transport calculations. We also find that

for a specific characteristic feature size, density fluctuations throughout the morphology are detrimental to exciton dissociation efficiency. Through our sequestered PCBM models, we found that uniformly dropping the density of a charge carrier density (in this case, the pure PCBM phase) will eventually lead to an abrupt drop in percolation that will effectively break the OPV device, regardless of the effects of annealing. Finally, with the use of our c-P3HT fiber template model we find that from a purely morphological standpoint, the introduction of a crystal fiber network of P3HT will enhance both exciton dissociation efficiency and charge collection efficiency. We also find that if hole mobility inside these crystal fiber networks is enhanced only in-plane, this will dramatically increase hole transport throughout the morphology.

APPENDICES

A.1 Derivation of Field from a Pair of Charges Across a Dielectric Interface

In this appendix, we derive the potential due to a charge in a dielectric medium which is adjacent to a different dielectric medium separated by an infinite plane. The basic form of the Coulomb potential, for a charge q in dielectric material ϵ is

$$V(r) = \frac{q}{\epsilon r},\tag{A.1}$$

where r is the distance from the charge and we are using CGS units.
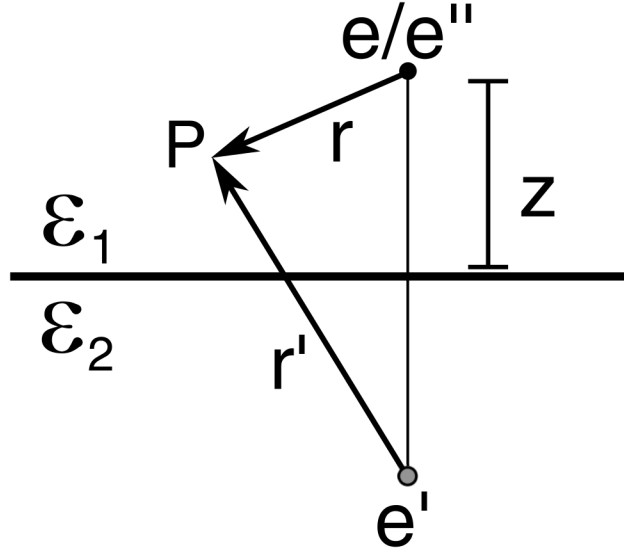
Figure A.1   Geometry of a single charge, e, adjacent to an infinite plane separating materials of different relative dielectrics, ϵ_1 and ϵ_2.

To begin with, we derive the potential at all points due to a single charge, as illustrated

in figure A.1. The charge, e, is a distance z away from the interface. Inside material ϵ_1, the potential at a point P will be due to the charge at a distance r and the image charge, e', which is a distance r' from point P. The potential due to this charge inside material ϵ_1 is

$$\phi_1 = \frac{e}{\epsilon_1 r} + \frac{e'}{\epsilon_1 r'}. \tag{A.2}$$

The field in material ϵ_2 will be due only to the effective charge, e'', which is the charge e screened by the dielectric boundary, such that it is in the same location but with a different magnitude. We write the potential in material ϵ_2 as thus

$$\phi_2 = \frac{e''}{\epsilon_2 r}. \tag{A.3}$$

At the boundary between the materials, in order to fulfill Maxwell's equations[142], the field and it's derivative scaled by the relative dielectric must be constant such that when $r = r'$

$$\phi_1 = \phi_2 \tag{A.4}$$

and

$$\epsilon_1 \frac{\partial \phi_1}{\partial n} = \epsilon_2 \frac{\partial \phi_2}{\partial n}, \tag{A.5}$$

where the derivatives, $\partial \phi / \partial n$ are taken normal to the boundary interface. These two boundary conditions mean that at $r = r'$ we may write

$$\phi_1(r) = \phi_2(r)$$

$$\frac{e}{\epsilon_1 r} + \frac{e'}{\epsilon_1 r} = \frac{e''}{\epsilon_2 r}$$

$$\frac{e + e'}{\epsilon_1} = \frac{e''}{\epsilon_2} \tag{A.6}$$

and

$$\epsilon_1 \frac{\partial \phi_1(r)}{\partial n} = \epsilon_2 \frac{\partial \phi_2(r)}{\partial n}$$

$$\epsilon_1 \frac{\partial}{\partial r} \left(\frac{e}{\epsilon_1 r} + \frac{e'}{\epsilon_1 r} \right) \frac{\partial r}{\partial n} = \epsilon_2 \frac{\partial}{\partial r} \left(\frac{e''}{\epsilon_2 r} \right) \frac{\partial r}{\partial n}$$

$$\epsilon_1 \left(\frac{-e}{\epsilon_1 r^2} + \frac{e'}{\epsilon_1 r^2} \right) = \epsilon_2 \left(\frac{-e}{\epsilon_2 r^2} \right)$$

$$e - e' = e'', \tag{A.7}$$

noting that e' is on the opposite side of the boundary as e, and thus it's derivative with respect to the normal direction will be opposite in sign. Using the results in equation A.6 and equation A.7 we may solve for e' and e'' to find

$$e' = \frac{e(\epsilon_1 - \epsilon_2)}{(\epsilon_1 + \epsilon_2)} \tag{A.8}$$

$$e'' = \frac{2\epsilon_2 e}{\epsilon_1 + \epsilon_2}. \tag{A.9}$$

As we are interested in a system which contains a pair of charges, we may add an

additional charge, q, which exists in material ϵ_2, as is illustrated in figure A.2 The potential on this charge would be the superposition of the field due to charge e in material ϵ_1 as is provided in equation A.3, and the charges own image, which is similar to the second term of equation A.2, seen as

$$\phi_q(r, z) = \phi_2 + \frac{q'}{\epsilon_2(2z)}.$$ (A.10)

By corollary, we know that the image charge, q', must have the value

$$q' = \frac{q\left(\epsilon_2 - \epsilon_1\right)}{\left(\epsilon_1 + \epsilon_2\right)}.$$ (A.11)

Making the final assumption that we are dealing with an electron and hole, and thus $q = -e$, we may write the potential experienced by charge q as

$$\phi_q(r, z) = \frac{2q}{\left(\epsilon_1 + \epsilon_2\right)} \left(\frac{1}{r}\right) - \frac{\left(\epsilon_2 - \epsilon_1\right) q}{\left(\epsilon_q + \epsilon_2\right) \epsilon_2} \left(\frac{1}{2z}\right),$$ (A.12)

where we may generalize that ϵ_2 is the material the charge of interest resides in and ϵ_1 is the opposite material. The first term is clearly the attraction due to opposite charges and the second is the image charge effect. Notice that if $\epsilon_1 = \epsilon_2$, this reduces to the familiar form given in equation A.1, which is what we would predict in uniform material, such as two charges in a vacuum.

The electrostatic potential for a linear dielectric system, W, can be expressed as

$$W = \frac{1}{2} \int \rho(\vec{r}) \phi(\vec{r}) \, dV$$ (A.13)

where the integral is taken over all space, $\rho(\vec{r})$ is the charge distribution and $\phi(\vec{r})$ is the electrostatic field. Using this, we may define the electrostatic potential of an arrangement of two charges of opposite charge, on either side of an infinite dielectric barrier as

$$W = \frac{-2q^2}{(\epsilon_1 + \epsilon_2)r_{12}} + \frac{q^2}{4z_1\epsilon_1}\frac{\epsilon_1 - \epsilon_2}{\epsilon_1 + \epsilon_2} + \frac{q^2}{4z_2\epsilon_2}\frac{\epsilon_2 - \epsilon_1}{\epsilon_1 + \epsilon_2}. \tag{A.14}$$

Note that the first term of equation A.14 is the interaction energy between the two opposite charges while the second and third terms are the interaction energy of the charges with their respective image charges. As with the potential, we see that in the case of $\epsilon_1 = \epsilon_2 = 1$ (vacuum conditions), the static potential energy reduces to the familiar solution of $W = z_1 z_2 / r_{12}$
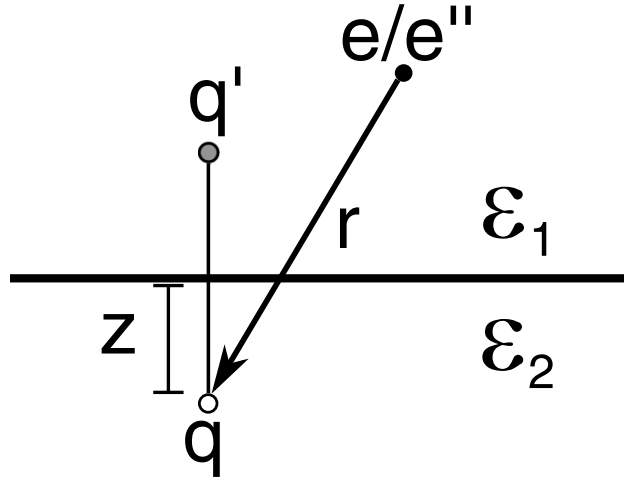
Figure A.2   Geometry of a pair of charges, with the potential on charge q given by equation A.12

A.2   Derivation of Basic Scattering Principles

A.2.1   Derivation of Single Slit Scattering

We begin by deriving the results of single slit diffraction, as seen in figure A.3. Assume a plane wave with wavelength θ is incident on a barrier, with a slit of width a. Every point along this slit, da, will act as a point source for a spherical wave propagating in all directions, with the assumption that all waves start out in phase from the slit. Thus, at an arbitrary point along the detector, the contributions from the top of the slit will have to travel a distance r_1, and the bottom of the slit will have to travel r_2. The difference of these lengths Δr, is therefore
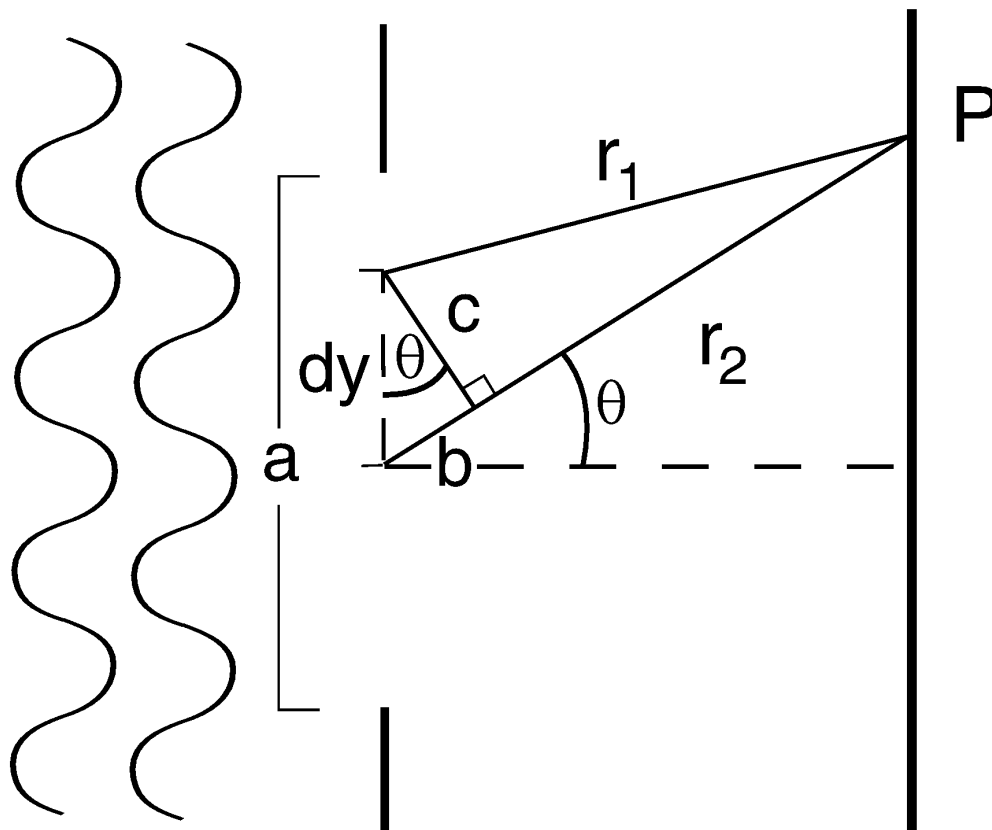
Figure A.3   Single slit example
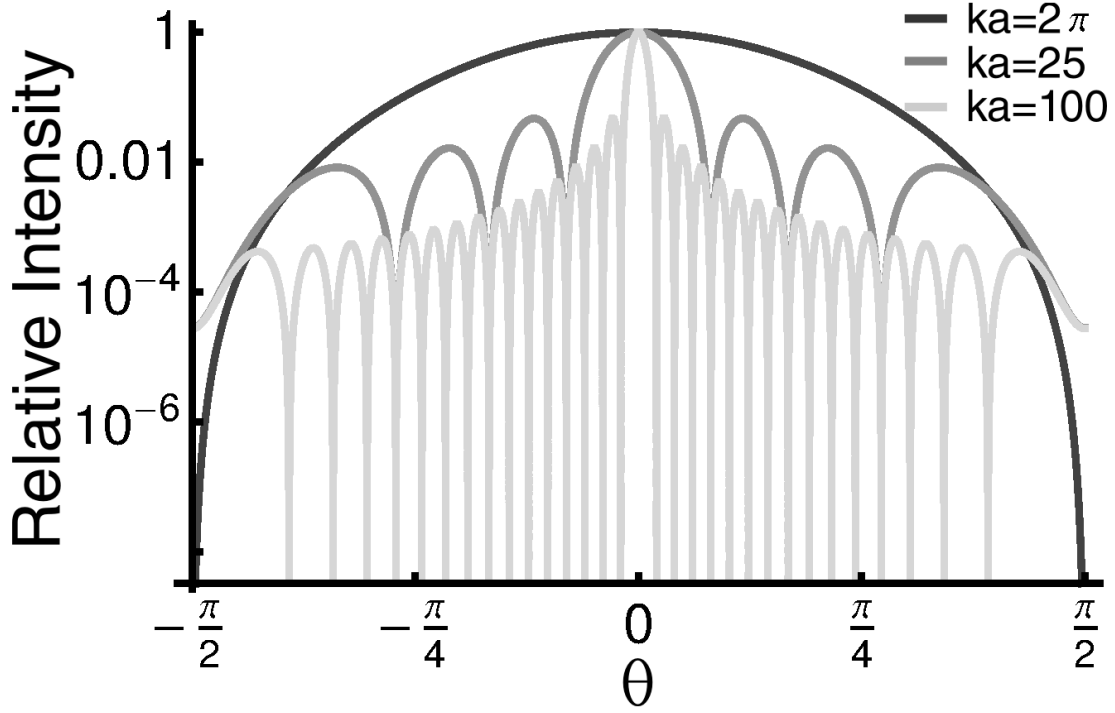
Figure A.4 Single slit example data

$$\Delta r = r_2 - r_1 = a\sin\theta. \tag{A.15}$$

If $a << \theta$, the slit will act as a point source, and a spherical wave will result. If $\lambda \approx a$, an interference pattern will occur, known as a "Fresnel diffraction" pattern if the detector is close to the slit or a "Fraunhofer" pattern if it is far away.

The contribution to a field, $\vec{E}$, from an arbitrary point P due to a small element of the slit of width dy, where the edge of slit distance to P is r_1 and r_2, assuming a constant source strength at the slit of ε_l (units of intensity per length) is given:

$$dE = \frac{\varepsilon_l}{r}dy\exp i\left(kr - \omega t\right) \tag{A.16}$$

Now, consider a tiny fraction of the entire slit, dy. As seen in figure A.3, r_2 is slightly

longer than r_1 by a length of $b = y \sin \theta$, and at this point line r_2 is a distance away from r_1 of $c = y \cos \theta$. We thus can express r_1^2 as

$$
\begin{aligned}
r_1^2 &= (r_2 - b)^2 + c^2 \\
&= (r_2 - y \sin \theta)^2 + (y \cos \theta)^2 \\
&= r_2^2 + y^2 \sin^2 \theta - 2r_2 y \sin \theta + y^2 \cos^2 \theta \\
&= r_2^2 + y^2 - 2r_2 y \sin \theta \\
&= r_2^2 \left[1 - \frac{2y}{r_2} \sin \theta + \frac{y^2}{r_2^2} \right]
\end{aligned}
$$

$$(\text{A.17})$$

The limit $y \ll r_1/2$, is the Fraunhofer regime and we may drop final term of equation A.17. We rewrite and expand this definition of r_1 as

$$
\begin{aligned}
r_1 &= r_2 \left[1 - \frac{2y}{r_2} \sin \theta \right]^{1/2} \\
&= r_2 \left[1 - \frac{y}{r_2} \sin \theta + ... \right] \\
&= r_2 + y \sin \theta.
\end{aligned}
$$

$$(\text{A.18})$$

For simplicity we here define $R = r_1$. Using this result in equation A.16 and taking $r \to R$ we find

176

$$dE = \frac{\varepsilon_l}{r} e^{i(kr-\omega t)} \mathrm{d}y$$

$$= \frac{\varepsilon_l}{R} e^{i(k(R-y\sin\theta)-\omega t)} \mathrm{d}y$$

$$= \frac{\varepsilon_l}{R} e^{i(kR-\omega t)} e^{-i(ky\sin\theta)} \mathrm{d}y. \tag{A.19}$$

We can then use A.19 to find the effect of all such small sections of the total slit, a, by integrating from $-a/2$ to $a/2$ to find E as

$$E = \frac{\varepsilon_l}{R} e^{i(kR-\omega t)} \int_{-a/2}^{a/2} e^{-i(ky\sin\theta)} \mathrm{d}y$$

$$= \frac{\varepsilon_l}{R} e^{i(kR-\omega t)} \left[\frac{e^{-iky\sin\theta}}{-ik\sin\theta} \right]_{-a/2}^{a/2}$$

$$= \frac{\varepsilon_l}{R} e^{i(kR-\omega t)} \left(\frac{e^{-i\frac{ka}{2}\sin\theta} - e^{i\frac{ka}{2}\sin\theta}}{-ik\sin\theta} \right)$$

$$= \frac{\varepsilon_l}{R} e^{i(kR-\omega t)} \frac{-2i\sin\left(\frac{ka}{2}\sin\theta\right)}{-ik\sin\theta}$$

$$E = \frac{\varepsilon_l a}{R} e^{i(kR-\omega t)} \frac{\sin\left(\frac{ka}{2}\sin\theta\right)}{\frac{ka}{2}\sin\theta}. \tag{A.20}$$

For convenience, we define $\beta = \frac{ka}{2}\sin\theta$, so that equation A.20 has the form

$$E = \frac{\varepsilon_l a}{R} \frac{\sin(\beta)}{\beta} e^{i(kR-\omega t)}$$

$$= \frac{\varepsilon_l a}{R} \operatorname{sinc}(\beta) e^{i(kR-\omega t)}. \tag{A.21}$$

We can define relative intensity of the delivered wave, I_{rel}, as

$$I_{\text{rel}} = |E|^2 = I_0 \operatorname{sinc}^2\beta, \tag{A.22}$$

where I_0 is the maximum intensity given by $\left(\frac{\varepsilon_l a}{R}\right)^2$. The sinc function behaves similarly to a sin function, but decays inversely with $|\beta|$, such that I_{rel} has an absolute maximum at $\beta = \theta = 0$. The descending maxima will occur at points satisfying $\beta = \tan\beta$ and the minima will occur at points satisfying $\beta = n\pi$ for all non-zero integer values of n.

At small angles of θ, distances between maxima becomes $\delta\theta = \frac{\lambda}{a}$. If one increases the slit width until $a \gg \lambda$, the distance between peaks at small θ tends toward 0, and a shadowing effect becomes dominant, rather than diffraction.

The general trends, over the range of θ from $-\pi/2$ to $\pi/2$ are that zeros only appear once $ka \geq 2\pi$, the peak at $\theta = 0$ is always I_0, and as ka increases, the width of this peak decreases. as new maxima appear with separation $\Delta\theta = \lambda/a$.

An alternative, and arguably simpler calculation of this scattering pattern is through the use of the Fourier transform. If one defines the single wide slit as an aperture, $A(x)$ as

$$A(x)_{\text{wide slit}} = \begin{cases} 1 & \text{if } |x| \leq a/2 \\ 0 & \text{otherwise,} \end{cases} \tag{A.23}$$

and after a quick change of variables where $q = 2\pi\sin\theta/\lambda = 2\pi k\sin\theta$ we find

$$E(x) = E_0 \int_{-\infty}^{\infty} A(x) e^{iqx}$$

$$= E_0 \int_{-a/2}^{a/2} e^{iqx}$$

$$= \frac{E_0}{iq} \left(e^{iqa/2} - e^{-iqa/2} \right)$$

$$= \frac{E_0}{iq} \left(2 \sin \left(\frac{qa}{2} \right) \right)$$

$$= \frac{2 E_0 \sin \left(\frac{qa}{2} \right)}{q}, \tag{A.24}$$

where we have once again recovered the sinc behavior seen in equation A.21.

A.2.2   Derivation of Double Slit Scattering

Consider the case of two slits, spaced a distance d apart, with slit width of a, with a plane wave incident on one side as demonstrated in figure A.5. The field propagated to the other side of the screen will be the sum of the two individual slits, as derived previously
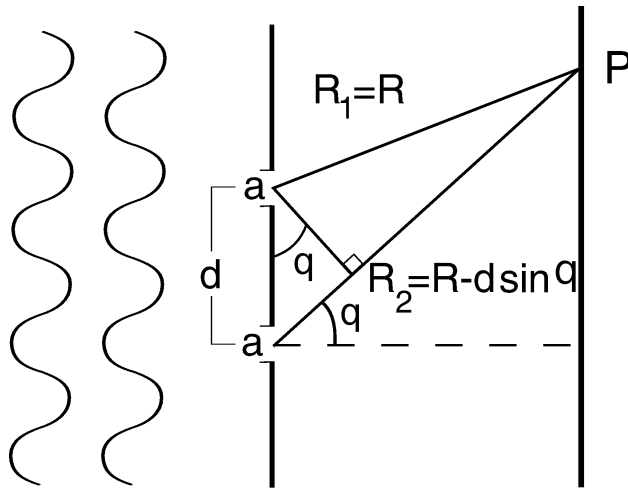
Figure A.5   Double slit example

179

$$E = \frac{\varepsilon_l a}{R_1} \operatorname{sinc}(\beta) e^{i(kR_1 - \omega t)} + \frac{\varepsilon_l a}{R_2} \operatorname{sinc}(\beta) e^{i(kR_2 - \omega t)}, \tag{A.25}$$

where R_1 and R_2 are the distances from the two slits to any point on the detector. For convenience, we define the paths from the two slits to the point P in terms of their separation, d, and the angle θ, as $R_1 = R$ and $R_2 = R_1 - d\sin\theta = R - d\sin\theta$. As such, we may now rewrite A.25 as

$$E = \frac{\varepsilon_l a}{R} \operatorname{sinc}(\beta) e^{i(kR - \omega t)} + \frac{\varepsilon_l a}{R - d\sin\theta} \operatorname{sinc}(\beta) e^{i(kR - kd\sin\theta - \omega t)}. \tag{A.26}$$

First, note that we assume $R \gg d$, as we are considering the situation where distance to the detector is much larger than the distance between the slits. As such, we reduce the denominator of the second term from $(R - d\sin\theta)$ to (R). Next, we define a variable similar to $\beta = \frac{ka\sin\theta}{2}$ from the single slit, but incorporating the distance between slits as $\alpha = \frac{kd\sin\theta}{2}$. We incorporate these changes into equation A.26 and reduce it to the form

$$\begin{aligned}
E &= \frac{\varepsilon_l a}{R} \operatorname{sinc}(\beta) e^{i(kR - \omega t)} + \frac{\varepsilon_l a}{R} \operatorname{sinc}(\beta) e^{i(kR - 2\alpha - \omega t)} \\
&= \frac{\varepsilon_l a}{R} \operatorname{sinc}(\beta) e^{i(kR - \omega t)} \left(1 + e^{-i2\alpha}\right) \\
&\quad \text{recalling that: } e^{i\alpha} + e^{-i\alpha} = 2\cos\alpha \\
&= \frac{\varepsilon_l a}{R} \operatorname{sinc}(\beta) e^{i(kR - \omega t)} \left(1 + e^{-i2\alpha}\right) \left(\frac{2\cos\alpha}{e^{i\alpha} + e^{-i\alpha}}\right) \\
&= \frac{\varepsilon_l a}{R} \operatorname{sinc}(\beta) (2\cos\alpha) e^{i(kR - \omega t)} \left(\frac{re^{-i\alpha}\left(e^{i\alpha} + e^{-i\alpha}\right)}{\left(e^{i\alpha} + e^{-i\alpha}\right)}\right) \\
E &= \frac{\varepsilon_l a}{R} \operatorname{sinc}(\beta) (2\cos\alpha) e^{i(kR - \alpha - \omega t)}. \tag{A.27}
\end{aligned}$$

Notice that this final form, equation A.27, is similar to the single slit diffraction pattern, equation A.21, but has an additional factor of $(2 \cos \alpha)$, and a phase shift in the harmonic function. Expressing relative intensity again through the use of A.22, we find the double slit intensity to be

$$I_{ds} = 4I_0 \cos^2 (\alpha) \operatorname{sinc}^2 (\beta). \tag{A.28}$$

Notice that the intensity of the double slits is the product of the intensity of the infinitely thin pair of slits (which is proportional to $\cos^2 \alpha$) and the intensity of a single wide slit (which goes as $\operatorname{sinc}^2 \beta$), a direct consequence of the Fourier relationship properties of a convolution as described previously in equation 4.5 as

$$f(x) = g(x) \otimes h(x) \Leftrightarrow F(k) = \sqrt{2\pi} \, G(k) \times H(k),$$

where $F(k), G(k)$, and $H(k)$ are the resultant Fourier transformed functions of $f(x), g(x)$, and $h(x)$ respectively. As the convolution of a pair of infinitely thin slits and a single finite "thick" slit results in two finite "thick" slits, the resultant scattering of two finite slits is the product of the scattering from an an infinitely thin pair and a single finite slit.

As the slits are brought closer, $d \to 0$, the factor $\alpha \to 0$, and the single slit case is recovered. As the slits become more narrow, $a \to 0$, the factor $\beta \to 0$, and the behavior of the traditional Young's double experiment emerges, in which the distance between maximas become $\delta\theta = n\theta$, with $n = 0, 1, 2, 3, ...$ and so on.

As with the single wide slit case, we may alternatively compute the scattering by defining an aperture function with two points distance d apart

$$A(x) = \delta_{x-d/2} + \delta_{x+d/2} \tag{A.29}$$

the scattering function is then a Fourier transforms

$$
\begin{aligned}
E(q) &= E_o \int_{-\infty}^{\infty} \left(\delta_{x-d/2} + \delta_{x+d/2} \right) e^{iqx} \mathrm{d}x \\
&= E_o \left(e^{ikd/2} + e^{-ikd/2} \right) \\
&= E_o \left[2\cos\left(\frac{dq}{2}\right) \right],
\end{aligned} \tag{A.30}
$$

which clearly reconstructs the cosine behavior in the wave, and thus cosine squared behavior in the intensity, as seen in equation A.28.

A.2.3 Origin of Nyquist Limits

Before discussing the various Nyquist limits placed on a Fourier transformation based scattering calculation, it is worth going through a simple example at the limits of analysis, a one dimensional delta function in real space f(x), and it's compliment in momentum space, F(k), and how this relates to the well known limits of the Heisenberg uncertainty principle. We begin with a straightforward Fourier transform of a delta function

$$F(k) = \text{F.T.}\,[f(x)] = (2\pi)^{-1/2} \int_{-\infty}^{\infty} dx\, e^{-ikx} f(x)$$

$$= (2\pi)^{-1/2} \int_{-\infty}^{\infty} dx\, e^{-ikx} \delta(x)$$

$$= (2\pi)^{-1/2}, \tag{A.31}$$

which is the expected result of a constant at all points in k-space, showing that a signal infinitely thin is composed of an infinite number of different Fourier contributions, seen as an infinitely wide signal in Fourier space. To get around this impasse in analysis, we model the delta function as a Gaussian, $P(x)$, defined

$$P(x) = A_x e^{-x^2/(2\sigma_x^2)}, \tag{A.32}$$

where the width is σ_x, we derive the normalization constant, A_x as

$$1 = \int_{-\infty}^{\infty} dx\, P(x) = \int_{-\infty}^{\infty} dx\, A_x e^{-x^2/(2\sigma_x^2)}$$

$$= A_x \sigma_x \sqrt{2\pi},$$

clearly showing that in order to normalize the probability, the prefactor must be

$$A_x = \frac{1}{\sigma_x \sqrt{2\pi}}. \tag{A.33}$$

Recalling that a wavefunction is related to a probability distribution as

$$P_x = |\psi(x)|^2 \,, \tag{A.34}$$

we may thus define $\psi(x)$ as a square root of the described normal distribution

$$\psi(x) = \sqrt{(P_x)} = \sqrt{A_x}e^{-x^2/4\sigma_x^2}. \tag{A.35}$$

Just as this wavefunction is described in real space as $\psi(x)$, so can it be described in momentum space as $\phi(k)$. Making the assumption that just as the position can be described as a normal distribution, $P(x)$, so can the momentum be assumed to fit such a distribution in k-space

$$\phi(k) = \sqrt{(P(k))} = \sqrt{A_k}e^{-k^2/4\sigma_k^2} \tag{A.36}$$

where

$$A_k = \frac{1}{\sigma_k\sqrt{2\pi}}. \tag{A.37}$$

As $\psi(x)$ and $\phi(k)$ are Fourier conjugates of one another and both are even functions we may relate though through the cosine Fourier transform as

$$\psi(x) = \sqrt{\frac{2}{\pi}} \int_0^\infty dk\, \phi(k) \cos(kx) \tag{A.38}$$

with the reverse transform being

$$\phi(k) = \sqrt{\frac{2}{\pi}} \int_0^\infty dx\, \psi(x) \cos(kx). \tag{A.39}$$

Using the definition of $\phi(k)$ from equation A.36 and $\psi(x)$ from equation A.35, we can

rewrite equation A.38 as

$$\sqrt{A_x}e^{-x^2/4\sigma_x^2} = \sqrt{\frac{2}{\pi}} \int_0^\infty dk \sqrt{A_k}e^{-k^2/4\sigma_k^2} \cos{(kx)}. \tag{A.40}$$

We can solve the integral on the right with the use of the solution

$$\int_0^\infty dx\, e^{-a^2 x^2} \cos{(bx)} = \frac{\sqrt{\pi}}{2a}e^{-b^2/4a^2}, \tag{A.41}$$

such that equation A.40 becomes

$$\sqrt{A_x}\,e^{-x^2/4\sigma_x^2} = \sqrt{\frac{2}{\pi}}\sqrt{A_k}\left[\frac{\sqrt{\pi}}{2(1/2\sigma_k)}e^{-x^2\sigma_k^2)}\right]$$
$$= \sigma_k\sqrt{2}\sqrt{A_k}\,e^{-x^2\sigma_k^2}. \tag{A.42}$$

In order for this equality to hold, one finds that the relationship between σ_x and σ_k must

be

$$\sigma_x^2\sigma_k^2 = \frac{1}{4} \tag{A.43}$$

or more simply

$$\sigma_x\sigma_k = \frac{1}{2}. \tag{A.44}$$

Note this equality exists only because this distribution of momentum and energy min-
imizes the uncertainty in both, as any function whose Fourier transform did not recover
itself would inherently have a different width (σ), and the product for a general function

could be larger than 1/2. The value of 1/2 on the RHS is a direct consequence of our use of the square-root of the probability, as this is how wavefunctions are described in quantum mechanics. If one were to instead perform an identical calculation using $P(x)$ and $P(k)$, one would find the product of the widths of those functions to be 1. Finally, through this discussion we have referred to σ as the width of a Gaussian distribution, but it could equally be considered an uncertainty of a measurement, where the center of the distribution is the measurement. Taking both these into account, we can write the relation

$$\Delta x \Delta k \geq \frac{1}{2}. \tag{A.45}$$

Using the relationship between momentum and wavenumber, $p = \hbar k$, where $\hbar$ is the reduced Planck's constant, one recovers the familiar form of the Heisenberg uncertainty principle

$$\Delta x \Delta p \geq \frac{\hbar}{2}. \tag{A.46}$$

Although it is entertaining to see that the Heisenberg uncertainty principle can be derived with a few simple assumptions and the Fourier transform, a more general concept is that the uncertainty (width) of one variable is inversely related to any the uncertainty in that function's Fourier conjugates. This is the origin of the concept of a Nyquist interval, dr_N, which states

$$dr_N = \frac{1}{2f_B} = \frac{2\pi}{2\omega_B}, \tag{A.47}$$

where B is the highest possible frequency of a system, and we have utilized the relation-

ship between ordinary frequency (f) and angular frequency (ω) of $f = 2\pi/\omega$. In the case

of the relationship between a PDF(r) and the scattering, I(q), which are Fourier conjugates

of one another in real (r) and wavevector (k) space. For example, the uncertainty of the

pair-distribution function[143] is inherent in the resolution in real space, here the Nyquist

interval $\mathrm{d}r_N$, but the limiting frequency, B, is more easily understood if we consider the

entire scattering profile to be symmetric about $q = 0$, such that it then resembles a probabil-

ity distribution with a width of q_{max}. As such, we recover the commonly used relationship

between resolution in the PDF(r) and q_{max}.

$$\mathrm{d}r = \frac{\pi}{q_{max}}. \tag{A.48}$$

A.3 Detailed examination of the First Reaction Method and Diffusion Rates

In order to verify the validity of the Walker/Greenham approach to charge transport in

Polymer-Fullerene based photovoltaics via the first reaction method (FRM) in this appendix

we examine the action of charge movement. Using FRM, particle movement is a process in

which all potential actions for a particle have an associated time, τ, generated for them:

$$\tau_i = -\frac{1}{\omega_i} \log(X) \tag{A.49}$$

Where ω_i is the characteristic rate for an event and X is a random number between 0

and 1. As this transport model occurs on a cubic lattice, there can be as many as 6 different

"hop" events for a particle; potentially less if a specific geometry bars transport in some of

the directions prior to calculation of a hop time in that direction.

In previous works[2, 18] the calculation of the characteristic hop rates associated with a specific mobility, μ, derive from the Einstein relation (equation A.50), and the relationship between hop frequency and diffusion constants (equation A.51) which we will derive later. These two equations are:

$$D = \frac{q}{k_b T}\mu \tag{A.50}$$

$$a^2 = 6D/\omega_i \tag{A.51}$$

where D is the diffusion constant, q is the charge, $k_B T$ is the thermal energy, μ is mobility, and a is the lattice constant (or characteristic hop length, which can only be the lattice constant in this model). By combining these equations, one generates a hop rate based on a given mobility:

$$\omega_i = \frac{6k_B T \mu}{qa^2} \tag{A.52}$$

A.3.1 Simple Diffusion

Before even approaching the validity of a charge hop rate between sites with varying energies (something integral to both Walker's and Greenham's transport model) let us look at the behavior of a simple diffusion in continuum compared to cubic lattice space. To study this diffusion behavior, we employed a simulation in which a diffusing particle is generated at origin, $R_o = (0,0,0)$, and then hops about the system randomly. By comparison, in the case of a cubic lattice, a hop is randomly chosen which moves the particle in one of the six

possible directions $(\pm x, \pm y, \pm z)$. For continuous diffusion, the diffuser will always hop with a distance of 1, but is in no way confined to cubic lattice directions, i.e. we allowed the diffuser to exist at non-integer coordinates and move in any direction. To facilitate uniform sampling on a sphere I select two random numbers: $u \in [-1, 1]$ and $\phi \in [0, 2\pi]$. These can then be translated to Cartesian coordinates as

$$
\begin{aligned}
x &= \sqrt{1 - u^2} \cos \phi \\
y &= \sqrt{1 - u^2} \sin \phi \\
z &= u.
\end{aligned}
\tag{A.53}
$$

To select a time for a hop we specify a general hop rate, ω_{hop}, which we then either explicitly use for every hop in diffusion (producing constant hop times) or employ in our FRM calculation through the use of equation (A.49).

A.3.2   Measuring the Effective Diffusion Constant

As we are interested in measuring the effective mobility, μ_{eff}, we here derive the relationship between μ_{eff} and the average distance a diffusing particle travels from the origin over time.

The average displacement of a 3-dimensional cubic lattice bound random walker, after a single hop that is equally likely to move in any of the 6 directions goes as the average of all 6 possible lattice moves. As such, the average radial position after a single hop will be $\langle r_1 \rangle = 0$ and the average variance after one hop will be $\langle r_1^2 \rangle = a^2$, where a is the lattice constant. After N-hops, we can clearly see that the average displacement is going to remain at the origin, but the average variance will grow with the number of hops such that

$$\langle r_N \rangle = N \langle r_i \rangle = 0 \tag{A.54}$$

$$\left\langle r_N^2 \right\rangle = N \left\langle r_i^2 \right\rangle = Na^2. \tag{A.55}$$

As the number of hops grows large, a site's occupation probability becomes a Gaussian distribution about origin, with a variance given above (and normalized) as

$$P_x(x) = \frac{1}{\sqrt{2\pi\sigma^2}} \exp\left[-\frac{(x-x_0)^2}{2\sigma^2}\right]. \tag{A.56}$$

Putting together similar expressions for P_y and P_z, we can define $P(r)$:

$$P_r(r) = P_x(x) \times P_y(y) \times P_z(z) \tag{A.57}$$

$$
\begin{aligned}
P_r(x,y,z) &= \left(\frac{3 \cdot \frac{3}{2}}{2a^3 N^{3/2} \pi^{3/2}}\right) \exp\left[-\frac{3\left(x^2+y^2+z^2\right)}{2a^2 N}\right] \\
&= \left(\frac{2\pi Na^2}{3}\right)^{-3/2} \exp\left[-\frac{3\,r^2}{2a^2 N}\right] \tag{A.58}
\end{aligned}
$$

Note that the probability distribution is isotropic (having no angular dependence), as is expected for a diffusing particle with no directional bias. The result of integration for the displacement is

$$\langle r \rangle = \int_0^{2\pi}\int_0^{\pi}\int_{-\infty}^{\infty} r\,\left(\frac{2\pi N a^2}{3}\right)^{-3/2} \exp\left[-\frac{3}{2a^2 N}r^2\right] r^2 \sin\theta\;\mathrm{d}r\,\mathrm{d}\theta\,\mathrm{d}\phi$$

$$= 0 \tag{A.59}$$

and the variance is

$$\langle r^2 \rangle = \int_0^{2\pi}\int_0^{\pi}\int_0^{\infty} r^2\,\left(\frac{2\pi N a^2}{3}\right)^{-3/2} \exp\left[-\frac{3}{2a^2 N}r^2\right] r^2 \sin\theta\;\mathrm{d}r\,\mathrm{d}\theta\,\mathrm{d}\phi$$

$$= N a^2. \tag{A.60}$$

So we see that the variance of a diffusing particle goes as the product of the number of hops and the average hop length squared. If particle hopping occurs at a constant rate of ω, then after a time t has passed, we can expect the number of hops taken to be $N = \omega t$. We express the variance of such a particle at time t to be:

$$\langle r^2 \rangle = N a^2 = \omega t a^2$$

or if solving the 1D form :

$$\langle x^2 \rangle = N a^2 = \omega t a^2 \tag{A.61}$$

Next we relate the diffusion constant itself, D, to the simulation measured variance, $\langle r^2 \rangle$. First we derive the relationship between the diffusion constant and the hopping rate. We start with the diffusion equation itself in 1-D:

$$\frac{\partial P_x}{\partial t} = D \frac{\partial^2 P_x}{\partial x^2} \tag{A.62}$$

If we plug the results of equ.(A.61) into equ.(A.56), and solve for D in equ.(A.62), one finds that in 1-D:

$$D = \frac{a^2\omega}{2} \Rightarrow \text{ or equivalently } \Rightarrow a^2\omega = 2D \tag{A.63}$$

such that when we then plug these results back into the 1D results of equ(A.61), we find:

$$\left\langle x^2 \right\rangle = 2Dt \tag{A.64}$$

To get higher dimensional forms of this result, we must simply add together the variances such that the result in 3D is

$$\left\langle r^2 \right\rangle = 6Dt \tag{A.65}$$

Now, we will use the equations derived and simple diffusion simulation described to examine the results of varying an explicitly given hop rate, ω_{hop}. We measure the variance squared over time, knowing from equ.(A.65) that this should produce a value of $6D$, the results of the calculation are shown in figure A.6. As we see, for both continuous diffusing (in all directions) and cubic diffusing (on a cubic lattice) the diffusion constant can easily and accurately be extracted. It is noteworthy that both the cubic and continuous diffusion average generate nearly identical values, illustrating that cubic hopping has no noteworthy effect on the results. Thus, the results of diffusion transport calculations in a cubic lattice model can be correctly assumed to be similar to the results for a real space model.
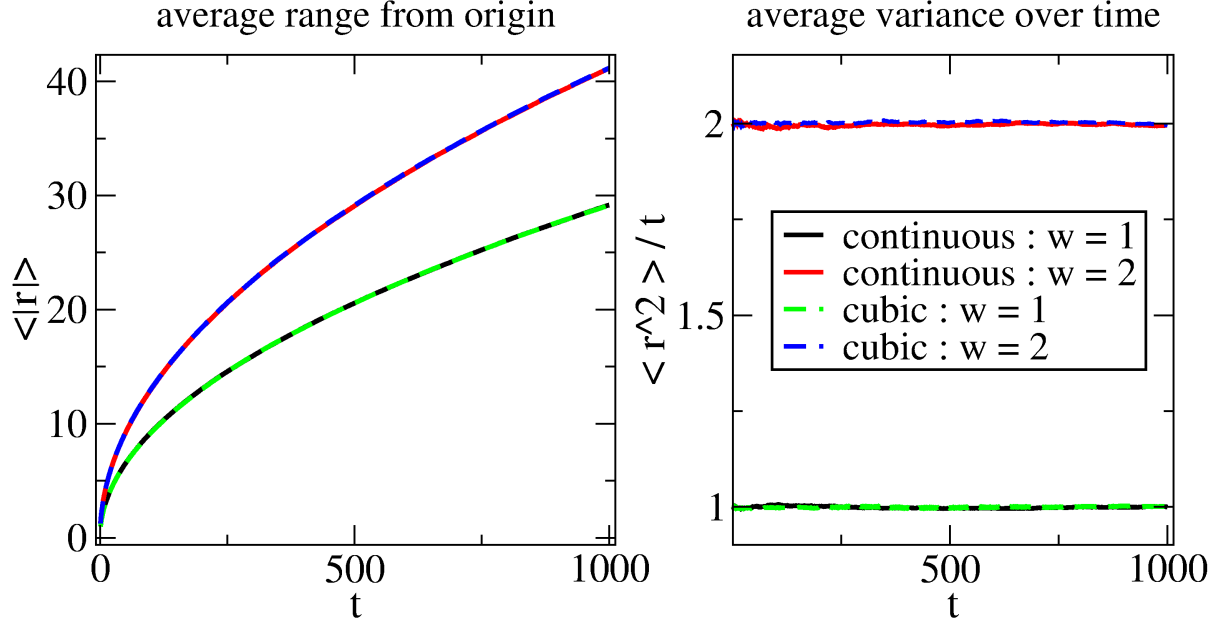
Figure A.6   A simple random walker simulation with hops either confined to a cubic lattice or allowed in all directions but with fixed hop distance. Averaged over 10^7 walkers. On the LHS is the average modulus of the radius traveled vs. time. On the RHS is the average variance over time vs time, which according to equ.(A.65), will give $6D$.

A.3.3   Correcting for attempt number

One problem we find with the FRM method as it has been employed previously is that no consideration has been taken for how the number of hop-actions possible will influence transport. For example, a diffuser in a cubic lattice which is in a corner will only have 3 potential movement actions considered in the FRM method, where as a diffuser in the bulk of the material will have 6 potential hop actions. Based on the semi-random nature of the FRM method, the more chances an action has to occur (in this case diffuser hopping), the faster an averaged selected event will be. We find this can be corrected by inversely scaling the average hop rate used to generate an event time (equation A.49) by the number of attempts a current action is allowed (i.e. 1/6 in the bulk and 1/3 in a corner), with the form

$$\omega_{eff} = \frac{\omega_{hop}}{N_{tries}}, \tag{A.66}$$

where ω_{eff} is the effective hop rate to use in the equation A.49 to generate an average hop rate of ω_{hop} when used over N_{tries} number of attempts.

To illustrate this problem and correction, we measure the value of $6D$ (being proportional to the variance over time) for a series of diffusers with hop rates generated using hop rates of $\omega = 1$ and $\omega = 1/6$ with the FRM method being employed in the standard way (6 attempts on a cubic lattice). We also show the results in which only $\omega = 1$ is employed, but only a single time is generated with the hop vector in the cubic lattice being randomly selected. The results are shown in figure A.7.
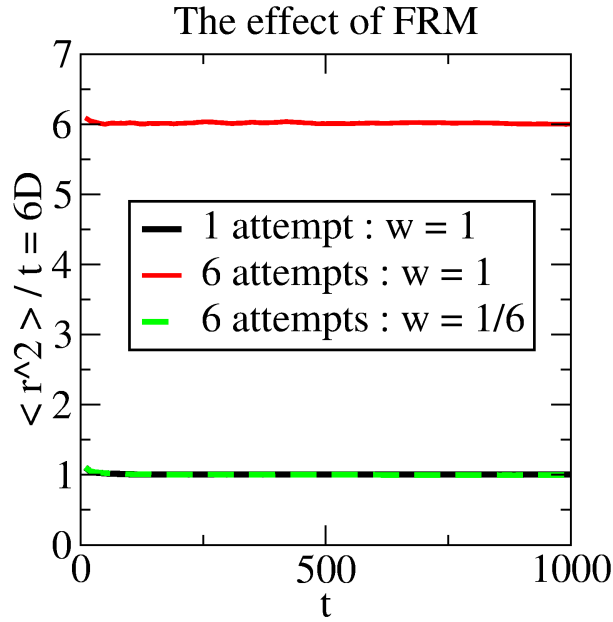
Figure A.7   A demonstration of how desired hop rate is affected by attempt rate in the FRM method.

As one can see, the measured diffusion constant is a factor of 6 too high for the standard FRM method implementation, resulting in a value of 6D=6 rather than the desired 6D=1 (seen in using A.51 with a $\omega_i = 1$ and $a = 1$.). The alternative method of randomly selecting a hop vector and calculating a time recovers the desired results, as does our proposed correction. This result shows that the previously uncorrected FRM method will on average

select a faster hop rate than desired.

A.4 Relationships between various correlation functions and the scattering profiles

Here, we outline the relationships between various frequently used functions defining structure and their scattering corollaries. Common variables used here are scattering power for a scatterer, f_i, scalar distance between two scatterers (i and j), r_{ij}, total number of scatterers in a sample, N, number density of scatterers, ρ_0. Note that although scattering power inherently has a q-dependence, in the small angle region scattering power may be considered constant[111].

A.4.1 Structural correlation functions definitions

Radial distribution function, $R(r)$, is given

$$R(r) = \frac{1}{\langle f \rangle} \sum_i \sum_j f_i^* f_j \delta(r - r_{ij}).$$ (A.67)

Real space pair density, $\rho(r)$, is given

$$\rho(r) = \frac{1}{4\pi r^2 N \langle f \rangle^2} \sum_{i \neq j} f_i f_j \delta(r - r_{ij}).$$ (A.68)

Atomic pair distribution function (PDF), $g(r)$, is given

$$g(r) = 4\pi r \left[\rho(r) - \rho_0\right] = \frac{1}{r N \langle f \rangle^2} \sum_{i \neq j} f_i f_j \delta(r - r_{ij}) - 4\pi r \rho_0.$$ (A.69)

Reduced pair distribution function, $G(r)$, is given

$$G(r) = 4\pi r \rho_0 \left[g(r) - 1 \right].$$

(A.70)

A.4.2 Scattering profile function definitions

The full scattering, $I(q)$, is given

$$I(q) = I_{coh}(q) + I_{incoh}(q),$$

(A.71)

where the incoherent scattering, I_{incoh}, is defined as,

$$I_{incoh} = \sum_i f_i^* f_i = N \left\langle f^2 \right\rangle,$$

(A.72)

and the coherent scattering, I_{coh} is,

$$I_{coh} = \sum_{i,j} f_i^* f_j \, \exp\left(i\, \vec{q} \cdot \vec{r}_{ij} \right).$$

(A.73)

The discrete scattering, I_d, which is the coherent component minus the incoherent, may be defined

$$I_d = I_{coh} - I_{incho} = \sum_{i \neq j} f_i^* f_j \, \exp\left(i\, \vec{q} \cdot \vec{r}_{ij} \right).$$

(A.74)

The total scattering structure function, $S(q)$, is defined as

$$S(q) = \frac{I_{coh}}{N \langle f \rangle^2} - \frac{\left\langle (f - \langle f \rangle)^2 \right\rangle}{\langle f \rangle^2},$$

(A.75)

which if we take into account angle-averaging, may be written as

$$S(q) - 1 = \frac{1}{N \langle f \rangle^2} \sum_{i \neq j} f_i^* f_j \exp\left(i \vec{q} \cdot \vec{r}_{ij} \right). \tag{A.76}$$

The reduced total scattering structure function, $F(q)$, being $[S(q) - 1]$ rescaled by q and averaged over all angles, may be written

$$F(q) = q \left[S(q) - 1 \right] = \frac{1}{N \langle f \rangle^2} \sum_{i \neq j} f_i^* f_j \frac{\sin \left(q \, r_{ij} \right)}{r_{ij}}. \tag{A.77}$$

The sine-transform of $F(q)$ generates a function, $k(r)$, which is defined

$$
\begin{aligned}
k(r) &= \frac{2}{\pi} \int_0^\infty \frac{1}{N \langle f \rangle^2} \sum_{i \neq j} f_i^* f_j \frac{\sin \left(q \, r_{ij} \right)}{r_{ij}} \sin(qr) \mathrm{d}q \\
&= \frac{1}{rN \langle f \rangle^2} \sum_{i \neq j} f_i^* f_j \left[\delta(r - r_{ij}) - \delta(r + r_{ij}) \right],
\end{aligned}
$$

limiting the calculation to values of $r > 0$ only, one finds

$$k(r) = \frac{1}{rN \langle f \rangle^2} \sum_{i \neq j} f_i^* f_j \delta(r - r_{ij}). \tag{A.78}$$

A.4.3   Correlation relationships

The relationships between the total scattering structure function $S(q)$, total scattering intensity $I(q)$, reduced total scattering structure function $F(q)$, and the coherent scattering intensity, $I_{coh}(q)$, are

$$S(q) = \frac{I(q)}{\langle f \rangle^2} = \frac{F(q)}{q} + 1 = \frac{I_{coh}}{N \langle f \rangle^2} - \frac{\langle (f - \langle f \rangle)^2 \rangle}{\langle f \rangle^2}. \tag{A.79}$$

The relationships between the real space pair density, $\rho(r)$, the radial distribution function $R(r)$, and Fourier transform of the reduced total scattering structure function, $k(r)$, the atomic pair distribution function, $g(r)$, and the reduced pair distribution function $G(r)$, are

$$\rho(r) = \frac{k(r)}{4\pi r} = \frac{R(r)}{4\pi r^2} = \frac{g(r)}{4\pi r} + \rho_0 = \frac{G(r) + 4\pi r \rho_0 \left(1 + 4\pi r \rho_0\right)}{16\pi^2 r^2 \rho_0}. \tag{A.80}$$

A.4.4 Relationship to the weighted pair density function

Our definition of the weighted pair density function, $w(r)$, which is only sampling a random number of pairs, N_p, is

$$w(r) = \sum_{i \neq j}^{Np} f_i^* f_j \delta(r - r_{ij}), \tag{A.81}$$

which, as the number of pairs sampled tends toward the total number of pairs in the system, asymptotically approaches a rescaled $\rho(r)$ as

$$\lim_{N_p \to \text{all}} [w(r)] = 4\pi r^2 N \langle f \rangle^2 \rho(r). \tag{A.82}$$

The effective scattering profile we calculate, $I^a(q)$, is

$$I^a(q) = C \sum_{R_{min}}^{R_{max}} w(r) \frac{\sin(q\,r)}{q\,r}, \tag{A.83}$$

where the sum is taken over r from the smallest to largest lengths used in $w(r)$, and C is a normalization constant used to fit simulations to experiment. As we have calculated

$I^a(q)$, it's closest scattering corollary is the coherent scattering, $I_{coh}(q)$, which has been angle averaged over the scattering interaction $\mathbf{q} \cdot \mathbf{r}_{ij}$, though as one can see in equation A.79, this quantity is closely related to many others.

Note also that we do not use actual scattering powers, f, as these are typically measured in units of $10^{-6}\,\text{Å}^{-2}$, instead using scaled scattering powers, b, with typical values of $0, 1, 5$, etc. If direct comparison to experiment is desired, correct unit scaling may be accounted for in the normalization constant, C.

BIBLIOGRAPHY

BIBLIOGRAPHY

[1] F. Yang and S. R. Forrest, "Photocurrent generation in nanostructured organic solar cells," *ACS Nano*, vol. 2, no. 5, pp. 1022–1032, 2008.

[2] P. K. Watkins, A. B. Walker, and G. L. B. Verschoor, "Dynamical monte carlo modelling of organic solar cells: The dependence of internal quantum efficiency on morphology," *Nano Letters*, vol. 5, no. 9, pp. 1814–1818, 2005.

[3] W. Chen, T. Xu, F. He, W. Wang, C. Wang, J. Strzalka, Y. Liu, J. Wen, D. J. Miller, J. Chen, K. Hong, L. Yu, and S. B. Darling, "Hierarchical nanomorphologies promote exciton dissociation in polymer/fullerene bulk heterojunction solar cells," *Nano Letters*, vol. 11, no. 9, pp. 3707–3713, 2011.

[4] W. Yin and M. Dadmun, "A new model for the morphology of P3HT/PCBM organic photovoltaics from small-angle neutron scattering: Rivers and Streams," *ACS Nano*, vol. 5, no. 6, pp. 4756–4768, 2011.

[5] S. van Bavel, E. Sourty, S. Veenstra, J. Loos, *et al.*, "Three-dimensional nanoscale organization of polymer solar cells," *J. Mater. Chem.*, vol. 19, no. 30, pp. 5388–5393, 2009.

[6] S. D. Oosterhout, M. M. Wienk, S. S. van Bavel, R. Thiedmann, L. J. A. Koster, J. Gilot, J. Loos, V. Schmidt, and R. A. J. Janssen, "The effect of three-dimensional morphology on the efficiency of hybrid polymer solar cells," *Nature Materials*, vol. 8, no. 10, pp. 818–824, 2009.

[7] D. R. Kozub, K. Vakhshouri, L. M. Orme, C. Wang, A. Hexemer, and E. D. Gomez, "Polymer crystallization of partially miscible polythiophene/fullerene mixtures controls morphology," *Macromolecules*, vol. 44, no. 14, pp. 5722–5726, 2011.

[8] J. W. Kiel, B. J. Kirby, C. F. Majkrzak, B. B. Maranville, and M. E. Mackay, "Nanoparticle concentration profile in polymer-based solar cells," *Soft Matter*, vol. 6, no. 3, pp. 641–646, 2010.

[9] J. W. Kiel, *NANOPARTICLE ASSEMBLY IN POLYMER BASED SOLAR CELLS*. PhD thesis, Michigan State University, 2010.

[10] D. Anderson, *Clean Electricity from Photovoltaics.* London: Imperial College Press, 2001.

[11] R. Gottschalg, *The Solar Resource and the Fundamentals of Radiation for Renewable Energy Systems.* Sci-Notes, Oxford, 2001.

[12] S. H. Park, A. Roy, S. Beaupre, S. Cho, N. Coates, J. S. Moon, D. Moses, M. Leclerc, K. Lee, and A. J. Heeger, "Bulk heterojunction solar cells with internal quantum efficiency approaching 100vol. 3, pp. 297–302, May 2009.

[13] S. Forrest, "The limits to organic photovoltaic cell efficiency," *MRS Bulletin*, vol. 30, pp. 28–32, 2005.

[14] M. A. Green, K. Emery, Y. Hishikawa, W. Warta, and E. D. Dunlop, "Solar cell efficiency tables (version 39)," *Progress in Photovoltaics*, vol. 20, pp. 12–20, JAN 2012.

[15] S. R. Forrest, "The path to ubiquitous and low-cost organic electronic appliances on plastic," *Nature*, vol. 428, pp. 911–918, Apr. 2004.

[16] R. Steim, S. A. Choulis, P. Schilinsky, and C. J. Brabec, "Interface modification for highly efficient organic photovoltaics," *Applied Physics Letters*, vol. 92, no. 9, p. 093303, 2008.

[17] R. Shikler, M. Chiesa, and R. H. Friend, "Photovoltaic performance and morphology of polyfluorene blends:the influence of phase separation evolution," *Macromolecules*, vol. 39, no. 16, pp. 5393–5399, 2006.

[18] N. C. Greenham and M. Gratzel, "Nanostructured solar cells," *Nanotechnology*, vol. 19, p. 420201, Oct. 2008.

[19] M. A. Brady, G. M. Su, and M. L. Chabinyc, "Recent progress in the morphology of bulk heterojunction photovoltaics," *Soft Matter*, vol. 7, no. 23, pp. 11065–11077, 2011.

[20] D. C. Coffey, O. G. Reid, D. B. Rodovsky, G. P. Bartholomew, and D. S. Ginger, "Mapping local photocurrents in polymer/fullerene solar cells with photoconductive atomic force microscopy," *Nano Letters*, vol. 7, no. 3, pp. 738–744, 2007.

[21] O. G. Reid, K. Munechika, and D. S. Ginger, "Space charge limited current measurements on conjugated polymer films using conductive atomic force microscopy," *Nano Letters*, vol. 8, no. 6, pp. 1602–1609, 2008.

[22] K. Maturova, R. A. J. Janssen, and M. Kemerink, "Connecting scanning tunneling spectroscopy to device performance for polymer: Fullerene organic solar cells," *ACS Nano*, vol. 4, no. 3, pp. 1385–1392, 2010.

[23] L.-M. Chen, Z. Hong, G. Li, and Y. Yang, "Recent progress in polymer solar cells: Manipulation of polymer:fullerene morphology and the formation of efficient inverted polymer solar cells," *Advanced Materials*, vol. 21, no. 14-15, pp. 1434–1449, 2009.

[24] E. J. Spadafora, R. Demadrille, B. Ratier, and B. Grevin, "Imaging the carrier photo-generation in nanoscale phase segregated organic heterojunctions by kelvin probe force microscopy," *Nano Letters*, vol. 10, no. 9, pp. 3337–3342, 2010.

[25] J. W. Kiel, A. P. R. Eberle, and M. E. Mackay, "Nanoparticle agglomeration in polymer-based solar cells," *Physical Review Letters*, vol. 105, no. 16, p. 168701, 2010.

[26] K. Schmidt-Rohr, "Simulation of small-angle scattering curves by numerical fourier transformation," *J. Appl. Cryst.*, vol. 40, no. 1, pp. 16–25, 2007.

[27] C. Groves, L. J. A. Koster, and N. C. Greenham, "The effect of morphology upon mobility: Implications for bulk heterojunction solar cells with nonuniform blend morphology," *Journal of Applied Physics*, vol. 105, no. 9, p. 094510, 2009.

[28] G. A. Buxton and N. Clarke, "Computer simulation of polymer solar cells," *Modelling and Simulation in Materials Science and Engineering*, vol. 15, no. 2, pp. 13–26, 2007.

[29] O. Stenzel, L. J. A. Koster, R. Thiedmann, S. D. Oosterhout, R. A. J. Janssen, and V. Schmidt, "A new approach to model-based simulation of disordered polymer blend solar cells," *Advanced Functional Materials*, vol. 22, no. 6, pp. 1236–1244, 2012.

[30] M. R. Hammond, R. J. Kline, A. A. Herzing, L. J. Richter, D. S. Germack, H. W. Ro, C. L. Soles, D. A. Fischer, T. Xu, L. P. Yu, M. F. Toney, and D. M. DeLongchamp, "Molecular order in high-efficiency polymer/fullerene bulk heterojunction solar cells," *ACS Nano*, vol. 5, no. 10, pp. 8248–8257, 2011.

[31] D. Olds, P. Duxbury, J. Kiel, and M. Mackay, "Percolating bulk heterostructures from neutron reflectometry and small-angle scattering data," *Physical Review E*, vol. 86, no. 6, p. 061803, 2012.

[32] P. Würfel, *Physics of Solar Cells: From Principles to New Concepts.* Wiley-VCH, 2005.

[33] L. C. Tom Markvart, *Practical Handbook of Photovoltaics: Fundamentals and Applications.* Elsevier Science Inc, 2003.

[34] S. Fonash, *Solar Cell Device Physics.* New York: Academic, 1980.

[35] J. Nelson, *The Physics of Solar Cells.* Imperial College Press, 2003.

[36] D. M. S. C. D. F. D. J. Ellison, J. Y. Kim, "Determination of quase-fermi levels across illuminated organic donor/acceptor heterojunctions by kelvin prove force microscopy," *Journal of the American Chemical Society*, vol. 133, pp. 13802–13805, 2011.

[37] U. Wolf, V. I. Arkhipov, and H. Bässler, "Current injection from a metal to a disordered hopping system. i. monte carlo simulation," *Phys. Rev. B*, vol. 59, pp. 7507–7513, Mar 1999.

[38] J. Bardeen, "Surface states," *Phys. Rev.*, vol. 71, p. 717, 1947.

[39] K. N. S.M. Sze, *Physics of Semiconductor Devices.* Wiley-Interscience, 2006.

[40] P. Landsberg, *Recombination in Semiconductors.* New York: Cambridge University Press, 1991.

[41] C. R. McNeill and N. C. Greenham, "Charge transport dynamics of polymer solar cells under operating conditions: Influence of trap filling," *Applied Physics Letters*, vol. 93, p. 203310, Nov. 2008.

[42] C. M. Ramsdale, J. A. Barker, A. C. Arias, J. D. MacKenzie, R. H. Friend, and N. C. Greenham, "The origin of the open-circuit voltage in polyfluorene-based photovoltaic devices," *Journal of Applied Physics*, vol. 92, pp. 4266–4270, Oct. 2002.

[43] J. Nelson, "Diffusion-limited recombination in polymer-fullerene blends and its influence on photocurrent collection," *Phys. Rev. B*, vol. 67, p. 155209, 2003.

[44] R. F. J.J.M. Halls, *Organic photovoltaic devices.* Imperial College Press, 2001.

[45] S. Gïes, H. Neugebauer, and N. S. Sariciftci, "Conjugated polymer-based organic solar cells," *Chemical Reviews*, vol. 107, no. 4, pp. 1324–1338, 2007. PMID: 17428026.

[46] P. Peumans, S. Uchida, and S. R. Forrest, "Efficient bulk heterojunction photovoltaic cells using small-molecular-weight organic thin films," *Nature*, vol. 425, pp. 158–162, Sept. 2003.

[47] C. Groves, R. A. Marsh, and N. C. Greenham, "Monte carlo modeling of geminate recombination in polymer-polymer photovoltaic devices," *Journal of Chemical Physics*, vol. 129, p. 114903, Sept. 2008.

[48] C. Y. Yang, J. G. Hu, and A. J. Heeger, "Molecular structure and dynamics at the interfaces within bulk heterojunction materials for solar cells," *Journal of the American Chemical Society*, vol. 128, no. 36, pp. 12007–12013, 2006.

[49] S. Athanasopoulos, E. Hennebicq, D. Beljonne, and A. B. Walker, "Trap limited exciton transport in conjugated polymers," *Journal of Physical Chemistry C*, vol. 112, pp. 11532–11538, July 2008.

[50] D. S. Ginger and N. C. Greenham, "Charge separation in conjugated-polymer/nanocrystal blends," *Synthetic Metals*, vol. 101, pp. 425–428, May 1999.

[51] R. A. Marsh, C. Groves, and N. C. Greenham, "A microscopic model for the behavior of nanostructured organic photovoltaic devices," *Journal of Applied Physics*, vol. 101, no. 8, p. 083509, 2007.

[52] R. A. Marcus, "Electron transfer reactions in chemistry - theory and experiment," *Journal of Electroanalytical Chemistry*, vol. 438, pp. 251–259, 1997.

[53] B. Ray, P. R. Nair, E. R. Garcia, and M. A. Alam, "Modeling and optimization of polymer based bulk heterojunction(BH) solar cell," *IEEE Electron Devices Meeting*, vol. , no. , pp. 1–4, 2009.

[54] A. B. Walker, "Multiscale modeling of charge and energy transport in organic light-emitting diodes and photovoltaics," *Proceedings of the IEEE*, vol. 97, pp. 1587–1596, Sept. 2009.

[55] E. Hennebicq, G. Pourtois, G. D. Scholes, L. M. Herz, D. M. Russell, C. Silva, S. Setayesh, A. C. Grimsdale, K. Mllen, J.-L. Brdas, and D. Beljonne, "Exciton migration in rigid-rod conjugated polymers: an improved frster model," *Journal of the American Chemical Society*, vol. 127, no. 13, pp. 4744–4762, 2005. PMID: 15796541.

[56] I. G. Scheblykin, A. Yartsev, T. Pullerits, V. Gulbinas, and V. Sundstrm, "Excited state and charge photogeneration dynamics in conjugated polymers," *The Journal of Physical Chemistry B*, vol. 111, no. 23, pp. 6303–6321, 2007.

[57] Y. Kanai and J. C. Grossman, "Insights on interfacial charge transfer across p3ht/fullerene photovoltaic heterojunction from ab initio calculations," *Nano Letters*, vol. 7, no. 7, pp. 1967–1972, 2007.

[58] Z. Li, X. Zhang, and G. Lu, "Dipole-assisted charge separation in organicinorganic hybrid photovoltaic heterojunctions: Insight from first-principles simulations," *The Journal of Physical Chemistry C*, vol. 116, no. 18, pp. 9845–9851, 2012.

[59] T. W. Holcombe, J. E. Norton, J. Rivnay, C. H. Woo, L. Goris, C. Piliego, G. Griffini, A. Sellinger, J.-L. Bredas, A. Salleo, and J. M. J. Frechet, "Steric control of the donor/acceptor interface: Implications in organic photovoltaic charge generation," *Journal of the American Chemical Society*, vol. 133, no. 31, pp. 12106–12114, 2011.

[60] T. Liu and A. Troisi, "Absolute rate of charge separation and recombination in a molecular model of the p3ht/pcbm interface," *The Journal of Physical Chemistry C*, vol. 115, no. 5, pp. 2406–2415, 2011.

[61] T. Liu, D. L. Cheung, and A. Troisi, "Structural variability and dynamics of the p3ht/pcbm interface and its effects on the electronic structure and the charge-transfer rates in solar cells," *Phys. Chem. Chem. Phys.*, vol. 13, pp. 21461–21470, 2011.

[62] F. J. Martinez-Veracoechea and F. A. Escobedo, "Bicontinuous phases in diblock copolymer/homopolymer blends: Simulation and self-consistent field theory," *Macromolecules*, vol. 42, no. 5, pp. 1775–1784, 2009.

[63] R. Hamilton, C. G. Shuttle, B. ORegan, T. C. Hammant, J. Nelson, and J. R. Durrant, "Recombination in annealed and nonannealed polythiophene/fullerene solar cells: Transient photovoltage studies versus numerical modeling," *The Journal of Physical Chemistry Letters*, vol. 1, no. 9, pp. 1432–1436, 2010.

[64] L. J. A. Koster, E. C. P. Smits, V. D. Mihailetchi, and P. W. M. Blom, "Device model for the operation of polymer/fullerene bulk heterojunction solar cells," *Phys. Rev. B*, vol. 72, p. 085205, Aug 2005.

[65] G. A. Buxton and N. Clarke, "Predicting structure and property relations in polymeric photovoltaic devices," *Physical Review B*, vol. 74, p. 085207, Aug. 2006.

[66] I. Hwang, C. R. McNeill, and N. C. Greenham, "Drift-diffusion modeling of photocurrent transients in bulk heterojunction solar cells," *Journal of Applied Physics*, vol. 106, p. 094506, Nov. 2009.

[67] Y. M. Nam, J. Huh, and W. H. Jo, "Optimization of thickness and morphology of active layer for high performance of bulk-heterojunction organic solar cells," *Solar Energy Materials and Solar Cells*, vol. 94, no. 6, pp. 1118 – 1124, 2010.

[68] N. Christ, S. Kettlitz, S. Zufle, S. Valouch, and U. Lemmer, "Trap states limited nanosecond response of organic solar cells," in *Numerical Simulation of Optoelectronic Devices (NUSOD), 2010 10th International Conference on*, pp. 69–70, IEEE, 2010.

[69] C. R. McNeill, I. Hwang, and N. C. Greenham, "Photocurrent transients in all-polymer solar cells: Trapping and detrapping effects," *Journal of Applied Physics*, vol. 106, p. 024507, July 2009.

[70] T. Kirchartz, B. E. Pieters, K. Taretto, and U. Rau, "Mobility dependent efficiencies of organic bulk heterojunction solar cells: Surface recombination and charge transfer state distribution," *Phys. Rev. B*, vol. 80, p. 035334, Jul 2009.

[71] R. Li, Y. Peng, C. Ma, R. Wang, Y. Wang, H. Xie, T. Yang, J. Xie, S. Yan, and J. Zhang, "Effect of mixture ratio on the performance of mdmo-ppv:pcbm bulk heterojunction solar cells: A numerical study," *Materials Science and Engineering: B*, vol. 172, no. 3, pp. 305 – 310, 2010.

[72] T. Kirchartz, W. Gong, S. Hawks, T. Agostinelli, R. MacKenzie, Y. Yang, and J. Nelson, "Sensitivity of the mott–schottky analysis in organic solar cells," *Journal of Physical Chemistry C*, vol. 116, no. 14, p. 7672, 2012.

[73] C. G. Shuttle, R. Hamilton, B. C. ORegan, J. Nelson, and J. R. Durrant, "Charge-density-based analysis of the currentvoltage response of polythiophene/fullerene photovoltaic devices," *Proceedings of the National Academy of Sciences*, vol. 107, no. 38, pp. 16448–16452, 2010.

[74] T. Kirchartz, J. Mattheis, and U. Rau, "Detailed balance theory of excitonic and bulk heterojunction solar cells," *Phys. Rev. B*, vol. 78, p. 235320, Dec 2008.

[75] L. Y. Meng, Y. Shang, Q. K. Li, Y. F. Li, X. W. Zhan, Z. G. Shuai, R. G. E. Kimber, and A. B. Walker, "Dynamic monte carlo simulation for highly efficient polymer blend photovoltaics," *Journal of Physical Chemistry B*, vol. 114, no. 1, pp. 36–41, 2010.

[76] L. Y. Meng, D. Wang, Q. K. Li, Y. P. Yi, J. L. Bredas, and Z. G. Shuai, "An improved dynamic monte carlo model coupled with poisson equation to simulate the performance of organic photovoltaic devices," *Journal of Chemical Physics*, vol. 134, no. 12, p. 124102, 2011.

[77] J. Anta, "Random walk numerical simulation for solar cell applications," *Energy & Environmental Science*, vol. 2, no. 4, pp. 387–392, 2009.

[78] J. C. Blakesley and D. Neher, "Relationship between energetic disorder and open-circuit voltage in bulk heterojunction organic solar cells," *Phys. Rev. B*, vol. 84, p. 075210, Aug 2011.

[79] C. Groves, R. G. E. Kimber, and A. B. Walker, "Simulation of loss mechanisms in organic solar cells: A description of the mesoscopic monte carlo technique and an evaluation of the first reaction method," *Journal of Chemical Physics*, vol. 133, no. 14, p. 144110, 2010.

[80] J. Nelson, J. J. Kwiatkowski, J. Kirkpatrick, and J. M. Frost, "Modeling charge transport in organic photovoltaic materials," *Accounts of Chemical Research*, vol. 42, no. 11, pp. 1768–1778, 2009.

[81] T. Offermans, S. Meskers, and R. Janssen, "Monte-carlo simulations of geminate electron-hole pair dissociation in a molecular heterojunction: a two-step dissociation mechanism," *Chemical Physics*, vol. 308, pp. 125–133, JAN 10 2005.

[82] C. Groves and N. C. Greenham, "Bimolecular recombination in polymer electronic devices," *Physical Review B*, vol. 78, no. 15, p. 155205, 2008.

[83] B. P. Lyons, N. Clarke, and C. Groves, "The Quantitative Effect of Surface Wetting Layers on the Performance of Organic Bulk Heterojunction Photovoltaic Devices," *Journal of Physical Chemistry C*, vol. 115, pp. 22572–22577, NOV 17 2011.

[84] C. Groves, J. C. Blakesley, and N. C. Greenham, "Effect of charge trapping on geminate recombination and polymer solar cell performance," *Nano Letters*, vol. 10, no. 3, pp. 1063–1069, 2010.

[85] B. Zacher and N. R. Armstrong, "Modeling the effects of molecular length scale electrode heterogeneity in organic solar cells," *The Journal of Physical Chemistry C*, vol. 115, no. 51, pp. 25496–25507, 2011.

[86] H. P. Yan, S. Swaraj, C. Wang, I. Hwang, N. C. Greenham, C. Groves, H. Ade, and C. R. McNeill, "Influence of annealing and interfacial roughness on the performance of bilayer donor/acceptor polymer photovoltaic devices," *Advanced Functional Materials*, vol. 20, no. 24, pp. 4329–4337, 2010.

[87] C. R. McNeill, S. Westenhoff, C. Groves, R. H. Friend, and N. C. Greenham, "Influence of nanoscale phase separation on the charge generation dynamics and photovoltaic performance of conjugated polymer blends: Balancing charge generation and separation," *Journal of Physical Chemistry C*, vol. 111, no. 51, pp. 19153–19160, 2007.

[88] M. Casalegno, G. Raos, and R. Po, "Methodological assessment of kinetic monte carlo simulations of organic photovoltaic devices: The treatment of electrostatic interactions," *Journal of Chemical Physics*, vol. 132, no. 9, 2010.

[89] J. Williams and A. B. Walker, "Two-dimensional simulations of bulk heterojunction solar cell characteristics," *Nanotechnology*, vol. 19, no. 42, 2008.

[90] D. T. Gillespie, "Exact stochastic simulation of coupled chemical reactions," *The Journal of Physical Chemistry*, vol. 81, no. 25, pp. 2340–2361, 1977.

[91] S. Westenhoff, W. J. D. Beenken, A. Yartsev, and N. C. Greenham, "Conformational disorder of conjugated polymers," *Journal of Chemical Physics*, vol. 125, p. 154903, Oct. 2006.

[92] S. Athanasopoulos, J. Kirkpatrick, D. Martinez, J. M. Frost, C. M. Foden, A. B. Walker, and J. Nelson, "Predictive study of charge transport in disordered semiconducting polymers," *Nano Letters*, vol. 7, pp. 1785–1788, JUN 2007.

[93] S. Athanasopoulos, E. V. Emelianova, A. B. Walker, and D. Beljonne, "Exciton diffusion in energetically disordered organic materials," *Phys. Rev. B*, vol. 80, p. 195209, Nov. 2009.

[94] W. B. Russel, D. A. Saville, and W. R. Schowalter, *Colloidal Dispersions*. New York: Cambridge University Press, 1989.

[95] N. Sutin, "Theory of electron transfer reactions: insights and hindsights," *Progress in inorganic chemistry*, vol. 30, pp. 441–498, 1983.

[96] J. R. Miller, L. T. Calcaterra, and G. L. Closs, "Intramolecular long-distance electron transfer in radical anions. the effects of free energy and solvent on the reaction rates," *Journal of the American Chemical Society*, vol. 106, no. 10, pp. 3047–3049, 1984.

[97] J. A. Barker, C. M. Ramsdale, and N. C. Greenham, "Modeling the current-voltage characteristics of bilayer polymer photovoltaic devices," *Physical Review B*, vol. 67, p. 075205, Feb. 2003.

[98] H. J. Snaith, N. C. Greenham, and R. H. Friend, "The origin of collected charge and open-circuit voltage in blended polyfluorene photovoltaic devices," *Advanced Materials*, vol. 16, pp. 1640–+, Sept. 2004.

[99] M. Dresch, R. Isidoro, M. Linardi, J. Rey, F. Fonseca, and E. Santiago, "Influence of sol-gel media on the properties of nafion-sio¡ sub¿ 2¡/sub¿ hybrid electrolytes for high

performance proton exchange membrane fuel cells operating at high temperature and low humidity," *Electrochimica Acta*, 2012.

[100] E. J. Roche, M. Pineri, R. Duplessix, and A. M. Levelut, "Small-angle scattering studies of nafion membranes," *Journal of Polymer Science: Polymer Physics Edition*, vol. 19, no. 1, pp. 1–11, 1981.

[101] G. Gebel and J. Lambard, "Small-angle scattering study of water-swollen perfluorinated ionomer membranes," *Macromolecules*, vol. 30, no. 25, pp. 7914–7920, 1997.

[102] D. Shah, P. Maiti, D. Jiang, C. Batt, and E. Giannelis, "Effect of nanoparticle mobility on toughness of polymer nanocomposites," *Advanced Materials*, vol. 17, no. 5, pp. 525–528, 2005.

[103] A. Huq, R. Welberry, and E. Bozin, "Advances in structural studies of materials using scattering probes," *MRS bulletin*, vol. 35, no. 07, pp. 520–530, 2010.

[104] D. Rangappa, K. Murukanahally, T. Tomai, A. Unemoto, and I. Honma, "Ultrathin nanosheets of li2msio4 (m= fe, mn) as high-capacity li-ion battery electrode," *Nano letters*, vol. 12, no. 3, pp. 1146–1151, 2012.

[105] D. Spagnoli and J. Gale, "Atomistic theory and simulation of the morphology and structure of ionic nanoparticles," *Nanoscale*, vol. 4, no. 4, pp. 1051–1067, 2012.

[106] E. Lorenz, C. Keil, and D. Schlettwein, "Structure and morphology in thin films of perfluorinated copper phthalocyanine grown on alkali halide surfaces (001)," *Journal of Porphyrins and Phthalocyanines*, vol. 16, no. 07n08, pp. 977–984, 2012.

[107] A. McGlashon, W. Zhang, D. Smilgies, M. Shkunov, K. Genevicius, K. Whitehead, A. Amassian, G. Malliaras, D. Bradley, M. Heeney, *et al.*, "Spectroscopic and morphological investigation of conjugated photopolymerisable quinquethiophene liquid crystals," *Current Applied Physics*, vol. 12, pp. e59–e66, 2012.

[108] H. Wang, H. Jeong, M. Imura, L. Wang, L. Radhakrishnan, N. Fujita, T. Castle, O. Terasaki, and Y. Yamauchi, "Shape-and size-controlled synthesis in hard templates: Sophisticated chemical reduction for mesoporous monocrystalline platinum nanoparticles," *Journal of the American Chemical Society*, vol. 133, no. 37, pp. 14526–14529, 2011.

[109] D. Williams and C. Barry, *Transmission Electron Microscopy: A Textbook for Materials Science.* Springer, 2009.

[110] D. S. Sivia, *Elementary Scattering Theory for X-ray and Neutron Users.* Oxford University Press, 2011.

[111] A. Guinier, G. Fournet, C. Walker, and K. Yudowitch, *Small-angle scattering of X-rays*, vol. 14. Wiley New York, 1955.

[112] J. O'Donnell, X. Zuo, A. Goshe, L. Sarkisov, R. Snurr, J. Hupp, and D. Tiede, "Solution-phase structural characterization of supramolecular assemblies by molecular diffraction," *Journal of the American Chemical Society*, vol. 129, no. 6, pp. 1578–1585, 2007.

[113] D. Schneidman-Duhovny, M. Hammel, and A. Sali, "Foxs: a web server for rapid computation and fitting of saxs profiles," *Nucleic acids research*, vol. 38, no. suppl 2, pp. W540–W544, 2010.

[114] F. Poitevin, H. Orland, S. Doniach, P. Koehl, and M. Delarue, "Aquasaxs: a web server for computation and fitting of saxs profiles with non-uniformly hydrated atomic models," *Nucleic acids research*, vol. 39, no. suppl 2, pp. W184–W189, 2011.

[115] D. Tiede, K. Mardis, and X. Zuo, "X-ray scattering combined with coordinate-based analyses for applications in natural and artificial photosynthesis," *Photosynthesis research*, vol. 102, no. 2, pp. 267–279, 2009.

[116] H.-C. Liao, C.-S. Tsao, T.-H. Lin, C.-M. Chuang, C.-Y. Chen, U.-S. Jeng, C.-H. Su, Y.-F. Chen, and W.-F. Su, "Quantitative nanoorganized structural evolution for a high efficiency bulk heterojunction polymer solar cell," *Journal of the American Chemical Society*, vol. 133, no. 33, pp. 13064–13073, 2011.

[117] N. A. Gumerov, K. Berlin, D. Fushman, and R. Duraiswami, "A hierarchical algorithm for fast debye summation with applications to small angle scattering," *Journal of Computational Chemistry*, vol. 33, no. 25, pp. 1981–1996, 2012.

[118] S. R. Kline, "Reduction and analysis of sans and usans data using igor pro," *Journal of Applied Crystallography*, vol. 39, no. 6, pp. 895–900, 2006.

[119] J. Pérez and Y. Nishino, "Advances in x-ray scattering: from solution saxs to achievements with coherent beams," *Current Opinion in Structural Biology*, 2012.

[120] R. Jones, S. Kumar, D. Ho, R. Briber, and T. Russell, "Chain conformation in ultrathin polymer films using small-angle neutron scattering," *Macromolecules*, vol. 34, no. 3, pp. 559–567, 2001.

[121] H. C. B. J. S. Higgins, *Polymers and Neutron Scattering.* Oxford Science Publications, 1996.

[122] B. H. Zimm, "Apparatus and methods for measurement and interpretation of the angular variation of light scattering; preliminary results on polystyrene solutions," *The Journal of Chemical Physics*, vol. 16, no. 12, pp. 1099–1116, 1948.

[123] H. Hoppe and N. S. Sariciftci, "Morphology of polymer/fullerene bulk heterojunction solar cells," *J. Mater. Chem.*, vol. 16, no. 1, pp. 45–61, 2006.

[124] H. Hoppe, M. Niggemann, C. Winder, J. Kraut, R. Hiesgen, A. Hinsch, D. Meissner, and N. Sariciftci, "Nanoscale morphology of conjugated polymer/fullerene-based bulk-heterojunction solar cells," *Advanced Functional Materials*, vol. 14, no. 10, pp. 1005–1011, 2004.

[125] J. Jo, S.-I. Na, S.-S. Kim, T.-W. Lee, Y. Chung, S.-J. Kang, D. Vak, and D.-Y. Kim, "Three-dimensional bulk heterojunction morphology for achieving high internal quantum efficiency in polymer solar cells," *Advanced Functional Materials*, vol. 19, no. 15, pp. 2398–2406, 2009.

[126] P. Vanlaeke, A. Swinnen, I. Haeldermans, G. Vanhoyland, T. Aernouts, D. Cheyns, C. Deibel, J. DHaen, P. Heremans, J. Poortmans, and J. Manca, "P3ht/pcbm bulk heterojunction solar cells: Relation between morphology and electro-optical characteristics," *Solar Energy Materials and Solar Cells*, vol. 90, no. 14, pp. 2150 – 2158, 2006.

[127] M. S. White, D. C. Olson, S. E. Shaheen, N. Kopidakis, and D. S. Ginley, "Inverted bulk-heterojunction organic photovoltaic device using a solution-derived zno under-layer," *Applied Physics Letters*, vol. 89, no. 14, p. 143517, 2006.

[128] Z. Xu, L.-M. Chen, G. Yang, C.-H. Huang, J. Hou, Y. Wu, G. Li, C.-S. Hsu, and Y. Yang, "Vertical phase separation in poly(3-hexylthiophene): Fullerene derivative blends and its advantage for inverted structure solar cells," *Advanced Functional Materials*, vol. 19, no. 8, pp. 1227–1234, 2009.

[129] R. G. E. Kimber, A. B. Walker, G. E. Schroder-Turk, and D. J. Cleaver, "Bicontinuous minimal surface nanostructures for polymer blend solar cells," *Physical Chemistry Chemical Physics*, vol. 12, no. 4, pp. 844–851, 2010.

[130] C. F. Majkrzak and N. F. Berk, "Exact determination of the phase in neutron reflectometry," *Phys. Rev. B*, vol. 52, pp. 10827–10830, Oct 1995.

[131] E. Teller, N. Metropolis, and A. Rosenbluth, "Equation of state calculations by fast computing machines," *J. Chem. Phys*, vol. 21, no. 13, pp. 1087–1092, 1953.

[132] R. Glauber, "Time-dependent statistics of the ising model," *Journal of mathematical physics*, vol. 4, p. 294, 1963.

[133] K. Kawasaki, "Kinetics of ising models," *Phase transitions and critical phenomena*, vol. 2, pp. 443–501, 1972.

[134] A. Nelson, "Co-refinement of multiple-contrast neutron/X-ray reflectivity data using MOTOFIT," *Journal of Applied Crystallography*, vol. 39, pp. 273–276, Apr 2006.

[135] A. Salleo, R. J. Kline, D. M. DeLongchamp, and M. L. Chabinyc, "Microstructural characterization and charge transport in thin films of conjugated polymers," *Advanced Materials*, vol. 22, no. 34, pp. 3812–3838, 2010.

[136] D. A. Chen, A. Nakahara, D. G. Wei, D. Nordlund, and T. P. Russell, "P3ht/pcbm bulk heterojunction organic photovoltaics: Correlating efficiency and morphology," *Nano Letters*, vol. 11, no. 2, pp. 561–567, 2011.

[137] B. A. Collins, J. R. Tumbleston, and H. Ade, "Miscibility, Crystallinity, and Phase Development in P3HT/PCBM Solar Cells: Toward an Enlightened Understanding of Device Morphology and Stability," *Journal of Physical Chemistry Letters*, vol. 2, pp. 3135–3145, DEC 15 2011.

[138] C. R. McNeill, "Morphology of all-polymer solar cells," *Energy and Environmental Science*, vol. 5, pp. 5653–5667, 2012.

[139] D. DeLongchamp, R. Kline, and A. Herzing, "Nanoscale structure measurements for polymer-fullerene photovoltaics," *Energy Environ. Sci.*, vol. 5, no. 3, pp. 5980–5993, 2012.

[140] W. Oosterbaan, J. Bolsée, A. Gadisa, V. Vrindts, S. Bertho, J. D'Haen, T. Cleij, L. Lutsen, C. McNeill, L. Thomsen, *et al.*, "Alkyl-chain-length-independent hole mobility via morphological control with poly (3-alkylthiophene) nanofibers," *Advanced Functional Materials*, vol. 20, no. 5, pp. 792–802, 2010.

[141] I. Hwang and N. C. Greenham, "Modeling photocurrent transients in organic solar cells," *Nanotechnology*, vol. 19, p. 424012, Oct. 2008.

[142] L. D. Landau and E. Lifshitz, *Electrodynamics of Continuous Media - 2nd ed.* Pergamon Press, 1984.

[143] C. Farrow, M. Shaw, H. Kim, P. Juhás, and S. Billinge, "Nyquist-shannon sampling theorem applied to refinements of the atomic pair distribution function," *Physical Review B*, vol. 84, no. 13, p. 134105, 2011.